The structure of the Magellanic Clouds traced by red clump stars at near-infrared wavelengths

Benjamin Tatton

Doctor of Philosophy

Department of Physics, Keele University

December 2018

Abstract

This thesis is about the Red Clump (RC) star population within the Magellanic Clouds. These are observed in the near-infrared $YJK_{\rm s}$ wavelengths using data obtained by the ESO public VMC survey. These were studied to shed more light on the internal structure and past and current evolution of this interacting system of dwarf irregular galaxies.

RC stars were selected from the colour magnitude diagram (CMD) using a contour method to assign the selection box and reddening vector. The $J - K_{\rm s}$ vs $K_{\rm s}$ CMD of the central 30 Doradus region of the Large Magellanic Cloud (LMC) region was analysed to determine the extinction content there, producing a reddening map. This was compared with other works including an optical reddening map which also used RC stars. The reddening map also proved to be a useful tool as a tracer of ISM features including the identification of molecular clouds.

The extinction maps were made in the $Y - K_{\rm s}$ colours for the whole LMC and whole SMC. These were then used to deredden the populations. These populations had their distribution examined in a number of ways including line of sight depth and residuals derived from least-squares plane fitting. The distorted structures found appear to be the product of interactions between the LMC and SMC.

RC content was also studied in the Magellanic Bridge region (lying between the LMC and SMC) where a RC population was found throughout the Bridge, mainly at LMC distance and mostly towards the LMC and SMC showing evidence of a tidally stripped SMC population. Maps were created showing this.

This thesis thus presents an unprecedented, global view of the stellar and interstellar structure of the interacting Magellanic Cloud, using an intermediate-age stellar tracer, piercing through and using dust.

Acknowledgements

The work presented in Chapter 4 of the thesis is based on the published and peer reviewed work of Tatton et al. (2013a). I thank the members of the VMC team who co-authored this work with me, and who provided helpful comments to the draft manuscript of this paper. These individuals are: J. Th. van Loon, M.-R. Cioni, G. Clementini, J. P. Emerson, L. Girardi, R. de Grijs, M. A. T. Groenewegen, M. Gullieuszik, V. D. Ivanov, M. I. Moretti, V. Ripepi, and S. Rubele. In more general terms the VMC team has provided me with feedback following talks I have given at their meetings. I give special thanks to two VMC members: Stefano Rubele for creating the PSF photometry catalogues and Smitha Subramanian for technical assistance on plane fitting.

My PhD was funded by an S.T.F.C. studentship awarded to Keele University (and also by Keele University themselves via the ACORN doctoral award scheme), these paid the course fees essential for my studying, travel expenses and a stipend.

To sound like the acknowledgement section of a paper for a second; I acknowledge the VISTA Data Flow System pipeline processing and science archive described in Irwin et al. (2004) and Cross et al. (2012). Nick Cross (and sometimes other VSA & CASU members) were there to provide technical support whenever I had problems.

For all the help and support with this long journey I would like to thank my supervisor Jacco van Loon and everyone else who offered (or gave) any help. The Keele University campus with its woodlands full of natural wonders have also provided respite.

Contents

List of Figures

List of Tables

1 Introduction

In this thesis I have used a particular type of red giant star ("Red Clump") to map the structure of two of the Milky Way's neighbouring galaxies, the Large Magellanic Cloud (LMC) and the Small Magellanic Cloud (SMC). These are known collectively as the Magellanic Clouds. This first chapter aims to introduce the context and reasons why this is interesting, particularly in relation to the formation and evolution of galaxies. It first presents an overview of the relevant topics, before delving into some more detail regarding what was known about the Magellanic Clouds and Red Clump stars. The chapter ends by defining the scientific questions that formed the basis for my work.

1.1 Overview

1.1.1 Galaxy formation and evolution

The baryonic evolution of the Universe is seen in summary through the way galaxies have formed and changed over cosmic time. But the physical causes for galaxy evolution take place on smaller scales, and to some extent continue to play in the nearby, present-day Universe. By studying nearby galaxies one may therefore find clues, or even insight into the formation and early evolution of galaxies. We, on Earth, inhabit a galaxy ourselves, and understanding how galaxies behave and change over time is of profound importance for understanding our own place in the cosmic history.

The current understanding of galaxy formation can be illustrated in the flow chart presented by Mo et al. (2010), represented here in Figure 1.1. It attempts to provide a blueprint for the formation of different types of galaxies, depending on what scenario applied to that particular one. It distinguishes between discy and spheroidal types of outcomes. The Magellanic Clouds, irregular gas-rich galaxies are discs but have yet to completely lose their gaseous discs (Nidever, 2014).

In observations of the early Universe galaxies are observed and there are two the-

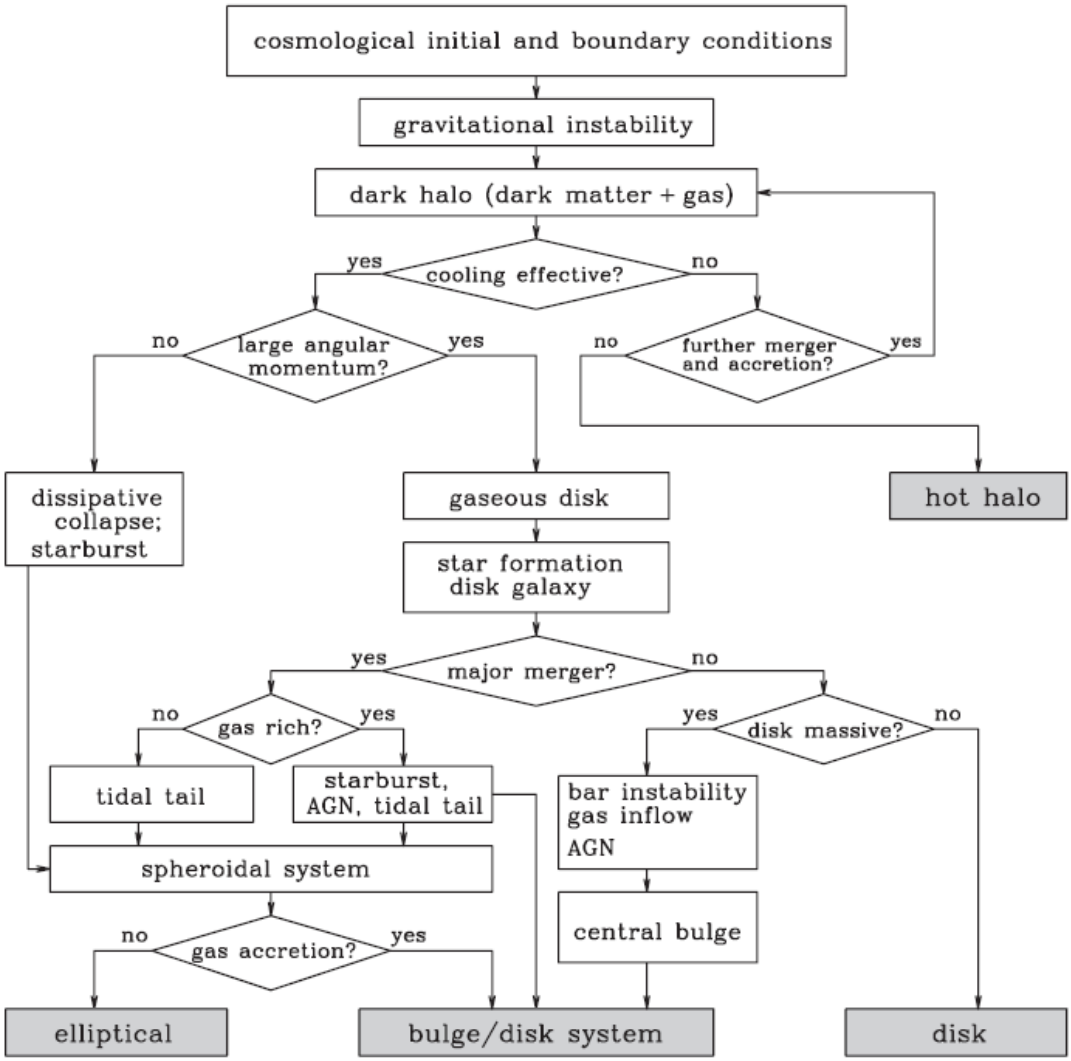

Figure 1.1: *(Figure 1.1. from Mo et al. (2010)).* A logic flow chart for galaxy formation. In the standard scenario, the initial and boundary conditions for galaxy formation are set by the cosmological framework. The paths leading to the formation of various galaxies are shown along with the relevant physical processes. Note however, that processes do not separate as neatly as this figure suggests. For example, cold gas may not have the time to settle into a gaseous disc before a major merger takes place.

ories that explain how these initial galaxies formed, known as top-down and bottom-up. Under the top-down scenario large gas clouds collapse under gravitational pull, fragmenting into galaxies. The bottom-up scenario on the other hand has clumps of matter about the size of globular clusters which collapse under self gravity to form dwarf galaxies. These dwarf galaxies undergo further gravitation, forming into larger galaxies and clusters of galaxies. Under the bottom-up scenario gravity is the mechanism of forming larger galaxies. A hybrid of these two theories best fits current observations although the top-down scenario is no longer widely accepted. For example within the Magellanic Clouds, the hierarchical structure of the Large Magellanic Cloud (LMC) is more easily understood from a top-down perspective (Efremov, 1995) but the Magellanic Clouds themselves appear to have satellites and might be merging which is an example of bottom-up.

Dark matter is a component of the standard model of the Universe which contains two types of matter; observable matter known as baryonic matter and non-observable dark matter. Zwicky (1933) identified this dark matter when finding discrepancies between expected virial mass and the actual mass in some clusters. Detection however has come more recently from studies into rotational curves of galaxies. For example, Persic & Salucci (1995); van Albada et al. (1985).

Dark matter halos are the foundation to galactic structure formation (Press & Schechter, 1974) because the visible stellar disc is embedded into this and the mass of the dark matter halo itself provides gravitational forces which prevent the high velocity stars and gas from being ejected from the galaxy. Dark matter halos form a part of some hierarchical scenarios such as gravitational collapse (White & Rees, 1978). The two main computational techniques for determining galaxy formation are Semi-Analytical Models (SAMs) and N-body simulations. The SAMs include baryonic matter properties (so can be linked to observations) but have the limitation of several properties being linked to one parameter. White & Frenk (1991) has the first SAMs. These were improved to track evolving dark matter halos (Kauffmann et al., 1993; Cole et al., 1994). More recently, reliability has been improved providing further agreement with observed data (e.g. Benson & Bower, 2010; Guo et al., 2011; Khochfar et al.,

2011). The N-body approach uses hydrodynamical simulations where models are used to describe gravitational laws and gas dynamics, whilst N-body simulations can treat stars. This approach has the drawback of requiring more computational power. Both techniques are fairly consistent with one another.

Dynamical evolution is how most elliptical galaxies are thought to have formed, as dynamical friction leads to the orbital energies and the matter being transferred. A distorted morphology of a galaxy (such as bridges and tails) is tied to its dynamical history (Toomre & Toomre, 1972). These dynamical processes include internal instabilities, tidal interactions and mergers (Dubinski, 1999). Interactions and distorted morphologies are both features of the Magellanic Clouds.

Interactions are an important driver of formation and evolution (Larson & Tinsley, 1978; Barnes & Hernquist, 1992). The hierarchical galactic formation model (Press & Schechter, 1974; White & Rees, 1978) describes galaxies forming from interactions and mergers. This is supported by a host of observations ranging from large spirals to dwarf galaxies (Noël et al., 2015). The Magellanic Clouds also have been interacting, both between themselves and the Milky Way.

The effects of interactions are seen in the appearances and star formation rates of galaxies. Galaxies form clusters and orbit around each other. These orbits can have epochs when two galaxies pass closer to each other. Galaxies are not single solid objects so when they pass each other they can undergo inelastic collisions (collisions where kinetic energy is not conserved) meaning some of the collision energy is transferred to the stars and gas in each galaxy. The tidal forces will often induce star formation and distort the spiral pattern in both galaxies (i.e. a morphological and mass evolution). If enough energy is transferred internally to the stars, then galaxies may merge. Depending on the epoch of the last major merger, a galaxy may end up resembling morphologically a spiral galaxy, or an elliptical galaxy.

Our key to observing past interactions comes from the stars which formed in them and there are two timescales to consider here. The first is the stellar lifetimes which post star formation are on the scale of $10^7 - 10^{10}$ yrs (this is important due to using these tracers related to when and where they formed) and the second is the dynamical

timescales (star orbits) which for medium size galaxies (i.e. the LMC) are on the scale of 10^8 yrs (important for populations settling, structure seen can be related to when and where they formed).

In this thesis I am studying the structure of the Magellanic System; which comprises of two galaxies which interact with each other and the Milky Way. The two galaxies are gas rich, star forming and have different structures between the Large and Small Magellanic Clouds; the LMC is a disc with spiral arms, whereas the Small Magellanic Cloud (SMC) is more distorted.

1.1.2 The Magellanic Clouds as a case study of galaxy structure and evolution

The details of how galaxies have evolved over cosmological times are imprinted in their star formation history (SFH), chemical enrichment and morpho-kinematic structure. The Local Group are the nearest group of such galaxies giving us the best insight into how groups of galaxies form, evolve and interact with each other. The Magellanic System (shown in Figure 1.2) is comprised of the two Local Group galaxies; the Large Magellanic Cloud (LMC; shown in Figure 1.3) and the Small Magellanic Cloud (SMC; shown in Figure 1.4), the Magellanic Bridge between them and the Magellanic Stream. The Magellanic Clouds lie in the Southern sky, around RA $\sim 4\overset{\text{h}}{.}5-6^{\text{h}}$ and Dec $\sim -65^\circ - -70^\circ$ (LMC) and RA $\sim 0\overset{\text{h}}{.}5-1^{\text{h}}$ and Dec $\sim -72^\circ - -74^\circ$ (SMC), though the Stream reaches the Northern sky. The Magellanic Clouds are of dwarf irregular morphology, meaning they are neither spiral nor elliptical in appearance and they are gas-rich but of relatively low mass and consequently metal poor. Also, the galaxies have interacted with each other in the past. In terms of size along each major axis the LMC and SMC have diameters of 4 kpc and 2.7 kpc, respectively (using axis values from Cook et al., 2014). While the LMC is the fourth largest body in the Local Group it is much smaller than the top three; M31, the Milky Way and M33. In M31 the stellar halo has been detectable at radii of 70 kpc (Chapman et al., 2006) and in M33 the 21-cm rotation curve extends out to 16 kpc (Corbelli & Salucci, 2000), these are much larger than the

LMC.

The LMC rotation curve implies a mass of $> 1.5 \times 10^{10} M_{\odot}$ (Schommer et al., 1992) while recent research finds an enclosed stellar mass implied from velocity of $1.7 \pm 0.7 \times 10^{10} M_{\odot}$ (van der Marel & Kallivayalil, 2014) and a total mass of $2.5 \times 10^{11} M_{\odot}$ (Peñarrubia et al., 2016). The factor of 10 difference seen in the work of Peñarrubia et al. (2016) suggests there is an extended dark matter halo surrounding the LMC. The SMC total mass is at least $6.5 \times 10^{9} M_{\odot}$ (Bekki & Stanimirović, 2009). For the gaseous mass Grebel (2004) reviewed this and LMC gaseous content is $0.5 \times 10^{9} M_{\odot}$ (Kim et al., 1998) which makes up around 9% of total mass. In the SMC the fraction of gaseous content is a much higher $\sim 21\%$ with an H I mass of $4.2 \times 10^{8} M_{\odot}$ (Stanimirović et al., 1999).

The LMC is ~ 50 kpc away and is seen from face on with inclination of $i \sim 23°$–$37°$ (van der Marel & Cioni, 2001; Olsen & Salyk, 2002; Subramanian & Subramaniam, 2010)[1], has an angular size of $645' \times 550'$[2] and a metallicity of $0.5\, Z_{\odot} - 0.33\, Z_{\odot}$[3] which decreases with distance to centre (Cioni, 2009)[4]. The LMC has an off-centred stellar bar which appears to be located on the plane of its disc (Subramaniam & Subramanian, 2009). The LMC itself is ~ 4 kpc thick along the line-of-sight (Subramanian & Subramaniam, 2009). This is quite thick when compared to edge-on spiral galaxies.

On the other hand, the SMC is highly inclined if viewed as a disc ($i = 65.^{\circ}5$), further away at a distance of ~ 61 kpc, having a smaller angular size ($320' \times 185'$[5]) and a metallicity of $0.25\, Z_{\odot} - 0.10\, Z_{\odot}$[6] which has a consistent, flat distribution (Cioni, 2009). The bar feature of the SMC is found in the centre with an Eastern extension known as the Wing (Gonidakis et al., 2009). The thickness of the SMC is more varied

[1] Some of the reason for this variance is due to the LMC disc being warped (Olsen & Salyk, 2002).

[2] `https://ned.ipac.caltech.edu/`

[3] Higher value is youngest stars from Cioni et al. (2011), lower value, population average from Kunth & Östlin (2000).

[4] However, when removing selection bias as Feast et al. (2010) did a much flatter gradient for the inner LMC is found with a dramatic drop at the outer part.

[5] `https://ned.ipac.caltech.edu/`

[6] Higher value is youngest stars from Cioni et al. (2011), lower value, population average from Kunth & Östlin (2000).

due to a more complex structure, being either in the range of $3-5$ kpc for the bar region (Subramanian & Subramaniam, 2009) or $10-20$ kpc overall (Hatzidimitriou & Hawkins, 1989; Gardiner & Hawkins, 1991; Groenewegen, 2000). This difference is due to the North–Eastern region and could be caused by a tidal interaction with the Milky Way (Gardiner & Hawkins, 1991).

Dynamical interactions between the LMC and SMC may have triggered episodes of star formation throughout their history (Zaritsky et al., 2004). Bekki et al. (2004) used simulations to investigate why the globular clusters in the LMC are $\sim$ 13 Gyr or $\sim$ 3 Gyr old and these simulations suggest the cause of the latter is strong tidal interactions which were triggered by the LMC and SMC having a near collision $\sim$ 4 Gyr ago. Such an event may have created the Bridge connecting the two galaxies as the Bridge contains a population of young stars and has a metallicity similar to the SMC's supporting a recent SMC origin (Cioni, 2009).

The Stream, unlike the Bridge appears to be an interstellar cloud complex covering much of the Southern sky and even continuing into Northern latitudes. It has a counter-stream, the Leading Arm, a scattering of clouds ahead of the LMC. The Stream, and what it reveals about the history of the Magellanic Clouds themselves and their interaction, is extensively discussed in the review by D'Onghia & Fox (2016).

The distance of the Magellanic System is special because at first approximation all objects appear to be at the same distance and close enough to be able to resolve in detail the stellar populations. Also this serves as an anchor point of the extragalactic distance scale due to a variety of distance indicators being capable of being used here to great accuracy.

From the above summary it is clear that the Magellanic System is a complex system of (at least) two distorted galaxies, raising multiple questions that await answers. Cioni et al. (2011) mention a number of these some of which I will repeat here: What is the origin of the Magellanic Clouds? What is their fate? Will the Bridge evolve into a galaxy of its own or will it be merged into the LMC? Does the LMC have an ordinary bar and how does it influence the LMC evolution? Or, is the offset bar actually a separate galaxy being merged into the LMC disc? Does the LMC have a metal poor

Figure 1.2: Photographic image of the Magellanic System (from `http://www.eso.org/public/images/b01/`), SMC is on the right and LMC on the left. The bright object to the West (right) of the SMC is the Galactic globular cluster 47 Tucanae.

old halo? Why is there a significant difference between the structure of gas and stars in the SMC? Does the SMC have a disc, or a bulge? What is certain is that the stellar populations must be resolved in detail to give us our best chance of answering these.

An additional motive to understand stellar structure is that stellar populations act as tracers of structure and of distance on the cosmological scale. The ultimate goal is to achieve an accurate value for the Hubble constant, H_0 but this requires the previous steps being as accurate as possible. With the advent of modern astronomy bringing with it wide-field high resolution surveys, our nearest Local Group galaxies can be resolved down to individual star level at faint magnitudes giving access to different tracers of stellar populations (at the distance of the Magellanic Clouds the near-infrared observations can reach stars like the Sun). With accurate distance indicators, even the distribution along the line-of-sight may be resolved, giving us a unique three-dimensional picture of a galaxy. The location of dust, betrayed by its reddening effect of stars within the galaxy adds further insight into the structure, and hence the evolution

Figure 1.3: Photographic image of the LMC taken by Yuri Beletsky (from `https://apod.nasa.gov/apod/ap080409.html`).

Figure 1.4: Photographic image of the SMC (from `https://apod.nasa.gov/apod/ap100903.html`). In addition to 47 Tucanae (right) is another globular cluster; NGC 362 (top).

of the galaxy.

1.2 Red Clump stars

The Red Clump (RC) stars are the main tools I use as a tracer for extinction, structure and ultimately stellar history. The RC stars are useful for mapping interstellar reddening and 3-D structure because of their large numbers and relatively fixed luminosity. The former gives us a large sample size that is well distributed (due to their ages they have mixed relatively well dynamically) and the latter means that changes in magnitude and colour due to reddening and distance (i.e. environment and structure) quickly dominate over those as a result of population differences.

In terms of star type the RC stars form a metal-rich counterpart to the horizontal branch. Stars in this phase of stellar evolution undergo core helium and shell hydrogen burning. RC stars are of intermediate age ($\sim$ 1–10 Gyr)[7] and mass ($\sim$ 1–3 $M_{\odot}$, Girardi & Salaris 2001); following the first ascent of the red giant branch (RGB) the RC phase typically lasts $\sim$ 0.1 Gyr (up to 0.2 Gyr). As a result they appear easily noticeable in CMDs of populations older than $\sim$ 0.5 Gyr as a clump of stars close to the RGB (Salaris, 2012, their figure 4.). A colour–magnitude diagram (CMD) is also shown in Figure 1.5.

The RC represents the intermediate-age population in a galaxy. It thus has unique diagnostic value as compared to their more massive siblings, the Cepheids, and their lower-mass, more metal-poor siblings, the RR Lyræ. Cepheids and RR Lyræ are galaxy structure tracers of choice because they are easily recognised through their characteristic variability, but they do not probe the vast part of a galaxy's evolution as the RC stars do, and they are less plentiful.

An early description of the RC stars can be found in Cannon (1970) and it makes the prediction of an abundance of these within the solar neighbourhood (from the study

[7]Except when in a metal rich population in which case it can be very old ($>$ 10 Gyr).

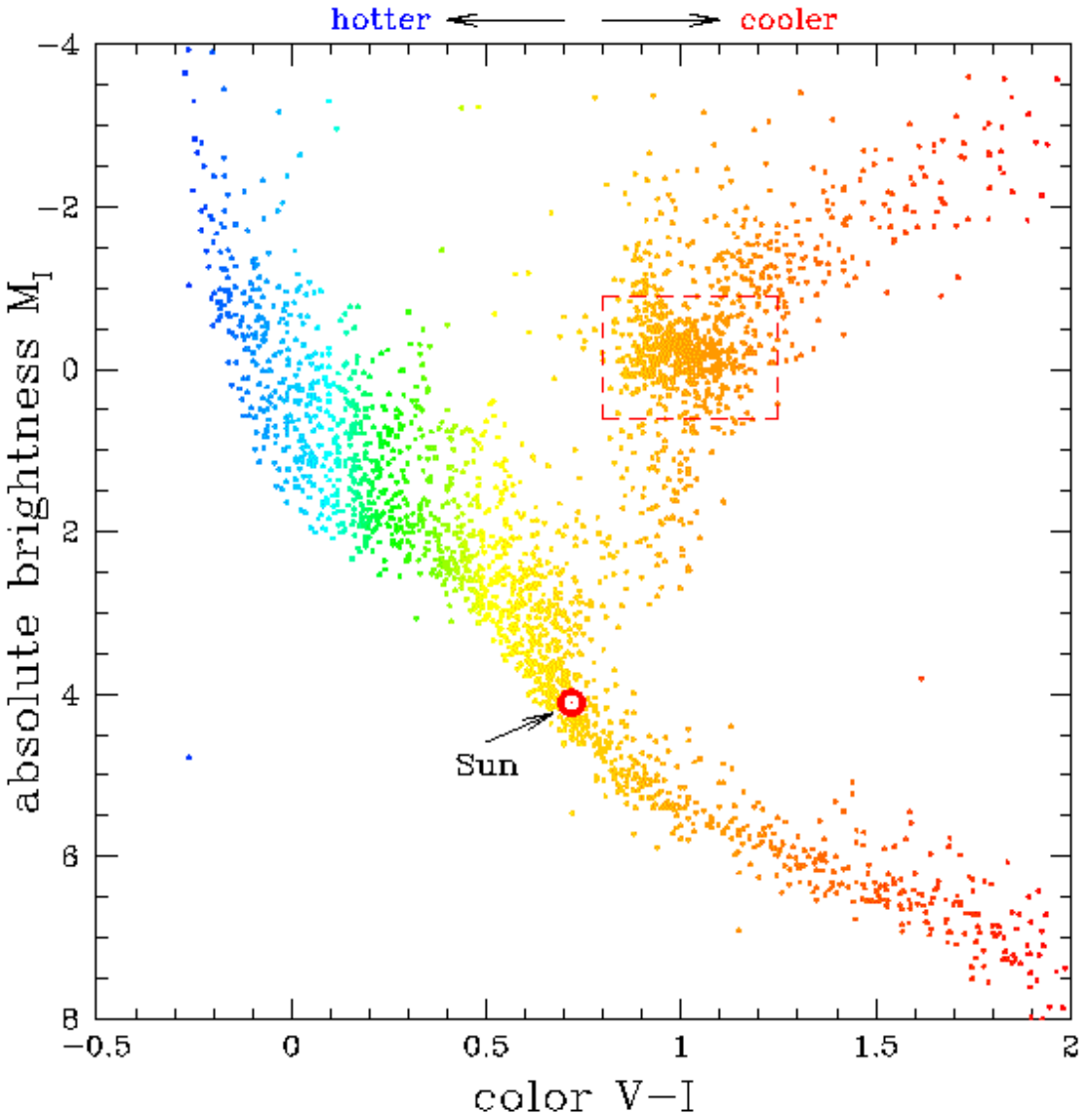

Figure 1.5: Absolute mag M_I vs. $V - I$ (from `http://www.astronomy.ohio-state.edu/~kstanek/CfA/RedClump/`) for Hipparcos data. Red Clump region outlined by red dashed line.

of 37 open clusters). This prediction was fully verified when the preliminary Hipparcos[8] catalogue was analysed by Perryman et al. (1995) (HR diagrams prior to this in the solar neighbourhood did not reach sufficient distance). The Hipparcos catalogue was published in 1997 (Perryman, 1997) and contains ~ 600 RC stars.

However, modelling work did not wait for observations with Faulkner & Cannon (1973) constructing an isochrone – this was the first time anyone had tried to do so. They concluded that the RC is the population I analogue of the horizontal branch. The modelled isochrone does have some differences when compared with the eventual observations though.

An important feature of the Red Clump is the Secondary Red Clump (SRC) feature. This is described in Girardi (1999) as being the youngest RC stars with an age of 1 Gyr. These are found up to 0.4 mag fainter than the main clump and are helium burning (with enough mass to ignite helium in non-degenerate conditions). Salaris (2012) provides further review of theory and methodology behind using the RC stars.

1.2.1 Hipparcos and the use of RC stars as distance indicators

Distance measurements using the RC stars began when the Hipparcos satellite data provided parallaxes for many of these stars. As the parallax is a direct, geometrical measure of distance, it enables a reliable calibration of the absolute magnitudes of RC stars.

The pioneering work in this regard is that of Paczynski & Stanek (1998), which used a high-quality I band Hipparcos selection to conclude that there is no colour dependence. This was despite theoretical models of the time showing a weak dependence of the bolometric magnitude on age and chemical composition. Thus, the I band can be used in applications of the RC as a standard candle with a luminosity function

[8]Hipparcos was a space mission launched in 1989. It lasted until 1993 (`http://www.rssd.esa.int/index.php?project=HIPPARCOS`).

that is well represented by a Gaussian. This was subsequently applied by Stanek & Garnavich (1998) and Udalski et al. (1998) to determine distances to M31 and the LMC, the latter of which (with a distance modulus of $(m - M) = 18.08 \pm 0.12$ mag) was ~ 0.4 mag smaller than other accepted values at the time, but comparable to the RR Lyrae studies that had also been calibrated with Hipparcos data (which have a distance modulus of $(m - M) = 18.26 \pm 0.15$ mag).

Later work by Udalski (2000), however, uncovered a weak dependence of the I-band absolute magnitude on metallicity (~ 0.13 mag dex^{-1}). Girardi & Salaris (2001) then calculated theoretical I-band RC magnitudes as a function of age and metallicity, that reproduced observations quite well.

Observationally, Grocholski & Sarajedini (2002) investigated the sensitivity of the RC K-band magnitude to metallicity and age, using 2MASS JK data for 14 open clusters and 2 globular clusters. They found that, for clusters younger than 2 Gyr, the absolute magnitude of the RC has a strong dependence on age; for older clusters, the dependence is largely on metallicity. This is consistent with the predictions by the Girardi & Salaris (2001) models. In general, the dependencies are weaker in the K band than in the I band, indicating that near-IR observations are preferred over optical measurements. This new calibration was applied to two star clusters in the LMC by Sarajedini et al. (2002) and Grocholski et al. (2007), the latter of which was consistent with Cepheid studies.

Motivated by this excursion into the near-IR domain, Salaris & Girardi (2002) explored the K-band behaviour in more detail, finding that the age dependence becomes a metallicity dependence after 1.5 Gyr (this agrees with Grocholski & Sarajedini (2002)) and the M_K decreases with increased stellar metallicity, Z. This is the opposite of what is seen in the V and I bands. While they confirmed that M_K is less sensitive to metallicity than M_V and M_I for stars younger than ~ 4 Gyrs, at older ages they found that M_K is affected more than M_I. Because the RC is dominated by populations younger than 4 Gyr, in this work I benefit from the weaker sensitivity in the K band.

The Hipparcos parallaxes have been revised over time, but the absolute magnitudes of the Hipparcos RC stars in I and K ($M_I = -0.22 \pm 0.0.3$ mag and

$M_K = -1.54 \pm 0.04$ mag) have not changed substantially (Groenewegen, 2008). These values agree with the theoretical values from Salaris & Girardi (2002) at the 1–2 σ level.

1.3 Extinction and reddening laws

Studies in galaxies are impeded by attenuation of starlight by dust in the interstellar medium (ISM) and its variance with wavelength (Gieren et al., 2013). By mapping the extinction we are able to reverse its effects and hence improve the reliability of the derived SFH and three-dimensional morphology. At the same time, the distribution of dust provides valuable insight into the structure of the ISM and its relation to recent, current and potential future star formation from dense molecular clouds.

Extinction varies with wavelength, making optical and infrared colour redder – hence this is referred to as reddening. Reddening is typically quantified using a colour excess (e.g., $E(B-V)$), while extinction is quantified for single bands. The attenuation A_λ is directly related to the optical depth of the dust column via:

$$A_\lambda = \Delta m = -2.5 \log e^{-\tau_\lambda} = 2.5 \tau_\lambda \log e = 1.086 \tau_\lambda \tag{1.1}$$

Extinction laws (discussed in sections 1.3.1 and 1.3.2) quantify these, where they are parametrised by the ratio of total to selective extinction: $R_V = A_V / E(B-V)$, where R_V is dependent on ISM conditions but 3.1 is a typical value for the Milky Way. In this thesis I determine reddening from colour excess which I convert into A_V extinction.

1.3.1 Extinction law – line-of-sight

Cardelli et al. (1989) found that the relationship between infrared, optical, and ultraviolet extinction can be described with one parameter R_V. They used a sample of 29 stars (this was a relatively large amount in 1989). O'Donnell (1994) applied some changes to this solution in the optical region of the curve. This has the effect of making it agree better with the $R_V = 3.1$ interstellar extinction curve.

However, there are problems with this law, an overview of which is given by Maíz Apellániz (2013). These include aspects such as the usage of R_V as a parameter as this is filter-integrated rather than monochromatic.

1.3.2 Extinction law – mixed geometry

A less commonly used Calzetti extinction law (Calzetti, 2001) can be applied to starburst regions as well as mixed dust source geometries (that is including scatter into and out of the line-of-sight). Fischera et al. (2003) provided an application of this.

1.3.3 R_V values

It is worth bearing in mind given my work is mainly in the near-infrared (NIR) that for wavelengths beyond $0.8\,\mu$m, R_V has little effect on the extinction curve. However, in the optical a change of $\Delta R_V = 0.7$ leads to 6% scatter in A_V/A_∞ (based on the sample of Clayton & Cardelli 1988). R_V varies from one sightline to another with values ranging from $2.1 - 5.8$ (Draine, 2003). The diffuse ISM has a mean R_V of ~ 3.1 (Savage & Mathis, 1979). Udalski (2003) infers $R_V \simeq 3.1$ towards the LMC. Gordon et al. (2003) also found, on average, little deviation in optical and UV extinction laws when testing these against various lines of sight for the Magellanic System.

However, for the SMC it is worth noting the extinction curve looks very different to that of the Milky Way. Figure 1.6 (a copy of figure 6 from Li et al. 2015) shows the extinction curve in the SMC bar region has an almost completely linear rise with λ^{-1} lacking the bump at 2175Å. This may be due to UV radiation and shocks from star formation destroying the carriers of this. However in sightlines that pass through the weaker star forming SMC Wing region there is a 2175Å bump present although at a lower intensity than in the Milky Way.

Despite variations in extinction law, the effect arising from that uncertainty on the distances, especially when determined at infrared wavelengths, may be modest. Gieren et al. (2013) concluded that changing R_V from 2.5 to 4.5 adjusted the derived

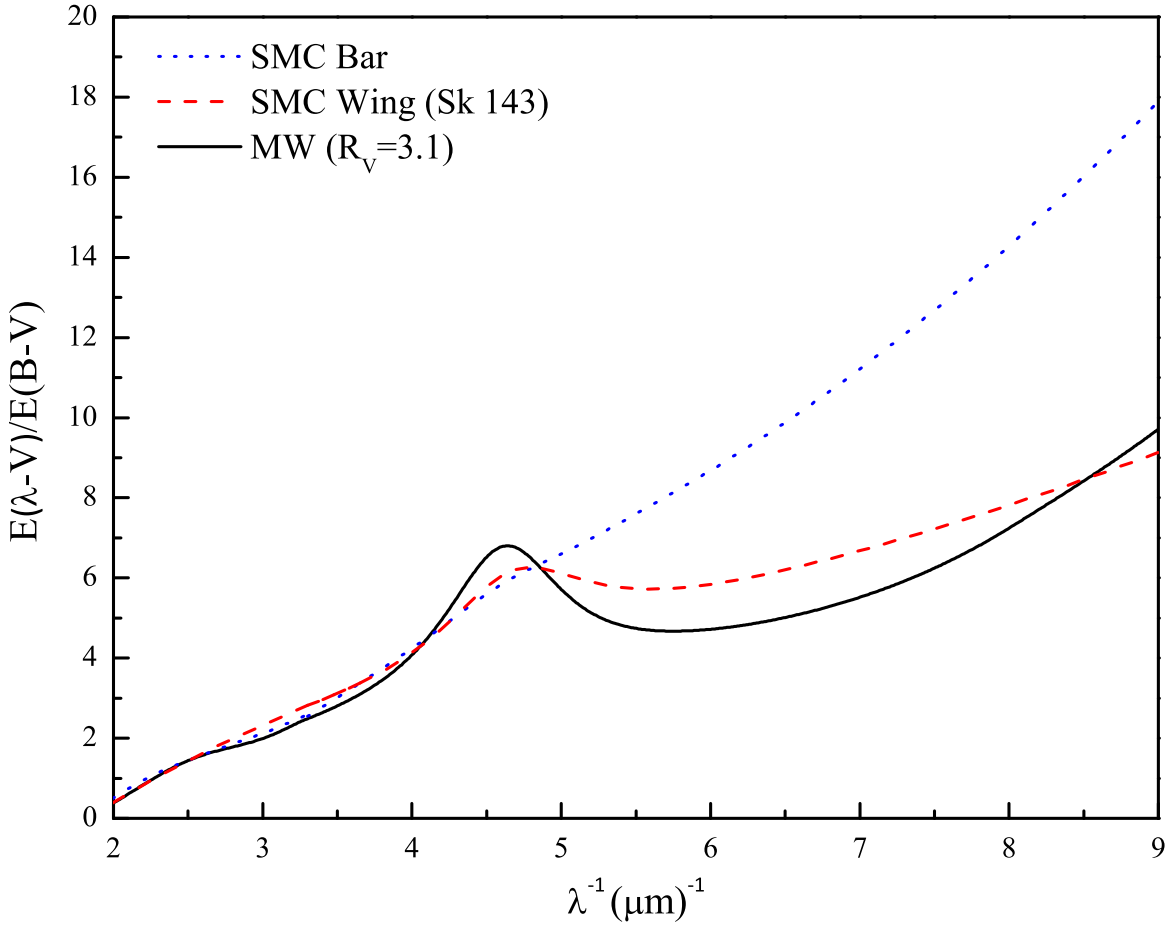

Figure 1.6: *(reproduction of figure 6 from Li et al. 2015).* Extinction curves at optical and UV wavelengths for Milky Way (solid back), SMC Bar (dotted blue) and SMC Wing star Sk 143 (dashed red).

distance modulus to M 33 from 24.63 mag to 24.60 mag, i.e. only by ±1.5% and within the statistical error of their adopted distance modulus of 24.62 mag.

1.3.4 Galactic extinction

An important aspect that influences the extinction we perceive within the Magellanic Clouds is the extinction in the line-of-sight towards the Magellanic Clouds. This is mainly comprised of the extinction within our galaxy, the Galactic extinction.

However, determining it directly in the Magellanic Cloud sightline will overestimate this as (in some measurements) the Magellanic Clouds may dominate this. This can be compensated for by taking the average of surrounding regions instead.

Burstein & Heiles (1978) used the 21-cm H I radio lines as a proxy of reddening. Assuming a constant dust-to-gas ratio measured in the diffuse ISM of the Milky Way, and assuming that H I provides a direct measure of the gas column density, the H I column density can be converted into A_V. The beauty of the method comes from the redshift of the Magellanic Clouds, which separates the H I arising in the Milky Way from that arising in the Magellanic Clouds. This allows the foreground material to be mapped across the faces of the Magellanic Clouds. The method was tested and verified in Burstein & Heiles (1982), including using background galaxies counts.

The more widely used measurements are from the microwave measurements published in Schlegel et al. (1998). These are produced from a composite of data from IRAS (Infrared Astronomy Satellite) and the DIRBE (Diffuse Infrared Background Experiment, situated on the COBE satellite). They processed these far-infrared (FIR) data to generate a column density map with the wavelength range of $100\,\mu\mathrm{m} - 240\,\mu\mathrm{m}$. The dust map was normalised to $E(B-V)$ reddening using the colours of background galaxies.

Schlafly & Finkbeiner (2011) and Schlafly et al. (2010) recalibrated the Schlegel et al. (1998) map using a band fitting method. In the direction of the LMC the recalibration changes individual band measurements but the overall colour is unmodified. These are the values I use when quantifying between the Galactic and Magellanic

extinction.

1.4 Magellanic Clouds

Despite being classed as irregular galaxies, the Magellanic Clouds have structure, and this structure is imprinted with the dynamical history of each of the Clouds and of the interaction between them. The structure is seen in the distribution and kinematics of the stars, as well as the ISM. These are briefly described below. The LMC is characterised by a disc – some even see spiral structure – a bar but no obvious centre, and regions of vigorous star formation offset from the centre. The SMC is characterised by a main body – which rather confusingly is often called the SMC bar – and the Wing, which is a broad extension towards the East. Whether either or both of the Magellanic Clouds possess a true halo is not yet established (cf. Dias et al. 2016).

Being among the nearest Local Group galaxies the Magellanic Clouds and their components have been studied in great detail. As a result, it is impossible to contain everything but the purpose of this section is to provide an overview of some of the work that has been done which is relevant for the research I present later on.

1.4.1 Distance

The motivations for studying distance lie in producing better luminosity measurements which in turn can lead to a more precise study of stars; along with accurate linear size scales it also allows for more meaningful studies of galaxies and large-scale structure. The distances to objects within galaxies also have implications for cosmology due to being a rung in the cosmological distance ladder (the information within a rung is used to determine the distances in the subsequent rung so by improving the accuracy of early rungs you can improve the accuracy of the final rung; the Hubble Constant).

While my work does not require an exact distance to the Magellanic Clouds (only the distances within) it is worth highlighting a few papers which have covered

distances. There will not be a look at every single measurement made (233 between 1990 and 2013 within the LMC according to de Grijs et al. 2014) but instead a look at some key moments and later on how different population tracers behave.

1.4.1.1 LMC – Historical moments & reviews

A turning point for current day values converging is the work done by Benedict et al. (2002) who used HST astrometry to derive trigonometric parallaxes for RR Lyrae stars obtaining absolute magnitude values. Shortly before, Freedman et al. (2001) presented the final results of the Hubble Space Telescope Key Project (HSTKP) which adopted an LMC distance of $(m - M_0) = 18.50 \pm 0.10$ mag based on Cepheid values.

A small review of 14 distance measurements for the LMC published between 2002–2004 done by Alves (2004) found a weighted average of $(m - M_0) = 18.50 \pm 0.02$ mag. A larger review of various tracers by Walker (2012) found that for five major tracers, (viz. Cepheids, red variables, RR Lyrae, RC stars and eclipsing binaries) the mean distance is $(m - M_0) = 18.48 \pm 0.05$ mag.

However, this convergence does have its critics as Schaefer (2008) believes the clustering of measures of the distance to the LMC after 2001 is biased because they cluster too closely to HSTKP values (with 68% of results being within 0.5σ) and that this does not follow a Gaussian distribution. This is commonly referred to as "publication bias".

The most recent comprehensive review is that of de Grijs et al. (2014) who statistically reviewed 233 LMC distance measurements published between 1990 and 2013. They provide a counter argument to Schaefer (2008) pointing out one particular problem of the Gaussian distribution of errors; that is, the measurements before 2001 also do not form such a distribution. They suggest a canonical distance modulus of $(m-M)_0 = 18.49 \pm 0.09$ mag from a careful, weighted combination of stellar population tracers. An analysis of the de Grijs et al. (2014) data by Crandall & Ratra (2015) also finds the error distributions to be non-Gaussian (having extended tails) possibly due to non-accounted for systematic errors. de Grijs et al. (2014) and Crandall & Ratra

(2015) both agree that the median statistics are narrower than Gaussian and this is a mixture of possible publication bias and correlations between measurements.

1.4.1.2 LMC – Distance tracers

Distance determination methods in general have several sources of error, including effects of chemical composition on determining absolute magnitude, effects of reddening modifying apparent magnitude and general statistical errors when sample sizes are small (which the RC does not suffer from except in very sparse systems such as ultra-faint dwarf galaxies). A selection of calculated distances to the LMC from the literature along with their associated error bars are shown in Figure 1.7. The figure highlights three standard candle based methods; RR Lyrae, RC and Cepheid variables. From this it is apparent why the RC is thought to give a "short" distance to the LMC.

Some of the reasons for this short distance are due to errors in other methods. For instance Cepheid variables are affected by metallicity (changing their light curves) and many of the older studies used Milky Way metallicity (Mottini et al., 2006). In addition Figure 1.7 does not take into account the regions of the LMC for which the distances were determined. For instance Eastern parts of the LMC are closer to us than the Western parts.

Regarding the Tip of the red-giant branch (TRGB) tracer Górski et al. (2016) provide an absolute magnitude calibration for the LMC and SMC finding discrepancies of 0.2 mag between NIR K and optical I wavelength bands. However, they do note that the population effect of the mean of RGB stars in the Magellanic Clouds (MCs) is the cause here.

In order to advance the distance determination to the Magellanic Clouds the 3-D structure of them must be better understood. This requires a large-scale survey of stars in the Clouds which allows for differences in magnitude to be accounted for (as more distant stars will be fainter). In order for this to be accurate differences in populations need accounting for and so does the reddening (both factors which affect magnitude). This is one of the motivations for the work I present here.

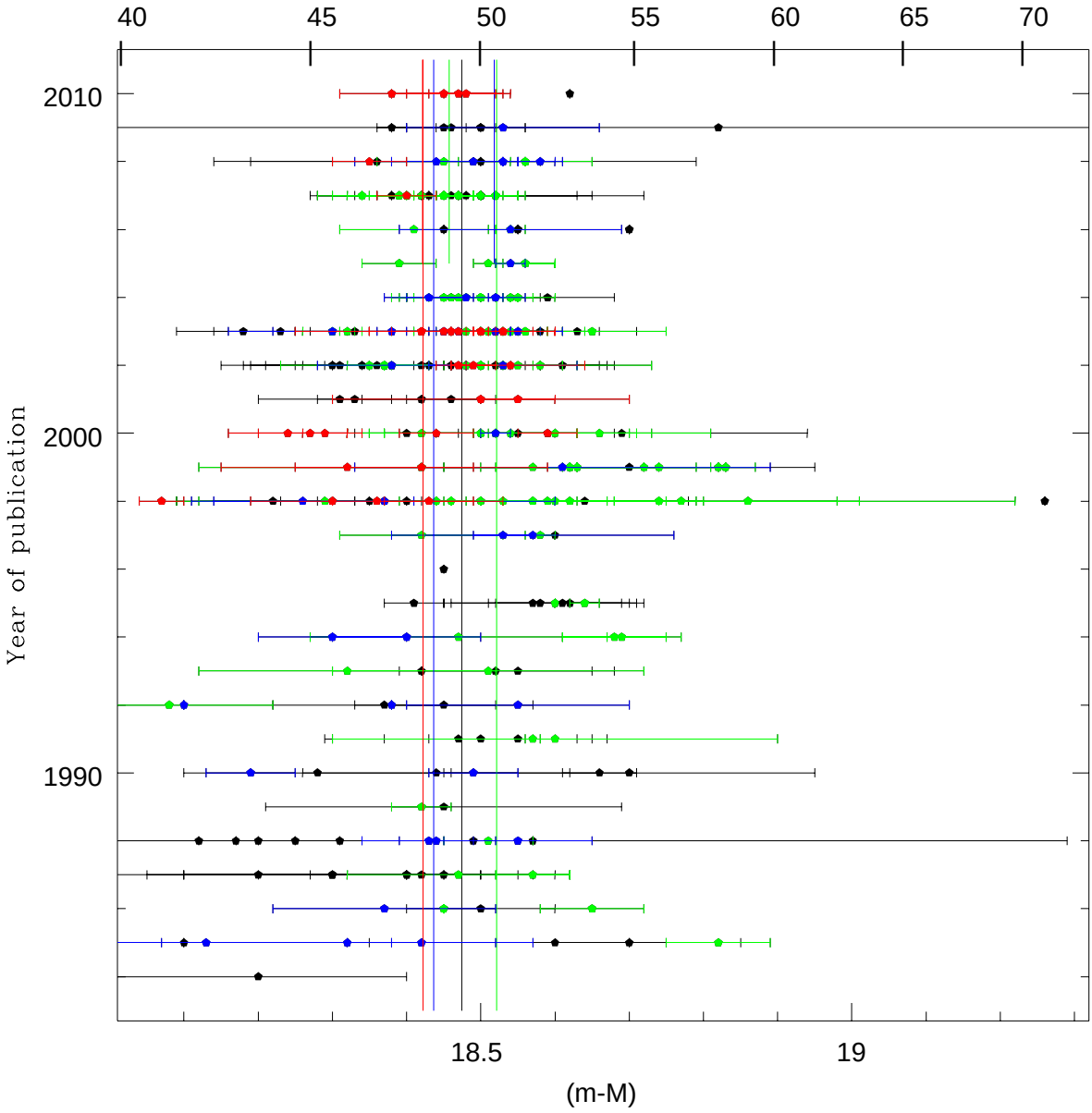

Figure 1.7: Distances to the LMC from values in the literature (data from NASA/IPAC Extragalactic Database; NED-`http://nedwww.ipac.caltech.edu/`) with distance (distance modulus bottom, kpc top) against year of publication. RC stars plotted in red, RR Lyrae in blue and Cepheids in green. Long vertical lines correspond to means of these, smaller vertical lines cover years after 2005.

1.4.1.3 SMC distances

In the literature the average distance of the SMC being 61 kpc is fairly well established. Figure 1.8 displays measurements taken from the database of de Grijs & Bono (2015)[9]. Values before 1963 have been omitted because these values have a narrower distance range.

There is a similar pattern to that shown in the LMC; the RR Lyrae and RC stars trace a shorter distance compared to the average while the Cepheid stars trace a longer distance. The geometry of the SMC itself is a source of uncertainty (Scowcroft et al., 2016) due to varied line-of-sight depth and a warped disc.

1.4.2 Extinction maps

The extinction within the Magellanic Clouds is both interesting and necessary to study due to the relation of the dust distribution to galactic structure and thus stellar populations and the effect it has on observations of the latter. Because of differences between the spatial distribution of the dust and that of the various stellar populations the extinction will be spatially variable. Adopting a single value will not generally be sufficiently appropriate, and it is necessary to create extinction *maps* and establish the link between the tracer of the extinction and the galactic structure of interest.

The literature mostly uses optical data with Zaritsky et al. (2004); Subramaniam (2005); Pejcha & Stanek (2009); Haschke et al. (2011) using this in the LMC and Zaritsky et al. (2002); Haschke et al. (2011) in the SMC. NIR data were used by Dobashi et al. (2008, 2009). In terms of stellar tracers the RC stars are used by Subramaniam (2005); Haschke et al. (2011) and RR Lyrae by Pejcha & Stanek (2009). The methodology for star selection and intrinsic colour are similar between Subramaniam (2005); Haschke et al. (2011) and their results show similar average extinction.

[9] `http://astro-expat.info/Data/smcdistbytracer.html` & `http://astro-expat.info/Data/smcdistbyyear.html`

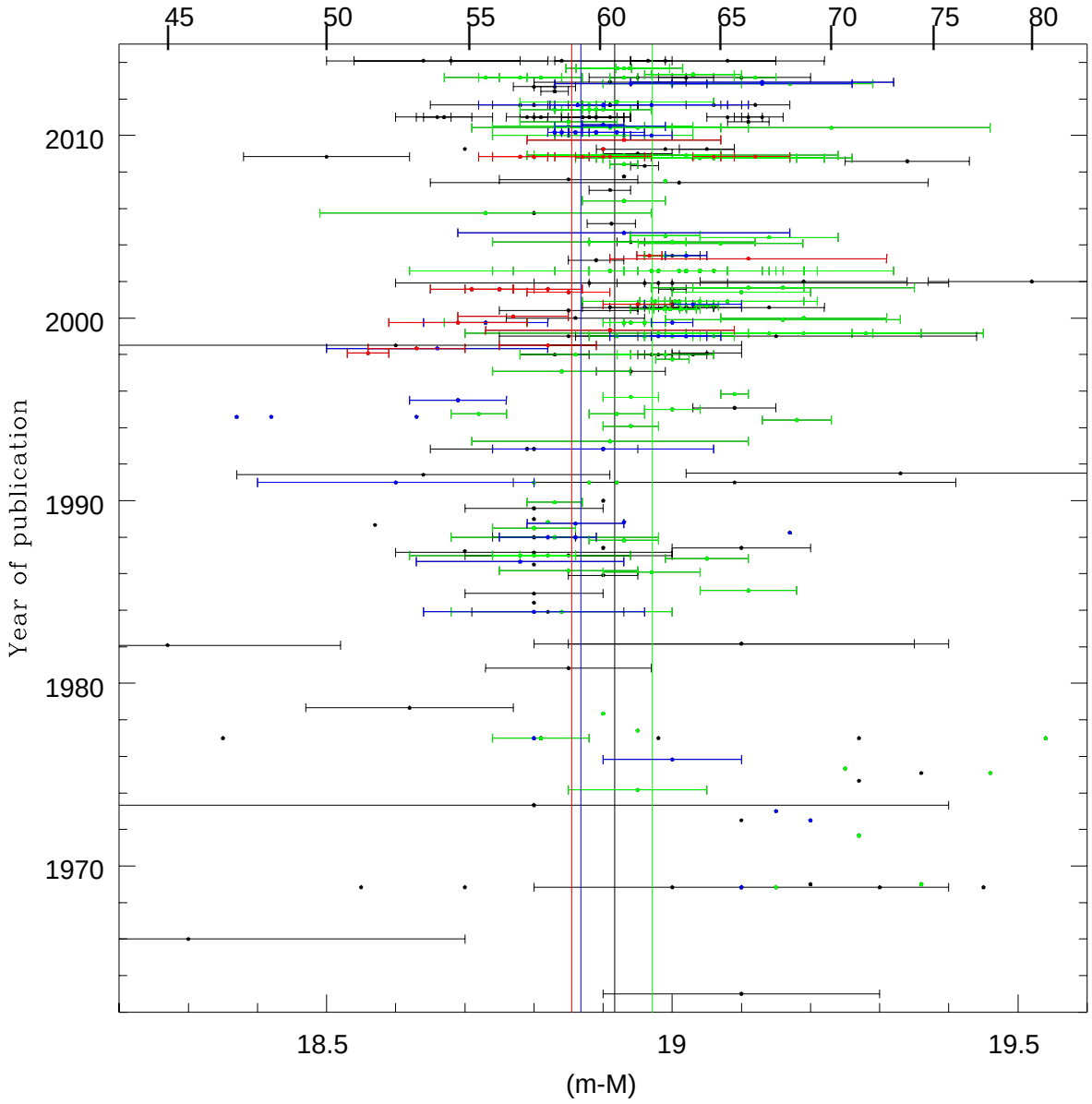

Figure 1.8: Distances to the SMC from values in the literature after 1962, data from de Grijs & Bono (2015) with distance (distance modulus bottom, kpc top) against year of publication. Red Clump stars plotted in red, RR Lyrae blue and Cepheids in green. Long vertical lines correspond to means of these.

Two direct reddening maps derived from the RC itself have been produced in the optical by selecting stars lying in the CMD range of $17.50 \leq I \leq 19.25$ mag and

$0.65 \leq (V-I) \leq 1.35$ mag for regions of a certain size. Then comparing Gaussian peaks of histograms to theoretical unreddened values, reddening values for each region are determined. The fitted histograms have a reduced χ^2 value determined for them with Subramaniam (2005) rejecting regions where this is greater than 2.5 and Haschke et al. (2011) re-evaluating regions where this is greater than 3 (as it usually means the CMD range has missed a large amount of the Red Clump).

The first of these, Subramaniam (2005) used Optical Gravitational Lensing Experiment II (OGLE II) data to produce a reddening map for the LMC bar region. The region was divided into 1344 sections each of which is $3\farcm56 \times 3\farcm56$. For the bar region the average reddening they find is $E(V-I) = 0.08 \pm 0.04$ mag. Compared to the H I maps of Kim et al. (1998) they find the high H I column density of the Eastern end of the bar only corresponds to a slight increase in reddening, suggesting the H I clouds are behind the bar. Since 2005, Subramaniam has continued to use reddening maps for dereddening purposes to estimate the depth of the LMC and SMC (Subramanian & Subramaniam, 2009) and determine if the LMC bar is part of the disc (Subramaniam & Subramanian, 2009). For both of these studies the maps are used as tools to reach the result rather than them being the result itself.

More recently, Haschke et al. (2011) used OGLE III to construct an entire LMC and SMC reddening map by using the RC method above and RR Lyrae. The RC method used a fairly low, but variable resolution as they split the system into subfields which always contain at least 200 RC stars. In total the LMC was divided into 3174 subfields and the SMC 693. These contain an average of 1257 and 1318 RC stars in the LMC and SMC for each subfield. For the RC method mean reddening values of $E(V-I) = 0.09 \pm 0.07$ mag and $E(V-I) = 0.04 \pm 0.06$ mag were found for the LMC and SMC. Haschke et al. compared their maps with other studies finding good agreement in general. They made the reddening maps for the RC method available online via a web form[10] and they also looked into the 3-D geometry of the Clouds.

Two other studies in the optical are those by Zaritsky et al. in the SMC (2002)

[10] `http://dc.zah.uni-heidelberg.de/mcx`

and LMC (2004). Both surveys used the UBV bands from Massey's bright star catalogue and I band data from DENIS (Zaritsky et al. 2002 also used OGLE) and their method of determining reddening is to calculate the effective temperature (T_E) and line-of-sight extinction (A_V) using their photometry and the models of Lejeune et al. (1997). They found the model is least degenerate between T_E and A_V for stars with derived temperatures in the ranges of $5500\,\mathrm{K} \leq T_E \leq 6500\,\mathrm{K}$ (cool) and $12000\,\mathrm{K} \leq T_E \leq 45000\,\mathrm{K}$ (hot). The maps are A_V values in these cool and hot ranges using sources where there is good quality photometry in all filters ($\sigma < 0.4$ mag for U and $\sigma < 0.2$ mag for B, V and I) and good model fits ($\chi^2 < 3$).

Dobashi et al. (2008, 2009) used the X percentile method (the former creating it) to derive reddening maps in the LMC (2008 study) and SMC (2009 study). The X percentile is an improvement on the NICE method which makes a cell around a dark cloud region assumed to be free of extinction, then uses the mean or median colour as an unreddened value (the mean is easily contaminated by foreground stars). X percentile instead uses the colour of the X percentile reddest star. The data used in the 2008 study are from 2MASS and the 2009 study 6X 2MASS as well as the InfraRed Survey Facility (IRSF) at the South African Astronomical Observatory (for improved sensitivity). Dobashi et al. (2008) produced an extinction map of A_V which is used to derive a dust absorption to gas column density ratio (A_V/N_H) and a ratio of CO line intensity to H_2 column density (X_{CO} factor) for 21 sub-regions. For the ISM part of the paper they used 21cm H I data from Kim et al. (2003). The molecular gas (CO) data come from Fukui et al. (2008). Dobashi et al. (2009) produced a map of $E(J-H)$ colour excess in which they found 10 dark cloud regions whose structure corresponds well with CO maps (from Mizuno et al. 2001 data). They also determined a dust-to-gas ratio (A_V/N_H) for these clouds.

Finally, Pejcha & Stanek (2009) investigated the structure of the LMC's stellar halo by using part of the OGLE III catalogue of 17,692 fundamental mode RR Lyrae stars (in total using 9393 stars out of this). They inferred unreddened $(V-I)_0$ by using the period–colour relation of RR Lyrae in M3 (due to the RR Lyrae of M3 all having a similar metallicity) which is then used to obtain intrinsic A_I reddening which is used to

correct the I magnitudes allowing for a line-of-sight distance to be determined. With this they investigated internal reddening of the LMC and also produced a 3-D plot of an isodensity surface which clearly shows the Eastern side of the LMC halo is nearer to us than the Western side.

I will be using the RC stars in the NIR to create reddening maps as a step towards determining three dimensional structure. This is combining the strength of the RC tracer in terms of the RC stars ubiquity and well defined magnitudes with those of the NIR wavelength to probe – and see through – even molecular cloud complexes.

1.4.3 Star formation history

The SFH of the Magellanic Clouds is very important because it has spatial variance and has been found to have an episodic nature rather than a constant rate. The timings of these episodes connect with the interaction history. It also has a bearing on the exact properties of the RC tracers that I use in my work, and how to place the structure traced by the RC stars within the context of the dynamical history of the MCs. I here describe some of the more recent work on deriving the SFHs of the LMC and SMC.

I make use of the SFH from the Vista Magellanic Clouds (VMC) survey. Kerber et al. (2009) assessed the expected accuracy of the SFH that the VMC survey would be able to achieve. They concluded the level of accuracy is sufficient to reveal significant imprints in the dynamical evolution of this unique and nearby stellar system, as well as possible signatures of the past interaction between the Magellanic Clouds and the Milky Way. Rubele et al. (2012) used VMC survey data to look at the SFH on tiles of the LMC. Mostly in outer regions (3 full tiles, broken up into subregions) but partially in the highly reddened central region too (2 small subregions). They found peaks in SFH at $\log(t/\mathrm{yr})$=9.3 and 9.7 (2 Gyr and 5 Gyr) for most subregions. The VMC survey has also looked at SFH for 10 tiles of the SMC (Rubele et al., 2015) finding two periods of enhanced star formation at 1.5 Gyr and 5 Gyr.

The episodic star formation is also covered in Cignoni et al. (2012); Weisz et al. (2013); Rezaeikh et al. (2014). Cignoni et al. (2012) examined 2 fields of the SMC bar,

finding that the bar initially had a low activity followed by an enhancement in the star formation rate that occurred 4–6 Gyr ago which has remained fairly constant since. The timing of this enhancement is thought to be similar to the epoch of the last major interaction with the LMC suggesting the close encounter was what triggered this star formation. Weisz et al. (2013) used HST CMDs to look at ancient SFH in the LMC and SMC, finding sharp increases in the SFH of both the LMC and SMC starting 3.5 Gyr ago. For the SMC this drove gas to the centre increasing star formation there (while decreasing it in the outer regions). They also found two peaks in the SMC SFH at 4.5 and 9 Gyr. Rezaeikh et al. (2014) presented the first reconstruction of SFH in the LMC and SMC that uses long period variable stars. This showed that the LMC globally had a single star forming epoch that occurred 10 Gyr ago. Inside the LMC bar they saw a second episode which began 3 Gyr ago, lasting until 2.5 Gyr ago. In the SMC there were two formation episodes which occurred 6 Gyr ago and 0.7 Gyr ago; the latter of these is discernible in the LMC as well suggesting that is linked to interactions between the Magellanic Clouds and the Milky Way while the formation of the LMC bar appears to be unrelated. They state that the differing initial formation epochs suggest that the LMC and SMC did not form as a pair.

SFHs can cover the last 0.5 Gyr by looking at younger populations (Joshi & Joshi, 2014) or finding star forming regions (Indu & Subramaniam, 2011). Joshi & Joshi (2014) determined the ages of LMC Cepheids to build a star formation scenario for the past 0.03–0.6 Gyr. The peak age distribution of the Cepheids suggests a star forming event taking place 0.15–0.2 Gyr ago and this may have been triggered by an encounter with the SMC. The Cepheids are found to be asymmetrically distributed in non-homogeneous clumpy structures in the South–East, away from the optical centre. Indu & Subramaniam (2011) identified star forming regions to look for directional star formation within the last 0.5 Gyr. They examined star formation in LMC centre, SMC centre and Wing regions. From their findings they proposed that H I gas in the LMC has been pulled North by gravitational interaction with the Milky Way in the past 0.2 Gyr. This gas (along with the star formation) has been shifted to the North and then North–East due to the motion of the Galactic Halo (this is similar to scenario

proposed by de Boer et al. 1998). Examining star forming regions can reveal the nature of the most recent star formation as shown in Gouliermis et al. (2012a,b). The SMC young bright main-sequence and faint pre-main-sequence stellar populations on the main body (NGC 346) and tip of the Wing (NGC 602) are highly hierarchically clustered, in agreement with other regions of the Magellanic Clouds observed with HST.

From these studies I am able to see that the consensus is that there are two major episodes of star formation in the SMC and the newer one of these is also closely associated with activity within the LMC suggesting they are linked to interactions with each other. The precise timings differ somewhat though. There are some indications that the formation of the bar is related to a distinct star formation history rather than a (purely) kinematic origin.

1.4.4 Metallicity and Gradients

The metallicity of a star describes the abundance of "metals" (non-hydrogen or helium elements). This is directly related to the ISM from which it formed and it thus serves as a memory of when and where it formed. There are several indices in use to quantify metallicity. The Z index is one of these (where $X + Y + Z = 1$; X and Y are hydrogen and helium). The more commonly used index however is [Fe/H] because iron content can be easily measured using spectroscopy. The [Fe/H] scale is logarithmic ($\log_{10}$) and calibrated with respect to the Sun (which has [Fe/H]= 0). There exist proxies to [Fe/H]. For the asymptotic giant branch (AGB) star populations, photometry using CMDs can be used to obtain the C to M (C/M) ratio (the ratio of C- and M-type AGB stars) which is then calibrated to [Fe/H] (Battinelli & Demers, 2005). Another commonly used proxy comes from the spectroscopic strength of three calcium lines found at 8498, 8542 and 8662Å known collectively as the Calcium II triplet (CaT). This has been calibrated with respect to [Fe/H] by Carrera et al. (2013) over a range of $-4 \leq$[Fe/H]≤ 0.5 dex.

Historical population averages of metallicity for the LMC and SMC are $0.33\,Z_{\odot}$

and $0.10\,Z_{\odot}$ respectively (Kunth & Östlin, 2000).

The presence of radial metallicity gradient in a galaxy indicates the presence of different stellar populations which are responsible for formation and evolution of the galaxy (Bernard et al., 2008; Cioni, 2009). This metallicity gradient may reflect a gradient in the metallicity of the ISM from which the stars formed, or indicate that the stars originally formed elsewhere. The age–metallicity relation (AMR) on the other hand shows how metallicity changes with respect to time instead of radius and this is inseparably linked to the SFH. I need to be aware of any metallicity variations among the RC stars as this could affect their properties on which I rely to determine their distances. I will now describe in more detail what is known about the metallicities, first in the LMC and then in the SMC, using different tracers.

The oldest, and likely most metal-poor, stellar populations can be traced by RR Lyrae variables. RR Lyrae populations within the LMC were studied in Gratton et al. (2004), Haschke et al. (2012c) and Deb & Singh (2014). Gratton et al. (2004) presented [Fe/H] metallicities for 98 RR Lyrae stars in the LMC bar finding an average of [Fe/H]$= -1.47 \pm 0.03$ dex. The data ranged between $-2.12 <$[Fe/H]< -0.27 dex but very few stars had [Fe/H]> -1 dex. Haschke et al. (2012c) looked at the metallicity distribution of the Magellanic Clouds using RR Lyrae stars from OGLE III. They found mean metallicity of [Fe/H]$= -1.50 \pm 0.24$ dex for the LMC. The spread exceeds 1 dex but they did not find any pronounced populations well below -2.0 dex. The differences in metallicities for the old populations make an origin from a single progenitor very unlikely. Deb & Singh (2014) used I band OGLE III data for fundamental mode RR Lyrae (RRab) stars in the LMC. They found three significant metallicity groups with [Fe/H] metallicities of -1.20 ± 0.12 dex, -1.57 ± 0.10 dex and -1.89 ± 0.09 dex. The distribution of these indicates that the formation of the LMC disc pre-dates the formation of the inner halo.

Cioni (2009) looked at the metallicity gradient of the LMC and SMC using the C/M ratio of the AGB star populations. She found in the LMC that metallicity decreases linearly as -0.047 ± 0.003 dex/kpc out to ~ 8 kpc from the centre (which has a value of [Fe/H]$= -1.04 \pm 0.01$ dex). The LMC gradient bears the signature

of two star forming episodes triggered by interactions with the SMC and Milky Way. However these LMC results may suffer from selection bias as Feast et al. (2010) re-analysed the data finding a much flatter gradient in the LMC. The younger RGB stars have a constant metallicity of [Fe/H]$= -0.66 \pm 0.02$ dex (Cioni, 2009).

The metallicity of RGB stars is more typically examined using the Ca II triplet spectroscopy as carried out by Carrera et al. (2008b). This comprised of four fields observed in the LMC located at galactocentric distances of 3°, 5°, 6° and 8° going North from the bar. The three inner fields have a constant metallicity, [Fe/H]$\simeq -0.5$ dex with the outer field being a lower [Fe/H]$\simeq -0.8$ dex. The authors suggested this is due to the outer region having a lower fraction of intermediate aged stars (as the AMRs are indistinguishable between the four fields).

Piatti & Geisler (2013) determine the AMR of the LMC field star population from ages and metallicities derived from Washington photometry. The composite AMR for the LMC finds old metal-poor stars preferentially formed in the outer disc while young and metal-rich stars are almost exclusive to the inner disc. This suggests an outside–in evolution of the galaxy. They found no significant metallicity gradient but instead found the metallicity of LMC fields had varied during the lifetime of the LMC. Comparing with models of AMR they found the LMC chemically evolved as neither a closed-box or bursting system but a combination during the lifetime (usually with bursting more dominant).

In the SMC, Haschke et al. (2012c) found a mean metallicity of [Fe/H]$= -1.70 \pm 0.27$ dex for the (old) RR Lyrae; again, the spread exceeds 1 dex but without pronounced populations below -2.0 dex. Deb et al. (2015) derived metallicities for the SMC using RR Lyrae stars and a period–metallicity relation. Although they found no statistically significant gradient, the median metallicity values varied spatially with a range between $-1.64 <$[Fe/H]< -1.94 dex.

Cioni (2009) examined the metallicity gradient of the SMC using the C/M ratio of the AGB star populations. This metallicity ([Fe/H]$\simeq -1.25 \pm 0.01$ dex) is fairly constant out to ~ 12 kpc.

The metallicity of RGB stars in the SMC was studied using the Ca II triplet

spectral lines in the works of Carrera et al. (2008a); Parisi et al. (2009); Dobbie et al. (2014b). Carrera et al. (2008a) used 350 RGB stars contained within 13 fields in a radius of 1° to 4° from the centre of the SMC. For the innermost regions average metallicity was [Fe/H]$\simeq -1$ dex and this decreased going further out. The authors noted this was the first detection of a spectroscopic metallicity gradient. They found this is related to an age gradient where the younger metal rich stars are concentrated in the central regions of the SMC. Parisi et al. (2009) studied RGB stars associated with 16 SMC clusters finding an average of [Fe/H]$= -0.96$ dex with $\sigma = 0.19$ and a bimodal distribution with peaks at -1.15 dex and -0.96 dex but there was no metallicity gradient seen. The AMR presents evidence of three phases of star formation; older than 11 Gyr, between 10–3 Gyr and 1–3 Gyr ago with greatest enrichment in the latter. Dobbie et al. (2014b) determined metallicities for 3037 RGB stars in the SMC. They found a median metallicity of [Fe/H]$= -0.99 \pm 0.01$ dex with an abundance gradient of -0.075 ± 0.011 dex deg^{-1} for the inner 5° suggesting this is the result of an increasing fraction of younger stars within the SMC. Interpreting their results they found the AMR for the North–East population lying 10 kpc in front of the SMC is indistinguishable from the main SMC. Additionally the metal poor and metal rich quartiles of the total sample are older and younger than 6 Gyr, respectively. They concluded that an increase in star formation around 5–6 Gyr ago was likely triggered by an interaction with the LMC.

In summary, abundances increase over time as reflected by the different tracers. RR Lyrae metallicites are lower than RGB star metallicities. The extent of the gradient is also different depending on tracer used. At the very least it does appear both MCs have regional differences in metallicity. In the context of my work the RC stars are most similar in age to the RGB stars.

1.4.5 Interstellar medium (ISM)

Besides stars, the Magellanic Clouds are rich in gas and dust. The latter affects the observation of the stellar tracers I am using, through attenuation. But I am also able

to use that to trace the ISM, in particular the clouds from which stars form. In this way I can connect the intermediate-age stellar structure with younger structures. Also, gas and stars are affected by different processes so their study is complementary.

1.4.5.1 Diffuse atomic gas

The gaseous discs of galaxies can be traced in H I and Hα. Within the Local Group the MCs are the only dwarf galaxies within 270 kpc of either the Milky Way or M31 that have (H I)$> 10^5\,M_\odot$ (Grcevich & Putman, 2009). It is believed that ram pressure was the mechanism that stripped the gas from the inner Local Group and this has consequences for star formation. The LMC and SMC allow these dynamics to be studied in detail because they are nearby and still have a lot of gas. This is regarded as evidence for them being on their first passage of the Milky Way (Besla et al., 2007). This ISM feature is traced by extinction and I do make direct comparisons to it.

Investigating luminosity, star formation and large scale emission Kennicutt et al. (1995) looked at Hα in the LMC and SMC. They found the fraction of emission (diffuse component $30\% - 40\%$) and integrated star formation rates were typical for Magellanic type irregular galaxies and found evidence for a gas threshold being required for star formation. The Hα traces both the ionizing radiation from the young massive stars, and the overall gas density, hence explaining the link with star formation. An atlas of Hα emission along the entire Southern sky has been published as the Southern H-Alpha Sky Survey Atlas (SHASSA; Gaustad et al. 2001)[11].

In the LMC H I observations find the disc is rotating, with turbulent and fractal structure shaped from dynamical feedback of star formation (Kim et al., 1998). These H I filaments have numerous shells and holes (Kim et al., 2003). The H I emission extends beyond the main body of the LMC finding arm features that extend from the LMC to the Bridge and Leading Arm (Staveley-Smith et al., 2003) and the H I clouds appear to form structures distinct from the giant molecular clouds (Kim et al., 2007).

[11] `http://amundsen.swarthmore.edu/SHASSA/`

The atomic (H I) to molecular transition (H_2) thus has a key role in the formation of structure in a galaxy.

In the SMC the ISM is also fractal in nature but with a hierarchy of H I cloud structures. Kinematic studies reveal the presence of supergiant shells (Stanimirović et al., 1999). The SMC has an intact, rotating H I disc which either survived the last close encounter with the LMC or quickly reformed (Nidever, 2014).

It is important to note the structure seen in the H I is not reflected in the stellar distribution as there are specific dynamical processes that affect the gas but not the stars (e.g. thermal expansion, ram pressure, radiation pressure). Other dynamical processes such as tidal effects do affect both gas and stars equally.

1.4.5.2 Molecular clouds

The coldest, densest regions of ISM are comprised of molecular hydrogen (H_2). These are called molecular clouds and are a contrast to the predominately ionised ISM. Within the molecular clouds are higher density regions of gas and dust known as clumps. The gravitational collapse of these clumps is the beginning of star formation hence why molecular clouds set boundaries on star formation rates.

Directly observing H_2 is difficult because its spectral lines are weak, they are cold dark regions and extinction means background objects do not reveal their presence. In the context of my thesis however, mapping extinction could reveal their presence albeit ambiguously. Traditionally, for studying the molecular cloud structure CO emission is commonly relied upon as a H_2 surrogate as the CO traces this star forming gas (Elmegreen, 2013). More massive giant molecular clouds are more likely to contain young stellar object candidates and these appear to be associated with CO emission forming a close link between giant molecular clouds traced by CO emission and massive star formation (Wong et al., 2011).

Within the LMC and SMC H_2 emission is UV excited and weak CO emission is always present towards regions of H_2 emission (Pak et al., 1998). The column density of molecular clouds increases where the metallicity decreases (Pak et al., 1998). Fukui

et al. (2008) identified 272 molecular clouds within the LMC and Cohen et al. (1988) find a complex of 40 molecular clouds extending South from 30 Doradus by 2.4 kpc, and within 30 Doradus find an extended high velocity CO component possibly accelerated by stellar winds and/or supernovae. Studies in the SMC found 21 giant molecular clouds in the North–West and South–West of the bar and H II regions within the Wing (Mizuno et al., 2001).

Bolatto et al. (2011) compared the molecular gas fraction in the SMC derived from a combination of H I and dust emission, to that observed in CO. They found that the molecular gas fraction is suppressed by about the metal depletion factor but CO is much more weakened than that. Jameson et al. (2018) found that the CO/H I fraction is strongly correlated with optical extinction, A_V. Bolatto et al. also found that the star formation as measured from Hα is more closely linked to the molecular gas density than to the total gas density.

Molecular clouds in older galaxies re-form due to processes such as shell ejection in older stars providing a new supply of gas. The relationship between HI and CO emission with the supergiant shells was examined by Dawson et al. (2013) to investigate the influence of the large-scale stellar feedback on the formation of molecular clouds in the LMC. Their findings suggest on a global level the supergiant shells are not a dominant driver of molecular cloud formation but that they do have a positive effect on the local level. Because RC stars are much more evenly spread than these ISM structures they form ideal tracers of the latter through intervening extinction.

1.4.5.3 Mid- and far-infrared emission

Surveys in the mid- and far-infrared (MIR & FIR) have been done in the LMC and SMC, taking advantage of the capabilities of the Spitzer Space Telescope. The IRAC and MIPS bands cover a wavelength range of 3.6–160 μm. The three surveys encompassing these are the Spitzer Surveying the Agents of Galaxy Evolution (SAGE) survey (Meixner et al., 2006) for the LMC, the Spitzer Survey of the SMC (S^3MC) (Bolatto et al., 2007) and its SAGE extension (Gordon et al., 2011).

Meixner (2008) reviewed the initial results from SAGE. The ISM in the LMC was investigated using the SAGE survey in Bernard et al. (2008). They found good correlation between the 160μm MIPS map and the 21-cm H I map of Kim et al. (2003). For three regions analysed in detail they found the dust-to-gas ratio of the LMC is around 6 times less than in the Milky Way. They used this ratio to determine a FIR excess map and found this to correlate well with H I gas suggesting that the gas is optically thick or cold. I make comparisons to SAGE within part of the LMC.

The Spitzer Survey of the SMC (S^3MC) was presented in Bolatto et al. (2007). They found the flux ratio of 8μm/24μm has large spatial variances unrelated to metallicity. Leroy et al. (2007) used this survey to find that the giant molecular clouds in the SMC appear to be gravitationally bound, identifying possible sites of cold dust and that gas densities and metallicity effects are responsible for a low H_2 to H ratio in the SMC.

1.4.5.4 Magellanic Stream

The Magellanic Stream is a vast neutral hydrogen structure (over 100°; Guhathakurta & Reitzel 1998) that trails behind the LMC and SMC in their orbit around the Milky Way and has an average metallicity of [Fe/H]$= -0.6 \pm 0.2$ dex (Wakker, 2001). Models of the origins of the Stream include an interaction between the LMC and Milky Way (Gardiner & Noguchi, 1996)[12] and ram pressure stripping gas from the outer LMC (Mastropietro, 2009). However Besla et al. (2010) used HST proper motion measurements to suggest the Magellanic Clouds are on their first passage of the Milky Way (and thus effects from it could not form the Stream). They make simulations of tidal interactions of the LMC stripping gas from the SMC which is then accreted in the direction of the Milky Way producing a Stream. Nigra et al. (2012) suggested that the Stream is likely to eventually reach the Milky Way disc.

[12]However, proper motion measurements from HST exceed the limits on this model (Kallivayalil et al., 2006b).

1.4.6 Geometry

1.4.6.1 Line-of-sight depth

Measurements of the thickness of the Magellanic Clouds are of interest in order to better understand the structure and history of them. The thickness of a galaxy is determined by the internal kinematics, which is the result from dynamical processes such as two-body encounters leading to relaxation within the dark matter potential, and disturbances caused by external tidal action or direct galaxy collision. Line-of-sight depths are usually measured in terms of the standard deviation of a distribution of distances, but different authors make different choices and also the true vertical structure may have a different profile.

Tables 1.1 & 1.2 summarise findings in the LMC and SMC, respectively. Within the LMC it would appear there is an age or population gradient because there are fairly different values between the Cepheid, RC and AGB star values. The AGB population is geometrically thick (Weinberg & Nikolaev, 2001), while the RC population suggests the LMC bar is flared because the bar and Northern disc have larger depths (Subramanian & Subramaniam, 2009).

Table 1.1: List of line-of-sight depths from the literature for the LMC

Publication	Depth (kpc)	Notes
Weinberg & Nikolaev (2001)	8.00	2MASS AGB
Subramanian & Subramaniam (2009)	0.5	OGLE II & MCPS RC; Minimum
Subramanian & Subramaniam (2009)	4.0 ± 1.4	OGLE II & MCPS RC; LMC bar average
Subramanian & Subramaniam (2009)	10.4	OGLE II & MCPS RC; Maximum;
Haschke et al. (2012a)	1.7 ± 0.2	OGLE III Cepheid; mean
Haschke et al. (2012a)	3.0	OGLE III Cepheid; maximum

In the SMC the full depth determined by Crowl et al. (2001) might be interpreted 6–12 kpc (e.g. Haschke et al. 2012b). Kapakos et al. (2011) suggested the metal-rich and metal-poor stars have different dynamical structures, where the metal-rich stars form a thin disc like structure and the metal poor-ones form a thicker halo or bulge structure. Kapakos & Hatzidimitriou (2012) found that the North–Eastern region appears to be thicker and the differing dynamical structures of the metal-rich and metal-poor stars were seen like they were in Kapakos et al. (2011). Section 5.2 of Subramanian & Subramaniam (2012) provides additional 1-σ depth values and maps. In the work of Deb et al. (2015) the two different absolute magnitude relations are period and Fourier coefficients (MVF) and a metallicity based relation (MVC). A future publication from Deb et al. will analyse this using OGLE-IV data (mentioned in the conclusions of Deb 2017).

A section of Stanimirović et al. (2004) reviewed findings noting that Zaritsky et al. (2002) had mentioned that differential extinction can lead to Cepheid distances being overestimated so more regions of the SMC might be in the depth range of the tidal radius (4–9 kpc). These Cepheid distances have the largest effect on historical values such as those of Mathewson et al. (1986, 1988) which were 30 and 20 kpc, respectively. Even at the time Welch et al. (1987) pointed out flaws with these measurements. Another example of abnormally large line-of-sight depth is found in Hatzidimitriou et al. (1993).

Table 1.2: List of line-of-sight depths from the literature for the SMC

Publication	Depth (kpc)	Notes
Hatzidimitriou & Hawkins (1989)	17, 7	2σ North–Eastern and South–Western
Gardiner & Hawkins (1991)	4–16	Range; 2σ depth dependent on portion observed (Northern and North–Western)
Crowl et al. (2001)	$4.1 \pm 0.8 - 6.3 \pm 1.3$	Cepheids; standard deviation of cluster distances from isochrone fitting i.e. 1σ depth; different RC distance variance assumptions change result
Groenewegen (2000)	14	NIR Cepheids, OGLE, DENIS, 2MASS P–L relations intrinsic front–back
Glatt et al. (2008)	~ 10	deep HST imaging
Subramanian & Subramaniam (2009)	3.44 ± 1.16	OGLE II RC: average depth of the disc
Subramanian & Subramaniam (2009)	4.17 ± 0.97	OGLE II RC: average depth of the North
Subramanian & Subramaniam (2009)	2.63 ± 0.80	OGLE II RC: average depth of the South
Subramanian & Subramaniam (2009)	3.09 ± 0.99	OGLE II RC: average depth of the East
Subramanian & Subramaniam (2009)	2.80 ± 0.92	OGLE II RC: average depth of the West
Kapakos et al. (2011)	4.13 ± 0.27	OGLE II/III RR Lyrae V-band: Central area 1σ
Kapakos & Hatzidimitriou (2012)	5.3 ± 0.4	OGLE II/III RR Lyrae V-band: Extended region 1σ
Subramanian & Subramaniam (2012)	4.57 ± 1.03	1σ OGLE III RC stars
Subramanian & Subramaniam (2012)	6–8	1σ OGLE III RC stars (North–Eastern regions)
Subramanian & Subramaniam (2012)	~ 14	4σ OGLE III RR Lyrae & RC stars front to back
Haschke et al. (2012b)	4.2 ± 0.4	OGLE III RR Lyrae
Haschke et al. (2012b)	$5.14 - 6.02$	OGLE III Cepheid; dependent on field selection
Subramanian & Subramaniam (2015)	8.1 ± 1.4	OGLE-III SMC disc z-distribution
Subramanian & Subramaniam (2015)	1.76 ± 0.6	OGLE-III SMC disc orientation corrected
Deb et al. (2015)	4.91 ± 0.65	OGLE-III data fundamental mode RR Lyrae (RRab); stars MVF relation

Continued on next page

Table 1.2: List of line-of-sight depths from the literature for the SMC

Publication	Depth (kpc)	Notes
Deb et al. (2015)	4.12 ± 0.71	OGLE-III data fundamental mode RR Lyrae (RRab); stars MVC relation

1.4.6.2 Orientation

By estimation of inclination (i; i.e. how face on or edge on they appear on the sky[13]) and position angle (PA; the direction of the major axis[14]) along the plane, one can probe warps in structure (regions which contradict these). The locations of these warps can inform us on dynamical features of the system and its history. In order that I probe structure, I estimate the orientation in my work.

LMC Table 1.3 provides a summary of viewing angle information form the literature. For the LMC, inclination can not be determined kinematically (although position angle can) because that requires assuming the disc to be circular (van der Marel, 2006). Instead a geometric consideration is made where an inclined disc will be brighter on one side than the other. This approach allows for relative distances of stars to be used instead (van der Marel et al., 2009). The position angle values in general see a far grater range of values likely due to different regional coverage though are commonly seen around 120° to 150°. Nikolaev et al. (2004) stated that the adopted LMC centre can cause variations of about 35° in the PA because concentric rings in the inner LMC are strongly dependent on these. van der Marel & Kallivayalil (2014) found different results between young and old populations. This points to no single solution which in turn implies structural distortion or changes to structure with different epoch.

A range of results have clearly been exhibited with inclinations ranging from 22° to 45°. There does not appear to be a general age based difference. Regional variance is seen with Weinberg & Nikolaev (2001) finding that inclination is steeper when including the LMC bar. This effect of the bar (a feature of the inner LMC) appears to be an anomaly with Subramanian & Subramaniam (2010) finding that orientation measurements differ at different radii with the inner disc being less inclined and having greater PA, a finding repeated in Subramanian & Subramaniam (2013).

[13]Where $i = 0°$ is face-on and $i = 90°$ is edge on.

[14]This direction is anticlockwise from North, where PA= 0° is a North–South direction and PA= 90° is an East-West direction.

Olsen & Salyk (2002) reported shallower inclination when including South–West fields. These South–West fields are 0.1 mag brighter than the plane (lying out of plane by up to 2.5 kpc). They argue that the cause of this 2 kpc wide South–West region being out of plane is due to interactions with the SMC or Milky Way. However Koerwer (2009) refute this as their best fitting plane has the South–West appearing dimmer but to a much smaller extent. Koerwer (2009) also found a depression in the North–East corner and the LMC appears to float about the plane. It would appear the outer LMC is more sensitive as Mackey et al. (2016) shows different results when modelling as a circular or elliptical disc. In summary the inner LMC North–East and South–West corners of the LMC are contributing factors to variance in results.

Table 1.3: List of position angle (PA) and inclination (i) from the literature for the LMC

Publication	i (°)	PA (°)	Notes
de Vaucouleurs & Freeman (1972)	27 ± 2	170 ± 5	Isophotes
Feitzinger et al. (1977)	33 ± 3	168 ± 4	H I, supergiant, PNe
Caldwell & Coulson (1986)	28.6 ± 5.9	142.4 ± 7.7	Optical Cepheid distances 73 stars
Laney & Stobie (1986)	45 ± 7	145 ± 17	14 Cepheids NIR
Welch et al. (1987)	37 ± 16	167 ± 42	23 NIR Cepheids
Luks & Rohlfs (1992)		162	H I
Kim et al. (1998)	22 ± 6	168	H I ATCA data; ellipse fitting & kinematic derivation
Weinberg & Nikolaev (2001)	24.4 ± 0.3	$\simeq$ 168–173	2MASS data
Weinberg & Nikolaev (2001)	38.2 ± 0.4		Including LMC bar
van der Marel & Cioni (2001)	34.7 ± 6.2	122.5 ± 8.3	NIR AGB stars (2MASS & DENIS)
van der Marel et al. (2002)		129.9 ± 6	Carbon stars
Olsen & Salyk (2002)	35.8 ± 2.4	145 ± 4	Optical RC stars
Olsen & Salyk (2002)	24 ± 2		Including brighter South–West fields
Nikolaev et al. (2004)	30.7 ± 1.1	151 ± 2.4	over 2000 Cepheids, MACHO data converted to 2MASS
Persson et al. (2004)	27 ± 6	127 ± 10	94 Cepheids NIR
Olsen & Massey (2007)		145.3	Red supergiants
Koerwer (2009)	23.5 ± 0.4	154.6 ± 1.2	NIR RC least-squares
Subramanian & Subramaniam (2010)	37.4 ± 2.3	141.2 ± 3.7	Optical MCPS least-squares plane
Subramanian & Subramaniam (2010)	23 ± 0.8	163.7 ± 1.5	Optical OGLE-III least-squares plane
Haschke et al. (2012a)	32 ± 4	115 ± 15	OGLE III RR Lyrae & Cepheids
van der Marel & Kallivayalil (2014)		147.7 ± 10	HST proper motion only
van der Marel & Kallivayalil (2014)		154.5 ± 2.1	PM data & young population LOS velocities
van der Marel & Kallivayalil (2014)		139.1 ± 4.1	PM data & old population LOS velocities

Continued on next page

Table 1.3: List of position angle (PA) and inclination (i) from the literature for the LMC

Publication	i (°)	PA (°)	Notes
Deb & Singh (2014)	36.43	149.08	OGLE-III RR Lyrae; least-squares plane
Deb & Singh (2014)	24.2	176.01	OGLE-III RR Lyrae; axis transformation
Subramanian & Subramaniam (2013)	26.6 ± 1.3	148.3 ± 3.8	NIR RC stars least-squares profile fitting
Subramanian & Subramaniam (2013)	25.7 ± 1.6	141.5 ± 4.5	NIR RC stars least-squares average
Balbinot et al. (2015)	38.14 ± 1.59	129.51 ± 1.08	Dark energy Survey, optical & NIR; All
Balbinot et al. (2015)	44.19 ± 1.80	125.96 ± 0.20	Young
Balbinot et al. (2015)	32.94 ± 1.25	127.40 ± 1.02	Old
Mackey et al. (2016)	33.14 ± 0.09	159.59 ± 0.12	Dark energy Survey, optical & NIR; Main sequence, outer LMC, circular disc
Mackey et al. (2016)	25.18 ± 0.71	185.0	elliptical disc, fixed PA

SMC Within the SMC less research has been done and the main focus has been on the central SMC, with the Wings of the SMC presenting a challenge, due to their warped structure and the possibility that the SMC is not fit by a plane but rather an ellipsoid. Large variance is seen as well in relation to this. Table 1.4 provides a summary of position angle (PA) and inclination (i) values.

For the inclination, contrasting values are seen where some studies found next to no inclination while others found very steep inclination. This does follow a clear age trend, with the younger stellar populations (Cepheid stars) producing steep inclination while older populations (RR Lyrae) are shallower. It is suggested by Haschke et al. (2012b) that this difference is due to interactions with the LMC and Milky Way which have given the younger population a much more tilted structure.

This is not the only trend as the main body is characterised by shallower values than the periphery. This main body is not misaligned or warped but the periphery is, possibly due to tidal forces from the LMC and SMC (Deb et al., 2015).

The range of position angles is much smaller in the SMC bar than other regions and this variance suggests the SMC is not a flat disc.

In the context of my work, there are no results presented using near-infrared data and there are very few values reported using RC stars.

Table 1.4: List of position angle (PA) and inclination (i) from the literature for the SMC.

Publication	i (°)	PA (°)	Notes
Caldwell & Coulson (1986)	70 ± 3	58 ± 10	Cepheids
Laney & Stobie (1986)	45 ± 7	55 ± 17	Cepheids
Kunkel et al. (2000)	73 ± 4		Radial velocities Carbon stars
Groenewegen (2000)	68 ± 2	238 ± 7*	(OGLE II, 2MASS and DENIS) Cepheids
Stanimirović et al. (2004)	40 ± 20	40 ± 10	H I
Subramanian & Subramaniam (2012)	0.58	55.5	OGLE III RC axis ratio
Subramanian & Subramaniam (2012)	0.50	58.3	OGLE III RR Lyrae axis
Haschke et al. (2012b)	74 ± 9	66 ± 15	OGLE III Cepheid
Haschke et al. (2012b)	7 ± 15	83 ± 21	OGLE III RR Lyrae
Dobbie et al. (2014a)	25–70	120–130	Spectra Disc model
Deb et al. (2015)	2.265 ± 0.784	74.307 ± 0.509	OGLE III RRab stars
Deb et al. (2015)	0.507 ± 0.287	55.966 ± 0.814	OGLE III Main body
Deb et al. (2015)	2.244 ± 0.024	85.541 ± 0.332	OGLE III North–East arm
Subramanian & Subramaniam (2015)	63.10 ± 0.96	151.5 ± 7.8	OGLE III Cepheids fundamental-mode
Subramanian & Subramaniam (2015)	66.30 ± 0.86	159.3 ± 10.2	OGLE III Cepheids first-overtone
Subramanian & Subramaniam (2015)	64.40 ± 0.66	155.3 ± 6.3	OGLE III Cepheids combined
Deb (2017)	2.30 ± 0.14	38.5 ± 0.3	OGLE-IV RRab stars
Deb (2017)	3.16 ± 0.19	38.0 ± 0.58	OGLE-IV RRab stars

*Subtracting 180° from this PA brings it in line with the other results.

1.4.6.3 Three-dimensional maps

In this thesis, I am going to construct three dimensional (3-D) maps of the Magellanic Clouds, to study their structure. In its most basic form a 3-D map can be thought of as line-of-sight distributions along multiple sightlines. This requires data on a lot of stars which is why there are close links to the orientation and position angle studies. Since large scale stellar surveys are required this is still a fairly new field of research for the Magellanic System. Weinberg & Nikolaev (2001) used the 2MASS data to look at the carbon long period variables which they used to probe 3-D structure. They were able to find several distinct populations, but 2MASS has limitations when it comes to the resolution and sensitivity.

As a result the main tool used to investigate the 3-D structure has been the long term Optical Gravitation Lensing Experiment (OGLE) which was initially about the Galactic bulge (Udalski et al., 1992) but has since expanded to cover the Magellanic System and is currently in its 4th major iteration (Udalski et al., 2015).

Lah et al. (2005) utilised period–luminosity relations of pulsating red giants in the OGLE II sample. For the LMC they were able to confirm the LMC having an inclined and possibly warped bar. Haschke et al. (2012a) examined the 3-D structure of the LMC making maps for RR Lyrae and Cepheid populations using OGLE III. They found that the distribution of the stars in the LMC can be described as an inclined disc.

For the SMC Lah et al. (2005) found a complex and patchy distribution about the mean; they also suggested that the large depth observed in many sightlines may conceal the true structure. Subramanian & Subramaniam (2012) studied the 3-D structure of the SMC using RC stars and RR Lyrae stars from OGLE III. They found that the North–Eastern part is closer to us and the line-of-sight depth for the whole SMC is large for both the RC and RR Lyrae populations. Haschke et al. (2012b) considered the 3-D structure of the SMC making maps for RR Lyrae and Cepheid populations using OGLE III. The distances between the populations are in good agreement with each other and they found a large depth of the SMC. They found the orientation of

the young populations and older populations to differ. The RR Lyrae stars are fairly homogeneous while the Cepheids follow the distribution of the bar with the North–Eastern part closer than the South–Western part. Interactions are possibly responsible for this elongated and tilted younger population.

In my thesis I will be taking advantage of the high resolution and sensitivity of the VMC survey as compared to the 2MASS survey, and its weaker sensitivity to extinction and age and metallicity variations than the optical OGLE survey, to use the less commonly used RC stars to obtain more robust and detailed 3-D maps of the LMC and SMC.

1.4.7 Tarantula Nebula/30 Doradus/R136

This central ionised gas (H II) region of the LMC is striking for its brightness and being the most active and largest star formation region in the Local Group. The region is very visible and was initially thought to have been a star, though its nebula nature was recognised in 1751 by French astronomer Nicholas Louis de la Caille[15]. Hyland et al. (1992) found the first evidence for star formation in the region, reporting four infrared protostars.

It is located at RA= $5^{\rm h}38^{\rm m}38^{\rm s}$ Dec= $-69°05'.16$. The R136 notation refers to the central cluster RMC 136 (RA= $5^{\rm h}38^{\rm m}42^{\rm s}.396$ Dec$-69°06'03''.36$) and the two components of a cluster of stars including Wolf–Rayet stars.

Such an interesting region continues to be the subject of study, of which I here mention some recent work on the ISM in and around 30 Doradus which is most relevant to my own work. On the basis of Spitzer mid-IR spectral cubes and mm-wavelength observations with the Atacama Large (sub-)Millimeter Array (ALMA), Indebetouw et al. (2009, 2013) traced variations in radiation temperature ranging between $30,000\,{\rm K} < T_{\rm rad} < 85,000\,{\rm K}$ and found a similar CO abundance to the LMC

[15] `http://messier.seds.org/xtra/Bios/lacaille.html`. de la Caille also made some star and nebula catalogues for the Southern hemisphere.

[16] RA= $75.^{\circ}6$ Dec= $-69.^{\circ}10$

mean but a possible reduction in the dust content by half.

The work of van Loon et al. (2013) used the Diffuse Interstellar Bands (DIBs) as a probe of the diffuse, cool–warm gas in 30 Doradus, utilising over 800 sightlines from the Very Large Telescope Flames Tarantula Survey (VFTS) sample (which mostly contains O- and B-type stars). The DIBs are suppressed both in the coolest, densest gas of molecular clouds, and in the immediate vicinity of young star clusters and OB associations. They also used higher resolution UVES spectra of stars in and around R136, to resolve the Na I line into half a dozen distinct kinematic components. They found stellar winds from R136 have created an expanding shell and evidence for infalling gas which they considered to be reminiscent of a galactic "fountain".

Torres-Flores et al. (2013) used data from the same VFTS project to analyse the kinematics of the line emission within a 10″ region in 30 Doradus, finding variations in Hα across the region. Sabbi et al. (2013) introduced the Hubble Tarantula Treasury Project (HTTP) aimed at making an inventory of pre-main sequence stars in 30 Doradus using the Hubble Space Telescope (HST). They also determined the reddening and found it to be variable but, surprisingly, with young stars having *lower* extinction than RGB stars. They suggested this could mean that 30 Doradus is in the foreground of the bulk of the dust.

I am going to study 30 Doradus and its surroundings in some more detail using the RC stars as tracers of the extinction throughout the region. I am going to assess the probability that 30 Doradus is indeed, as suggested by Sabbi et al., in the foreground of the disc of the LMC. I am also going to use the extinction to locate the molecular clouds associated with this star-forming complex. This part of the LMC thus forms a good test bed for my methodology before applying it to the Magellanic Clouds as a whole.

1.4.8 LMC bar

Bars are a feature commonly found in late-type spiral galaxies and Magellanic irregulars (de Vaucouleurs & Freeman, 1972). An interesting question is whether the bars in spiral

galaxies are the same (having the same origin) as the Magellanic ones. A bar does not have a precise definition but it describes a central region of a galaxy. For spiral type galaxies a rectangular, central cigar shaped feature is referred to as the bar whereas in dwarf galaxies it is something detected with a kinematic signature (the kinematic signature is also seen in spiral galaxies). The kinematic signature forms due to the family of orbits within the bar being different from those within the disc (or halo).

When it comes to the literature about the LMC bar however, I would like to focus on three topics: orientation and position with respect to the disc, structure (such as warps) and populations. Within these topics contrasting (and contradictory) results are generally found.

Zhao & Evans (2000) suggested the off-centred bar is misaligned and offset from the LMC disc and that the cause of this is tidal interactions with the SMC and the Milky Way. An alternative hypothesis is the bar is not a structure originating from the LMC but instead a swallowed dwarf galaxy. Similar to in biology how eukaryotes at some point in the past probably swallowed viri and simple bacteria, that then became organelles inside the cell. Nikolaev et al. (2004) also find the bar is slightly offset toward the Milky May by ~ 0.5kpc.

Girardi & Salaris (2001) found the absolute magnitude of the RC stars within the LMC bar to be around $\Delta I = 0.02$ mag brighter than those in the outer fields, suggesting the bar might be lying in front of the disc by ~ 0.5 kpc. Nikolaev et al. (2004) confirmed this, though they did find it to be aligned with the disc plane. Koerwer (2009) found the bar to stretch along a North–West to South–West line through the origin of a fitted plane and to be floating about 1 kpc (0.04 mag) nearer to us. He was unclear what the cause could be as it could be population, geometric and crowding effects. Haschke et al. (2012a) found the bar is partially in front of the LMC disc and is visible in both younger and older stellar populations.

But does appearing to be in front of the disc mean it is not is part of the disc? Zaritsky (2004) suggested the bar is the result of viewing a triaxial stellar bulge that is embedded in a highly obscuring thick disc from looking at $UBVI$ photometry of the central 64 deg^2 area of the LMC. Subramaniam & Subramanian (2009) used dereddened

OGLE-III I band photometry of RC stars to look at the inner LMC region. Looking at the mean magnitudes for regions sized $4.44' \times 4.44'$ they found no difference between bar or disc concluding that the bar is part of the disc. They did find dispersion about the mean for the bar and the disc suggesting the disc is thicker here, which is a finding also made by Subramanian & Subramaniam (2009).

Does the structure appear warped or not? van der Marel (2001) used NIR star count maps and found the bar had a smooth structure. Contradicting this, Koerwer (2009) found the bar itself has warps and structures (the amplitudes of which are 1 kpc or 1.5 kpc). Subramaniam (2003, 2004) found a warp in the form of the magnitudes of the inner LMC bar varying in the East–West direction with both East and West being closer to us than the centre.

Population differences have been seen between RR Lyrae and Cepheid stars in OGLE data Haschke et al. (2012a) and Van der Swaelmen et al. (2013) reached similar conclusions based on spectroscopic abundances. Specifically Van der Swaelmen et al. (2013) observed the bar has more scatter in [α/Fe] and an offset in Y, Zr and Na elements. They postulated that new star formation of massive stars injects freshly synthesised α-elements, while new metal-rich AGB stars produce the Y, Zr and Na elements. Hence, the differences between the bar and the disc provide evidence of an episode of enhanced star formation a few Gyr ago in the central parts of the LMC leading to the formation of the bar. In other words it is not a dynamically (or interaction) driven over-density but created from star formation. Although it could be a combination of the two. Maybe this induced both star formation and, subsequently dynamically the structure we see today.

In summary, the LMC bar is found in front of the disc but the population is not separate from the disc making that region of the LMC geometrically thick. It sometimes appears distorted though, which makes it unclear if it is aligned with the disc or not. Findings can differ depending on population tracer used. In my thesis I am looking at the 3-D structure of the Magellanic Clouds so the kinematics of the LMC bar are not so relevant but the population composition and the 3-D structure of course are. I will inevitably investigate the disc alignment and position of the LMC

bar hopefully shedding some light on these ambiguities.

1.4.9 Interactions

As introduced in Section 1.1.2, the discovery of a Bridge of gas connecting the Clouds and a stream of gas trailing was immediate and unequivocal proof of the Clouds having interacted with one another some time in the past Gyr or so, through tidal forces and possibly more direct contact. Being so close to the Milky Way (closer than some globular clusters) means that also the tidal action of the Milky Way and ram pressure from the hot gas in its halo should have affected the Clouds.

An example of more recent work is the study of the ages of globular clusters in the Magellanic Clouds by Bekki et al. (2004), who found they had formed either within a few Gyr of the Big Bang ($\sim$ 13 Gyr ago) or as recently as $\sim$ 4 Gyr ago. Using gasdynamical N-body simulations of the orbital evolution of the LMC and SMC they found that the first close encounter between the Clouds happened $\sim$ 4 Gyr ago. This strong tidal interaction induced dramatic gas cloud collisions which lead to an enhancement of the formation of globular clusters. They also predicted a stellar stream originating from the LMC – this is not the same as the gaseous Stream, and it has not (yet) been found.

It became clear that in order to constrain the interaction and dynamical history of the Clouds, more accurate measurements of the orbital speed were necessary. Using the HST to make precise proper motion measurements, Kallivayalil et al. (2006b,a) found that these values still allowed for either an unbound pair of galaxies, or for a galaxy pair that has been in place for as long as the Universe has existed (a Hubble time), depending on the assumptions about the dark matter potential of the Milky Way. Besla et al. (2007, 2010) remodelled the orbital history of the Clouds and found they could well just be on their first passage by the Milky Way. Besla et al. (2012) and Diaz & Bekki (2012) went one step further in suggesting that much of the morphological distortion of the Clouds is due to their mutual interaction over the past few Gyr before they met the Milky Way: the stream by tidal action of the LMC upon the SMC,

and the warped offset bar of the LMC by a direct encounter with the SMC. Olsen & Massey (2007) suggested the velocity dispersion of young stars in the LMC disc has been increased through tidal heating, and Mackey et al. (2016) found structures in the periphery of the LMC disc which Besla et al. (2016) explained in terms of tidal distortions.

Nidever et al. (2008) suggested that some of the Stream gas may actually originate from the Tarantula region in the LMC, not just from the SMC. Stars and clusters from the LMC might have made it all the way to the SMC, as Glatt et al. (2008) found a relatively metal-rich sample of intermediate-age clusters previously believed to belong to the SMC, in fact to lie in front of the SMC at a distance comparable to that of the LMC. A decrease in metallicity of the youngest, compared to the intermediate-age populations in clusters (van Loon et al., 2005) and the field (Rubele et al., 2011), on the other hand, suggested that SMC gas might have fallen *into* the LMC, with Olsen et al. (2011) finding evidence for stars in the LMC to have been accreted from the SMC.

Hammer et al. (2015) present one of the most sophisticated models to date of the history of the Magellanic Clouds' gas structures, suggesting the Stream is an entwined pair of filaments – one originating from the LMC and the other from the SMC. A combination of tidal effects and ram pressure stripping is invoked to explain these structures, with a most recent close encounter between the LMC and SMC to have taken place $\sim$ 200–300 Myr ago. These outcomes depend on the assumed mass profiles of all three galaxies involved, as well as the precise space velocities, and so additional independent constraints are needed, in the form of the distribution, kinematics, ages and metallicities of the stellar populations in each of the Clouds.

In this thesis I look in particular at the distribution of the intermediate-age populations, $\sim$ 1 Gyr of age, after the strong encounter between the Clouds a couple of Gyr ago but before the most recent encounter when they also approached the Milky Way.

1.4.9.1 Magellanic Bridge

In Chapter 7 I search for evidence of stellar populations within the Magellanic Bridge – the gas region which is between the LMC and SMC and connecting these two. The gas is thought to be tidally stripped from the MCs during interactions with each other and the Milky Way.

Hindman et al. (1963b) conducted a low resolution (2.°2) neutral hydrogen survey of the Magellanic System. They not only found gas content within the Magellanic Clouds, but between them appearing to form a Bridge. This discovery was further detailed in Hindman et al. (1963a) as an H I envelope embedding the LMC and SMC. It was checked to continuously link the Clouds rather than being extensions towards them.

As such most of the research conducted on the Bridge is on the dynamics and the gas content (e.g. Barger et al. (2013) mapped Hα emission). There have been searches for evidence of a stellar population because the tidal stripping effect should yield some sort of population too. Recently there have been discoveries of stellar populations lying within the Bridge.

Irwin et al. (1985) used one of the UK Schmidt fields to discover blue main-sequence stars (of $\sim$ 100 Myr old) extending 9° East of the SMC along the H I ridge extending from the SMC Wing, towards the LMC. Irwin et al. (1990) extended this study by covering a wider area (two more fields) and using spectroscopy to verify stellar type, distance and radial velocity consistent with the Magellanic Clouds.

A series of three papers on the young intercloud population were published between 1998 and 1999. In the first of these, Demers & Battinelli (1998) used BV photometry of the SMC Wing and Bridge to find a slight distance gradient going from the SMC Wing towards the LMC, and evidence for a younger main sequence population (formed 10–25 Myr ago). In the second one, Battinelli & Demers (1998) looked at the mid–West region of the LMC for evidence of recent star formation, finding none. In the third, Demers & Battinelli (1999) looked at the South–Western LMC periphery ($\sim$ 2 deg^2). While predominantly finding intermediate aged populations, the younger

population of these suggests star formation occurred up to 0.8 Gyr ago in these regions.

Harris (2007) used CRI photometry[17] of 12 Bridge regions (shown in Harris 2007, Fig. 1), following the H I ridge as he was interested in stars formed by tidally stripped gas as well as any tidally stripped stars. He found a younger population in the Western part as others previously had (e.g. Demers & Battinelli 1998). He found Eastward of RA= 45° that this is truncated and suggested this is due to the H I gas density falling below the threshold required for star formation. Likewise he was not able to find evidence of an older stellar population (i.e. tidally stripped stars). This has the implication of all stars in the Bridge formed there in situ and that only gas was stripped.

But more recently, evidence of an older population has grown. Bagheri et al. (2013) detected an older population of RGB and AGB stars within the Bridge. The data used were 2MASSS and WISE and the Bridge region covered $-77° < \text{Dec} < -69°$ and $30° < \text{RA} < 60°$ (to remove contamination from LMC and SMC). Foreground removal was conducted using a region centred on $l = 292°$, $b = 39°$ (same Galactic longitude as the Bridge for similar reddening but positive latitude to remove effect of MCs). The first removal method binned a CMD area then determined probability of an object belonging to the Bridge from that (cutting those with $< 75\%$ chance); this yielded an over-density. The second method used a colour cut on two-colour diagrams. The populations of these are characterised using the Nikolaev & Weinberg (2000) populations (boxes on CMD regions to denote different star types).

Noël et al. (2013) presented the first results from the MAGellanic Inter-Cloud program (MAGIC) and used synthetic CMD techniques to detect intermediate aged star populations (required to explain the tidal stripping origin of the Bridge). They looked in two fields (covering an area of 1.12 deg^2). Their distribution suggests the stars have been tidally stripped from the SMC (from the absence of intermediate aged stars nearer the SMC) although it is not fully conclusive and spectral studies will be required. Noël et al. (2015) expanded their work to ten fields lying perpendicular to

[17]Washington C, Harris R and Counsins I.

the main H I ridge. The main findings were young, intermediate and old age stars have distinct spatial distributions. Young stars correlate with the H I suggesting they had been formed in situ or were stripped from the SMC along with the gas. Intermediate aged stars are spread out and have similar properties to stars located ~ 2 kpc from the centre of the SMC suggesting they were tidally stripped from there. Finally, the old stars extend from the SMC suggesting they are part of an extended metal-poor stellar halo.

Nidever et al. (2013) examined the stellar component of the Magellanic Bridge by looking at the Eastern and Western sides of the SMC and the line-of-sight depth of the RC stars in these. They identified a ~ 55 kpc stellar structure in the Eastern SMC and suggested this is a stellar counterpart of the H I Magellanic Bridge that was tidally stripped from the SMC ~ 200 Myr ago during a close encounter with the LMC.

Skowron et al. (2014) studied the Bridge using the new OGLE IV data covering over 270 deg^2. They removed foreground by using tiles away from the Bridge to act as a sample foreground tile. They normalised and binned the CMD of these Bridge tiles and the foreground tiles and subtracted the CMDs from each other. This enabled them to observe multiple populations, not just the RC. They confirmed that for the younger population, while a majority of stars are found within the Western part of the classical Bridge there is also a small but statistically significant population extending towards the East, forming a continuous stream of stars. The distribution of these is centred on two regions, one close to the SMC and one mid-way between the Clouds, which they named "OGLE island". When comparing with H I density the region close to the SMC matches well while OGLE island is offset by $\sim 2^\circ$ North. For the intermediate aged RC stars they find presence of these in the Southern and central parts of the Bridge. These populations deviate from the radial profiles of the galaxies implying these are a tidal stream of stars or that the galaxy halos overlap.

Clusters have also been looked at in the Bridge region. Most recently Bica et al. (2015) studied 14 of these with B and V photometry obtained from the Southern Astrophysical Telescope. Values for reddening ($0.01 < E(BV) < 0.05$ mag), ages ($7.3 < \log\,(t/\mathrm{yr}) < 8.3$), metallicity ($0.001 < Z < 0.010$ dex) and distances were

obtained. The metallicity range fits young LMC and SMC populations and from the distances the Bridge appears as a structure connecting the LMC farside in the East to the foreground of the SMC in the West. Most of the clusters are tidal dwarf candidates suggesting part of the Bridge evolving into a tidal dwarf galaxy. Nishiyama et al. (2007) also suggested the Magellanic Bridge has the potential to evolve into a dwarf galaxy if it maintains current star formation but caution that velocity measurements indicate the gas could be absorbed into the Magellanic Clouds.

Belokurov et al. (2016) used the Gaia DR1 to investigate the Magellanic System. For the Bridge they found the young Main Sequence stars follow the HI gas but the older RR Lyrae are offset by around 5°. By assuming a constant absolute magnitude for the RR Lyrae they found two RR Lyrae structures along the Bridge. The first is at around the distance to the LMC and the second forms a distance gradient between the SMC and LMC. This suggests the Bridge is a composite structure of two stellar streams, one for each MC.

Mackey et al. (2017) examined the Eastern half of the Bridge using the Dark Energy Camera examining the young stellar populations. The youngest populations (< 30 Myr) are likely to have formed in situ as evidenced by them being projected on top of the densest HI regions.

I aim to look for intermediate aged RC stars within the Magellanic Bridge. I started this before the work of Skowron et al. (2014).

1.5 Scientific questions addressed in this thesis

The goal of this thesis is to provide new insight into the structure of the Magellanic Clouds by making use of the well-defined luminosity and colour of RC stars. Because the structure of the MCs is the product of the star formation, stellar evolution and internal dynamics of each of the MCs as well as the interaction between them and the Milky Way, the ultimate aim is to better understand this relation between evolution over time, and structure as seen today.

There are three specific questions I will address. The first is the issue of the position and orientation of the LMC bar. The literature is ambiguous despite it being well studied. Answers to the questions whether the bar resides within the disc or not, and whether it is inclined with respect to the disc will have important implications for its formation and the impact the interaction between the two MCs might have had.

The second question concerns the tidal warps and tails in the LMC disc and extending from the SMC. These structural distortions are the result of the interaction of the MCs and the MW and their accurate definition will constrain models that can be made to describe the interaction history.

The third is more open ended; does using intermediate-aged RC stars reveal dynamical features that have hitherto evaded detection? Does it show substructure beyond a warped LMC disc and a stretched-out SMC? Does it reveal links between structure imprinted in intermediate-age populations and that traced by older stars on the one hand, and younger populations and active star-forming regions on the other? Does this place time stamps on the processes that led to the structure we see in these populations?

In order to achieve this, I take advantage of the well-defined luminosity and colour of RC stars to make maps of the distances to these stars across the Magellanic System (i.e. a clear map of structure). In the process, I make maps of the interstellar attenuation, which I not only use to correct the observed brightness and colour for the effects of attenuation and reddening, but which I also use to locate molecular cloud complexes that resemble the youngest structures within these galaxies. The novel factor in my work is that I am using the most sensitive near-IR survey of the Magellanic Clouds by far, which is the VMC survey.

The RC stars are firstly used to produce reddening maps:

- I thus map the distribution of interstellar dust to show how this galactic component compares to other gaseous and stellar components. Since dust is formed around dying stars, but is processed in the ISM and regulates the internal radiation field and heating before it takes part in star and planet formation, it

is important to understand how the dust is distributed within a galaxy.

- I use the dust map of the 30 Doradus region in conjunction with neutral atomic hydrogen gas to infer the molecular gas fraction, and thus locate the molecular clouds that may go on to form stars. These new stars will inherit this current structure within the ISM, but they will be affected in future mostly by stellar evolution and stellar dynamics.

- I use the reddening maps to de-redden the photometry of the RC stars so that accurate distance moduli can be derived, these being essential for a quantitative analysis of galactic structure. While the effect of reddening at the near-IR wavelengths of my data is already greatly reduced compared to optical data, it can still affect the accurate description of subtle features and must therefore be done with care.

I then use the, extinction-corrected, apparent brightness of the RC stars to derive their distance moduli, and thus:

- I map the distribution of RC stars across the Magellanic System, illustrating their two-dimensional (projected) structure and densities. I focus on intermediate aged stars, which formed from ISM structure in the past. These have since been redistributed as a result of dynamics over the past few Gyr, but some of the initial structure may have been preserved.

- I map the distance to the Magellanic Clouds, and variations of the distance across the Magellanic Clouds. This gives us the third spatial dimension, and thus a complete and non-degenerate picture of the structure of the Magellanic System.

- I interpret and model these variations in distance in terms of an inclined disc, revealing any tidal deformations which are the result of galaxy interactions.

- Specifically, I map the line-of-sight depth across the Magellanic Clouds, and

any discrete structures such as multiple overlapping components that may be related to the interaction between the Magellanic Clouds and the Milky Way.

The structure of this thesis is as follows. In Chapter 2, I discuss the VMC survey providing information on the instrumentation, observations and the data products resulting from these. In Chapter 3, I detail the main method for selecting RC stars used in successive chapters as well as methods pertaining to quantifying the geometric structure of the MCs. In Chapter 4 (an adaptation of Tatton et al. 2013a), I analyse the 30 Doradus tile with regards to the reddening and extinction and compare these with other reddening map publications and various forms of ISM tracers. In Chapters 5 & 6, I analyse the 3-D structure of the LMC and SMC including line-of-sight depths and fitting planes. In Chapter 7, I attempt to find RC stars in the Magellanic Bridge. Due to the low density nature of the Magellanic Bridge, Galactic foreground subtraction is necessary as an additional step. Finally, in Chapter 8 I present my summary, conclusions and possible avenues for future work.

2 Observations and data – the VISTA telescope and the VMC survey

The primary observational data used in this thesis come from photometry data taken as part of the Vista Magellanic Clouds (VMC) Survey. As the name suggests the observations are taken using the Visible and Infrared Survey Telescope for Astronomy (VISTA; Emerson et al., 2006; Dalton et al., 2006). I here describe the telescope, detector, observations and data processing and highlight issues that are relevant to the analysis I have performed and which I present in subsequent chapters.

2.1 VISTA telescope and the VMC survey

VISTA is located at the Paranal Observatory in Northern Chile, it has a 4m mirror and Infrared (IR) camera composed of an array of 16 Raytheon VIRGO 2048×2048 $20\,\mu$m pixel detectors in a 4×4 pattern. These are shown in Figure 2.1.

Each detector is spaced apart by 90% detector width along the x-axis and 42% along the y-axis. The arrangement is shown in Figure 2.2. By combining 6 stepped exposures (paw-prints) into one tile, an area of $1.5\,\mathrm{deg}^2$ is covered at least twice[1], with a pixel size of $0\farcs34$.

The VMC survey is a uniform and homogeneous survey of the of the Magellanic System (MS) in the NIR and has two main scientific goals; to determine the spatially-resolved star formation history (SFH) and the 3D structure. The VMC survey is performed in the Y, J and K_s filters (centred at $1.02\,\mu$m, $1.25\,\mu$m and $2.15\,\mu$m respectively), in the VISTA (Vega mag) photometric system. The transmission curves for the VISTA filters are shown in Figure 2.3. The reasons for the VMC survey choosing

[1]Regions have at least 2 pointings (after combining jitters) for each paw print. The underexposed regions ($\times 1$) at two edges are not included in our regions but should be recovered when adjacent tiles are observed. Other small regions have up to 6 overlaps which are accounted for in the confidence maps.

Figure 2.1: Photographs (from `http://www.eso.org/sci/facilities/paranal/instruments/vircam/inst.html`) showing the VISTA telescope (top panel) and the VIRCAM detector focal plane (bottom panel).

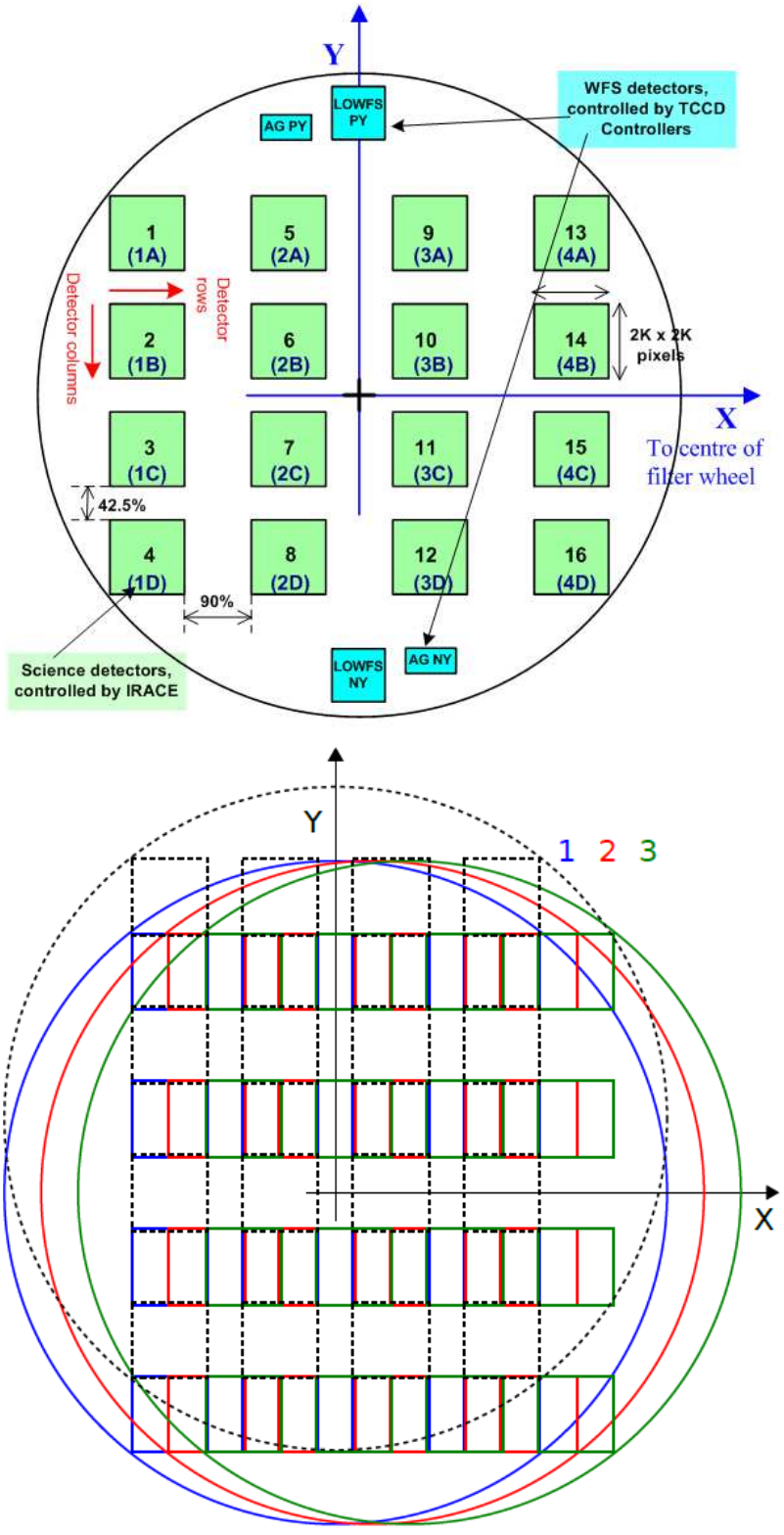

Figure 2.2: VISTA detector array pictures (from `http://www.eso.org/sci/facilities/paranal/instruments/vircam/inst.html`). Shown is an arrangement of the focal plane (top) and an illustration of the offsets used (bottom); the x axis offsets are coloured and a dashed line illustrates the position of the y axis offset.

Y, J and K_s filters are given in Cioni et al. (2011); a wide wavelength range is required for good characterisation of the subgiant branch used in deriving SFH. The J band is chosen over the H band due to the bluer J band suffering less from atmospheric effects, for comparative observations with previous surveys and because the relationship between $J-H$ and $J-K_s$ are quite linear (meaning the H band provides little additional information). Y is chosen over Z due to Y having a reduced confusion limit[2]. The K_s filter is required to study variable stars because period–luminosity relationships (for RR Lyrae and Cepheid stars) are less affected by uncertainties in reddening and metallicity at this wavelength.

Once complete (expected in 2019), the survey will cover $\sim 180\,\mathrm{deg}^2$ of the MS (see Figures 2.4–2.6). The average 5σ magnitude limits[3] are $Y = 21.9$ mag, $J = 22.0$ mag, $K_s = 21.5$ mag; about 5 mag deeper than those of the 2 Micron All Sky Survey (2MASS)[4].

As part of the VMC goals each tile was observed at different epochs. Each epoch has 5 jitters[5] resulting in the median time for exposure per paw-print, per epoch being 800s in Y and J and 750s in K_s. In total there are 3 epochs for Y and J and 12 for K_s. The combined average total exposure, per paw-print, is 2400s in Y and J and 9000s in K_s. A more thorough description of the VMC survey can be found in Cioni et al. (2011).

The areas that the VMC survey covers are shown in Figures 2.4 to 2.6 *(these are repeats of figures included in Cioni et al. 2011)*. Information on individual tiles used are supplied in their respective chapters.

[2]A combination of two criteria required to detect a point source; the source flux is much brighter than the background fluctuations (photometric criterium) and the source is far from other sources of similar brightness so they can be detected individually (source density criterium). Further information can be found at `http://elte.prompt.hu/sites/default/files/tananyagok/InfraredAstronomy/ch11.html`

[3]Estimated using ESO VIRCAM Exposure Time Calculator v3.3.3 with settings of: blackbody with T=5000K, Airmass=1.6, Seeing= $1''(K_s)$, $1''.1(J)$ and $1''.2(Y)$, Point Source, DIT=1 sec, Total Exposure Time = 2400s (Y), 2400s (J) and 9000s (K_s).

[4]`http://www.ipac.caltech.edu/2mass/overview/about2mass.html`

[5]Exposures taken at slightly different positions for two main reasons; firstly, to remove stars in producing a sky for sky subtractions and secondly, to filter out cosmic rays and bad pixels.

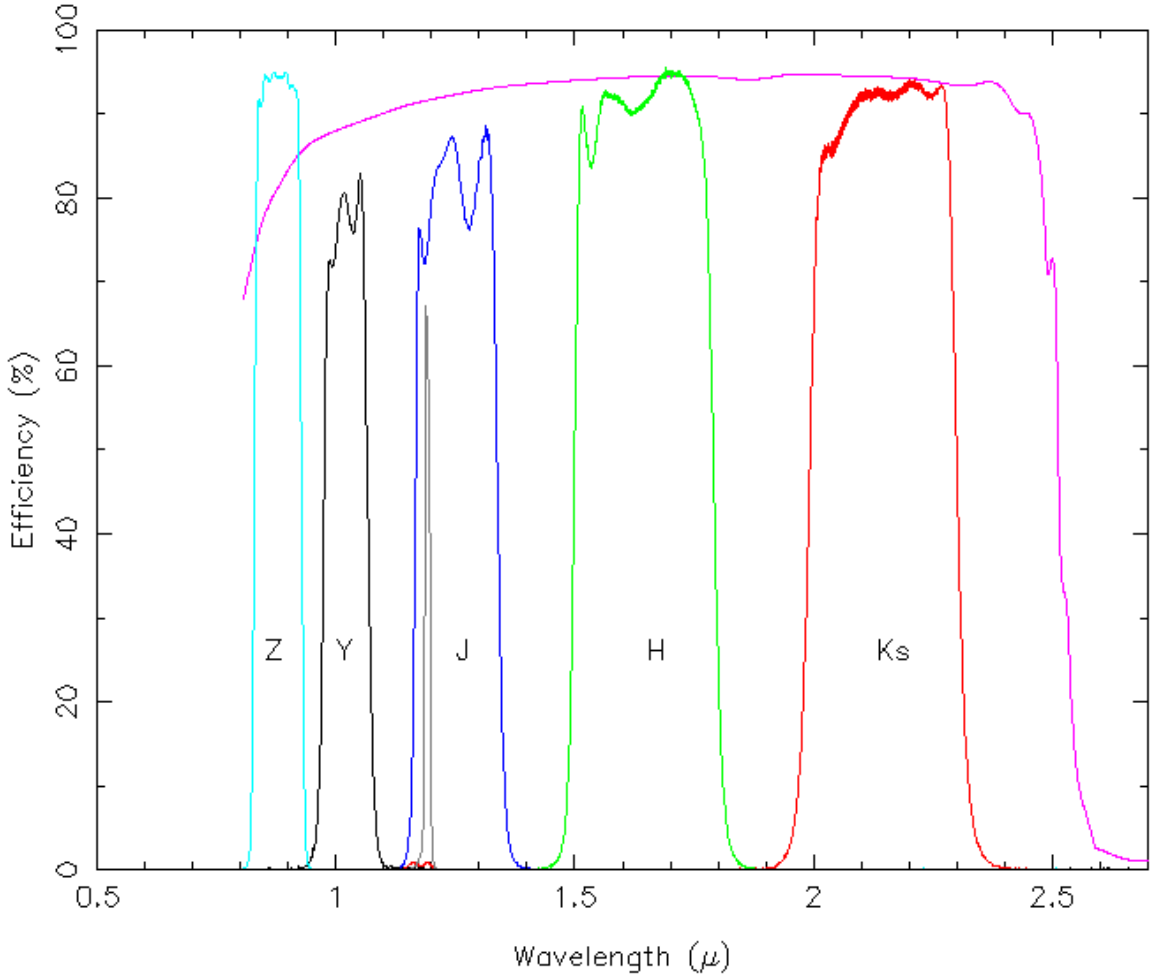

Figure 2.3: The VISTA $ZYJHK_{\rm s}$ filter transmission curves (form `http://casu.ast.cam.ac.uk/surveys-projects/vista/technical/filter-set`) showing transmission efficiency vs. wavelength. Overplotted in purple is a sample detector quantum efficiency curve. For the VMC survey the $YJK_{\rm s}$ bands are used.

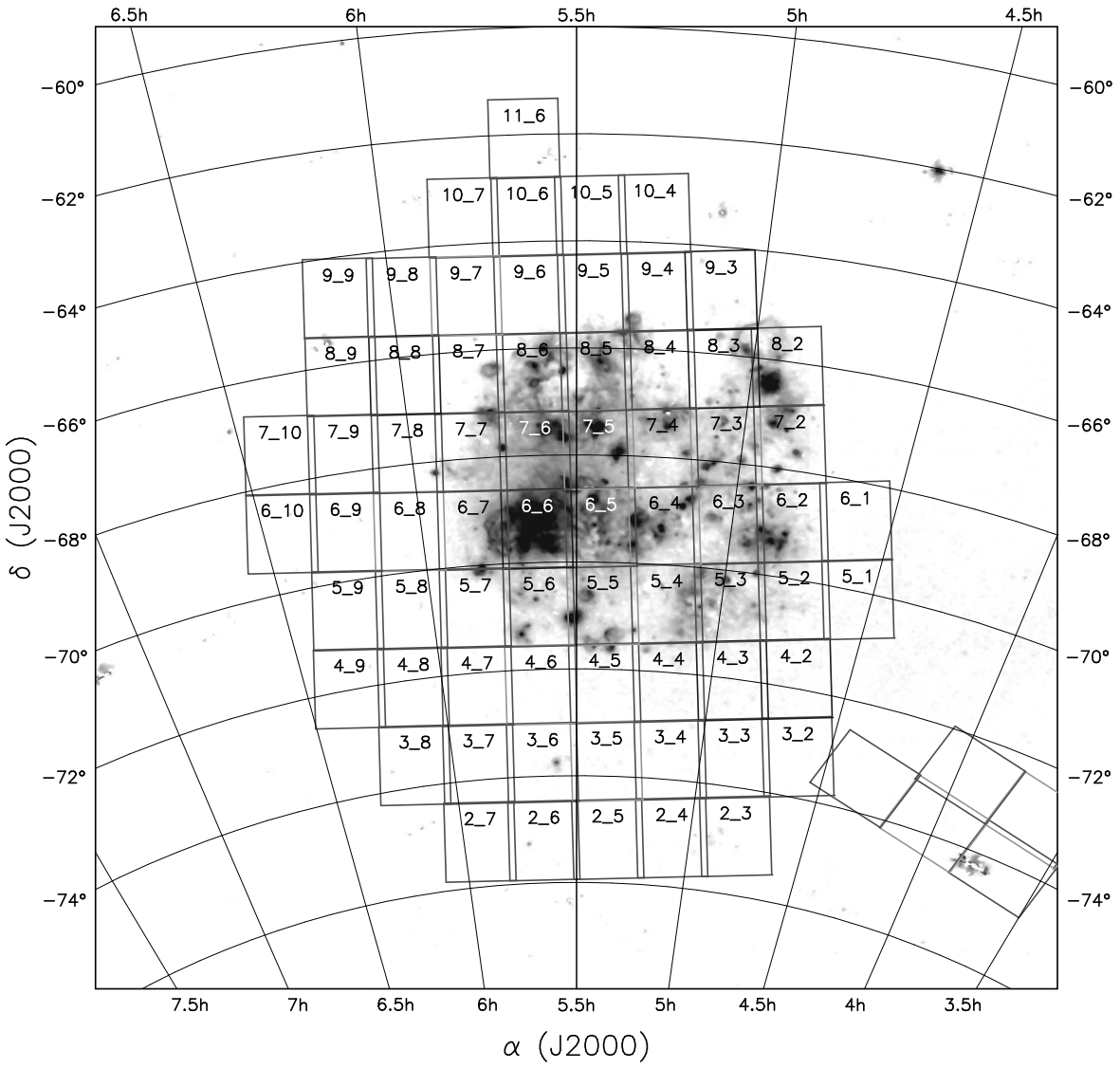

Figure 2.4: *(figure reproduced from Cioni et al. 2011)* LMC area tiled for VMC observations. The underlying image shows the Hα distribution from Gaustad et al. (2001).

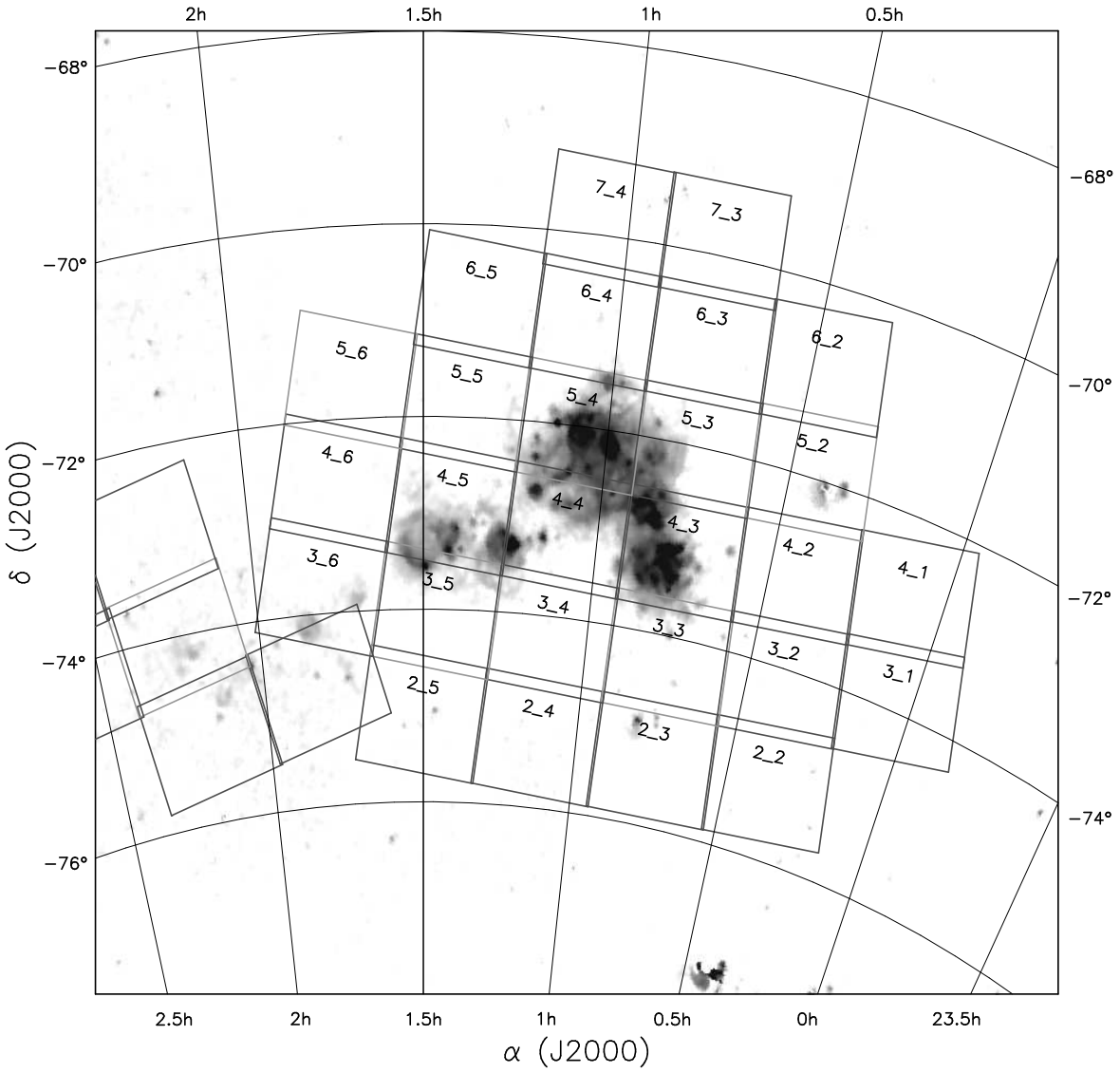

Figure 2.5: *(figure reproduced from Cioni et al. 2011)* SMC area tiled for VMC observations. The underlying image for the SMC shows Hα distribution from Gaustad et al. (2001).

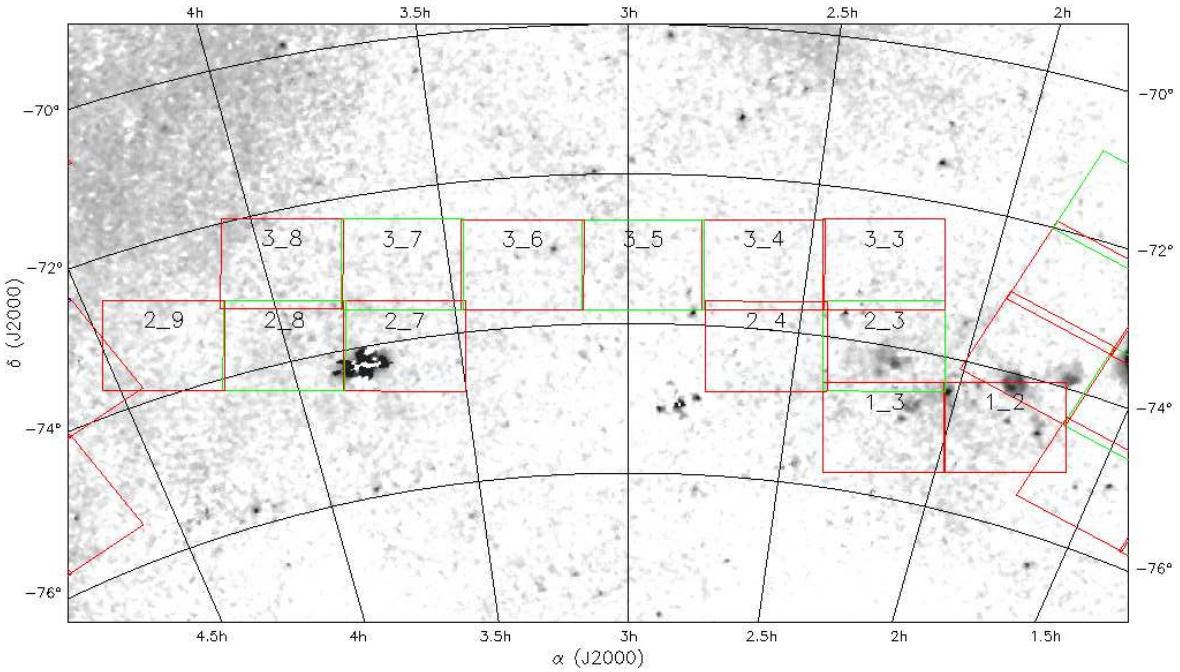

Figure 2.6: *(figure reproduced from Cioni et al. 2011)* Bridge area tiled for VMC observations. The underlying image for the Bridge shows the H I distribution from McClure-Griffiths et al. (2009).

The data used were retrieved from the VISTA science archive (VSA)[6]. The VSA and the VISTA Data Flow System pipeline are described in detail by Cross et al. (2012) and Irwin et al. (2004), respectively with some details given in the next subsection.

2.2 Data flow, data reduction and data archive

An initial simplified real-time first-pass for the data reduction is conducted immediately after the observations are taken in Paranal. This is for quality control purposes. The raw observation data are transferred via FTP to ESO in Garching where these data are ingested into the ESO raw data archive and a second reduction pipeline is run. The purpose of this second pipeline is to monitor instrument health, generate calibration data and provide library calibration frames (used in the summit pipeline in Paranal). This process typically takes about 5 days from observation. The file transfer process previously involved hard drives (USB discs), which were physically shipped.

These data are then forwarded to Cambridge where the science data reduction takes place using the Vista Data Flow System (VDFS[7]) pipeline made by the Cambridge Astronomical Survey Unit (CASU[8]). These products are then ingested into the Vista Science Archive (VSA) hosted by the Wide Field Astronomy Unit (WFAU) in Edinburgh.

2.2.1 VDFS reduction steps

The following sub-subsections contain a brief description of the steps the VDFS pipeline carries out. This information is based on what is provided on the CASU webpage[9].

[6] Chapter 4 uses the v20120126 release and PSF photometry (see section 2.3.1).
[7] `http://casu.ast.cam.ac.uk/surveys-projects/vista/vdfs`
[8] `http://casu.ast.cam.ac.uk/surveys-projects/vista`
[9] `http://casu.ast.cam.ac.uk/surveys-projects/vista/technical/data-processing`

2.2.1.1 Reset, dark, linearity, flat and de-striping correction

The reset correction is similar to the debias operation done in CCD data reduction. The debias operation[10] extracts the useful portion of CCD data by masking defects, correcting gain and the amount of charge left behind in a pixel on a readout transfer (known as deferred charges) and setting saturated values (flagged as bad or corrected to a defined limit). Reset frames are taken for each exposure and subtracted. This step has an effect in estimating the linearity of the detectors (see below).

The dark correction is a dark frame subtraction using a mean dark frame estimated from a series of exposures with an opaque filter inserted. This additionally corrects several other additive electronic effects.

The linearity correction is required due to the VISTA detector not having a linear response. The non-linearity is estimated from timing information for the readout, exposure and reset image. There is no shutter on the camera and the default double-correlated sampling mode is subtracted prior to writing images.

The flatfield correction removes small scale quantum efficiency (QE) variations from the detector and the large scale vignetting (reduction in brightness towards the edges of the image) of the camera (plus dust specks, scratches and other inhomogeneities on the filter and optics). This is done by dividing by a mean twilight flatfield image. Additionally the global flatfield properties of each detector are used to gain-normalise each detection into a common (median) system. The flat frame is also used to derive initial confidence maps, as dead/hot pixels are easy to detect in flat frames.

The de-striping is a necessary step as there is a horizontal stripe pattern in the background introduced by the readout electronics for the VISTA detectors. While each exposure has a different pattern, each group of four detectors has the same pattern in these exposures (as they are read out by the same IRACE controllers[11]). This provides a layer of redundancy in estimating the stripe pattern.

[10] See `http://star-www.rl.ac.uk/docs/sun139.htx/sun139ss12.html` for additional information.

[11] See `https://www.eso.org/sci/facilities/develop/detectors/controllers/irace/aboutirace.html` for more information.

It is worth noting that VISTA operates in correlated double sampling (CDS) mode[12]. The "reset" frame is taken; as readout at the beginning of the exposure, so what actually gets recorded is the difference between this frame and another one taken at the end of the timed exposure (TEXP). This is done on-board VIRCAM.

2.2.1.2 Sky background correction

The sky background correction removes the large scale spatial background emission of the atmosphere and additive effects. The background map is estimated using algorithms that combine science images with rejection or masking. In the presence of large extended objects, offset sky exposures are used instead to create a background map. For the VMC observations, the sky background is estimated, for each paw-print, from all paw-prints observed for one tile in a given band and at a given time (Cioni et al., 2011).

It is noted getting this step correct is one of the biggest difficulties in near-infrared image processing.

2.2.1.3 Jittered and paw-print stacking

Infrared observations are broken up into shorter exposures with the telescope moved slightly between each, due to bad pixels and other cosmetic defects. The jittered images are shifted and combined into a single stacked image where detected objects are used to determine the shift. This allows bad pixels to be rejected by using good pixels from other exposures.

[12] A method of measuring the output of a sensor. Outputs are measured twice: once with a known condition and once with an unknown condition (see `https://en.wikipedia.org/wiki/Correlated_double_sampling`).

2.2.1.4 Point source extraction

This is the start of catalogue generation where the information on objects is extracted from the stacked paw-prints. These include positions, fluxes and shapes which are combined to generate morphological classifications and form the basis of the calibration and quality control (QC) information.

2.2.1.5 Astrometric and photometric calibration

Objects in the catalogue are matched with 2MASS sources to calibrate the world coordinate system of VISTA images to an accuracy better than 50 milli arsec (0.″05). Photometric zeropoints are determined to an accuracy of $1\% - 2\%$ (depending on wave band) by using the 2MASS magnitudes (converted into VISTA photometry) in conjunction with colour equations. This is a revision of the approach used for UKIRT (a $ZYJHK$ telescope) described in Hodgkin et al. (2009) and is described in more detail within González-Fernández et al. (2018). The 2MASS photometry itself was zero point calibrated using calibration tiles being observed hourly and fits were created based on these data (Skrutskie et al., 2006). $HK_{\rm s}$ data employed, a linear fit across a night whereas J used an hour to hour interpolation due to the band's sensitivity to variable water vapour opacity.

This relies on the assumption that for the majority of stars there is a simple linear equation relating 2MASS and VISTA colours. It is worth noting that while this does cover the majority of stars it was recently found to not be true for A0 stars. This means extra steps are required to produce Vega magnitudes because in a Vega based photometric system an A0 star has 0 colour in all bands, irrespective of filter used. Details of the colour equations used to do this are provided in González-Fernández et al. (2018).

2.2.1.6 Tiling

It is required that the stacked pawprints are combined into tiles. Once this is done the catalogue steps are repeated to achieve full photometric depth. To prevent spurious structures from being included in the edges between detectors the stacked pawprints are pre-filtered using a nebulosity filter which removes structures larger than 30 arseconds. Sections 3 and 7.4 of González-Fernández et al. (2018) provide more information on this.

2.2.2 Vista Science Archive

The data are ingested in the VSA (this is similar to the WFCAM science archive detailed in Hambly et al. 2008) and archived onto the VSA website[13]. The VSA can be queried using a webform, SQL and sources can be cross-matched with other datasets using its built-in data[14] or by being given a list of coordinates.

After the data have been reduced using the VDFS pipeline at CASU it is ingested into the VSA which is part of WFAU in Edinburgh. The VSA itself is a development of the WFCAM science archive (detailed in Hambly et al. 2008).

These reduced data are turned into three types of table; *vmcDetection*, *vmcSource* and *vmcSynoptic*. The vmcDectection table contains catalogues for individual observations, one per paw-print. The vmcSource table is a list of sources obtained from the deep stack images and each source is matched in the three VMC Y, J and $K_{\rm s}$ bands. This is the table I use in this thesis. The vmcSynoptic table contains colour info and multi-epoch information for individual observations, making it more suited to studying variable stars.

VMC being a public survey means that data for each tile are submitted to ESO for release to the general astrophysical community approximately 6 months after a tile

[13] `http://horus.roe.ac.uk/vsa/`
[14] Which includes a number of non-VISTA surveys such as 2MASS and Spitzer.

has been completed (all epochs in all bands).

2.3 Photometry

The end product of the VDFS ingested into the VSA is aperture based photometry. The VMC consortium also creates Point Spread Function (PSF) photometry for completed tiles. These are then added to the VSA. As tiles that have incomplete observations are still useful there are times when aperture photometry has to be used. In aperture photometry a region around each star (the aperture) is extracted and the sky background is subtracted. The remaining counts are the luminosity. This is very simple but has drawback of not producing complete results when sources occupy spaces smaller than the aperture (here, a 2 arcsec diameter).

2.3.1 PSF photometry

Point spread function (PSF) photometry was used instead of aperture photometry for the 6_6 tile analysis covered in Chapter 4 primarily due to crowding in that region (illustrated in Section 2.4.2.1). It was also used for the SMC structure analysis in Chapter 6 because it was available for all relevant tiles.

The following paragraph uses elements of section 2.1 of Rubele et al. (2012). PSF photometry was created for the VMC science goal of the star formation history because it produces deeper catalogues (particularly in crowded tiles) than the aperture photometry the VSA provides. The PSF photometry is produced firstly by using the DAOPHOT package within IRAF (Stetson, 1987) where the PSF package is used to produce the PSF model and the photometry is performed using ALLSTAR with a radius of 3 pixels (2.5 in the 6_6 tile), which is comparable to the 2 arcsec diameter of the aperture photometry. The DAOPHOT PSF model is a hybrid of Gaussian, Moffat and Lorentz fits.

The drawback of PSF photometry is that a PSF model must be fitted and this requires good quality data that is not of variable seeing (also the target has to be a point source; which stars are). These data requirements in particular can be a problem with many ground based observations. While it is true PSF photometry produces deeper catalogues in the crowded regions, in non-crowded regions there is little to be gained.

2.3.2 Completeness and crowding

Incompleteness is caused by the magnitude limit of VISTA for dimmer stars and crowding (stellar environments of high density) for brighter stars. In the case of the former the 5 sigma magnitude limits are stated earlier but lie between 21.5 mag and 22.0 mag depending on passband.

Some of the science goals of the VMC survey do require completeness of stellar photometry to be known across the MS (i.e. their distribution mapped both for magnitude and position). This is carried out through the standard procedure of artificial star tests (adding artificial stars of known magnitude and positions to the images and then finding these in the derived catalogues).

For the relatively low density 8_8 LMC tile such a test is described in Cioni et al. (2011). A region of 4000 × 4000 pixels was extracted from the deep tile image and PSF photometry was performed (as this was carried out prior to VSA being available). Artificial stars were positioned at the same random positions for each of the $YJK_{\rm s}$ images (so they are present in all passbands) with mutual distances greater than 30 pixels so as not to overcrowd the image. The artificial stars spanning small bins of colour and magnitude are grouped together to produce estimates of the ratio between recovered and added stars (the completeness) as a function of position in the CMDs.

Figure 2.7 *(a reproduction of Figure 11 from Cioni et al. 2011)* shows the found completeness as a function of magnitude for each of the three passbands for single epoch and deep stacks. Completeness was found to be over 90% at $K_{\rm s} = 18.0$ mag for a single epoch and over 95% in a deep stack. Considering the magnitude of the

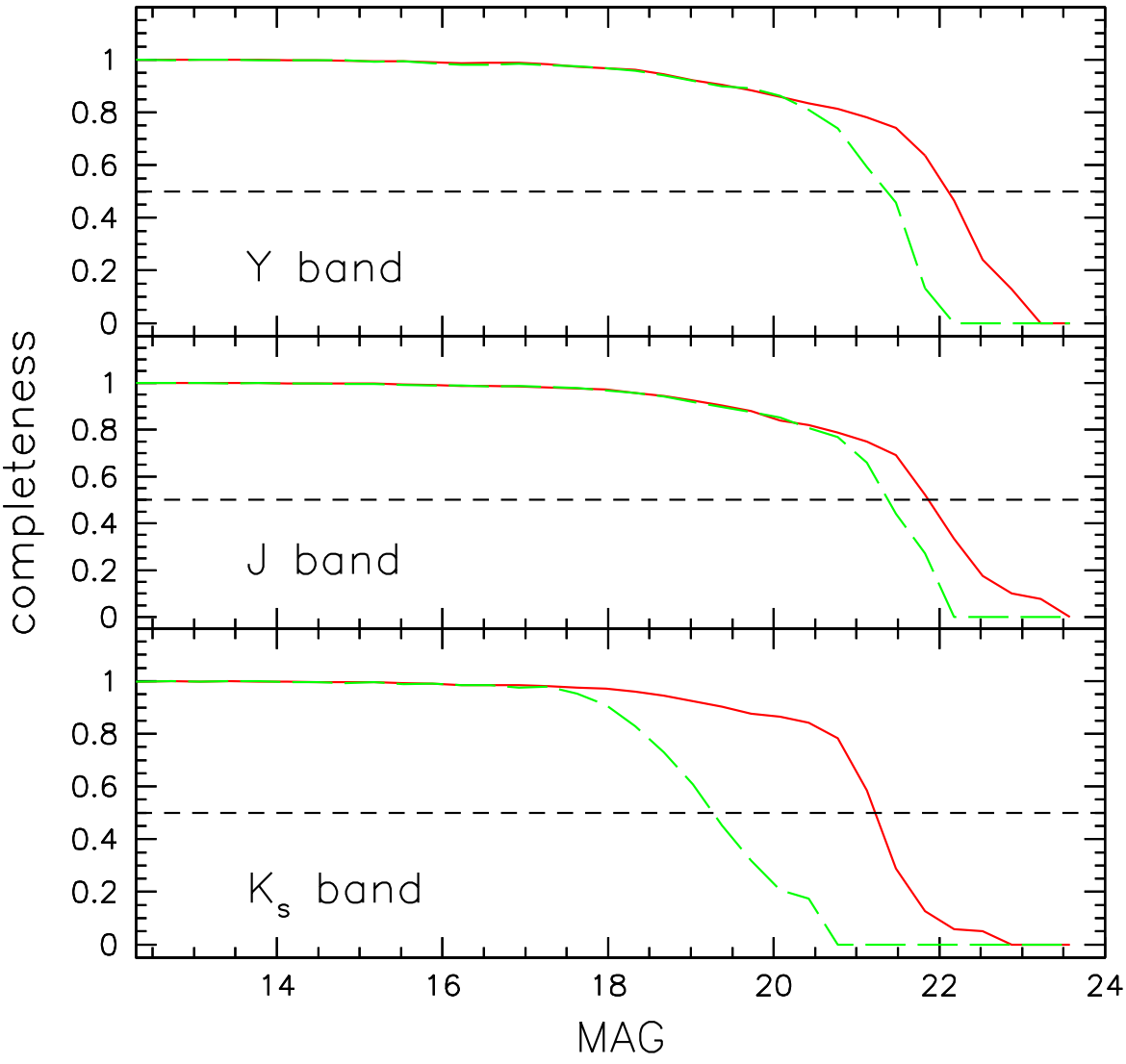

Figure 2.7: *(figure reproduced from Cioni et al. 2011)* Completeness results for the 8_8 LMC tile for single epoch (dashed line) and deep stacks (continuous line). Horizontal dashed line indicates 50% completeness.

red clump stars is brighter than this a single K_s epoch is sufficient for observations. In terms of Y and J very few RC stars are dimmer than 19.5 mag which is where the 90% completeness is found for those bands. These results are in good agreement with the simulated VMC images of Kerber et al. (2009).

More recently, Rubele et al. (2015) found the typical 50% completeness limit in the outermost SMC tiles to be at about 22.3, 22.1 and 20.8 mag in the Y, J, K_s filters, respectively using their PSF photometry. For the Y and J filters, these results show greater completeness than Figure 2.7.

However, the source crowding is seen to be an issue in dense regions such as R136 in the 6_6 LMC tile (see section 2.4.2.1). As far as completeness is concerned for crowded tiles Figure 2.8 shows this for the 6_6 LMC tile and the less crowded 8_8 LMC tile. The completeness drops at brighter magnitudes in the denser field. The scope of my work broadly covers the K_s band between 16 and 19 magnitude which has an average completeness over 70% with brighter than 17 mag being over 90% in the more crowded region. The less crowded region remains over 90% throughout. In terms of the Y and J bands the completeness offset exceeds average RC colour at the brighter end but for the dimmer end this offset narrows as the magnitude limit begins to apply an effect. This potentially means high extinction is biased towards brighter stars in crowded regions as the most reddened, faintest stars become undetected. In other words, for completeness=90% the $Y - K_s$ colour is 0.5 mag while at completeness=75% this is 0.25 mag.

2.4 Problems with observations & data processing

2.4.1 Technical issues

The CASU website lists several known problems with the observations (`http://casu.ast.cam.ac.uk/surveys-projects/vista/technical/known-issues`).

2.4.1.1 Dectector 16

The major technical issue encountered in the VMC survey (and VISTA based observations in general) is the variable quantum efficiency that affects detector 16. This makes flatfielding impossible for that detector and is especially problematic in the top

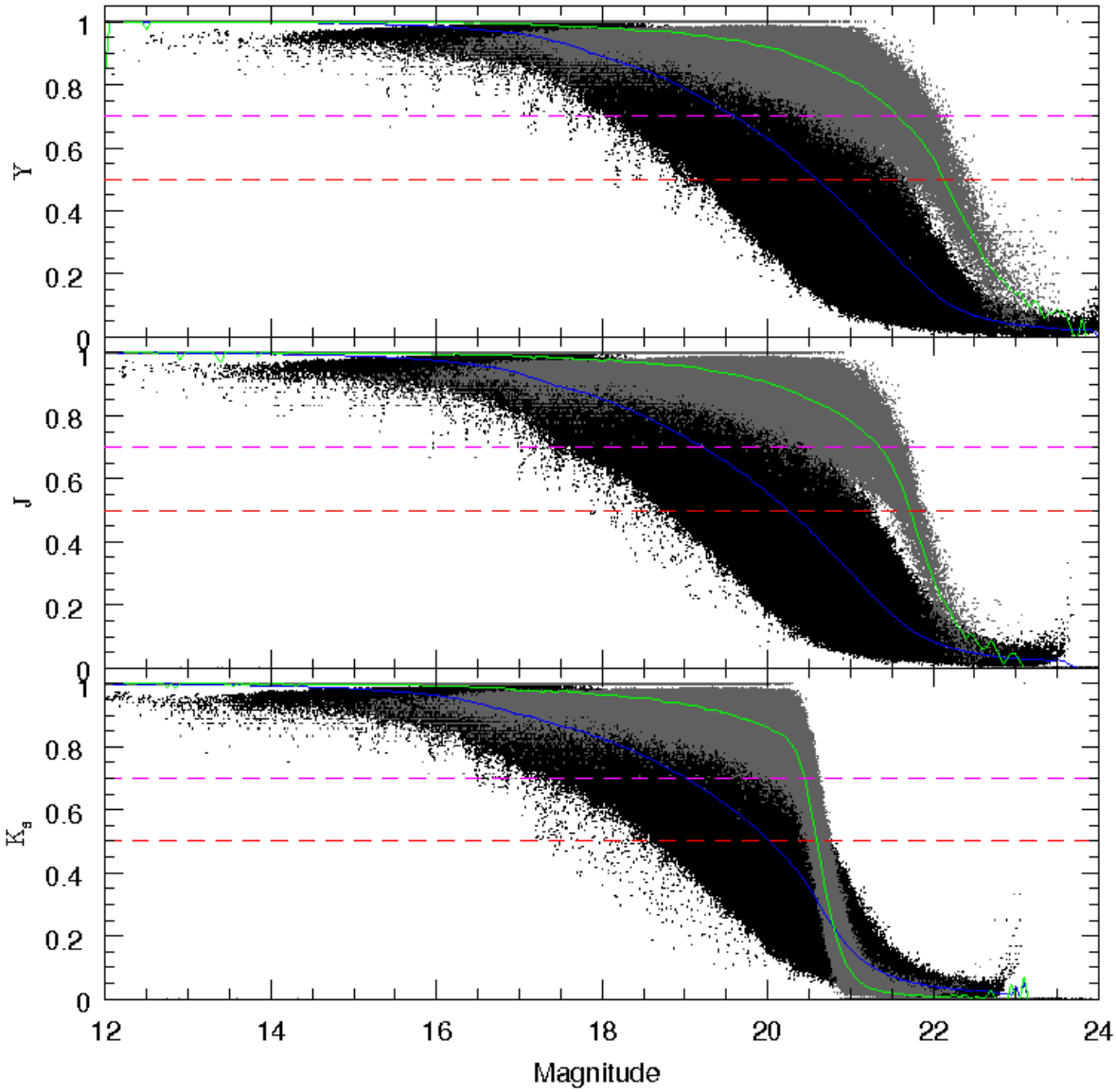

Figure 2.8: Completeness results from the artificial star tests on the PSF photometry for the 6_6 LMC tile (black dots) and 8_8 LMC tile (grey dots). Averages (using bin size 0.05 mag) are shown in solid blue and green lines for LMC tiles 6_6 and 8_8, respectively. Horizontal dashed lines indicate 70% and 50% completeness.

half. The resulting effect is quite small in the K_s band but is very noticeable in the Y and J bands. As a result, one should be vigilant for any strange patterns present in part of the South–West of a tile in the LMC and South–East in the SMC.

2.4.1.2 Tiling issues

In the SMC there persists a narrow gap ($< 0.^{\circ}5$ in RA) between tiles 5_3 and 5_4 and in the LMC there is a slightly wider gap ($\sim 0.^{\circ}6$ in RA) between tiles 4_4 and 4_5 (these are unlike the rest of the survey, where connecting tiles overlap). The cause of this is due to limitations in the acceptable positioning of tile centres by the ESO provided system employed for the survey. Even with manual adjustment it would not help because the tiling software makes automatic adjustments to these for positioning of standard stars. Figure 2.9 shows a screenshot of the SMC tiling within this software. Proposals for additional observations to resolve this have been submitted.

2.4.2 Data reduction glitches

The VSA website `http://horus.roe.ac.uk/vsa/knownIssues.html` provides a list of known issues regarding data reduction. Below, I describe a few of these issues which I discovered while analysing the data and how these were resolved.

2.4.2.1 Confidence bug

An error in the source flagging was found for the aperture photometry. I uncovered this while I was doing my LMC 6_6 tile analysis covered in Chapter 4 and this was resolved by using PSF photometry instead of aperture photometry. The PSF photometry was also a preferred option due to the better performance in crowded regions, which is demonstrated in Figure 2.10. Figure 2.10 shows density maps of aperture and PSF photometry in the LMC 6_6 tile. Table 2.1 lists some of the known features

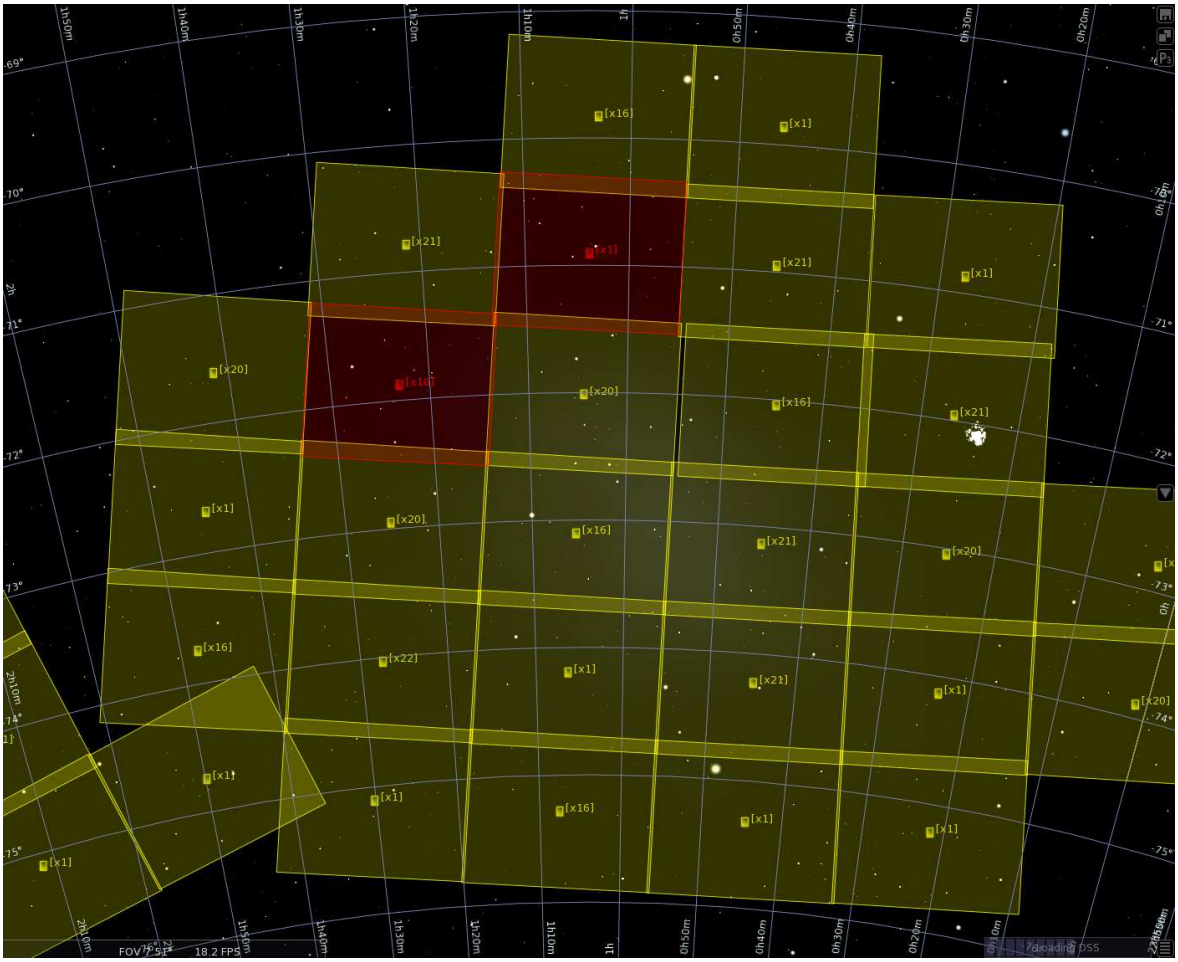

Figure 2.9: A screen grab of the SMC tiling from the ESO tiling software used. Notice the gap in coverage of the two tiles seen in the third row; tiles 5_3 and 5_4.

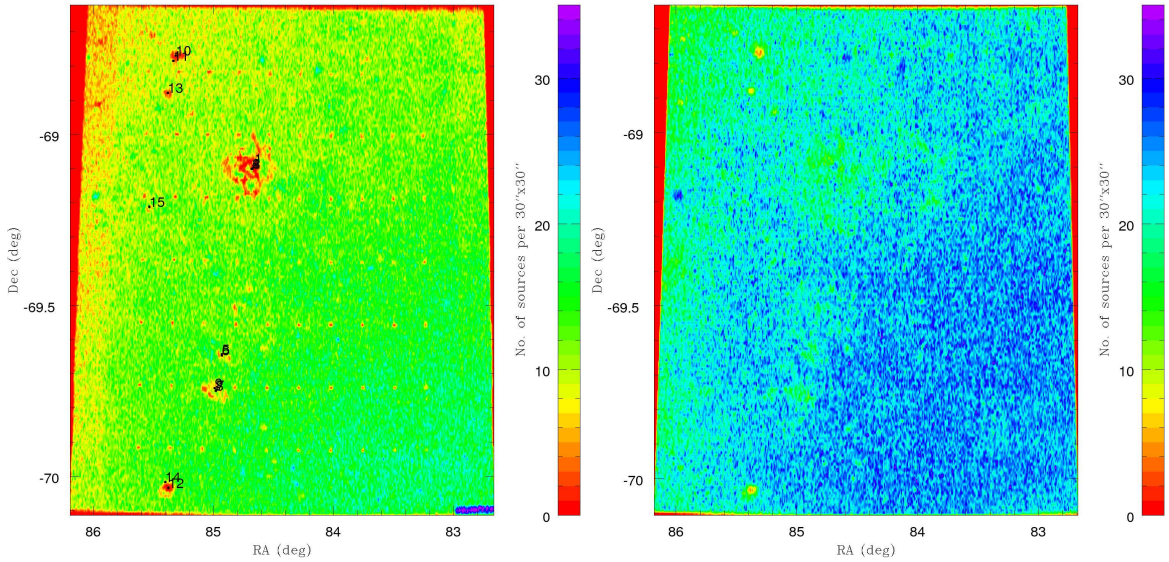

Figure 2.10: Density map containing all K_s band stars for tile 6_6 using aperture photometry (left), PSF photometry (right) from the VMC v20120126 release. The low density gaps are described in Table 2.1 and the majority are no longer present in the PSF photometry. Those which remain cover smaller regions than before. The 10×7 pattern of small gaps in the aperture photometry is due to a now corrected VSA bug.

associated with these incomplete regions, with star clusters and H II regions being the most prevalent.

However, Figure 2.10 does not just have natural features resulting in gaps but artificial ones too. These present themselves in the form of an evenly spaced, 10×7 pattern of small gaps. These were caused by a VSA software bug where the confidence values in these regions (due to overlap from multiple detectors or paw prints) caused an integer overflow resulting in them being misreported as having low confidence. After being reported, this bug was fixed in future releases including the more recent data releases used in this thesis.

Table 2.1: Objects associated with regions containing apparent gaps in Figure 2.10.

Object	no.	RA $^\circ$	Dec $^\circ$	Object type
Tarantula Nebula	1	84.658	−69.085	H II (ionised) region
NGC 2070	2	84.675	−69.100	Cluster of stars
R136	3	84.675	−69.101	Cluster of stars
BAT99 111	4	84.679	−69.101	Wolf–Rayet star
N 160A-IR	5	84.929	−69.643	Young stellar object
NGC 2080	6	84.929	−69.647	Cluster of stars
LH 105	7	84.975	−69.748	Association of stars
NGC 2079	8	84.979	−69.750	Cluster of stars
LHA 120-N 159	9	84.988	−69.743	H II (ionised) region
HD 38617	10	85.312	−68.770	K3III star
H88 310	11	85.333	−68.785	Cluster of Stars
HD 38706	12	85.374	−70.034	M4III star
HD 38654	13	85.379	−68.879	M0/M1 star
LHA 120-N 177	14	85.400	−70.017	H II (ionised) region
NGC 2100	15	85.533	−69.212	Cluster of stars

All data from SIMBAD (`http://simbad.u-strasbg.fr/simbad/`). Objects given in J2000 coordinates.

2.4.2.2 Poor seeing

VSA release v20130805 revealed problems within the J band. These took the form of a grid pattern seen in Figure 2.11 (this pattern is most easily seen when looking at $Y - J$ colours; it is not seen in $Y - K_{\rm s}$). This was only seen in some tiles suggesting an observation problem. Upon investigation, poor seeing in some pawprints was to blame. This previously did not occur due to part of the reduction pipeline being changed involving the CASU code used in the mosaicking stage (the deep pawprints were consistent across releases) but it is unclear why the old code did not reveal the problem. Upon further investigation it was found that a substantial fraction of the stacks used in the deep tile in problematic regions were from poor and unstable nights. Figure 2.12 shows the average zero points for a selection of tiles. The fields with the most spread are where poor/variable data have been stacked resulting in the problems seen.

Much of the LMC was of low enough reddening that usage of the Y band was suitable so this problem could be avoided in Chapter 5. Chapter 7 covers an unaffected region.

However, in the case of the SMC a couple of tiles harbour the same problem; SMC tiles 6_3 and 4_6, where the Y band is affected in a similar manner with variable zero points seen between exposures (a range of ~ 0.7 mag). Table 2.2 shows Y and J band observation logs for tile 6_3. The PSF photometry for the SMC excluded these poor observations and so are unaffected. These were used instead in Chapter 6. PSF catalogues have not been produced for the whole of the LMC yet.

2.4.2.3 Tile edges when not using all flags

Once the VMC survey continued developing, I noticed unusual behaviour in the overlap regions in the tiles harbouring a very high density. This seemed more prevalent along the right ascension axis.

Through comparing the older VSA data releases and the PSF photometry the

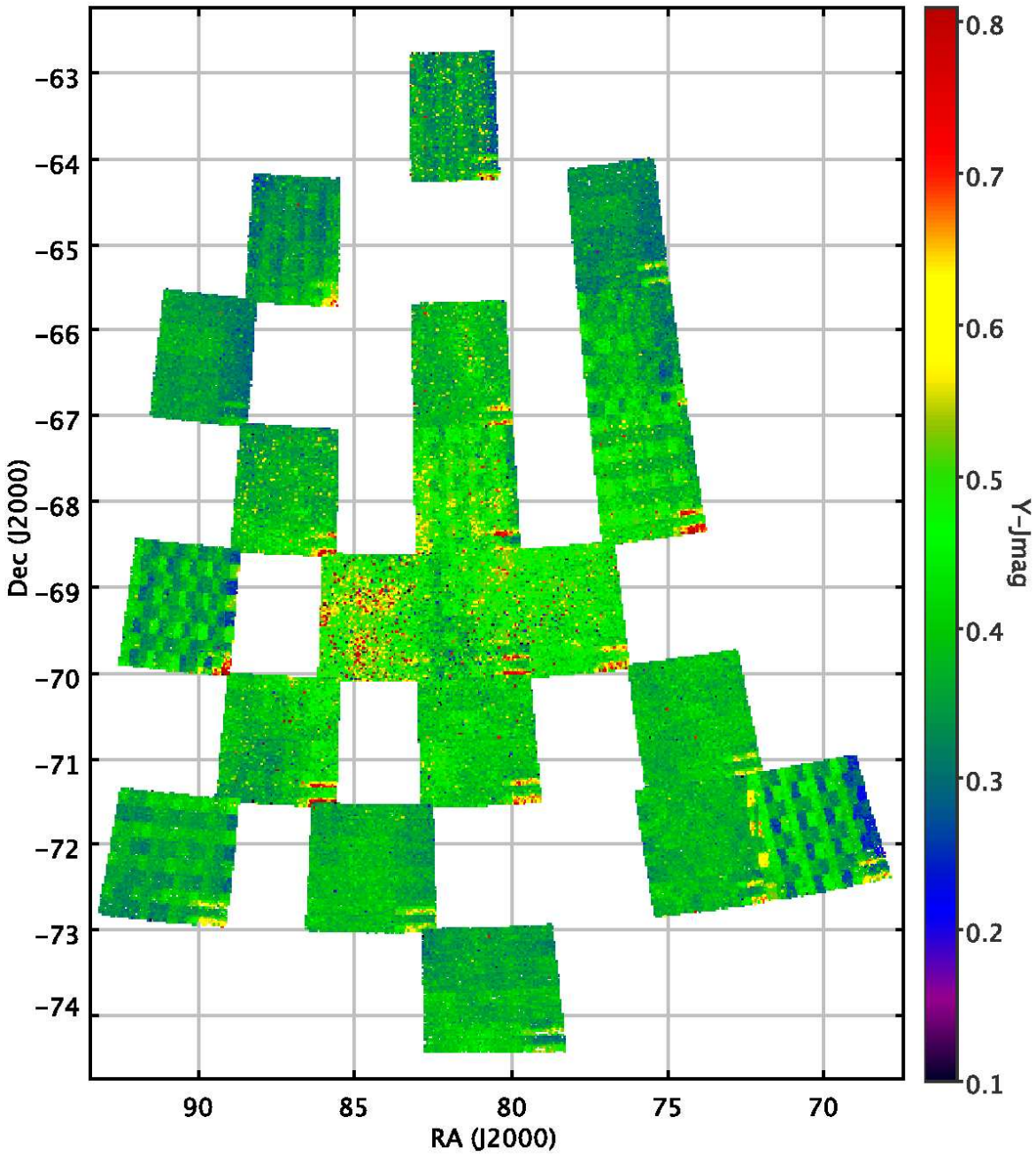

Figure 2.11: $Y - J$ magnitude map for the LMC observations. Notice the 13×8 grid pattern seen in some tiles (especially clear in the South–West tile 4_2) but absent from central tiles covering the LMC bar and 30 Doradus.

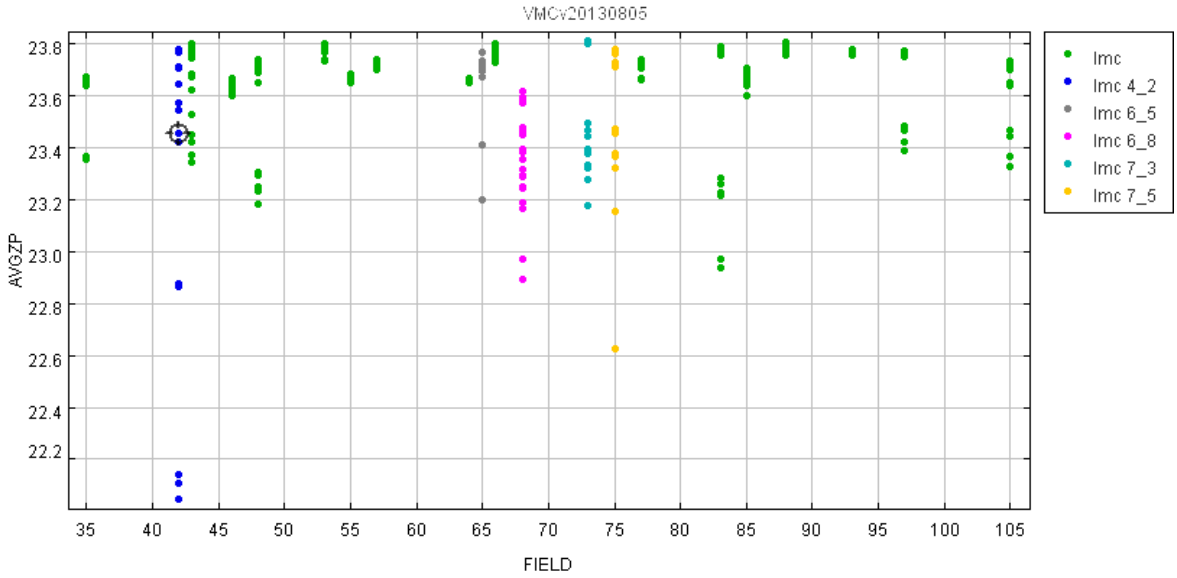

Figure 2.12: J band average zero points for a selection of LMC tiles from VSA release v20130805. The fields with the most spread are where poor/variable data have been stacked resulting in the problems seen.

Table 2.2: Part of VMC observation logs for SMC tile 6_3 showing Y band and J band. Large zero point variation can be seen in Y (a range of ~ 0.7 mag) but not in J (range of 0.12 mag).

Date	Tile	Type	Seeing	Ellipt	ZP	Maglim
30/07/11	6_3	Y1	1.22	0.04	22.86	21.01
30/07/11	6_3	Y2	1.18	0.05	23.28	21.42
20/08/11	6_3	CY2	1.28	0.06	23.34	21.03
17/09/11	6_3	CY1	0.90	0.13	23.48	20.80*
20/09/11	6_3	CY1	1.00	0.06	23.55	21.40
04/09/11	6_3	J1	0.98	0.10	23.68	21.09
04/09/11	6_3	J2	0.96	0.09	23.68	21.18
06/09/11	6_3	CJ2	0.96	0.07	23.73	20.81
20/09/11	6_3	CJ1	0.94	0.06	23.80	21.02

* 1 paw-print, 3 images (i.e. incomplete).

high density was caused by double counting of sources within these regions. A contour map example is shown in Figure 2.13.

The solution was thankfully trivial and involves using the priOrSec[15] flag attribute as detailed in the example in section 4.2.4 of Hambly et al. (2008) and repeated below:

where frameSetID=***** and (priOrSec=0 OR priOrSec=frameSetID)

This selects either sources with no duplicates (priOrSec=0) or – for regions that contain duplicate sources (i.e. the tile edges) – only the primary source (priOrSec=frameSetID). Here, the primary source is the one with the most filters and the fewest quality bit flags and ***** is the framesetID you are using.

The framesetID contains the data for only that tile so these can be used to select individual tiles. The frameSetID of each tile changes with each VSA data release but can easily be determined by searching for stars around the centre of a tile and specifying the frameSetID as the output.

[15]A shortening of Primary or Secondary.

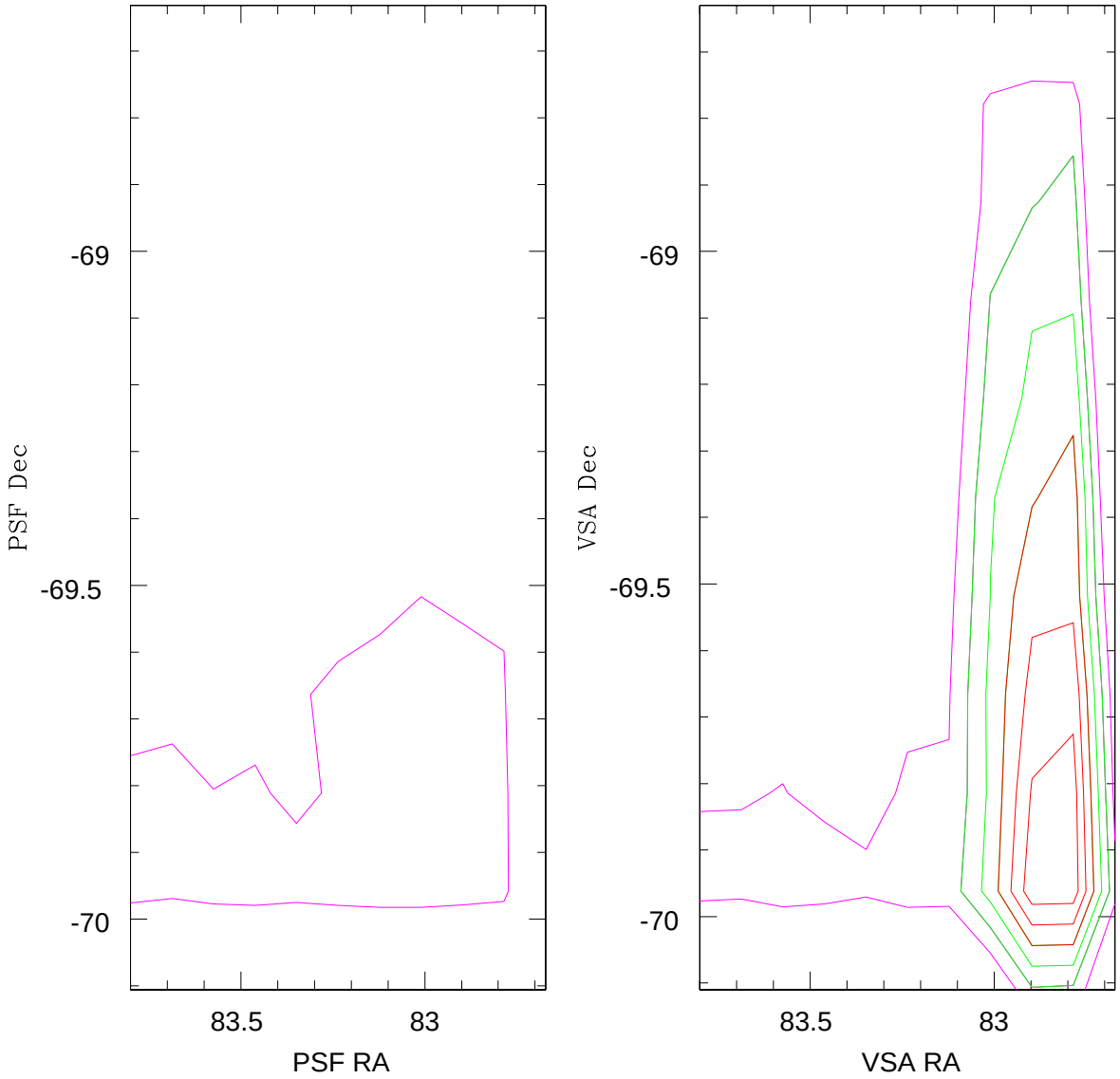

Figure 2.13: Contour map containing overlap region of LMC tiles 6_6 and 6_5 observed with PSF photometry (left) and aperture photometry from VSA (right) when not making use of priOrSec flag. The contour levels represent source counts of 3500 (magenta) 4200, 4900 (green) 5600, 6300 and 7000 (red) in a 10×10 grid.

3 Method

In this chapter I set out the main methodology used in the subsequent chapters. These comprise of: the selection method used to select Red Clump (RC) stars from the CMD, how the extinction is determined for these using an intrinsic colour, how the extinction is used to obtain a reddening-free magnitude estimate and how a plane is fitted to determine structure. These serve to be general methods with specific adjustments covered in later chapters.

3.1 Red Clump star selection

In order to use the RC stars, I first identify and select them from the data. This is conducted by using their position on the colour–magnitude diagram (CMD). When looking at histograms of colour and magnitude in a CMD for the Magellanic Clouds in the NIR, typically two peaks are clearly seen for both colour and magnitude; the more extended bluer dimmer peak corresponds to the lower main sequence in the Galactic foreground and the bright narrower peak corresponds to the RC in magnitude and the RGB and RC in colour.

Since the RC is contained within a compact CMD area, it is possible to study it using a carefully chosen selection box; while many studies in the literature adopt a selection box whose size and position generally remains unchanged regardless of where in the Magellanic Clouds they are used I feel this would be unwise for studying a wide area because there will be magnitude variances due to distance differences and potential colour and magnitude differences due to population effects. In addition larger selection boxes mean greater amount of contaminations from non-RC populations. Another difference in the selection boxes I use is due to being concerned about extinction and so the magnitude ranges covered will vary with respect to colour (as reddened stars have dimmer magnitudes). In other words the selection box I use resembles a parallelogram.

The basis of how my work creates a unique selection box for each tile lies in binning a CMD (K_s vs. $J - K_s$ or $Y - K_s$ for extra sensitivity when extinction is low; as is the case for most of the Magellanic Clouds[1]) and then plotting contours over this, the contours being constructed up to the densest bin. Surrounding the peak of this contour map is the RC. The contour levels help define the magnitude range, with the colour range determined from the histogram of the sources within the magnitude range. Cut-offs are made when the source levels drop to near zero or when other features start to dominate – such as Galactic foreground. This was done for each tile. As follows is a revision of how it was described in Tatton et al. (2013a). As such, examples will be used for the 30 Doradus tile of the VMC survey.

This selection box is suitable because it is calibrated to the star population in the tile and suits the intrinsic properties of the RC, having a fairly fixed magnitude and colour. While the magnitude does change with respect to age and the colour and magnitude changes with respect to metallicity these changes are small enough that the selection box remains fairly small.

3.1.1 Defining the Red Clump

With reference to Figure 3.1, I am zooming in on an area of the LMC 6_6 tile CMD in which high stellar surface density is related to the RC. A contour map for stellar density is built using a bin size resolution of 0.05 mag in K_s magnitude range and 0.01 mag in $(J - K_s)$ colour. The contour lines are drawn with the cell containing the most stars as the peak level. The cyan contours are where the sources range from 5%–30% of this peak with a step of 5%. As the densest region is more compact there are additional green contours drawn whose lines cover 50%–100% densities (where 100% is the densest cell/pixel) with steps of 10%; I also add a red contour showing 1% density. The green contours coincide with the RC and the 30% and 25% cyan contours surround this feature. The 20% contour extends to $K_s = 17.6$ mag. This is $\Delta K_s \simeq 0.4$ mag below

[1]When extinction is not low this does not effectively probe the highest extinction regions.

the 30% contour. This feature is made up of RGB stars and the Secondary Red Clump (SRC) feature. SRC stars are helium burning (with enough mass to ignite helium in non-degenerate conditions), found up to 0.4 mag away from the main clump and are the youngest RC stars with an age of 1 Gyr (Girardi, 1999). The smaller density of the SRC and the fact it may be less uniform across the whole LMC (due to the young age) mean we do not make efforts to include it in our RC star selection.

Several approaches can be taken for defining RC selection. A fixed range in colour and magnitude is one possibility. However, contamination issues (caused by RGB stars) arise due to covering a large magnitude range. From the contour lines I am able to see that for the bluer colours ($(J - K_{\rm s}) < 0.5$ mag) the density levels are essentially constant with respect to colour but for redder colours ($(J-K_{\rm s}) > 0.6$ mag) the contours stretch in colour and magnitude. This gradient is caused by the attenuating effects of dust and is described by the reddening vector. This effect is clear in high extinction regions but not seen in lower extinction regions. The magnitude range for the selection of RC stars depends on colour, tracing the reddening vector; in this way I can keep it narrow enough such as to minimise contamination by non-RC sources. To determine the $K_{\rm s}$ cuts I first determine the reddening vector as the gradient between the RC peak and the reddest point on the 5% contour level (the 1% contour level is too noisy and the 10% contour level does not account for the reddened RC stars as well as the 5% contour level does). The line between these two points is shown in magenta in Figure 3.1 and the gradient is 0.754. The magnitude range is determined from the highest and lowest $K_{\rm s}$ magnitudes of the 30% contour. This region covers $\Delta\, K_{\rm s} = 0.54$ mag for any given colour. The reason for choosing the 30% contour is using lower % contours makes the magnitude range too broad, increasing RGB star contamination while using higher % contours makes the range too narrow, losing distance modulus variance. In some tiles the magnitude range becomes broad in the 30% contour at the dimmer end (caused by a prominent secondary RC). In this case the magnitude of the dimmest end of the 50% contour and brightest end of the 30% contour is used as the range instead.

An alternative method to determine the gradient of the reddening vector is to use the VISTA filter application of the Girardi et al. (2008) extinction coefficients from

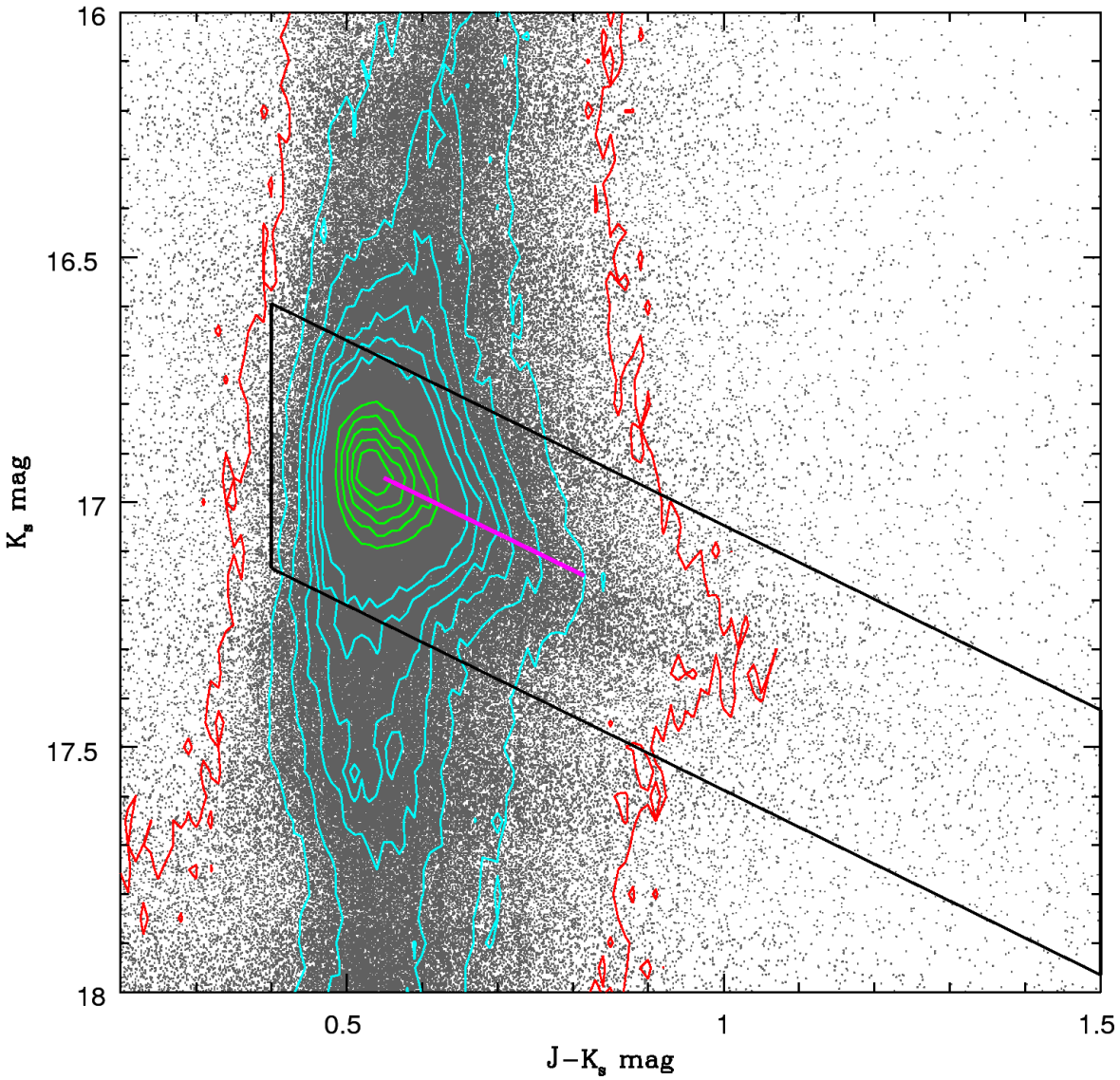

Figure 3.1: $K_{\rm s}$ vs. $(J - K_{\rm s})$ CMD for LMC 6_6 tile with stellar density contour lines added (red: 1% of peak, cyan: 5%–30% of peak with step of 5%, green: 50%–100% of peak with step of 10%). Estimated reddening vector is in magenta and RC selection box used in the LMC 6_6 tile is marked in black.

VMC Paper IV (Rubele et al., 2013)[2]. For a typical RC star in the LMC ($T_{\rm eff}$ = 4250 K, $\log g = 2$) the gradient is 0.741, agreeing well with the previous measurement meaning that either value can be used in lower extinction tiles where there is a less clear reddening effect observed.

In the case of LMC tile 6_6 the colour range excludes stars bluer than $(J - K_{\rm s}) = 0.4$ mag and redder than $(J - K_{\rm s}) = 1.5$ mag to minimise contamination from young main sequence stars and background galaxies, respectively. From Figure 3.1, the contribution of stars redder than $(J - K_{\rm s}) > 1.0$ mag is minor but is required to probe the reddest populations. However, when the colour range extends too far into the red, the reddest populations will manifest themselves on a reddening map as uniform noise because at this point it is dominated by background galaxies.

The final selection box for LMC tile 6_6 plotted in black in Figure 3.1 is the area of the CMD where the following equations are satisfied:

$$0.4 \leq (J - K_{\rm s}) \leq 1.5\,{\rm mag} \tag{3.1}$$

$$K_{\rm s} \geq 0.754 \times (J - K_{\rm s}) + 16.293\,{\rm mag} \tag{3.2}$$

$$K_{\rm s} \leq 0.754 \times (J - K_{\rm s}) + 16.833\,{\rm mag} \tag{3.3}$$

This definition is a compromise between including all (100% of) RC stars at the cost of contamination (mostly from RGB stars but also background galaxies) and smaller, contamination free selections (at the cost of not including all RC stars, especially at higher extinction which are of interest in my work due to revealing structure).

3.2 Interstellar extinction

3.2.1 Reddening map

The reddening map I am going to present in Chapter 4 shows the reddening in a colour excess form, $E(J - K_{\rm s})$, which is obtained using:

$$E(J - K_{\rm s}) = (J - K_{\rm s})_{\rm obs} - (J - K_{\rm s})_0, \tag{3.4}$$

[2]This is described in further detail in Section 3.2.2.

where $(J - K_s)_{obs}$ is the observed colour of a RC star and $(J - K_s)_0$ is the colour of a non-reddened RC star known as the intrinsic colour. For Chapters 5 & 6 the J band is replaced with the Y band.

3.2.1.1 Finding intrinsic colour

To determine the intrinsic colour, I make use of version 2.3 of the Padova isochrones[3], using the evolutionary tracks of Marigo et al. (2008) and Girardi et al. (2010), converted to the VISTA Vegamag system as described in Rubele et al. (2012). The RC star phase is a well understood part of stellar evolution with good correspondence between observation and predictions.

As intrinsic colour varies with metallicity and age, I constrain the possible age and metallicity ranges using the SFH produced in Rubele et al. (2012) for the LMC (for tiles 4_3, 6_6, 8_3 and 8_8) and Rubele et al. (2015) for the SMC (for tiles 3_3, 3_5, 4_3, 4_4, 4_5, 5_3, 5_4, 5_6, 6_3 and 6_5). These SFHs are fairly consistent for ages older than 1 Gyr. I used their data for the best fitting age–metallicity relation (AMR) as input for the Padova isochrones. Updated VMC SFH results for the SMC have been published (Rubele et al., 2018), and I will use those to check to what extent my structure maps may be affected by remaining variances in age and metallicity.

The metallicity is converted onto the Z scale using the relation; $\log Z = [\mathrm{Fe/H}] - 1.7$. Figure 5 of Caputo et al. (2001) shows this relation for LMC, SMC and Galactic Cepheids. Two sets of isochrones are produced; the first, younger set covers $\log(t/\mathrm{yr}) = 9.1$–$9.4$ with $Z = 0.0125$ and the second, older set covers $\log(t/\mathrm{yr}) = 9.4$–$9.7$ with $Z = 0.0033$ ($\log(t/\mathrm{yr}) = 9.4$ appears in both due to the SFH histogram bins overlapping). The age steps are $\Delta\log(t/\mathrm{yr}) = 0.1$ for both. Foreground Galactic extinction was not accounted for as we want to find total reddening (when using the Schlegel et al. (1998) value; $A_V = 0.249$ mag, the $(J - K_s)$ colour is reddened by 0.04 mag).

As the isochrone tables are in absolute magnitude we apply an LMC distance

[3] http://stev.oapd.inaf.it/cgi-bin/cmd_2.3

modulus of 18.46 ± 0.03 mag (Ripepi et al., 2012)[4] to the K_s magnitude. For the SMC a distance modulus of 18.96 mag (de Grijs & Bono, 2015) is used instead.

Figure 3.2 shows the CMD region of the RC stars (from LMC tile 6_6) and the isochrones for only the helium burning phase (after the RGB phase). Shown are the contours and RC selection box like in Figure 3.1, distance error for isochrones is shown in the top left corner, and the isochrones are plotted in blue and red for the younger and older sets, respectively. The earlier, more age dependent phases (younger than ~ 2 Gyr; $\log(t/\mathrm{yr}) < 9.4$) do not make sense for a majority of the data as it would suggest unusually low or negative reddening. Also, the $\log(t/\mathrm{yr}) = 9.1$ track lies outside our RC selection. The older tracks are contained within a narrower range of ~ 0.025 mag in colour and all but the end stages of helium burning are within the RC selection. The average along the older tracks, $(J - K_s)_0 = 0.495$ mag, is adopted as the intrinsic colour.

3.2.1.2 Estimating intrinsic colour without SFH

Sadly the SFH is not available for every observed tile. Due to this it is important to have an alternative approach to estimate intrinsic colour.

Studies in the literature also make assumptions about intrinsic colour, normally adopting to use a fixed value for the entire system they are observing. For example Haschke et al. (2011) mentions values given in Girardi & Salaris (2001). When one considers there does not appear to be a metallicity gradient observed within the LMC this approach, while not ideal, is still suitable to adopt. The tile by tile basis does have the advantage of allowing for exceptions to be made if required.

For the LMC I use an intrinsic colour of $(Y - K_s)_0 = 0.84$ mag while for the lower metallicity SMC an intrinsic colour of $(Y - K_s)_0 = 0.7625$ mag is used. These are derived from the averages of the isochrones from the star formation histories (where available) and were assessed by overplotting these isochrones onto CMDs.

[4]This is consistent with 18.48 ± 0.05 mag (Walker, 2012).

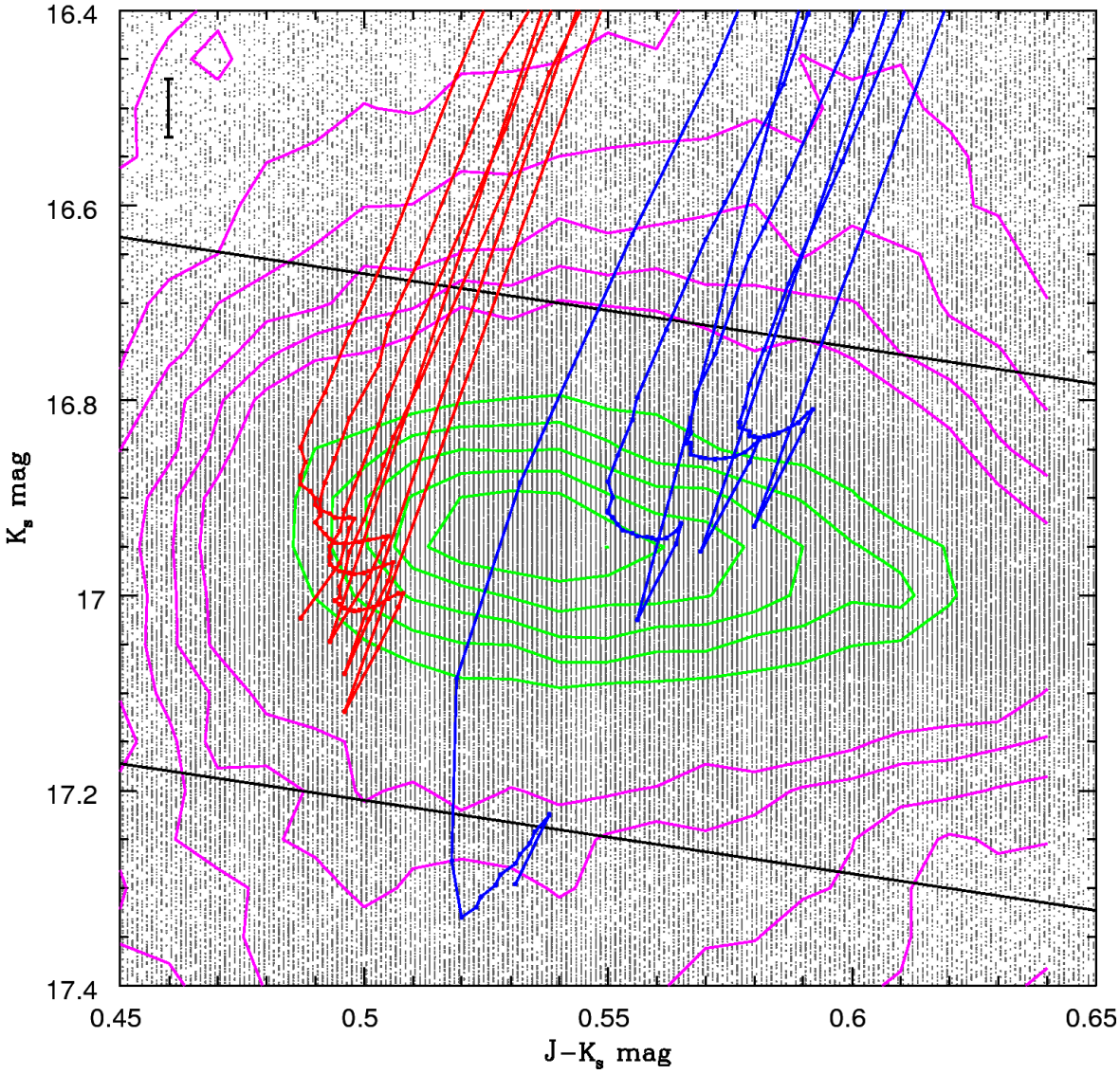

Figure 3.2: K_s vs. $(J - K_\mathrm{s})$ CMD of LMC tile 6_6 with isochrone lines for the helium burning sequence for two metallicities and the appropriate age ranges: younger, more metal rich ($\log(t/\mathrm{yr}) = 9.0$–$9.4$, $Z = 0.0125$) are in blue and the older, more metal poor ($\log(t/\mathrm{yr}) = 9.4$–$9.7$, $Z = 0.0033$) are in red. The black error bar in the top left represents error in LMC distance. Magenta and green contours are described in Figure 3.1. The RC peaks are consistent with the red isochrones when accounting for foreground Galactic extinction (estimated to be $J - K_\mathrm{s} = 0.04$ mag from Schlegel et al. 1998). As photometry is less accurate than the millimag level the values are only recorded to 0.001 mag precision. This can be seen visually when zoomed in on CMDs as is the case here.

Table 3.1: Extinction ratio A_λ/A_V for the Cardelli et al. (1989) extinction law for VISTA passbands for a typical RC star.

VISTA filters	Z	Y	J	H	K_s
λ_eff (μm)	0.8763	1.0240	1.2544	1.6373	2.1343
w_eff (μm)	0.0780	0.0785	0.1450	0.2325	0.2600
A_λ/A_V	0.5089	0.3912	0.2825	0.1840	0.1201

Referring back to Figure 3.2 one can see variations of up to $\Delta K_\mathrm{s} = 0.2$ mag and $\Delta(J - K_\mathrm{s}) = 0.1$ mag depending on age and metallicity. In other words RC stars vary on a ± 0.1 mag scale but the bulk of population will not vary too much over the Magellanic Clouds because both galaxies are characterised by continuous star formation and chemical evolution.

3.2.2 Reddening law & conversion to A_V

The attenuation of interstellar dust is often expressed in terms of A_V, the magnitude dimming at visual wavelength. The extinction curve relates this to A_λ, the magnitude dimming at wavelength λ. The relation between A_V and reddening $E(Y - K_\mathrm{s})$ is:

$$A_V = \frac{E(Y - K_\mathrm{s})}{A_Y/A_V - A_{K_\mathrm{s}}/A_V} \tag{3.5}$$

For consistency with the VMC survey and the Padova isochrones, I use the same extinction coefficients from Girardi et al. (2008) with the VISTA filter update from Rubele et al. (2012). The extinction coefficients are based on the stellar spectra from Castelli & Kurucz (2004), in addition to the Cardelli et al. (1989) extinction curve. The VISTA filter transmission curves are fully accounted for giving it an advantage over Cardelli's curve alone (see Appendix A.1.2). Table 3.1 gives the values relative to A_V for a typical RC star ($T_\mathrm{eff} = 4250\,\mathrm{K}$, $\log g = 2$). I find $E(J - K_\mathrm{s}) = 0.16237 \times A_V$ and $E(Y - K_\mathrm{s}) = 0.2711 \times A_V$.

3.2.3 Dereddening

With an extinction value for every RC star it is possible to obtain values for $K_{\rm s}$ magnitudes free from extinction. This is used for distance determination purposes in Chapters 5 & 6. This dereddening method is only applied to the $K_{\rm s}$ magnitudes and involves using the calculated reddening vector and extinction value.

The de-reddened magnitude can be expressed as:

$$(K_{\rm s})_0 = K_{\rm s} - G \times E(Y - K_{\rm s}), \tag{3.6}$$

where $(K_{\rm s})_0$ is the resulting dereddened magnitude and G is the ratio of total to selective extinction:

$$G = \frac{A_{K_{\rm s}}/A_V}{A_Y/A_V - A_{K_{\rm s}}/A_V} \tag{3.7}$$

In other words G is the reddening vector. This procedure is not carried out when $E(Y - K_{\rm s})$ is less than zero.

3.3 Distance modulus map

Dereddened magnitudes are essential to obtaining accurate distance measurements which in turn can be used to map out structure. Due to the limits of precision on the photometry, there is a limit to what levels of structure can be probed. This is also affected by distance. As a reminder the distance modulus equation is as follows:

$$(m - M) = 2.5 \log \frac{d^2(\rm kpc)}{(0.01)^2} = 5 \log\, d(\rm kpc) + 10 \tag{3.8}$$

Where m is apparent magnitude and M is the absolute magnitude. So using this and considering a distance difference of 5 kpc, at 50 kpc this gives us:

$$\Delta(m - M) = 0.207\,\rm mag \tag{3.9}$$

Meanwhile at 1 Mpc (edge of the Local Group) this same distance difference gives us:

$$\Delta(m - M) = 0.011\,\rm mag \tag{3.10}$$

For the VMC data, photometric errors in the K_s band are typically 0.01 mag; In other words, there are distance errors (on individual stars) on the order of 0.2 kpc at the distance of the Magellanic Clouds.

An additional effect posed by distances is the perspective on the sky, which causes two points behind the mid-plane to be further apart than two points on those same two lines-of-sight in front of the mid-plane.

3.4 Plane fitting

In order to find out the inclination and position angle (the orientation) of the LMC or SMC we must fit a plane to the disk. This involves converting RA, Dec and distance into a Cartesian co-ordinate system.

The motivation for finding out the inclination and position angle is that these factors are important in dictating the 3D structure. It is also of interest to see how these findings compare with measurements from the literature as deviations may be due to the tracer used, revealing possible sub-structure and changes due to the dynamical history of the system.

In order to fit a plane to the data, representing a disc-like configuration, we must remove the projection issues arising from the spherical co-ordinates that our current projection provides. This is done by transforming the current co-ordinate system of RA, Dec and measure of distance into a Cartesian co-ordinate system where the x-axis is anti-parallel to RA, the y-axis parallel to Declination and the z-axis is towards the observer. The transformation in the literature[5] typically takes the form of:

$$x = -D \sin(\alpha - \alpha_0) \cos\delta \tag{3.11}$$

$$y = D \sin\delta \cos\delta_0 - D \sin\delta_0 \cos(\alpha - \alpha_0) \cos\delta \tag{3.12}$$

$$z = D_0 - D \sin\delta \, sin\delta_0 - D \cos(\alpha - \alpha_0) \cos\delta \tag{3.13}$$

[5]e.g. Subramanian & Subramaniam (2010, 2013); van der Marel & Cioni (2001).

where (α_0, δ_0) and (α, δ) are the RA and Dec of the centre of the system and the sub-region, respectively. The (D_0, D) components are the distance to the centre of the system and sub-region, respectively. While sub-regions can take the form of individual sources this approach is rarely taken for plane fitting, with censuses in sub-regions for a certain density being used instead. Before I use this grid to obtain structural parameters, I will first show how these transformations occur.

3.4.1 Cartesian co-ordinate system

The equation outlined in Section 3.4 is derived following van der Marel & Cioni (2001) and Weinberg & Nikolaev (2001). The former (van der Marel & Cioni, 2001), concerns itself with converting the equatorial co-ordinates to angular coordinates and then converting these into a three axis Cartesian co-ordinates system (x,y,z) which has an origin at the centre of the system (i.e. centre of LMC or SMC), an x-axis anti-parallel to RA, a y-axis parallel to declination and a z-axis increasing towards the observer with the following transformations:

$$x = -D \sin\rho \cos\phi \tag{3.14}$$

$$y = D \sin\rho \cos\phi \tag{3.15}$$

$$z = D_0 - D \cos\rho \tag{3.16}$$

By substitution of the following three equations derived from the cosine, sine and analogue formulae one obtains the equations 3.11–3.13:

$$\cos\rho = \sin\delta \ \sin\delta_0 - \cos(\alpha - \alpha_0) \cos\delta \tag{3.17}$$

$$\sin\rho \cos\phi = \sin\delta \cos\delta_0 - D sin\delta_0 \ \cos(\alpha - \alpha_0) \cos\delta \tag{3.18}$$

$$\sin\rho \sin\phi = \delta \cos\delta_0 - sin\delta_0 \ \cos(\alpha - \alpha_0) \cos\delta \tag{3.19}$$

The argument behind the spherical to Cartesian co-ordinate translation is similar to the Equatorial to Galactic co-ordinate conversion which is why it may seem familiar. This is covered in Binney & Merrifield (1998, pg. $30-31$) & Green (1985, pg. $40-42$).

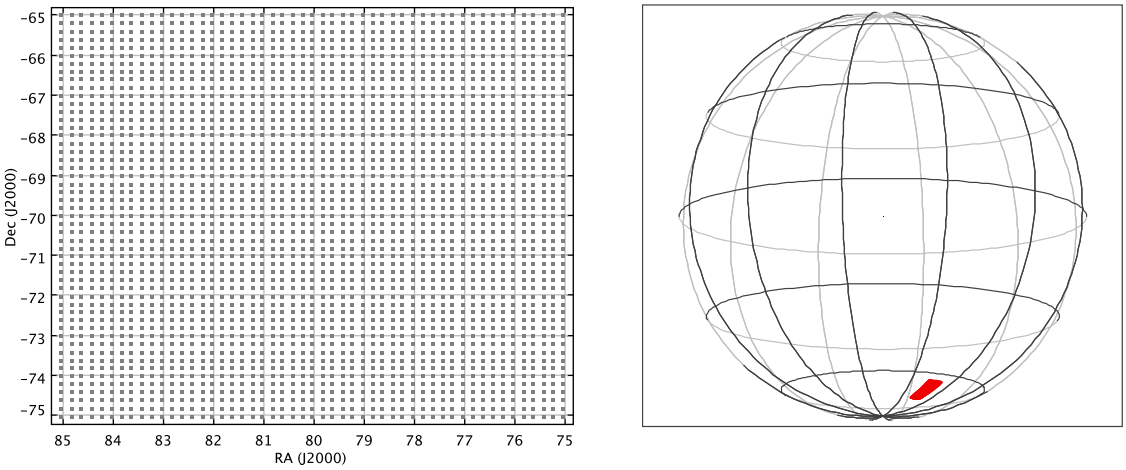

Figure 3.3: Equidistant test grid from two perspectives: head on Dec vs. RA (left) and a three dimensional spherical plot (right).

3.4.2 Examples of transformations

The first example takes the form of an equidistant test grid of RA= 75° to 85°, Dec= −65° to −75° with a bin size of 0.2° in both RA and Dec[6]. In the following figures I illustrate this in two ways, from directly looking at it head on (in Dec vs. RA) and a three dimensional view (Figure 3.3).

When the centre (RA= 80°, Dec= −70°) is set as a zero point the transformations are illustrated in Figure 3.4. Firstly, again by directly looking at it (in a y vs. x perspective) and secondly, a three dimensional view. From the shading we can see that the centre is the closest point to the observer and the outer edges are the furthest.

[6]Due to the grid being equidistant the value used will not change the appearance of the transformation, only how it scales.

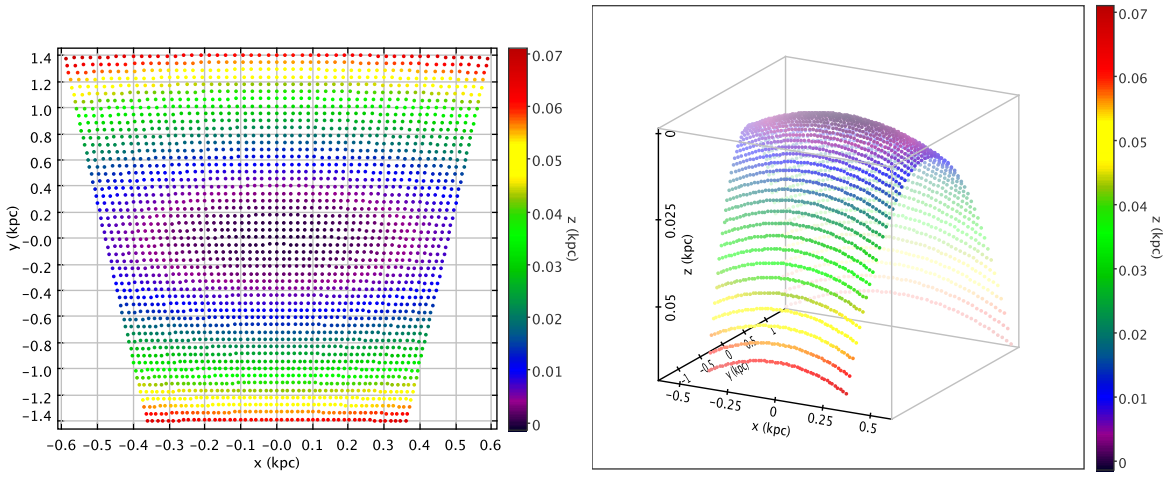

Figure 3.4: Equidistant test grid transformed into Cartesian co-ordinates shown from two perspectives: head on y vs. x (left) and a three dimensional plot (right). Values of z coloured in both.

3.4.3 Centre of the LMC

The central point of the plane is the centre of the system. For the LMC there is a small variation between the gaseous (H I) centre and the optical centre of the LMC. This is significant enough to warrant investigating both of these centres. Their coordinates are:

H I: RA= 79.°4 Dec= −69.°03; Optical: RA= 79.°9 Dec=−69.°45.

3.4.4 Fitting & solving a plane equation

In fitting the planes I have used two IDL routines; planefit.pro written by H.T. Freudenreich and an MPfit based routine. Both of these produce consistent results. But it is still useful to have some understanding of the mechanics behind these.

There are several methods to fitting plane equations onto the transformed co-ordinates. Standard plane equations normally take the form of:

$$z = Ax + By + C \tag{3.20}$$

$$0 = Ax + By + Cz - D \tag{3.21}$$

These are both forms of each other (assuming a normalised plane the latter has the constraint of $A^2 + B^2 + C^2 = 1$, e.g. Subramanian & Subramaniam (2010)) and we use the former.

The coefficients (A, B, C) can be obtained from the x, y, z values by applying a least-squares fit. From:

$$Mn = g, \tag{3.22}$$

where n is a vector $[\,A,\, B,\, C\,]$, g is a vector $[\Sigma\, xy,\, \Sigma\, yz,\, \Sigma\, z\,]$ and M is a 3×3 matrix:

$$\begin{bmatrix} \Sigma\, xx & \Sigma\, xy & \Sigma\, x \\ \Sigma\, xy & \Sigma\, yy & \Sigma\, y \\ \Sigma\, x & \Sigma\, y & \Sigma\, N \end{bmatrix} \tag{3.23}$$

Sometimes the x, y, and z values are expressed in a form of $(x_i - x_0)$, where x_0, y_0 and z_0 denote the centre of the plane (i.e. the mean value of x, y, and z).

With these coefficients the parameters are then obtained by inverting the matrix. I will now explain some of the proof for the least-squares fit in more detail.

3.4.4.1 Least-squares fit

The method of least-squares is used in many data fitting scenarios. The principle is to find a model (a best fit) which minimises the sum of the squared residual values (the difference between the observations and the model).

For a set of N points (with coordinates x_i, y_i, z_i), the aim of least-squares is to minimise the following function,

$$Q = \Sigma\, R_i^2, \tag{3.24}$$

Where R_i is the distance of a point i from the plane: $R_i = Ax_i + By_i + Cz_i - D$.

By partially differentiating Q one arrives at the following equations:

$$\partial Q/\partial A = \Sigma(2x_i(Ax_i + By_i + Cz_i - D)) = 0 \tag{3.25}$$

$$\partial Q/\partial B = \Sigma(2y_i(Ax_i + By_i + Cz_i - D)) = 0 \tag{3.26}$$

$$\partial Q/\partial C = \Sigma(2z_i(Ax_i + By_i + Cz_i - D)) = 0 \tag{3.27}$$

$$\partial Q/\partial D = \Sigma(-2(Ax_i + By_i + Cz_i - D)) = 0 \tag{3.28}$$

A thing to note is that $\Sigma\, D = ND$. As $D = Ax_i + By_i + Cz_i$ this can be arranged as $\Sigma\, D = (Ax_i + By_i + Cz_i)/N$. This can be written as $D = (Ax_0 + By_0 + Cz_0)$ where $x_0 = \Sigma\, x_i/N$, $y_0 = \Sigma\, y_i/N$ and $z_0 = \Sigma\, z_i/N$. Substituting this into the above equations and simplification leads to $Mn = 0$, where n is a vector $[\, A,\, B,\, C\,]$ and M is a matrix described earlier:

$$\begin{bmatrix} \Sigma\,(x_i - x_0)^2 & \Sigma\,(x_i - x_0)(y_i - y_0) & \Sigma\,(x_i - x_0)(z_i - z_0) \\ \Sigma\,(x_i - x_0)(y_i - y_0) & \Sigma\,(y_i - y_0)^2 & \Sigma\,(y_i - y_0)(z_i - z_0) \\ \Sigma\,(x_i - x_0)(z_i - z_0) & \Sigma\,(y_i - y_0)(z_i - z_0) & \Sigma\,(z_i - z_0)^2 \end{bmatrix} \tag{3.29}$$

The above derivation can be found in the maths notes Suhail A. Islam published online[7]. Further reading on plane fitting can be found in Blow (1960) and Schomaker et al. (1959).

3.4.5 Obtaining position angle and inclination

The final step is to obtain the position angle (PA) and inclination (i) of the fitted plane. These are obtained by using the A, B and C coefficients as follows:

$$i = \arccos(C/\sqrt{(A^2 + B^2 + 1)}) \tag{3.30}$$

$$\mathrm{PA} = \arctan(-A/B) + sign(B)\pi/2 \tag{3.31}$$

In the latter equation *sign* refers to the positive or negative sign of the B coefficient. In the case of a normalised plane (the planes I look at are not) the inclination can be expressed as $i = \arccos(C)$.

An additional step that could be taken using the plane solution is transforming the Cartesian co-ordinates into the plane of the galaxy, also explained in van der Marel & Cioni (2001). The purpose of that is to give a measure of actual depth as opposed to line of sight depth. I have chosen not to do this because the SMC does not have a clear plane of symmetry. Instead I will look at the residuals.

[7] `http://www.sbg.bio.ic.ac.uk/~islam/plane.html`.

3.4.6 Residuals

The residual value is simply the observed z value subtracted by the z value given by the fitted plane. This in turn reveals if a source lies in front of, or behind the plane. Likewise, the dispersion (assuming a Gaussian distribution) or spread in residual value quantifies the depth along the line of sight. Photometric errors also contribute. If the true dispersion is σ and the photometric errors are σ_e then the observed dispersion is $\sigma' = \sqrt{\sigma^2 + \sigma_e^2}$. This true dispersion is a result of a spread in distance modulus but can also include spread in population (i.e effects due to any variances in age and metallicity).

4 Dust around the 30 Doradus star forming complex

In this chapter I use Red Clump (RC) stars selected from the near-infrared (NIR) photometry of the VMC survey to construct interstellar reddening maps for the central LMC 6_6 tile[1]. This region of the LMC is interesting because it contains the famous Tarantula Nebula (30 Doradus) mini starburst – the most active star formation region in the Local Group – centred around the compact massive cluster RMC 136a (hereafter R136 – see Evans et al. 2011). The tile further contains several supernova remnants, the most famous of which is SN1987A, a number of star clusters, H II regions and the Southern molecular ridge (Wong et al., 2011). The South–West part of this tile covers part of the LMC bar, characterised by a high stellar density.

The RC stars are selected from the CMD, their extinction is determined using an intrinsic colour from isochrones and presented is a dust map for the 30 Doradus field in both A_V and $E(J-K_\mathrm{s})$. This map samples a region of $1^\circ \times 1\overset{\circ}{.}5$, containing $\sim 1.5 \times 10^5$ RC stars which probe reddening up to $A_V \simeq 6$ mag. I compare my map with maps from the literature, including optical extinction maps and radio, mid- and far-infrared maps of atomic hydrogen and dust emission. I also estimate column density to locate molecular clouds.

4.1 Photometry

For this work within the 6_6 tile I use PSF photometry for reasons outlined in Section 2.4.2.1. In PSF photometry I can use photometric error and sharpness[2] for quality control. I plot photometric error and sharpness against magnitude for each band in Figure 4.1. Contour lines depict density of stars, relative to the densest region, for

[1] Centred at RA= $05^\mathrm{h}\,37^\mathrm{m}\,40\overset{\mathrm{s}}{.}0$ (J2000), Dec= $-69^\circ\,22'\,18''$ (J2000).

[2] An image-peculiarity statistic produced from the IRAF DAOPHOT allstar task used for producing PSF photometry (outlined in Rubele et al. 2012).

regions of 0.5 mag and 0.01 mag error or 0.2 sharpness. Levels of 1%, 5%–30% (step 5%), 50%–100% (step 10%) are drawn in Figure 4.1, in red, cyan and green, respectively. The saturation limit is shown in magenta. Sources are extracted by the aperture-photometry pipeline up to 2 magnitudes above this limit; see Gullieuszik et al. (2012).

The patterns are very similar in each band; when sources are fainter the photometric error becomes larger and a similar change occurs in sharpness. A small number of sources exhibit a spike in error and sharpness at about 16.5–17.5 mag, which precedes the more exponential rise. Their location with respect to the peak suggests this is caused by source blending or crowding effects, accentuated as the wings of the distributions are more densely populated by the large number of RC stars at those magnitudes. There is also a similar effect for bright objects with a large increase about the saturation limit and a separate, smaller increase seen beyond it. Both cases represent very low source density. I filter the selection to only include sources with sharpness between -1 and $+1$ in every band because very sharp points are likely to be bad pixels and un-sharp points are likely to be extended sources (such as cosmic rays). The top panel of Figure 4.1 shows the effect this filtering has on photometric error (note: the photometric error is not filtered aside from sources outside of the sharpness range being excluded). Using this filtering reduces the total number of sources to 9.35×10^5 (from 1.59×10^6).

I am using the J and K_s bands. Usage of the Y band is covered in Appendix A.1.3.

4.2 Colour–Magnitude Diagram

Figure 4.2 shows the CMD for tile 6_6, containing approximately 10^6 stellar sources. This is an old population; the main sequence, RGB and RC populations are all resolved, and the asymptotic giant branch (AGB) is partly seen (the VISTA saturation limit prevents the full AGB population being seen; see Gullieuszik et al. 2012 for details) and the tip of the RGB (TRGB) is clearly seen at $K_\mathrm{s} = 12$ mag, consistent with literature

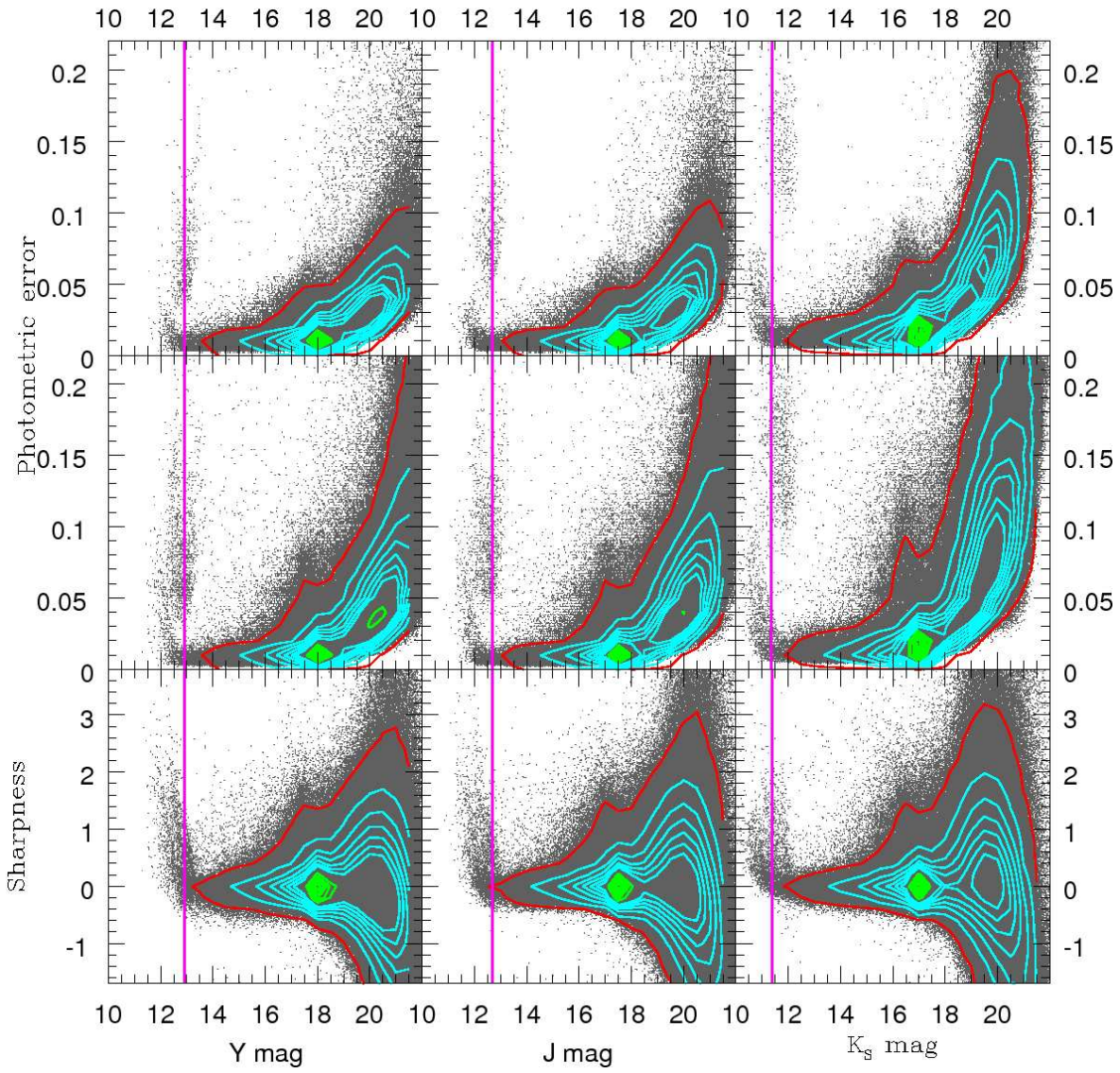

Figure 4.1: Sharpness (bottom) and error (middle and top; middle for all values of sharpness, top for sharpness between -1 & $+1$) vs. magnitude for K_s (right), J (middle) and Y (left). Contours are overplotted in red, cyan and green, saturation limit in magenta.

findings (e.g. Cioni et al. 2000). There is a noticeable amount of excess sources beyond $(J - K_s) = 1.5$ mag and $K_s = 16.5$–19 mag. These are typical magnitudes and colours of background galaxies (Kerber et al., 2009).

As the CMD is extremely dense in certain regions (the RC in particular), a contour map of stellar density is overplotted in cyan on Figure 4.2. The lines are built with a bin size resolution of 0.05 mag in K_s and 0.01 mag in $(J - K_s)$. The contour lines are drawn with the cell containing the most stars (1172) as the peak level and the cyan contours are where the number of sources range from 5%–30% of the peak, with a step of 5%.

The panels to the top and right of the CMD are histograms of colour (top) and magnitude (right) with the same bin sizes. The major peaks ($K_s = 17$ mag and $(J - K_s) = 0.6$ mag) are within the RC region while the minor peaks ($K_s = 19$ mag and $(J - K_s) = 0.2$ mag) are due to the main sequence.

4.3 Defining the Red Clump

The contour method defined in Chapter 3.1 is used here to define the RC sample. To recall, this is the area of the CMD where the following equations are satisfied:

$$0.4 \leq (J - K_s) \leq 1.5\,\text{mag} \tag{4.1}$$

$$K_s \geq 0.754 \times (J - K_s) + 16.293\,\text{mag} \tag{4.2}$$

$$K_s \leq 0.754 \times (J - K_s) + 16.833\,\text{mag} \tag{4.3}$$

Applying this selection yields a total of 150,328 RC stars. A problem with any selection for the RC is contamination from other components. These vary along my colour selection but include intermediate mass He-burning stars, young main sequence stars, background galaxies and, around the peak of the RC population, the first ascent of the RGB. In Figure 4.3 I show histograms (luminosity functions) of K_s magnitude, for strips in $(J - K_s)$ colour; I show these histograms including all sources (in black), as well as after excluding stars satisfying the RC selection criteria (in dashed-grey).

Using the histogram I estimate the amount of non-RC population inside the RC

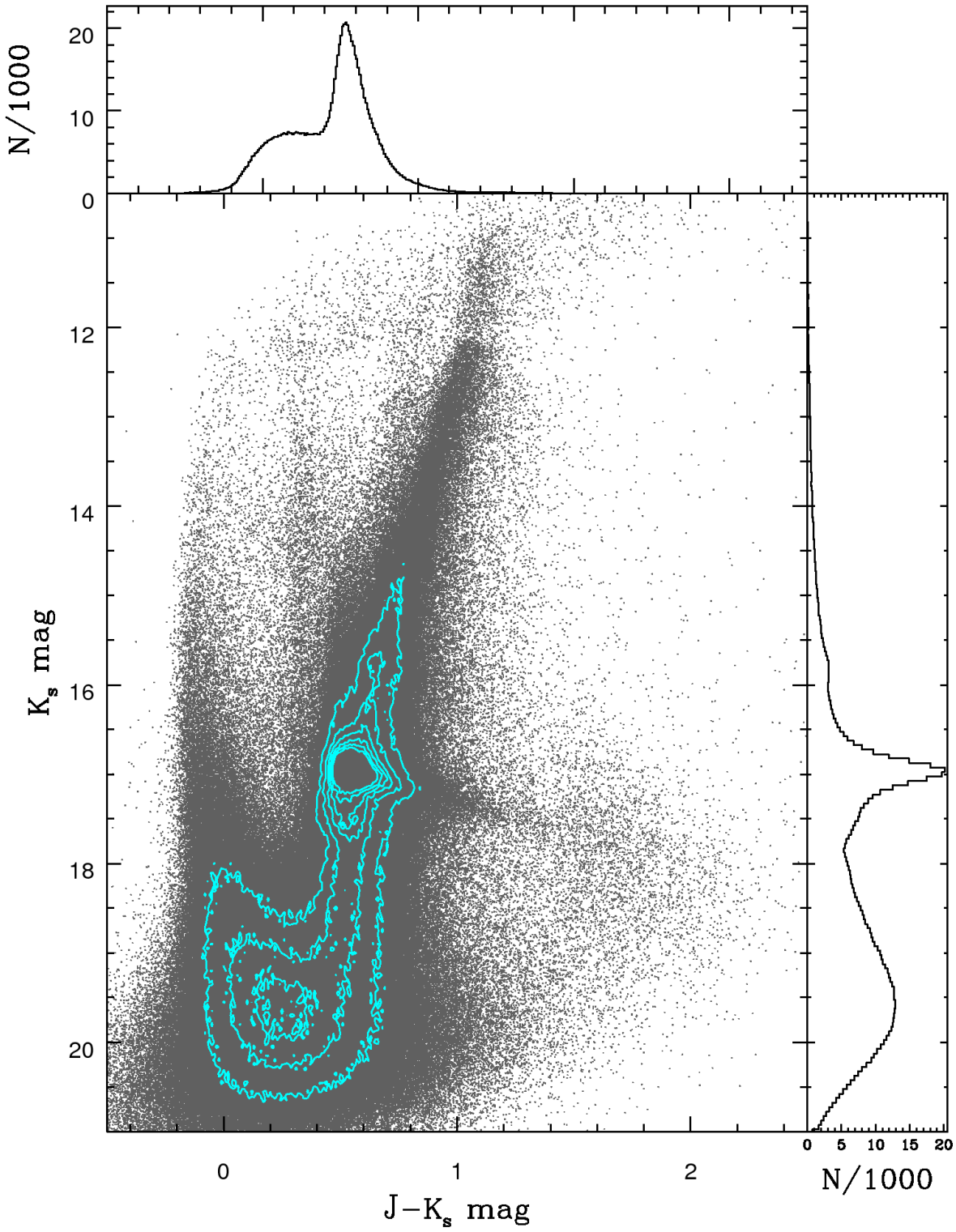

Figure 4.2: $K_{\rm s}$ vs. $(J - K_{\rm s})$ CMD of LMC field 6_6 accompanied by cyan contours representing density, and histograms of $(J - K_{\rm s})$ (bin size 0.01 mag) and $K_{\rm s}$ (bin size 0.05 mag). It can be seen that this field is largely made up of main sequence, RGB and RC stars.

selection by interpolating from points lying outside of the RC selection. In performing the interpolation, care was taken not to overestimate contaminants by using the distribution excluding RC selection (shown in dashed grey in Figure 4.3) and interpolating between 0.55 mag from the brightest zero and 0.75 mag away from the dimmest zero. This interpolation is shown in dashed-red in Figure 4.3.

These points excluded the fringes of the non-selected RC population as these have a large spread in magnitude, a larger degree of RGB contamination (for some colour ranges) and are minor compared to the selected RC population, which justifies their exclusion from the selection.

I can see in all panels, except the bluest, a bump where the RC occurs and this is covered by the magnitude range chosen. The bluest colour bin ($(J - K_s) = 0.2$–0.4 mag, not part of the RC selection) lack this feature and the reddest colour bin ($(J - K_s) = 1.3$–1.5 mag) starts to have this feature become less distinguishable from contaminants.

In the panels covering $(J - K_s) = 0.4$–0.6 mag there is an unusual knee-like bump at dimmer magnitudes compared with the more normal distribution of the other panels. This is a mixture of the RGB continuum (the RGB is found at $(J - K_s) \simeq 0.5$ mag for these colours) and SRC.

4.4 Stellar and Red Clump population density and distribution

To gauge how well the RC (and hence, the estimated reddening) represents the stellar population as a whole, I compare the distribution on the sky of the RC against that of all stars and other populations using the following CMD selections:

- All stars: CMD range of $12 \leq K_s \leq 20$ mag and $(J - K_s) \leq 1.5$ mag.
- RC stars: defined on the basis of the selection box in Section 4.3 (using equations 4.1–4.3).
- All except RC: all stars range excluding the RC selection box.

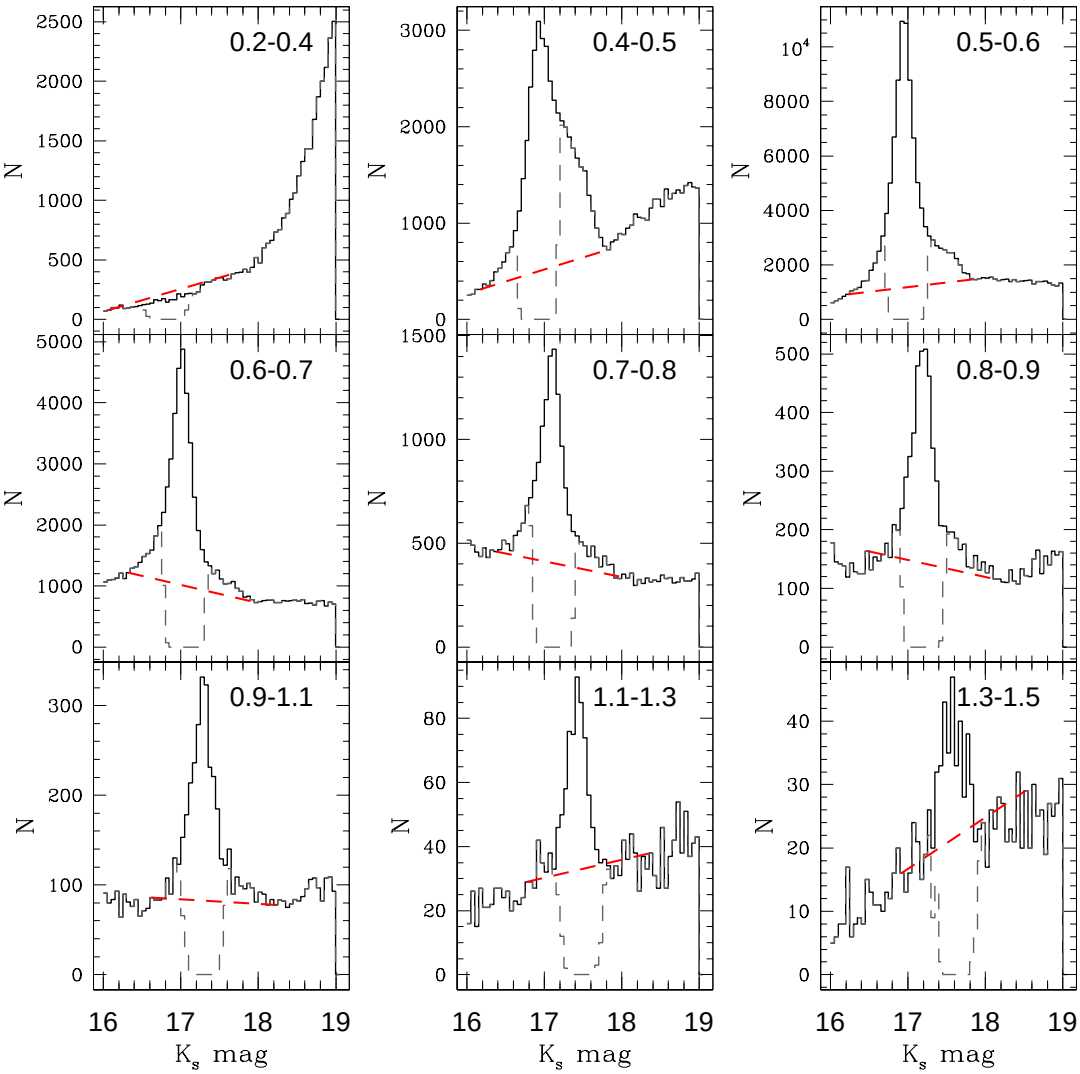

Figure 4.3: $K_{\rm s}$ band histograms (luminosity functions; bin size of 0.05 mag) for $(J-K_{\rm s})$ colour given in panels. Black: all stars, dashed grey: excluding RC stars, dashed red: contamination interpolation.

- Lower main sequence: sources within $16.5 \leq K_{\rm s} \leq 20$ mag, bluer than $(J - K_{\rm s}) \leq 1.5$ mag and excluding the RC stars selection.
- RGB and other giants: $12 \leq K_{\rm s} \leq 16.5$ mag, $(J - K_{\rm s}) \leq 1.5$ mag and excluding the RC selection.
- Background galaxies: $(J - K_{\rm s}) \geq 1.5$ mag for $12 \leq K_{\rm s} \leq 20$ mag.

The magnitude range is chosen due to completeness of the CMD and photometric errors beyond these boundaries (see Figure 4.1; regrettably, this does exclude what can be seen of the AGB population) and the colour limit eliminates effects of background galaxies on the selection.

For each of those selections, I then produce contour maps of stellar density for regions sized $5' \times 5'$. The output is displayed for 10 evenly spaced contour levels between zero and the peak density. Figure 4.4 shows these for the distribution of all stars (top–left), RC stars (top–middle), all stars except RC stars (top–right), main sequence stars (bottom–left), RGB and other giant stars (bottom–middle) and background galaxies (bottom–right).

The general trends seen are an increase in sources towards the South–West region (this region is where the LMC bar crosses the tile) and a decrease surrounding the 30 Doradus region (RA=84.°65, Dec=−69.°08). However, neither of these trends are identical for all populations. In particular the main sequence population (Figure 4.4, bottom–left) has less of an increase towards the LMC bar. This may be due to the main sequence stars being more abundant throughout the tile because the population distribution is flatter, as very few areas have contour levels below 50% of the peak. The main sequence peaks in Southern and Western regions, where the bar region is more abundant than in the North–East.

The intermediate aged RGB and RC populations (Figure 4.4, top– and bottom–middle) increase towards the bar, which suggests the bar itself is of intermediate age and not particularly metal poor. This matches the findings of Cioni (2009); the RGB star content of the bar is a few Gyr old and has a metallicity of [Fe/H]$= -0.66 \pm 0.02$ dex. The drop in the North–East region (clearer in these intermediate aged populations) correlates with areas of redder colour, such as regions 0-2 and 1-2 in Figure A.2.

The background galaxy distribution (Figure 4.4, bottom–right) is not flat or uniform as would be expected. If I ignore the lowest 2 contour levels I find a few areas contain nearly all of the remaining 8 contour levels. I investigated the possibility of these areas being galaxy clusters but did not find any to be known at the co-ordinates. However, it is also possible these are highly reddened RC stars, excluded by the colour cut-off (defined due to high amounts of noise). The presence of H II regions (LHA 120-N 159, LHA 120-N 157) in these areas suggests that this is the case. The RGB and other giant star distributions similarly lead to an unexpected find in the form of the peak region around R136 (in addition to the more typical peak around the LMC bar). This feature may be giant or pre-main sequence stars included in the CMD cut off as I did not define a lower colour limit. I return to this point in Section 4.7.5. From looking at these different populations, the density distributions should be taken into consideration when comparing RC to non RC populations, especially for the younger main sequence stars.

4.5 Reddening values

Reddening values were determined following the procedure described in Section 3.2.1 and $(J - K_s)_0 = 0.495$ mag, is adopted as the intrinsic colour.

Comparing with Table A.1, I see for regions 0-0, 3-1 and 3-2 the median is around $E(J - K_s) \simeq 0.035$ mag. This is consistent with the foreground Galactic extinction estimate of $(J - K_s) = 0.04$ mag from Schlegel et al. (1998). For the whole tile the mean is $E(J - K_s) = 0.091$ mag, more than double the foreground Galactic estimate because Schlegel et al. do not (and did not intend to) account for the additional reddening within the Magellanic Clouds.

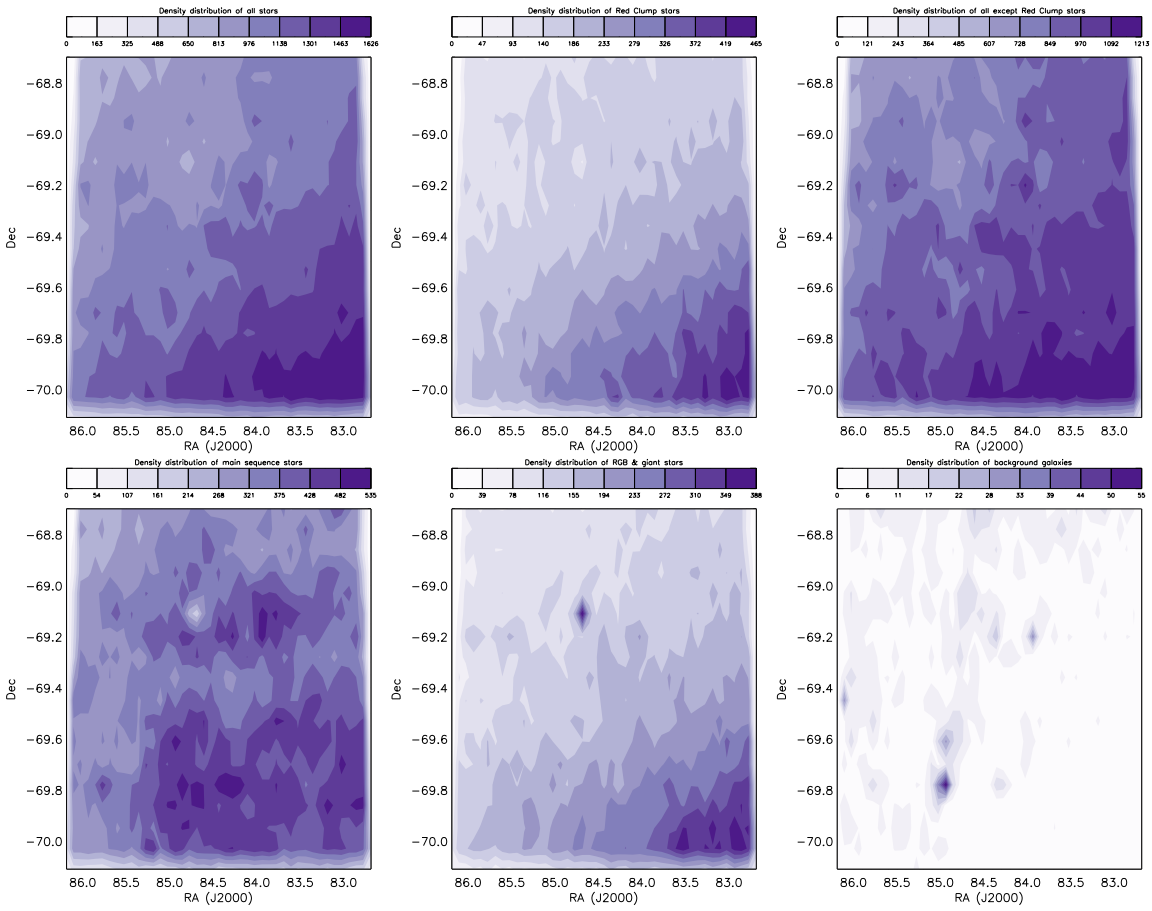

Figure 4.4: Density of all stars (top–left), RC stars (top–middle), all except RC stars (top–right), main sequence stars (bottom–left) and RGB & giant stars (bottom–middle) and background galaxies (bottom–right) within the field for regions of $5' \times 5'$.

4.6 Results

4.6.1 Reddening map

The RC star extinction map for the tile is shown in Figure 4.5; a histogram of the extinction scale (in A_V and $E(J-K_\mathrm{s})$) is shown in Figure 4.6. There is a small gap in coverage around star forming region NGC 2080 and little coverage within R136 (Section 4.7.5 looks at R136 in more detail). As most locations contain high and low extinction stars (due to multi-layered structure) in close proximity, it is difficult to assess the impact from this map alone. In Section 4.6.3.1 I look at eight maps covering more limited $E(J-K_\mathrm{s})$ extinction ranges.

4.6.1.1 Issues with method and data

Within the K_s vs. $(J-K_\mathrm{s})$ CMD there is some potential overlap between what I select as RC stars and the RGB. As these stars will also be affected by reddening it is important to know where they lie on the intrinsic CMD; if the RGB stars are at the same intrinsic colour as the RC stars then the extinction will be the same. However, if the RGB stars are intrinsically redder, the extinction is partially overestimated. Using the isochrones produced in Section 3.2.1.1 (for Section 4.5) I find the RGB lies at $(J-K_\mathrm{s}) = 0.53$–0.57 mag (brighter magnitudes having redder colour), a difference of $\sim 0.05 \pm 0.02$ mag from the mean RC star. However, the first ascent of the RGB covers a large magnitude range with stars moving at approximately 0.017 mag/Myr which could mean a fairly low stellar density of these. Taking a typical RC lifetime of 0.1 Gyr an RGB star moves a total of 1.7 mag in this time. The RC selection box I use is about 0.54 mag meaning it would take an RGB star $\sim 32\%$ of the RC lifetime to cross the RC.

In reality though, the first ascent of the RGB concentrates at the luminosity where the H-burning shells meets the composition discontinuity left by the first dredge-up. This is known as the RGB bump. For LMC metallicities this luminosity is at the same

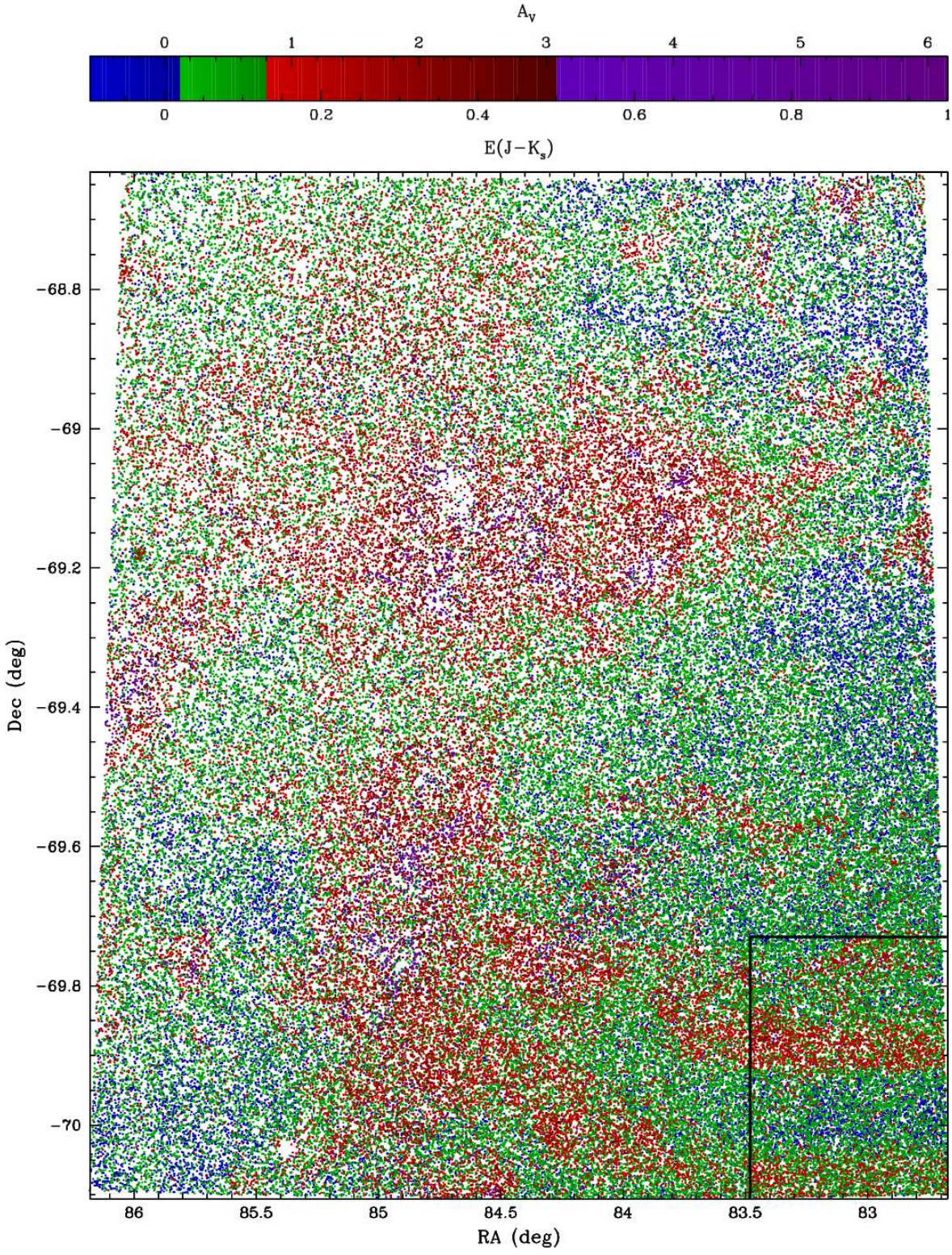

Figure 4.5: Extinction map for whole tile. Colour scale is shown on top ($E(J - K_s)$ scale below and A_V scale above) and reused in Figure 4.6. The black line marks the location including the effects of the two offset observations by detector 16 (see Section 4.6.1.1 for more information).

level of the RC, and the feature thus overlaps (and is hidden by) the RC. Also, the RGB evolution slows down at the RGB bump so that the movement outlined above is overestimated. The effect the RGB has on the reddening map is important for low reddening ($E(J-K)_{\rm s} \simeq 0.1$ mag, $A_V \simeq 0.6$ mag) where this might be overestimated in some instances but is less important for higher extinction.

The photometric errors and intrinsic spread in the RC lead to about 14% of the RC selection having unphysical negative reddening.

On the instrument itself, detector 16 has variable quantum efficiency in the top half, especially noticeable in low background conditions. As a result, flat fielding is worse for the regions covered by that detector, particularly for the outer half. The region that the two observations within detector 16 covers in this work is the dense LMC bar. The poor flat fielding is seen from the two strong horizontal lanes of apparently high extinction seen in the region, which correspond to the two offset observations from the outer half of detector 16. A method to gauge the effect is to see if any features in this region are also seen in non-VMC observations for this region. This is done in Section 4.7.4. The region affected is RA $< 83.^{\circ}48$ and Dec $< -69.^{\circ}73$ and has been marked on Figure 4.5.

4.6.2 Using the data

In order to make the data products useful to the community I made reddening maps available in several formats[3]. One of these is a complete catalogue containing for each RC star mean, median and maximum values (as well as dispersions) for surrounding regions of sizes $30''$, $1'$ and $5'$. The probability map for reddening in those regions has been made available as a cumulative probability data cube.

This is available from CDS[4]. A sample of the table is shown in Table 4.1. The data cube is in the form of FITS files linearly projected in 16 slices.

[3]These are published as part of Tatton et al. (2013b)

[4]`http://vizier.u-strasbg.fr/viz-bin/VizieR?-source=J/A+A/554/A33`

Table 4.1: Table of RC stars, giving position, reddening and statistics on RC stars surrounding it for 3 diameters; 30″, 1′ and 5′. Two sample lines are displayed; the full table is available electronically from the CDS. Ellipsis indicate missing columns.

RA	Dec	$E(J-K_s)$	30″					
(J2000)		mag	N	σ	Mean	Median	Maximum	N
84.4710	−70.1051	0.1575	1	0.0000	0.1575	0.1575	0.1575	...
84.7594	−70.1042	−0.0395	2	0.1945	0.0980	0.2355	0.2355	...

4.6.3 Distributions of reddening along the line-of-sight

The aim of this subsection is to try and identify where dust lies in relation to RC stars.

4.6.3.1 Sub-maps: $J-K_s$ slices

Figure 4.7 shows contour density maps for individual slices of extinction, to show a clearer picture of the regional distribution of extinction. The contours are drawn based on the density of RC stars per $5' \times 5'$ split into 10 levels. The legend gives the number of stars at each contour level (on the bottom) and the probability of stars in that region having the same extinction (on the top). Table 4.2 describes the number of stars contained in each slice and the extinction range covered by each slice. Slice 2 is the most numerous containing $\sim 26\%$ of all the RC stars while slices 1–4 cover $\sim 88\%$ of all the RC stars.

The 1st and 2nd slices are virtually inverted in the 4th and 5th slices. This suggests the latter slices are the reddened population from the former slices. However, this view is complicated by slices 6, 7 and 8 also containing populations absent from slices 1, 2 and 3.

The probabilities given in the legend of Figure 4.7 are an estimate of the probability of a star in a given sightline, having extinction within that extinction range, based on the total number of stars in all slices. I see that around R136 nearly all the

Table 4.2: Number of RC stars in each colour slice (extinction ranges given) and total number of RC stars.

Slice	N_{RC}	$E(J-K_s)$		A_V	
		min	max	min	max
...	...	mag		mag	
1	24738	−0.095	0.005	−0.584	0.031
2	38868	0.005	0.055	0.031	0.339
3	34381	0.055	0.105	0.339	0.645
4	34014	0.105	0.205	0.645	1.260
5	10851	0.205	0.305	1.260	1.875
6	3968	0.305	0.405	1.875	2.489
7	2439	0.405	0.605	2.489	3.719
8	1069	0.605	1.005	3.719	6.177
Total	150328				

sources are found in slices 5–8, suggesting that the dust lies in front of the stars here. If the assumption is made that the RC decently represents the tile as a whole, the probability maps can be used for reddening estimates of other star populations. From Section 4.4 I see other intermediate aged populations match the RC star distribution well while earlier evolutionary phases correlate less. In particular I found relatively few RC sources in the North–West and relatively many RC sources for small regions of the South–West. One sees that both of these regions are almost exclusively comprised of stars in slices 1–4. The South–West region contains the LMC bar which is likely to be in front of the LMC (see Chapter 5 for more), or has little dust obscuring it.

Finally, the peaks in the background galaxy distribution in Figure 4.4 correspond to regions in slices 7 and 8. This suggests those peaks are further reddened RC stars missed from my selection due to the background as a whole being more dominant when looking at the whole tile.

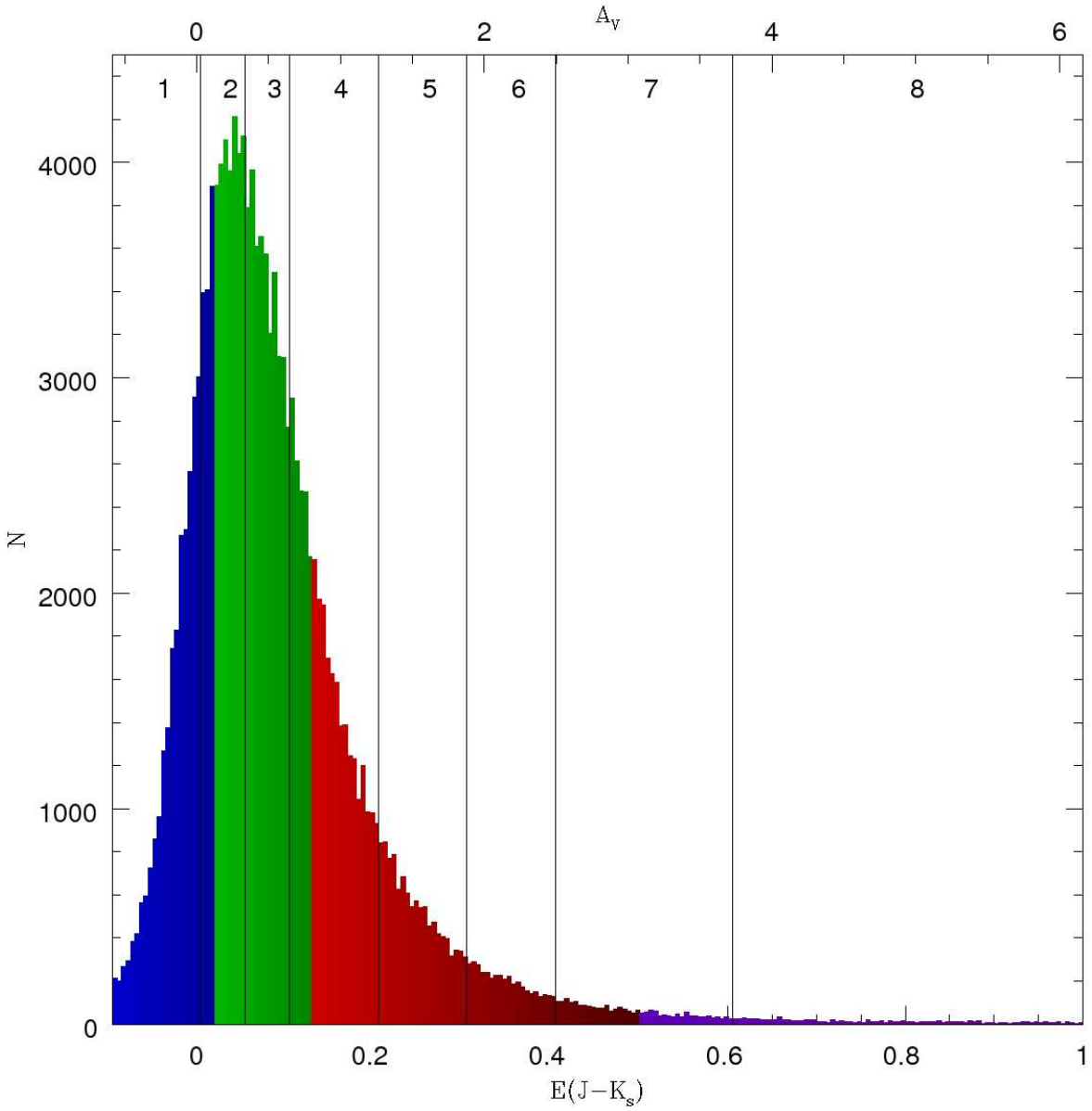

Figure 4.6: Histogram of $E(J-K_{\rm s})$ (bottom) and A_V (top) distribution with bin size of 0.005 mag. Green is the region covering 50% of the sources centred on the median where darker blue is lower than this and brighter red higher and purple extremely high (covering the sparsely populated upper 50% of the reddening range). The numbers and vertical lines detail the colour slice regions used in Section 4.6.3.1.

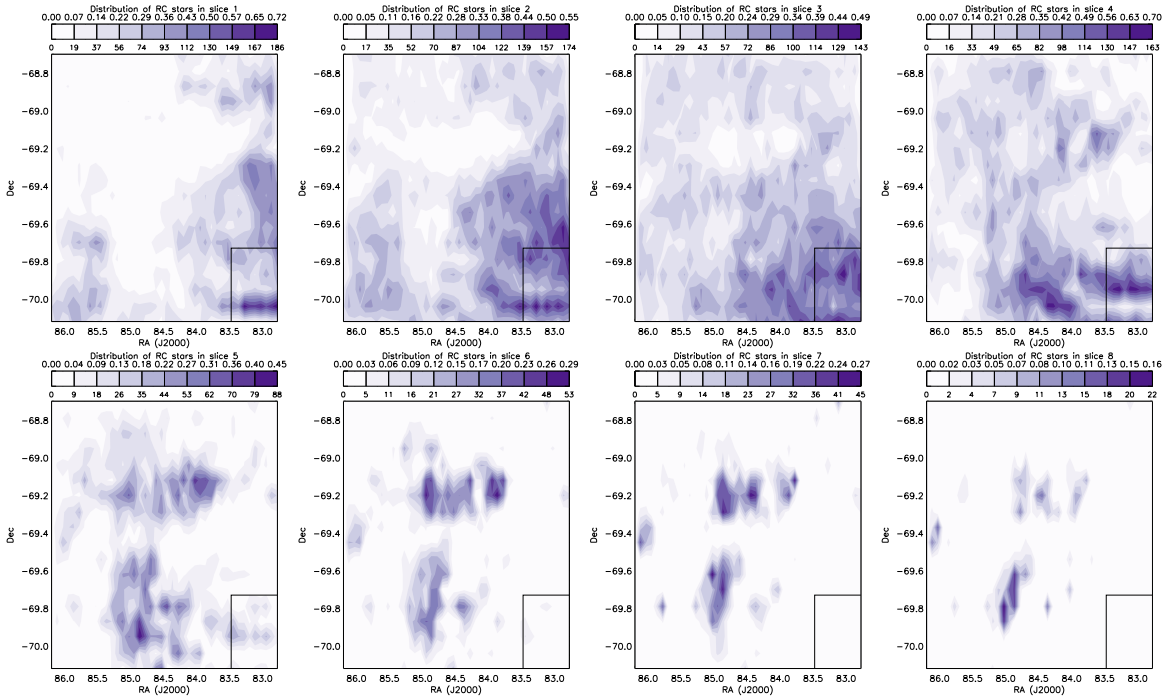

Figure 4.7: Contour map of number of RC stars (bottom legend) and probability of RC star (top legend) within $5' \times 5'$ bins for each colour slice. Region containing detector 16 is outlined in black. $E(J - K_s)$ and A_V range of each colour slice are given in Table 4.2.

4.6.3.2 Reddening dispersion

I measure dispersion of reddening for RC stars to try and learn about the relative locations of stars and dust. A population with low dispersion will contain less dust while higher dispersion can be related to stars being embedded within the dust or it can show a significant fraction lies behind dust clouds. Investigating higher moments[5] can help distinguish between these possibilities.

For a map based comparison of reddening variance I select RC stars within a $30''$, $1'$ and $5'$ diameter of every RC star. I then find the standard deviation (σ) of these selections. Figure 4.8 shows the resulting maps. These have some similarity to the reddening map in that σ is higher in regions covered by higher extinction slices. Less similarity is seen in the $30''$ map though the regions of greatest σ are also the regions of greatest reddening (but the regions surrounding these have much lower values than in the $1'$ and $5'$ maps, this is due to a $30''$ diameter resulting in small samples and σ being zero). Likewise, the $5'$ diameter map is more similar to the reddening map where the higher dispersion is associated with the regions containing the populations of reddening slices 5–8 (in Figure 4.7). This increase in σ is due to high extinction regions covering a much larger range of extinction values than the low extinction regions.

The larger extinction range is caused either by the RC stars being in front and behind the dust or them being embedded within the dust. To investigate this I looked at a higher moment, the kurtosis, finding for the $5'$ diameter there is a high kurtosis for low extinction regions (as the data is largely around the peak) while high extinction regions had a lower kurtosis, but these values were still close to those of a normal distribution that you would expect from embedding within the dust.

4.6.3.3 Dependence of reddening on distance

Another measure of the relative location of dust and stars is the change in reddening with respect to luminosity. RC stars near the bright edge of the reddening selection

[5]Measures of shape of a distribution of points.

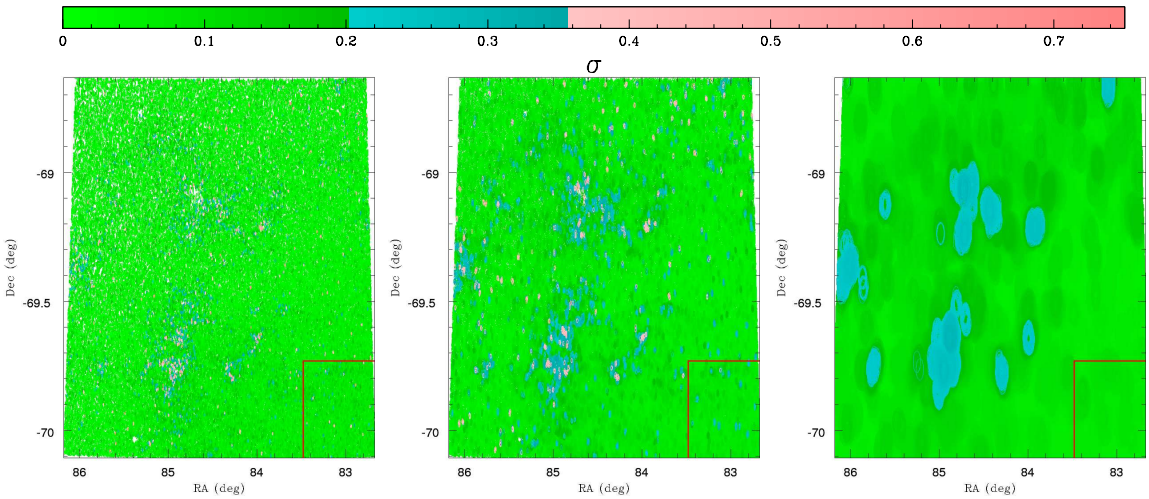

Figure 4.8: Maps of σ for RC stars within 0.′5 (left), 1′ (middle), 5′ (right) diameter of each RC star. Values shown in legend.

box will in general be nearer to us than stars near the faint edge of the reddening selection box, reflecting differences in distance modulus. The more distant stars are more likely to lie behind more dust than stars near the front of the LMC, and thus, I expect the more distant stars to be more heavily reddened.

When splitting my RC selection into 5 equal magnitude ranges, which follow the reddening vector, I observe a decrease in mean and median reddening with respect to increasing magnitude (decreasing luminosity). This is caused by the intrinsic slopes of the RC, RGB and SRC rather than the reddening (which would be expected to cause the opposite effect). This effect is more clearly shown in Figure 4.3 where the $0.4 \leq (J - K_{\rm s}) \leq 0.5$ mag panel has a bump at dimmer magnitudes from the SRC while the $(J - K_{\rm s}) = 0.5$–0.7 mag panels have a slight bump at brighter magnitudes.

To examine the effect of magnitude on the reddening distribution[6] I use histograms of colour on the 5 magnitude ranges. I choose the 2$^{\rm nd}$ and 4$^{\rm th}$ parts (which have a difference of $K_{\rm s} = 0.21$ mag, a distance of 5 kpc) as a contrast for comparison

[6]Absolute magnitude is no longer affected by reddening, but reddening may be dependent on apparent magnitude as these have some relation to location within line-of-sight.

because the outermost parts are more affected by the intrinsic slope and RGB stars (while the central part will not show as much contrast). These histograms are normalised to the total number of RC stars included in the parts (rather than to the peak as the height of the peak may vary) and also plotted are the ratio of the less luminous part divided by the more luminous part. Figure 4.9 shows these plots. I see that for higher reddening the further, less luminous component has up to 35% more highly reddened stars than the closer, more luminous component and this effect becomes stronger with extinction. While there is some small number statistics it shows to a small extent that the most highly reddened stars will be more frequently found to be less luminous and most distant.

4.6.4 Total hydrogen column density

It is possible (making assumptions about the composition and radius distribution of dust particles) to use extinction to estimate the total hydrogen gas column density ($N_{\rm H}$ in units of cm^{-2}) from its relation to A_V;

$$\frac{N_{\Sigma\,\rm H}}{A_V} = x \times 10^{21}\,{\rm cm}^{-2}, \tag{4.4}$$

where $N_{\Sigma\,\rm H}$ is the sum of molecular, atomic and ionised hydrogen content and x varies throughout the literature; Güver & Özel (2009) find $x = 2.21 \pm 0.09$. However, this is for Galactic regions where the dust-to-gas ratio (and metallicity) is higher than it is in the LMC. To account for this ($Z_{\rm LMC} = 0.5 \times Z_{\rm MW}$), I halve A_V. This is more easily expressed by (and has the same effect as) doubling the Güver & Özel (2009) value for x.

I use the above equation to estimate total hydrogen column density [7] for regions of $1' \times 1'$ using three different measures of density. The first measure (maximum) selects the star with the highest reddening in a region because this would be affected by (and hence measure) the most gas. A drawback of this method is that it might

[7] Referred hereafter as Inferred total hydrogen column density and Inferred total H.

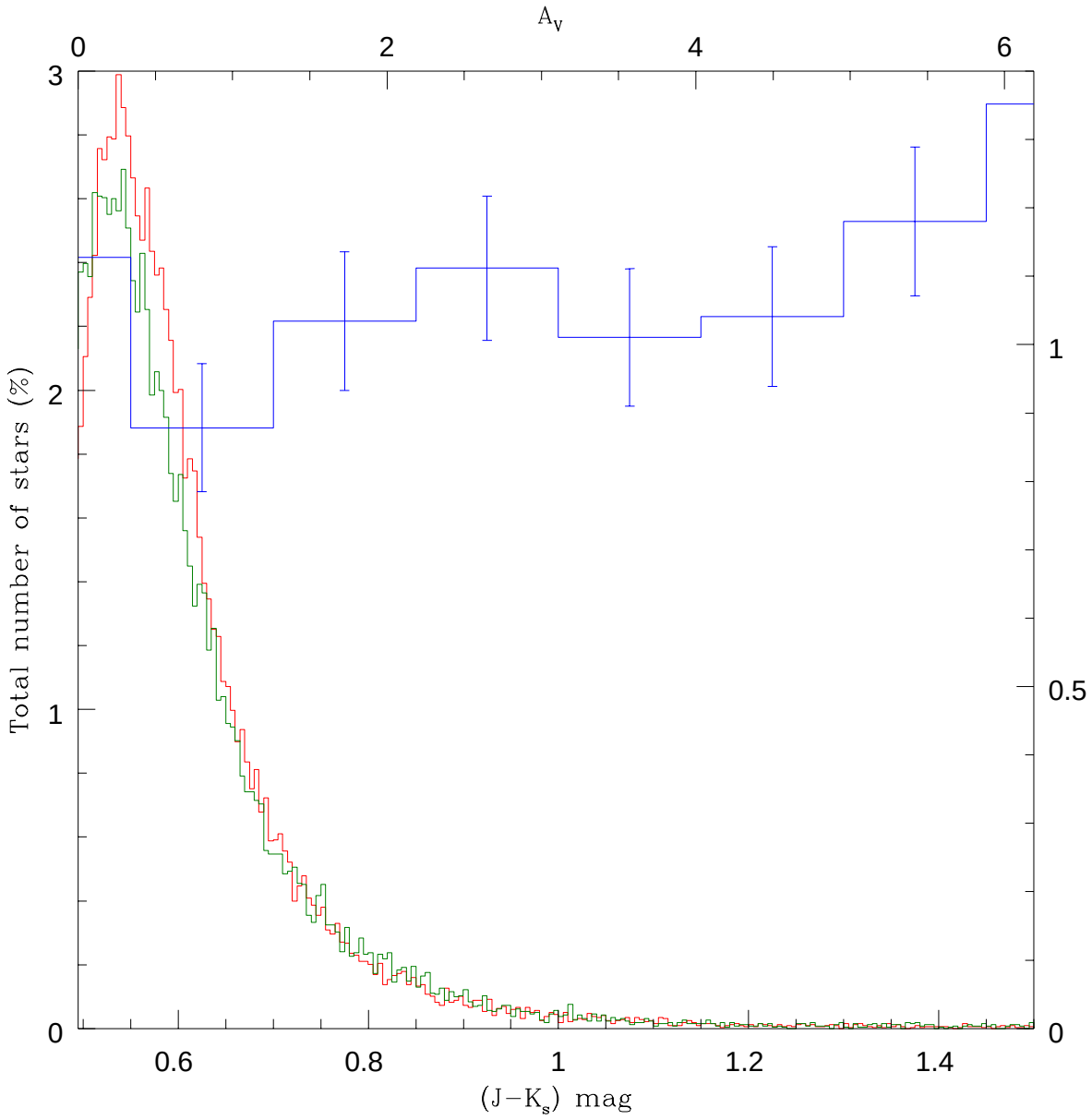

Figure 4.9: Histograms of more luminous (red) and less luminous (green) RC stars, normalised to total number of stars in selection. In blue is the ratio of less luminous to more luminous stellar numbers using a larger bin size (ratio given on right y-axis). Sources within detector 16 region have been excluded from selection.

provide an overestimate for regions of small scale structure (as these small scale results are magnified to arcminute scales). As a countermeasure I also look at the mode and median (the former is defined from histograms of bin size $0.44 \times 10^{21}\,\mathrm{cm}^{-2}$ where the peak is taken as the mode) although these are skewed by stars in front of the ISM and gas column.

Figure 4.10 shows maps for the three methods (from left – maximum, – mode, – median), the right panel shows the density represented by the pixel count and histograms of the source distributions are overplotted. I see that the peak extinction is affected somewhat by random noise from the reddest RC star selection, possibly including some background galaxies. However, small-scale structure with a dense column density (such as molecular clouds) may be responsible. I also see that Figure 4.10 has maximum column densities as high as $25 \times 10^{21}\,\mathrm{cm}^{-2}$; such concentrations are no longer atomic hydrogen but almost exclusively molecular hydrogen, meaning that the maps can be compared with molecular clouds surveys. I revisit this point in Section 4.7.3.

When comparing the maximum with the mode and median, I noticed that a small region around RA= 84°, Dec= −69.°6 is not present in the latter two, implying that the stars are mostly in front of the feature here. There are known H II regions (LHA 120-N 154 and DEM L 248) and a molecular cloud nearby ([FKM2008] LMC N J0536-6941; see Section 4.7.3).

I also use these maps in Section 4.7.2 where I compare them with H I column densities measured from observation.

4.7 Discussion

4.7.1 Comparison with optical reddening

Haschke et al. (2011) produced optical reddening maps using OGLE III data for the LMC and SMC and have made these data available via a webform[8]. Their selection

[8] http://dc.zah.uni-heidelberg.de/mcx

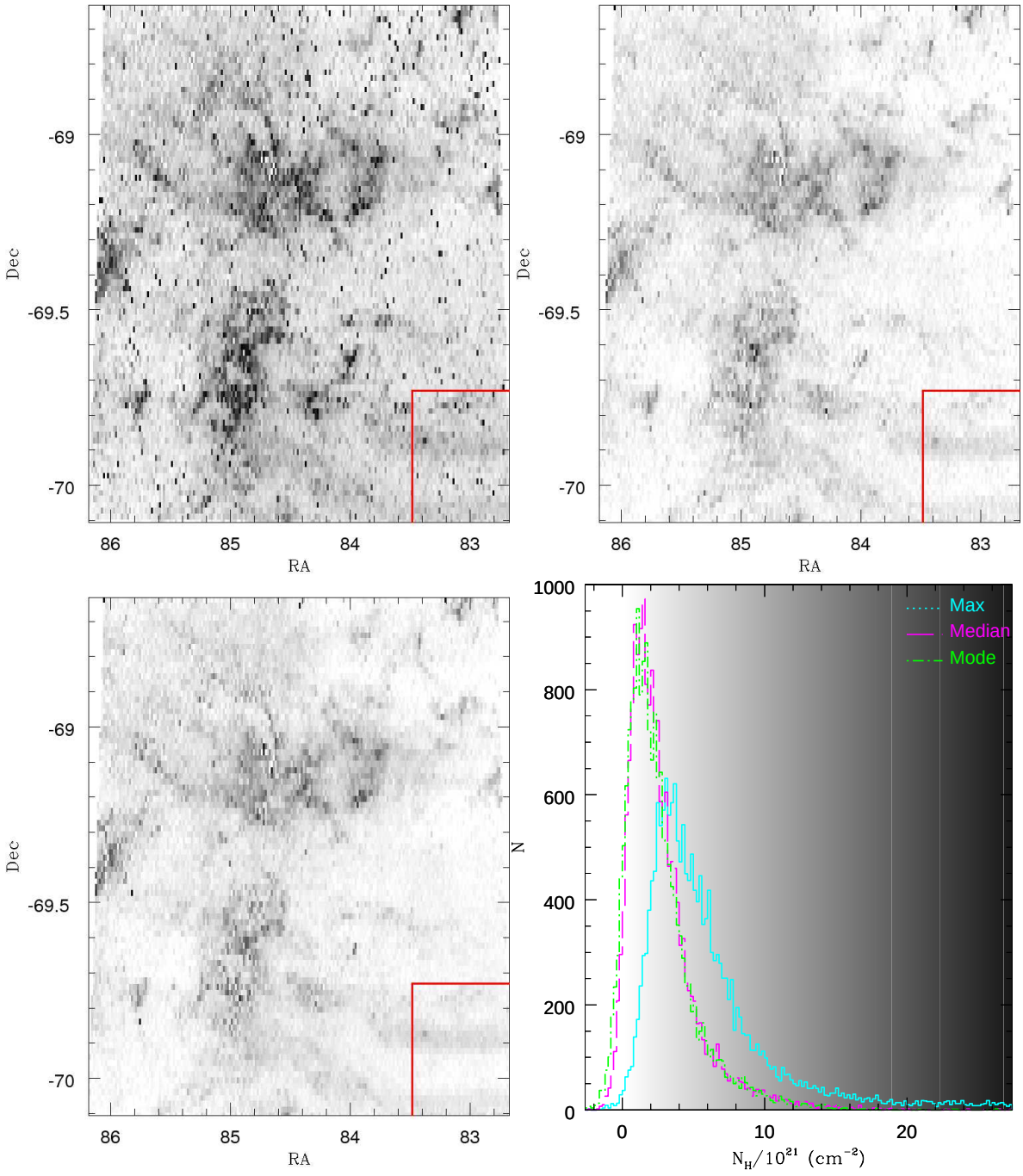

Figure 4.10: Maps of inferred total H column density for $1' \times 1'$ regions of the 6_6 tile. Maps are based on maximum (top–left), mode (top–right) and median extinction (bottom–left). The region containing detector 16 is outlined in red. Histograms of inferred total H column density are shown in the bottom–right panel.

criteria define the RC as being in the CMD region of $17.50 \leq I \leq 19.25$ mag and $0.65 \leq (V - I) \leq 1.35$ mag for sub fields containing at least 200 RC stars, where the sub field sizes range from $4\farcm5 \times 4\farcm5$ to $36' \times 36'$, based on number of RC stars. A histogram was then taken which has a Gaussian plus second order polynomial fitted to it, the peak of which was taken to be the mean and was tested against the reduced χ^2; where fields with values greater than 3 were flagged for inspection by eye. For the LMC four fields were affected, which was caused by the histogram being double peaked due to the RGB.

Their overall LMC average was $E(V - I) = 0.09 \pm 0.07$ mag; although, for the region I am comparing this average is $E(V - I) = 0.13$ mag. They also inspected, by eye, regions where $E(V - I)$ exceeded 0.2 mag (these are 2% of the LMC fields; totalling 60 regions). There were 23 regions which had $E(V - I) \geq 0.25$ mag; 16 are in the region I am comparing. These regions were better represented by moving the RC box to $17.5 \leq I \leq 19.5$ mag and $0.9 \leq (V - I) \leq 1.8$ mag. The mean was calculated as before. For most of these regions the extinction remains unchanged but the 1σ width becomes much larger (more so in the red than the blue). The extinction values in these recalculated regions are not given in their output tables but are given in Table 2 of Haschke et al. (2011).

Their selection box follows a linear selection (rather than a reddening vector) which is between 3–4 times larger than mine and because of this there is greater RGB contamination (largely accounted for by the use of a second-order polynomial).

I compared their $E(V - I)$ values to my $E(J - K_\mathrm{s})$ using two methods. The first method (fixed range) uses the same RC selection as Section 4.3 and the second method (sliding range) re-defines the RC selection as a fixed box as follows:

$$[(J - K_\mathrm{s})_\mathrm{P} - 0.25] \leq (J - K_\mathrm{s}) \leq [(J - K_\mathrm{s})_\mathrm{P} + 0.45]\,\mathrm{mag} \tag{4.5}$$

$$[(K_\mathrm{s})_\mathrm{P} - 0.5] \leq K \leq [(K_\mathrm{s})_\mathrm{P} + 0.5]\,\mathrm{mag} \tag{4.6}$$

$(J - K_\mathrm{s})_\mathrm{P}$ and $(K_\mathrm{s})_\mathrm{P}$ are the densest 0.05×0.05 mag areas of the CMD for that region.

For both methods I calculate the mean, median and standard deviation (σ) for

Table 4.3: Average $E(J-K_{\rm s})$ for comparison methods.

	Range	
	Fixed mag	Sliding mag
Mean	0.081	0.074
Median	0.068	0.066
Sigma	0.087	0.082

each region. The average value for each region is summarised in Table 4.3. The $E(J-K_{\rm s})$ median is found to be consistent because both selections cover the colour range where the highest density of RC stars lie. The mean and σ $E(J-K_{\rm s})$ have greater differences because the sliding range is narrower in colour than the fixed range. However, the narrower colour in the sliding range is more consistent with the work I am comparing with.

I compare the optical extinction with the average of the mean and median results for the second method. The values are then all converted into A_V using Schlegel et al. (1998) for the optical data and Section 3.2.2 for my NIR $E(J-K_{\rm s})$. These are referred to as A_V (Haschke) and A_V (This Work; hereafter TW), respectively.

Figure 4.11 compares the extinction values with the 1σ widths plotted as error bars. Squares and triangles are for points where my selection has more than and less than 200 stars, respectively. The purple hexagons show the A_V values of the recalculated $E(V-I)$ values (and their error bars) from Haschke et al. (2011) against the A_V of my work. Three red lines are drawn showing gradients of 1, 0.75 and 0.5. A positive trend is observed but considering both are measuring A_V there is considerable deviation from a linear fit beyond $A_V = 0.4$ mag (and up to $A_V = 0.4$ mag there is considerable scatter but the middle ground is a linear fit). The best fitting red line for higher values of A_V has a gradient of 0.75, representing the Haschke et al. A_V being 75% of my A_V, provided I use the recalculated reddening values. In the intermediate

range of $0.5 < A_V(\mathrm{TW}) < 0.8$ mag I see the greatest deviation with Haschke et al. reporting low extinction. Looking at the sky location of these points I find the majority of these points are in the region affected by Detector 16 (see Section 4.6.1.1) where my data are unreliable.

There are some factors to consider regarding differences:

[1] Some difference might arise from the extinction within the NIR being much less (approximately a factor of 3 less), meaning the NIR is a less sensitive probe of lower extinction and hence an under estimate.

[2] The Galactic foreground may have some influence. According to Schlegel et al. (1998) this contributes $E(J-K) = 0.04$ mag and $E(V-I) = 0.103$ mag. This could explain why the zero points do not join exactly at $E(V-I) = E(J-K_\mathrm{s}) = 0$.

[3] Also, I must not ignore the difference in intrinsic colour. Haschke et al. assume a metallicity of $Z = 0.004$ and obtain $E(V-I)_0 = 0.92$ mag (Olsen & Salyk, 2002). I, on the other hand, used a metallicity of $Z = 0.0033$. To test the difference, I produced isochrones (as done in Section 3.2.1.1, but instead for the V and I bands), finding an intrinsic colour of $E(V-I)_0 = 0.90$ mag. Using this would redden the Haschke et al. values slightly with the largest effect seen for the lowest reddening.

Next I examine the effect of sky position on relative extinctions. This is shown using two maps in Figure 4.12; the first map is an $E(J-K_\mathrm{s})$ map using the Haschke et al. regions and the second map is the extinction ratio of $A_V(\mathrm{Haschke})/A_V(\mathrm{TW})$. For the second map I omit regions where $A_V(\mathrm{TW}) \simeq 0$ because these outliers yield a very high ratio in comparison with the rest of the data. These maps are shown in the left and middle panels of Figure 4.12. A histogram of the A_V ratios is shown in the right panel of Figure 4.12; the peak is at $A_V(\mathrm{Haschke})/A_V(\mathrm{TW}) = 0.75$ with a fairly even distribution on both sides of the peak. In dashed blue is the histogram when excluding the detector 16 region. The distribution is more positively skewed, caused by fewer lower extinction regions sampled.

When I compare the two maps there is a lower $A_V(\mathrm{Haschke})/A_V(\mathrm{TW})$ ratio at higher extinction (and the detector 16 region) and the opposite for lower extinction. The cause is likely to arise from a combination of the optical being more sensitive to

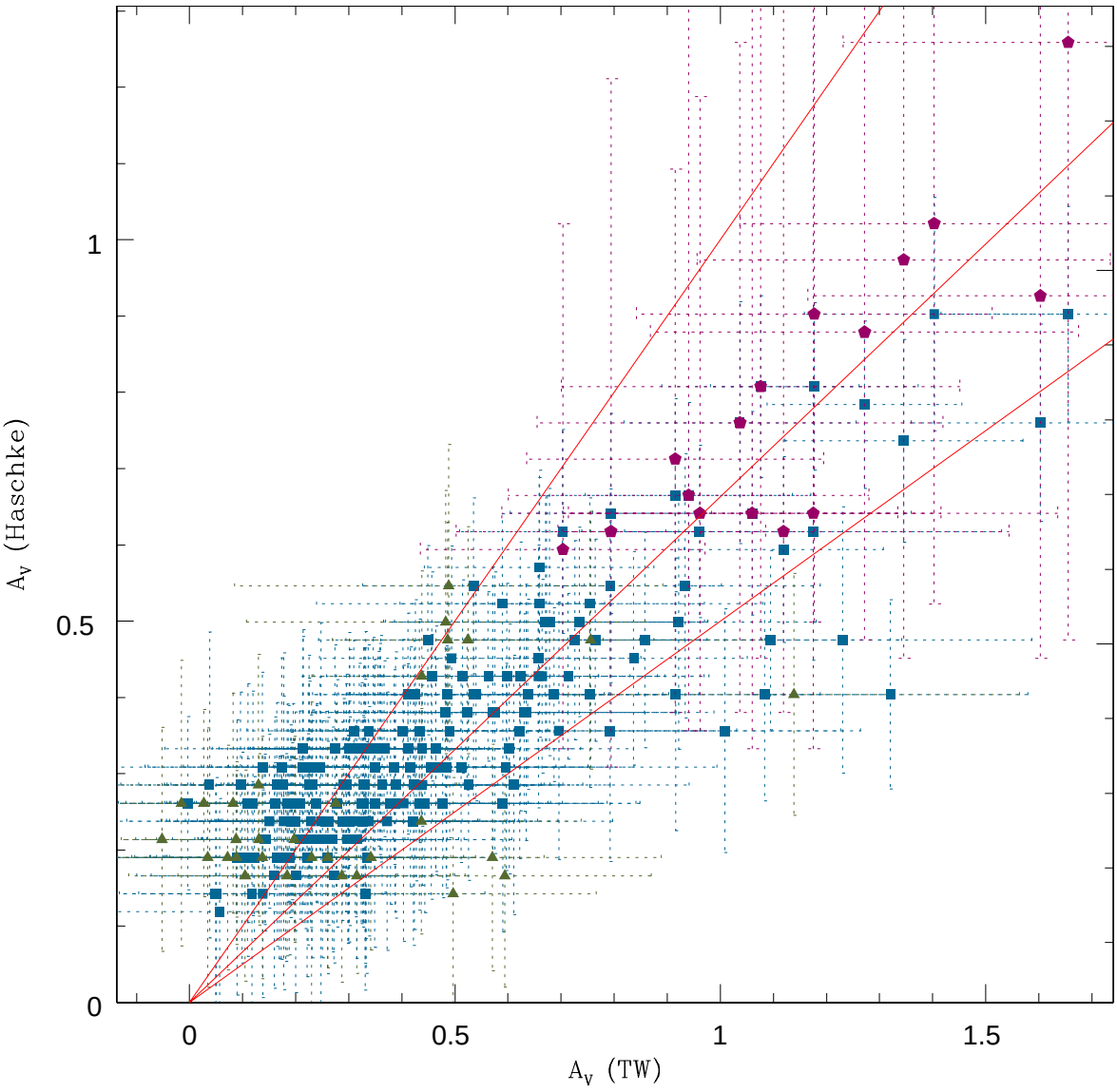

Figure 4.11: Comparison between A_V (Haschke) and A_V (TW), conversion from Schlegel et al. (1998) and Section 3.2.2, respectively. Squares indicate regions with over 200 stars while triangles indicate regions with less than 200 stars. Purple hexagons are the values for the recalculated regions. Regions within detector 16 have been excluded from the plot. Red lines represents gradients equal to 1, 0.75 and 0.5.

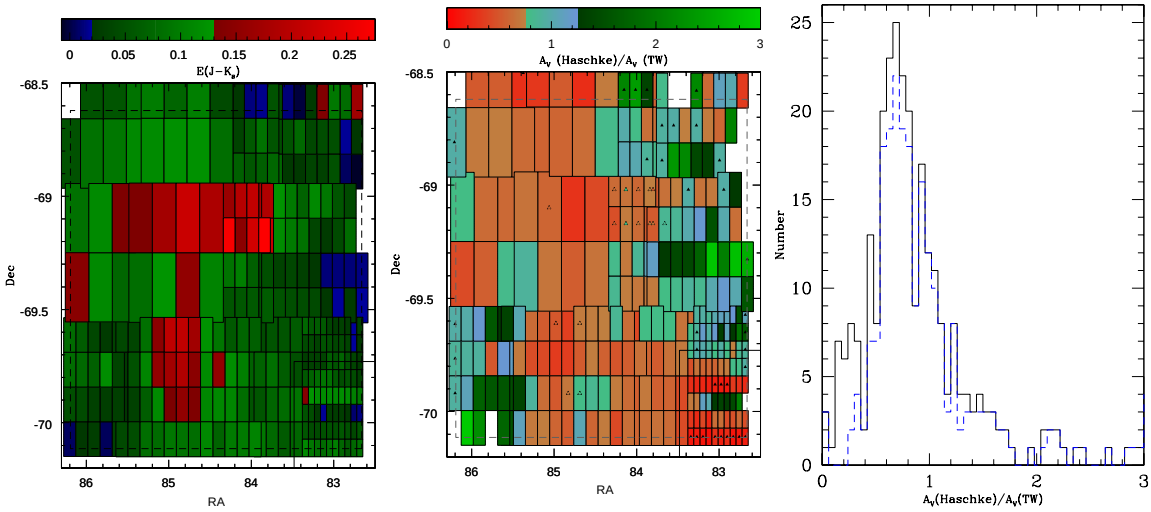

Figure 4.12: Map of sky showing extinction values (left) and A_V(Haschke)/A_V(TW) (middle). The dotted outline is the boundary of my tile. Black triangles on a cell indicate that particular cell was made using data that comprise of fewer than 200 stars, detector 16 region outlined in black. Coloured triangles on a cell indicate recalculated extinction ratio (where colour of the triangle is the recalculated value). Empty cells are where $E(J - K_s) \simeq 0$ mag (excluded due to producing extreme values in the ratio range). Right: histogram of A_V(Haschke)/A_V(TW), the dashed blue histogram excludes the detector 16 region.

lower reddening and the intrinsic colour used being bluer than mine. Meanwhile, for higher reddening, the OGLE-III data are prevented from detecting the stars with the most reddening, as these lie outside of the Haschke et al. selection box.

Haschke et al. already consider the latter by inspecting these regions by eye and re-drawing the star selection boxes to better cover these regions. The values in these regions have been over plotted as outlined, coloured triangles in the middle panel of Figure 4.12. Little change is seen because this does not take into account the 1σ widths associated with these values (which tend to be skewed toward higher extinction).

Note that the criteria for re-drawing the selection do not consider regions which have both low and high extinction populations. This could lead to some cases of the high extinction component being completely missed. My star-by-star reddening derivation is clearly superior in this regard.

Haschke et al. also used the OGLE III data to produce an RR Lyrae extinction map (shown in their Figures 9 and 10) which, visually, appears to agree better with my result. However, tabular data are not provided because the stars are sparsely distributed (with 120 having estimated extinction, using the mean of the surrounding cells due to no RR Lyrae stars contained in them). This suggests that at optical wavelengths, extinction derived from RR Lyrae stars is more reliable than that of the RC.

The VMC survey has also made use of the RR Lyrae stars OGLE III database (Soszyński et al., 2009) in studying reddening (Moretti et al., 2014), producing two maps. The first map shows reddening derived from the relation between intrinsic colour, $(V-I)_0$ and V-band amplitude (Piersimoni et al., 2002). As OGLE III provides I-band amplitudes these were scaled to V-band amplitudes using a fixed scaling factor (1.58, Di Criscienzo et al. 2011). The second map uses the visual V Period–Luminosity relation (which has large dispersion due to varied reddening range) paying attention to stars with $V > 20.5$ mag and stars with $20 < V < 20.5$ mag. Regions containing these stars trace structures that could be associated with reddening excess due to dust in the regions. These regions correspond to the high reddening regions of the first map suggesting this is the case.

Both of these maps agree with what is shown in Figure 4.5. The median reddening value of the first map, $E(V-I) = 0.11 \pm 0.05$ mag agrees excellently with the Haschke et al. (2011) RR Lyrae reddening median value of $E(V-I) = 0.11 \pm 0.06$ mag. For the RC stars of Haschke et al. (2011) the difference in reddening values was calculated (for each RR Lyrae star within a RC field) finding a median difference of 0.00 ± 0.05 mag.

4.7.2 Comparison with H I

The H I observations come from the Australia Telescope Compact Array (ATCA) observations presented in Kim et al. (1998). They are in the form of a $1998 \times 2230 \times 120$ data cube containing 120 channels covering a heliocentric velocity range of 190–387 $\mathrm{km\,s^{-1}}$, at a velocity separation of 1.65 $\mathrm{km\,s^{-1}}$. The resolution per pixel is approximately $1' \times 1'$. The area that covers my tile is 243×270 pixels. Due to the H I emission being a combination of column density, H I nuclear spin temperate and background emission this will not always be a perfect mirror of the column density.

In a few of the regions surrounding and within 30 Doradus the emission features become absorption features. This is due to nearby bright sources affecting the instrument normalisation leading to overcompensation, or due to self-absorption (Figure 1 of Marx-Zimmer et al. (2000) identifies these regions as absorption sites). However, the total number of pixels affected by this (12×8 and 3×3) are a small minority of the total (243×270) and have been excluded from analysis. Figure 4.16 shows the total H I emission in the top–right panel.

I convert the emission from surface brightness (Jy beam $^{-1}$) into column densities ($\mathrm{cm^{-2}}$) using equations 1 and 5 from Walter et al. (2008). This is then compared with the inferred total column density derived in Section 4.6.4. For convenience in comparing Figure 4.10 with the top–right panel of Figure 4.16, column densities are given in Table 4.4.

I compare the measured H I and inferred total H (derived from A_V) column densities using two methods. The first (individual) method compares the total column

Table 4.4: Table of total H I emission and corresponding total H I column density.

Emission (Jy beam $^{-1}$)	Column density (cm^{-2})
4	2.03×10^{21}
8	4.06×10^{21}
11	5.58×10^{21}
15	7.61×10^{21}
19	9.64×10^{21}

density of each RC star against the measured column density at the location of that RC star and the second (group) method compares mean and maximum total column densities for a region of RC stars equal to one pixel of the H I data. As the A_V is a surrogate of all the H content rather than just the H I I expect to find agreement between the two data.

The measured H I column density vs. Inferred total H column density for both methods is shown in the panels of Figure 4.13. Overplotted are gradients of 2:1, 1:1 and 1:2 and contours (10 density levels of 10%–100% of maximum, for bin sizes of 2% in each axis data range). I see the best fit to the measured H I vs. maximum inferred total H is the 1:1 line up to about $N_H = 6 \times 10^{21}$ cm^{-2} where the measured H I levels off. The best fit to the measured H I vs. mean inferred total H is the 2:1 line, supporting the hypothesis that for a given sightline, on average half the stars lie in front of the H I column. The levelling off is once again observed.

There are a number of possible causes for this effect. To highlight a few:
[1] The $1'$ resolution of the emission does not resolve the small structure causing the extinction;
[2] The instrumentation only detects up to 0.8 Jy beam^{-1} for a given velocity channel. As the spectrum peaks in a certain range this might mean the instrumentation becomes saturated, which is reflected in the observed plateau.

[3] Hydrogen becomes molecular in the dustiest clouds and thus H I ceases to contribute to the column density. Additionally, the levelling off effect begins at $N_H = 4 \times 10^{21}$ cm^{-2} marking this as the start point of atomic–molecular transition.

The latter is the most likely and can be checked by focusing on the upper end of maximum extinction and seeing where these lie in relation to known molecular clouds. This is performed in Section 4.7.3.

I also measured the velocity of the peak emission finding this lies between the 40$^{\text{th}}$ and 60$^{\text{th}}$ channel (256–289 km s^{-1}), a range which got slightly narrower for higher extinction. To demonstrate this, I split the H I map into 8 extinction slices (using the ranges from Table 4.2) by using the maximum extinction calculated for Figure 4.13. For each slice I then calculate spectra by averaging the emission for each of the 120 velocity channels contained in each extinction slice. The resulting 8 spectra are shown in Figure 4.14. I see the distribution narrowing, the average grows and the peak of the graph tends to appear in slightly lower channels with increasing extinction, this is demonstrated with the FWHM and central peak plotted in Figure 4.14. This reinforces what can be deduced from Figure 4.13; for high extinction, the distribution narrows and a higher ratio of sources reach the plateau value.

4.7.3 Comparison with molecular clouds

In Figure 4.13 I saw that the observed H I started to level off after $N_H \simeq 4 \times 10^{21}$ cm^{-2} (i.e. saturation is sufficient to begin formation of H_2) and generally finished off around $N_H \simeq 6 \times 10^{21}$ cm^{-2} where in between is a mixture of H_2 and H I due to the transition being incomplete and observing some H I in front of the site of transition. Figure 1 of Schaye (2001) shows hydrogen column densities as a function of density and the fractions of H I and H_2 compared to the total hydrogen and the H_2 dominates this at $N_H \simeq 5.6 \times 10^{21}$ cm^{-2}. Figure 2 of Schaye (2001) shows the metallicity vs. total H I content and there is little change between Galactic and LMC metallicity.

The maximum total H emission map produced in Section 4.6.4 is used to identify potential molecular cloud regions. This is done by boxcar smoothing the data (to

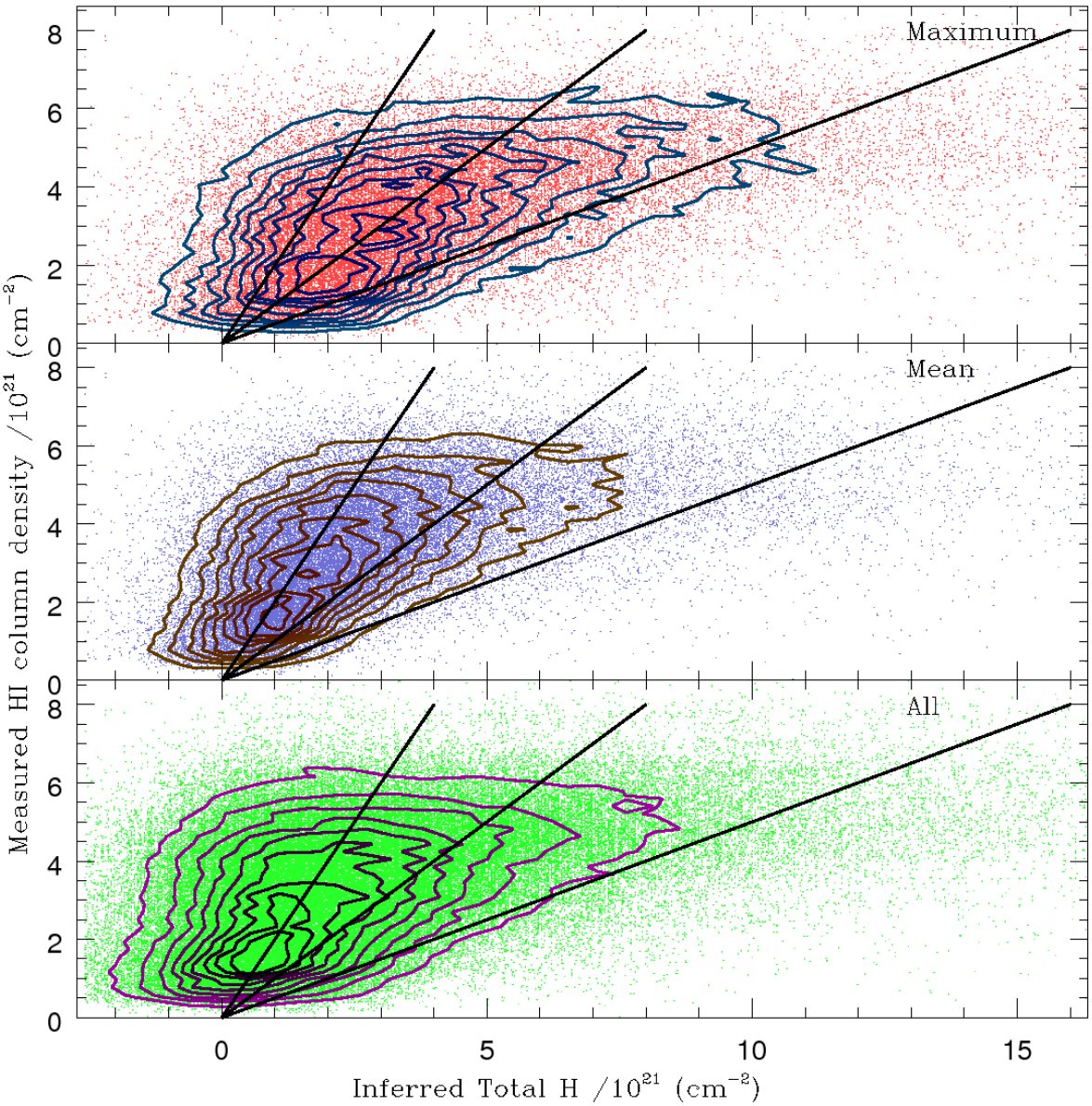

Figure 4.13: Measured H I column density vs. inferred total column density (converted from extinction). Points depict individual values, contours show increasing source density (10 levels ranging from 10%–100% of highest density for bin size of 2% × 2% for each axis length), darker lines are higher density. Lines show gradients of 2, 1 (i.e. $N_{\rm H} = N_{\rm H}$) and 0.5. Analysis excludes regions within detector 16.

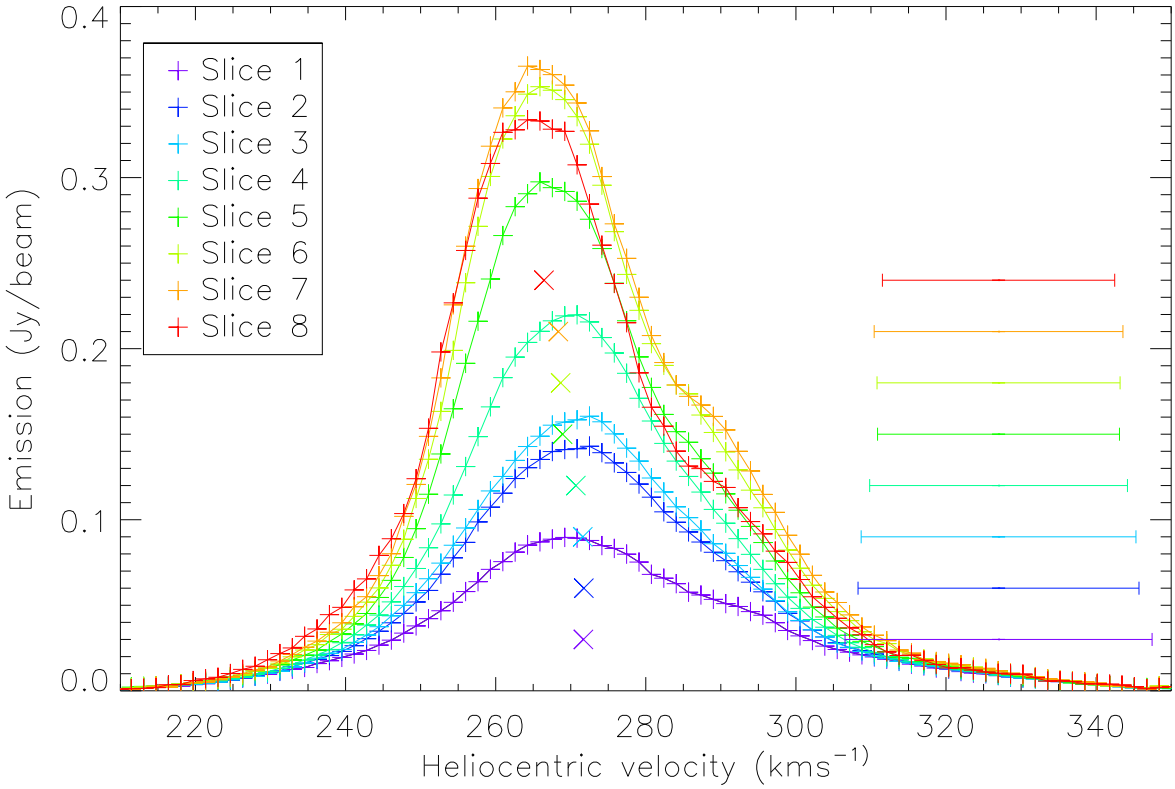

Figure 4.14: Mean H I emission for each velocity slice and extinction slice for mean extinction of each pixel. Extinction ranges of each slice are given in Table 4.2. Peak of emission tends slightly to higher velocity in early slices and distribution of emission narrows for highest extinction.

remove noise) and then applying a cut of $N_H > 8 \times 10^{21}\,\mathrm{cm}^{-2}$. This cut is required because only at high densities does hydrogen become molecular. I also look at sites where $N_H > 6 \times 10^{21}\,\mathrm{cm}^{-2}$ because I have seen the atomic–molecular transition to be largely complete at this level. These are then compared with identified molecular cloud sites from the literature obtained via a SIMBAD[9] query. A majority of these originate from the work of Fukui et al. (2008) (who used CO as a surrogate for H_2) who also provide size estimates. Figure 4.15 shows the map with these identified sites overplotted and their radii drawn where possible.

On the whole I find good agreement with increasing column density showing scaled reddening to be an effective tool for finding molecular clouds. However, it is not an absolute tool as I have regions of high density where there are no known nearby molecular clouds and a few regions in the North where Fukui et al. (2008) has identified clouds which I find to be below $N_H = 8 \times 10^{21}\,\mathrm{cm}^{-2}$. These regions are identified as LMC N J0532−6838, LMC N J0535−6844, LMC N J0532−6854 in table 1,3 of Fukui et al. (2008). They have fairly low CO luminosities. Also, one is a small cloud; LMC N J0536−6850, which Fukui et al. (2008) do not derive properties for.

When comparing the top–right panel of Figure 4.16 with Figure 4.15 I see that in some regions, where the H I emission levels off ($N_H > 11$ Jy beam^{-1}) does not correspond to molecular clouds sites. The North–East region (which is also a region of low RC star density; see top-middle panel of Figure 4.4) is one notable example.

4.7.4 Comparison with dust emission

Reddening is caused by dust in front of a star (dust extinction); a comparison between the extinction and emission may reveal the relative location of the stars and dust. A complicating, but in itself interesting factor is that reddening probes a very narrow column – a stellar diameter wide or 10^{-7} pc for a typical RC star – whereas the angular resolution of images is typically 0.1–10 pc at the distance of the LMC; com-

[9] `http://simbad.u-strasbg.fr/simbad/`

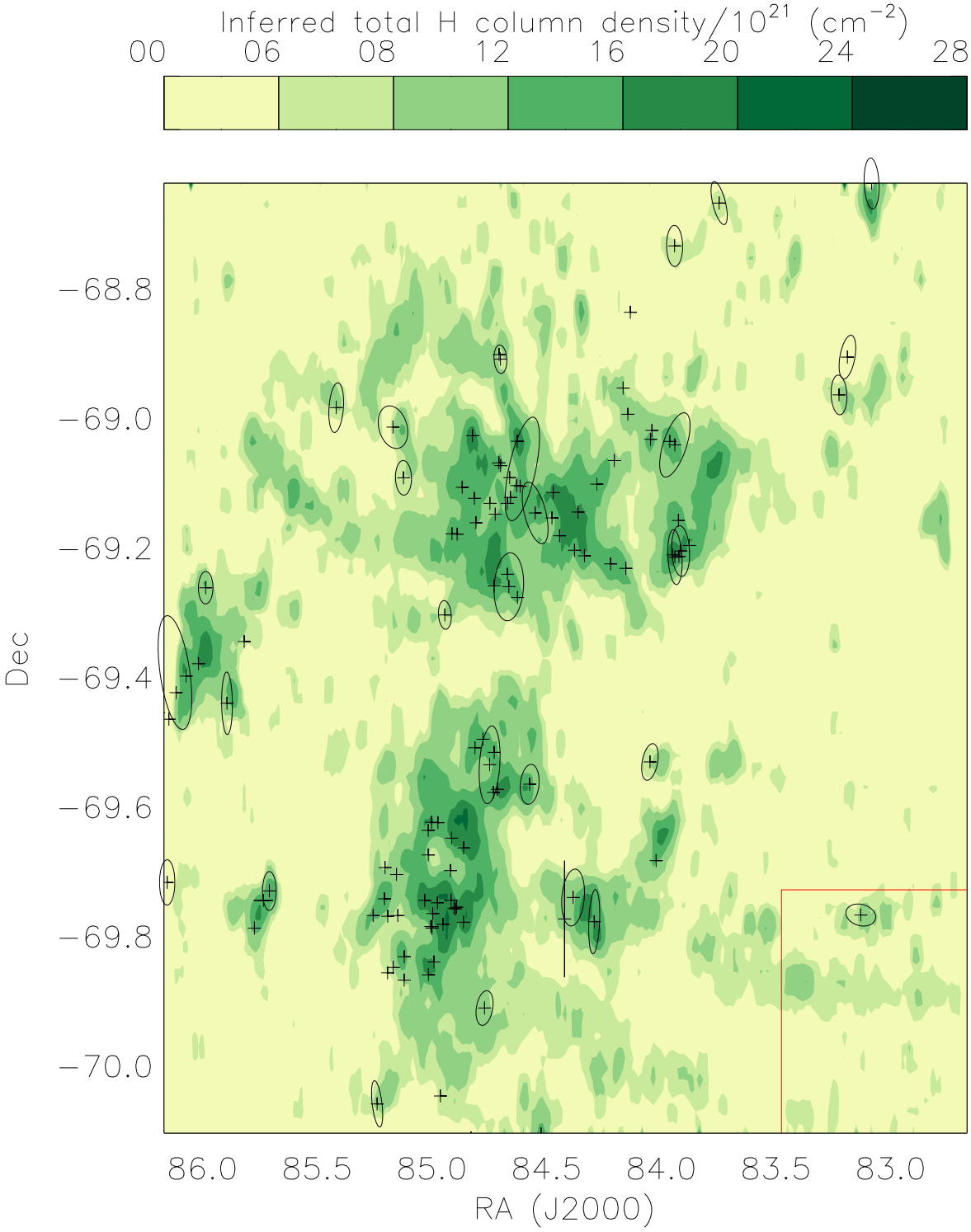

Figure 4.15: Smoothed total H column density map identifying regions where $N_H > 8 \times 10^{21}\,\mathrm{cm}^{-2}$. Plusses in black are molecular clouds identified in the literature with ellipses drawn where Fukui et al. (2008) estimate properties.

parison between reddening and emission maps can therefore reveal information about the smallest scales at which the dust clouds present structure.

To this aim I compare my extinction map with the Multiband Imaging Photometer for Spitzer (MIPS) maps from the Surveying the Agents of Galaxy Evolution (SAGE) survey (Meixner et al., 2006). SAGE is a uniform and unbiased survey of the LMC in the IRAC and MIPS bands of the Spitzer Space Telescope (covering a wavelength range of 3.6–160 μm). The MIPS data I am using are the 24 μm and 70 μm maps which have pixel sizes of $2\farcs49$ and $4\farcs80$, respectively. The 160 μm map is not used because the dominant foreground source (the complex Milky Way cirrus) has not been removed.

The shorter wavelength 24 μm data trace warmer and smaller dust grains while the longer wavelength 70 μm data trace larger, cooler dust grains. The maps being used have had the residual foreground and bright point sources removed.

Like in Section 4.7.2, I am comparing my extinction map to these emission maps in two ways. The first way is by obtaining the corresponding MIPS emission value for each of my RC stars (individual method) and the second way is by obtaining extinction over a range of MIPS pixels with means, modes and maximum values produced (group method). The pixel ranges chosen result in similar resolutions for both 24 μm and 70 μm data (see sections 4.7.4.1 & 4.7.4.2 for exact numbers).

For both methods I produce two diagrams with contour plots overlaid comparing emission (presented on a logarithmic axis due to the wide range of values) against extinction. The reason for overlaying contours is to identify where the majority of the data lies more easily and the significance of outliers is overestimated from looking at diagrams alone (because in high density regions sources heavily overlap, lowering their visual impact). The reason for two plots is that the second one applies boxcar smoothing with a filter size of 3 to the emission and extinction. The smoothing reduces noise and outliers. I also fit linear relations (emission increase per 0.01 mag of extinction increase) to the Maximum extinction.

For the group method I also produce maps of the comparison, for easier regional inspection of data and comparison with prior maps.

The average extinction is expected to generally increase with respect to emission. However, when it does not this either means that the star population lies in front of that traced ISM feature or the extinction sightlines miss the ISM because its structure is very clumpy. The maximum extinction values should show a tighter, more continuous correlation with surface brightness.

4.7.4.1 24 μm emission

The data I am using are the second MIPS data release from early 2008. For these data the individual MIPS observations were mosaicked to match the size and positions of the $1^\circ \times 1^\circ$ Spitzer InfraRed Array Camera (IRAC) tiles the SAGE programme also observed. MIPS tiles 22, 23, 32 and 33 contain the area of my extinction map. These tiles were cropped to only cover the areas within my extinction map. The emission range is much greater in the Eastern tiles than in the Western tiles (due to the Southern molecular ridge and 30 Doradus). However, the overall majority of the emission lies within a similar emission range for all tiles. For the second method each comparison pixel in my reddening map is equal to 13×13 pixels of the MIPS map making each of my comparison pixels sample a $32\farcs37 \times 32\farcs37$ region.

To account for the range of emission values for the map I define contour levels using a power law ($10^{x/5.6}$) rather than linear values. There are some gaps in the emission map arising from bright source subtraction leading to over subtraction in some regions (e.g. centre of 30 Doradus at RA= $84\fdg6$, Dec= $-69\fdg1$). The map is shown in the top–left panel of Figure 4.16 for the emission range of 1–2471 MJy sr^{-1}.

4.7.4.2 70 μm emission

For this wavelength I used the 2009 release of the full 70 μm mosaic containing the combined Epoch 1 and Epoch 2 data. This being a full mosaic, unlike the 24 μm data, all of the observing area is contained in a single combined file which I again cropped. However, the effects of detector variance are more visible in this format and at this

wavelength. These effects were the main reason for opting to apply boxcar smoothing to the group method described above.

With the second method each comparison pixel in my reddening map is equal to 7×7 pixels of the MIPS map (this was chosen due to the pixel count of the cropped MIPS map for this tile, also tested were 1×1, 2×2 and 14×14). This means the second method covers areas of $33\farcs6 \times 33\farcs6$.

Unlike the $24\,\mu$m data a linear emission scale of 15–315 MJy sr^{-1} with steps of 20 MJy sr^{-1} suffices for showing the data. This range allows the map shown in the top–middle panel of Figure 4.16 to cover approximately the same regions as the $24\,\mu$m map.

4.7.4.3 The comparisons

Note that the FIR emission is a combination of dust emissivity, $N_{\rm dust}$ and $T_{\rm dust}$ (via the Planck function) and $T_{\rm dust}$ will be higher and emission brighter in the immediate vicinity of H II regions.

The first comparison I perform is by directly looking at the reddening and the emission maps. These are shown in Figure 4.16. There is good correlation between emission peaks and high extinction. For example, the bright FIR emission around 30 Doradus[10] and the southern molecular ridge[11] is matched by high reddening. With regard to correlation between lower extinction and emission, the non-mapped emission regions (those with FIR emissions below 1 MJy sr^{-1} at $24\,\mu$m and below 15 MJy sr^{-1} at $70\,\mu$m) correspond to reddening slices 1–3[12].

However, there are two types of regional differences I observe; regions where high extinction is found but there is less emission and the opposite where strong emission is found without corresponding extinction.

[10] RA=84.°8, Dec=−69.°1
[11] RA=85.°0, Dec=−69.°75
[12] colour excess of $E(J-K_{\rm s}) \leq 0.105$ mag and $A_V \leq 0.605$ mag.

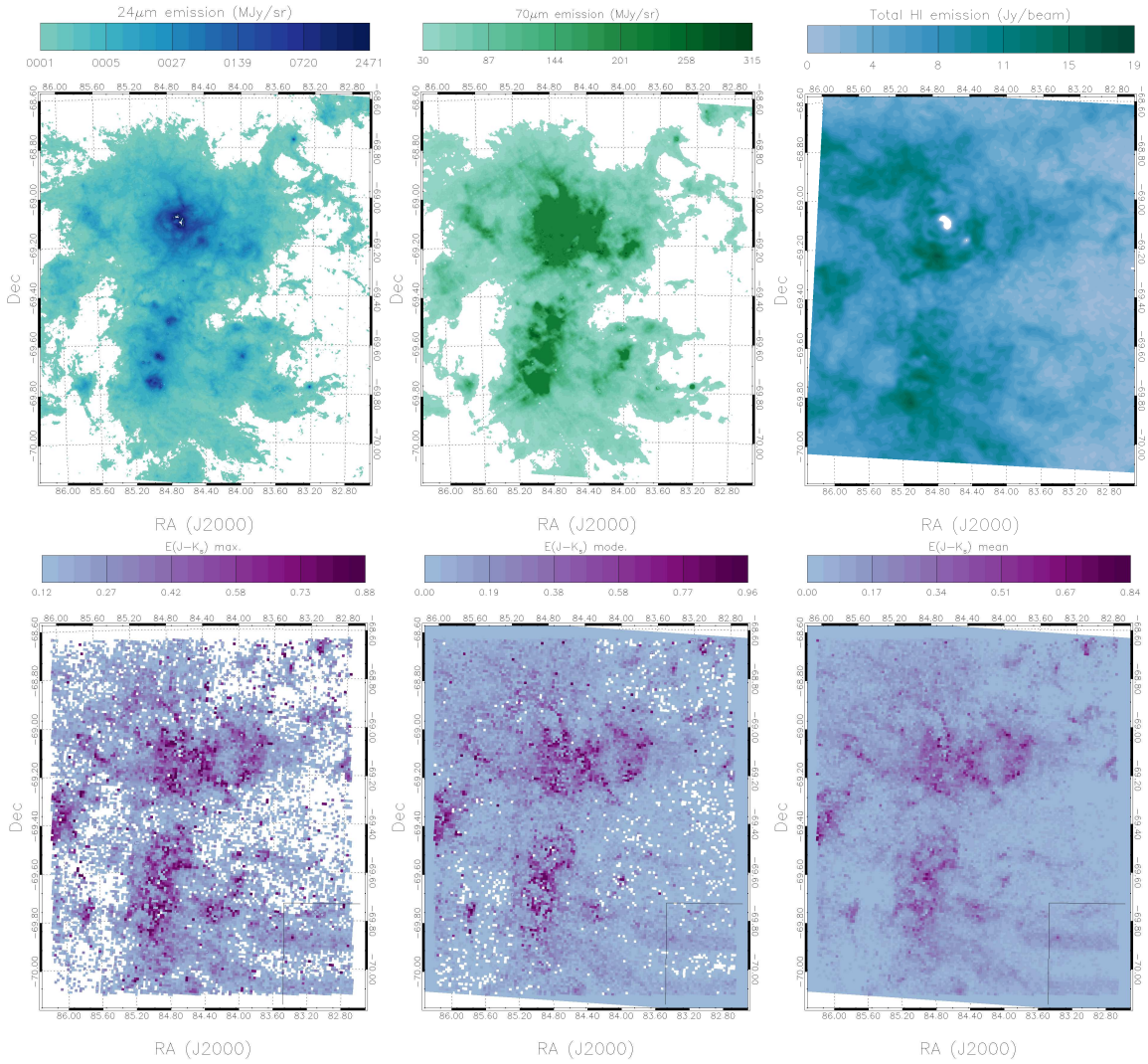

Figure 4.16: Top–left: The 24 μm FIR maps with emission scale of 1–2471 MJy sr^{-1}. Top–middle: The FIR 70 μm map with emission scale of 30–315 MJy sr^{-1}. Top–right: Total H I emission (Jy beam^{-1}). Sources outside stated limits are omitted from these maps. Bottom: The peak (left), mode (middle) and median (right) extinction map from my data for the tile using the group method. Sources outside of scale are omitted from these maps.

Two prominent regions with high extinction and less emission are found in the East[13] and a crescent West of R136[14]. If I assume the FIR emission source is the sole cause of extinction then this would mean that this emission has a much stronger effect in this region. A more likely explanation is that these are regions where the dust clouds have small scale structure that is diluted by the FIR emission, but revealed by the RC stars (I see this in all my reddening maps). When examining these regions in prior comparisons, I find optical extinction (in Figure 4.12) is around 60%–80% of the NIR extinction and the measured H I map (top–right panel of Figure 4.16) agrees with the eastern region but only the bottom half of the crescent. Interference patterns caused by the nearby 30 Doradus (evident from the ring like structure seen in the measured H I map) may be a possible cause. The Eastern region contains known molecular clouds (Figure 4.15) while the crescent region has molecular clouds in the top and bottom regions but not the middle. These molecular clouds regions were also based on the H I data.

Two examples of the opposite effect (bright FIR emission but lower extinction), are found around RA=83.°2, Dec=−69.°8 and RA=84.°0, Dec=−69.°6. These are fairly small structures (too small to be detected in the regions sampled in Figure 4.7). Also the narrow sightlines of the RC mean that compact clouds will not be reflected in extinction if there is not a RC star detected behind them and the likelihood of missing such clouds increases for smaller structures. Given the second region is only partially missed suggests this is the case. Finally, the first region also lies just within the detector 16 region (which as a whole does not correlate well with the features seen in the FIR maps).

Another comparison I perform is by comparing emission with extinction on a region-by-region and star-by-star basis (like was performed for the H I data in Section 4.7.2). To account for decreasing source density at higher emissions I plot emission on a logarithmic scale while the contours are plotted the same as in Figure 4.13 except the

[13]RA=86°, Dec=−68.°4
[14]RA= 84.°0, −69.°0 ≤Dec≤ − 69.°2

bin sizes now cover 1% of the x-axis range and 2% of the y-axis range. For the group methods I plot linear fits (which appear curved due to log scale) for each comparison where the gradient is twice as steep for the mean comparison as it is for the maximum, accounting for the fact that on average half of RC stars are in front of the dust. These comparisons exclude sources from within the detector 16 region and regions where there is zero or negative emission (caused by bright source subtraction). I supplement each comparison with a boxcar smoothed version.

Figures 4.17 and 4.18 compare the 24 μm and 70 μm emission to the $E(J - K_s)$ extinction. The individual methods in the bottom panels consistently show low source density ($< 10\%$) above $E(J - K_s) = 0.3$ mag. A tail of sources around 10 MJy sr^{-1} is seen above $E(J - K_s) = 0.5$ mag in the 24 μm emission. The 70 μm emission distribution is similar to the H I (Figure 4.13) with high emission found for much of the extinction range.

I see for the group methods that the chosen linear fits fit the contour ranges well. However I should focus on where this is not the case because this can help us identify regions of interest. In general these regions are more common in the 24 μm emission than in the 70 μm emission.

I have mapped some of these regions in Figure 4.19. The extinction vs. emission ranges depicted in each colour are shown in the panels adjacent to the maps in the figure. Regions below the linear fit line represent where the emission does not detect the effects seen in reddening while above the linear fit is where RC stars do not probe this. I notice the H II regions where massive hot stars lie are responsible for the strongest emission (much stronger than a linear increase would suggest). The heat produced by these stars have the greatest effect on the small dust grains (probed by the 24 μm emission) and this effect does not lead to reddening increases on the same scale which is why these regions are brighter in the 24 μm emission. Regions with very low emission compared to maximum extinction (shown in magenta) are scattered around the tile edges at 24 μm but at 70 μm they generally outline the warm H II regions suggesting the two are linked. The fact the maximum extinction is greater also, suggests the dust content is structured on smaller scales in these regions; this is backed by this not

being observed for the mean. Alternatively, the radiation field from the H II emission affects the 24 μm emission more greatly (which is seen by the larger green regions). The regions where there are linear tails in the emission (blue selection) are found in the 24 μm emission around the previously mentioned crescent and Eastern regions of high emission and lower extinction. In the 70 μm these tails surround the H II regions instead. These tails are evident in the mean so effects in these regions are affecting some or most of the RC stars suggesting this dust content belongs to a larger structure. These observations suggest the dense dust is found around the H II regions (and it may be that I am unable to probe the highest extinction of these regions, which explains why the reddening appears smaller) with the density decreasing around them but having small-scale structure.

However, it should be considered that dust grains can have their radii and emissivity modified from being coated by other elements causing their extinction law to change. When this occurs this can lead to an overestimate of the column density and thus, an apparent non-linear increase with respect to reddening such as seen with the H_2O ice (Oliveira et al., 2009). I did observe a non-linear increase to the 24μm emission, though this can be attributed to heating which makes ice grains an unlikely candidate. Even so, the reddening, as expected, is not exclusively caused by a single form (composition, size and temperature) of dust grain.

4.7.5 Reddening around R136

In Section 4.4 and in Figure 4.5, I noticed that RC stars were lacking within the R136 region. In this subsection I explore making use of other stellar tracers to complement the extinction map for this region.

In Section 4.4 I noticed a high density of stars around the R136 region in the CMD selection brighter than $K_s = 16.5$ mag (a CMD range which I defined as being of intermediate age). In the CMD shown in Figure 4.20 I focus on this part of the CMD, ignoring the RGB. The sources around R136 (in burgundy) are mainly found at $(J - K_s) \simeq 0.2$ mag (much bluer than the RGB) and resemble the reddened population

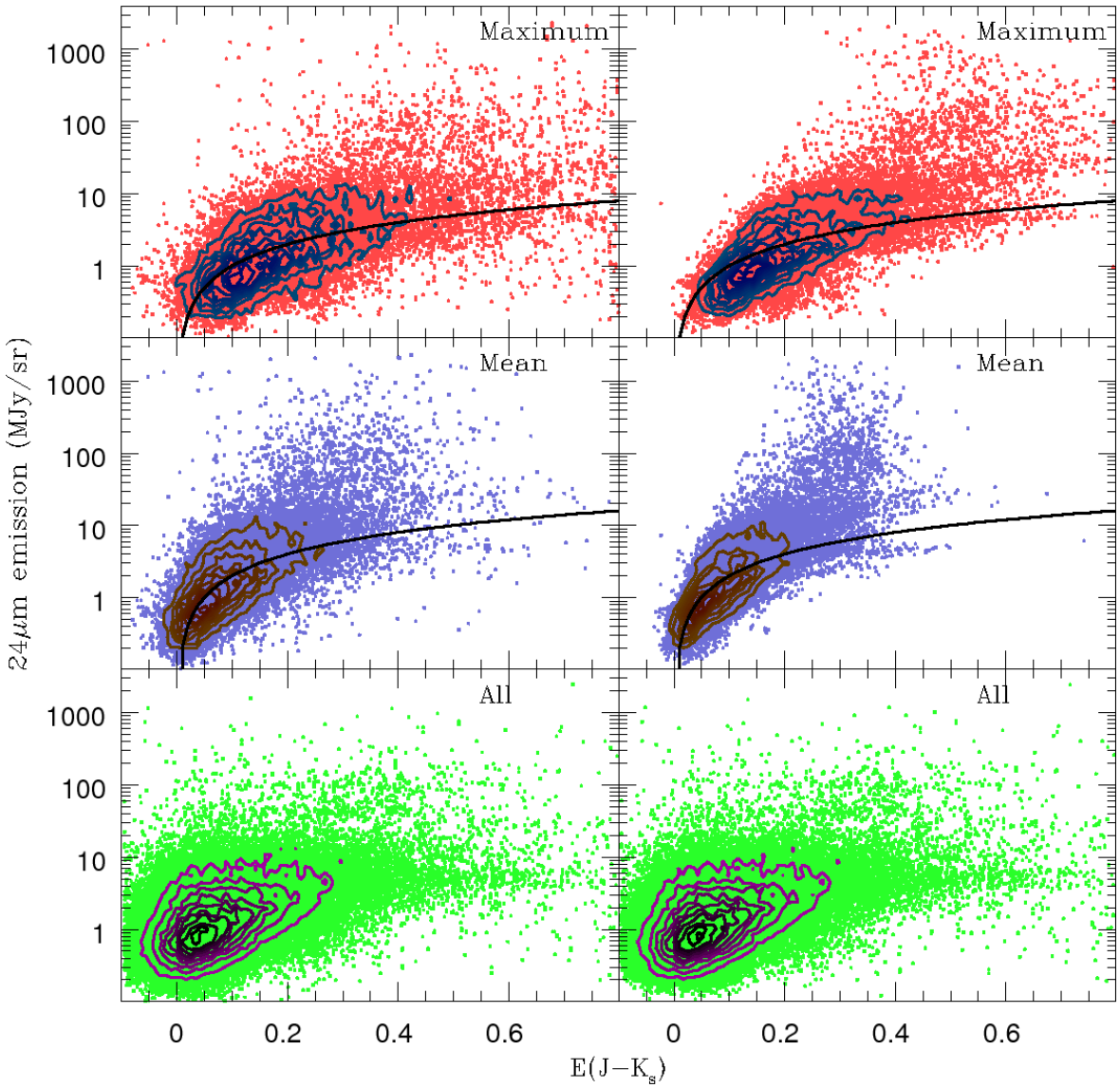

Figure 4.17: 24μm emission vs. $E(J-K_{\rm s})$ extinction for individual method (bottom) and group method means (middle) and maximum (top). Contours represent increasing source density. Right panel applies boxcar smoothing to the data. The linear fits applied are: Emission= $20 \times E(J-K_{\rm s})$ MJy sr^{-1} to the mean and Emission= $10 \times E(J-K_{\rm s})$ MJy sr^{-1} to the maximum.

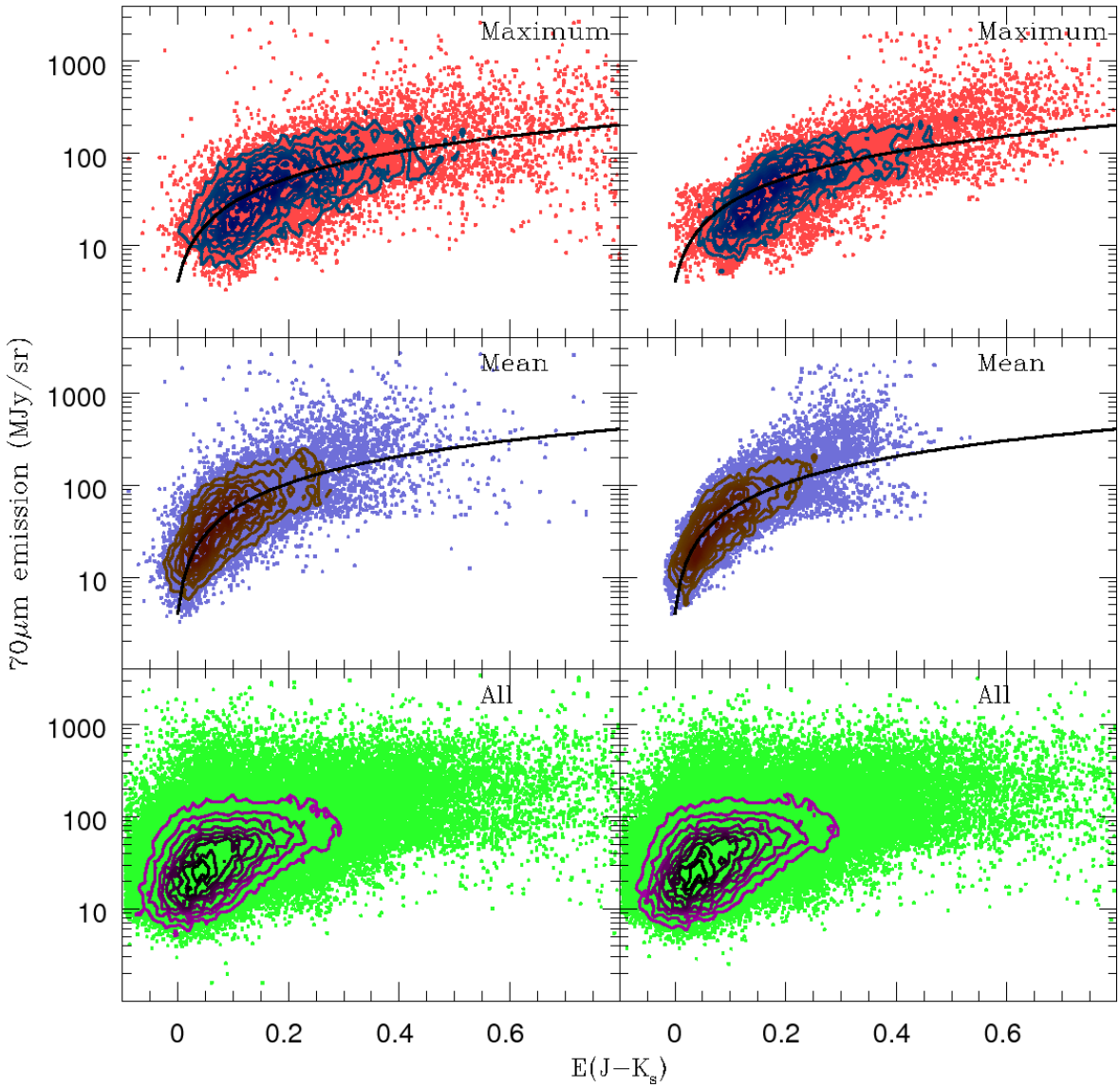

Figure 4.18: 70μm emission vs. $E(J-K_{\rm s})$ extinction for individual method (bottom) and group method means (middle) and maximum (top). Contours represent increasing source density. Right panel applies boxcar smoothing to the data. The linear fits applied are: Emission= $(500 \times E(J-K_{\rm s})+4)$ MJy sr^{-1} to the mean and Emission= $(250 \times E(J-K_{\rm s})+4)$ MJy sr^{-1} to the maximum.

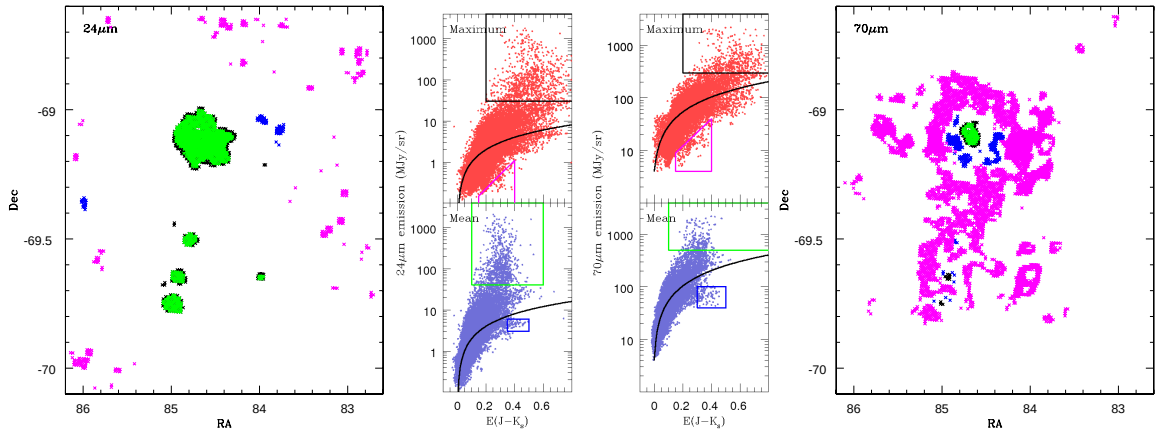

Figure 4.19: Regions of higher and lower than linear increase in emission for 24 μm (left) and 70 μm (right). Smoothed emission vs. $E(J-K_{\rm s})$ with selection regions outlined are shown in adjacent panels. Green selection largely overlaps black selection.

of young sources (in grey) at $(J-K_{\rm s}) \simeq 0$. The histograms in Figure 4.20 show that the magnitude of stars around R136 follows the same pattern as the rest of the tile. The colour on the other hand, is offset confirming the earlier observation.

This offset can be used to estimate the intrinsic colour of the population by assuming that the bulk of the population in the tile is not affected by reddening and so adopting a baseline colour of $(J-K_{\rm s}) = -0.115$ mag. However, as this is estimated from the CMD it is affected by foreground Galactic extinction and so to account for this I must also subtract this, $\Delta(J-K_{\rm s}) = 0.04$ mag, finding an intrinsic colour[15] of $(J-K_{\rm s})_0 = -0.155$ mag.

The reddening I can probe using these stars is limited to $A_V \simeq 2.9$ mag due to contamination from the redder supergiant and RGB populations. However, this should be sufficient for R136 itself as it is not highly reddened (although its surroundings are). I use the reddening to firstly, contrast the effect reddening has on young and intermediate aged populations, and secondly, better examine this region as the young population gives use more coverage in the centre compared to the RC stars.

[15]Note that isochrone tracks (including version 2.4 of the Padova isochones, Bressan et al. 2012) do not cover this region of the CMD.

Table 4.5: Mean and median reddening for R136 selection and RC stars.

Selection	$E(J-K_s)$ (mag)	
	Mean	Median
R136	0.288	0.280
RC	0.297	0.271

The reddening map I produce is shown in Figure 4.21 with the R136 selection plotted as squares (left panel, total 407 sources) and the RC stars plotted as circles (right panel, total 500 sources). I use the same scale as Figure 4.5. Distribution-wise the younger population is found more towards the centre than the RC stars and the reddening probed is slightly lower but covers a narrower range. The mean and median reddening (given in Table 4.5) are very similar for the two populations (with a difference of around 0.01 mag). The larger mean in the RC stars and hence the larger difference between the mean and median is due to the RC stars probing a larger extinction range.

Another comparison that can be made is with the Diffuse Interstellar Bands (DIBs) analysed in van Loon et al. (2013). They have compared DIB equivalent widths (combining the Galactic and LMC components) to A_V measured from the Very Large Telescope Flames Tarantula Survey (VFTS) sample (which mostly contains O- and B-type stars). This is shown in Figure 14 of van Loon et al. (2013) (hereafter, Figure vL). I compare the DIB equivalent widths with the reddening of my younger (R136) and intermediate (RC) aged star populations. For my younger selection, I select stars within a $1''$ radius and $5''$ radius, averaging extinction where there is more than 1 star. I also do the same for the RC, but due to fewer stars I have to use radii of $5''$ and $15''$ instead. Figure 4.22 shows the results of DIBs 4428Å and 6614Å equivalent widths (with Galactic and LMC components combined) with wider radii points plotted in green and red (for young and RC stars respectively) and the smaller plotted in black and grey (for young and RC stars respectively). The point sizes are based on number of sources within radii (larger radii contain more sources) where green points use a smaller scale than black points.

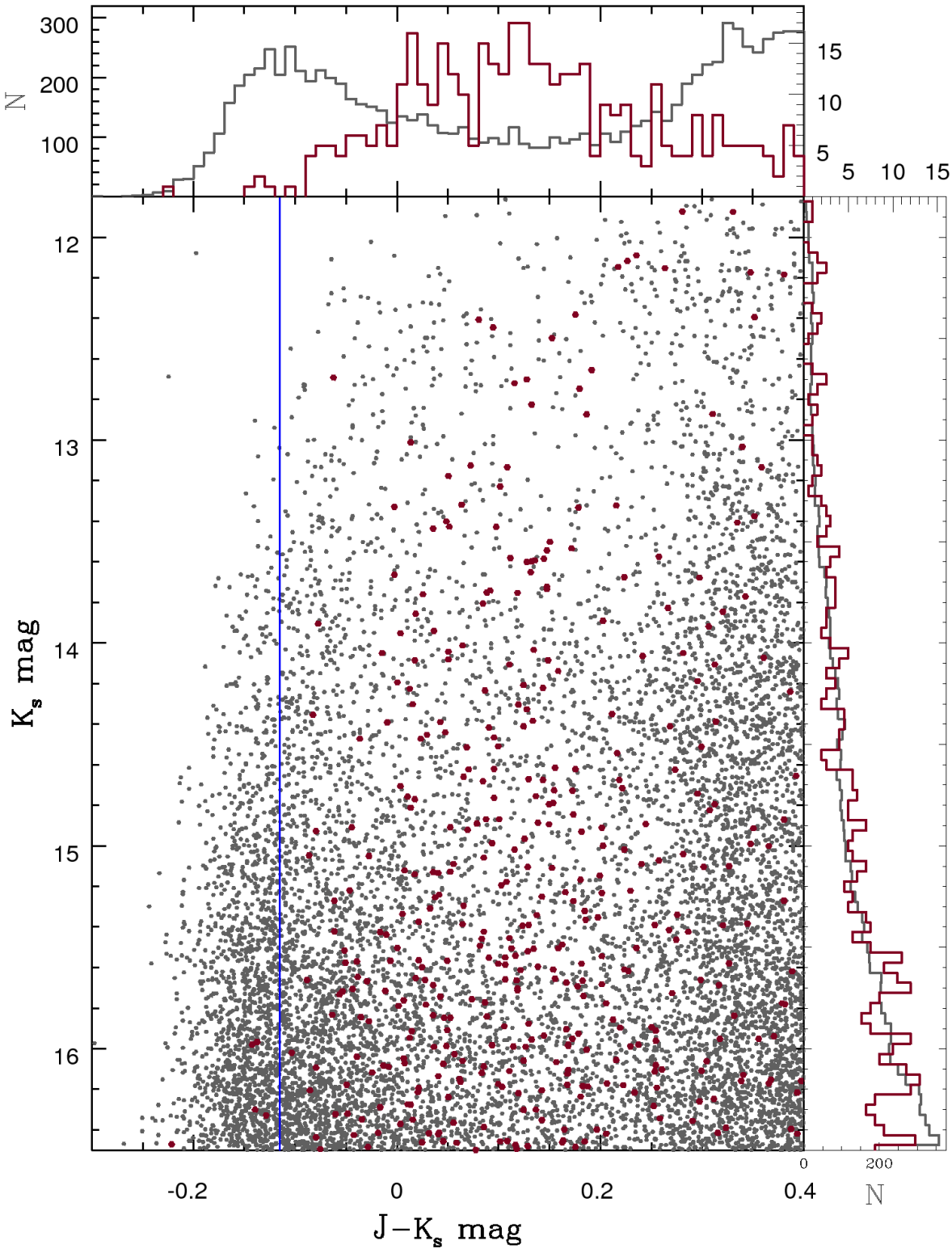

Figure 4.20: CMD of all stars (grey) and stars around R136 (burgundy). Also plotted are histograms of colour and magnitude (bin sizes are the same as used in Figure 4.2). Magnitude distribution is similar for both sets. Colour distribution shows an offset of $\sim$ 0.2 mag in the R136 region indicating reddening. Vertical blue line at $(J - K_s) = -0.115$ mag is the baseline colour.

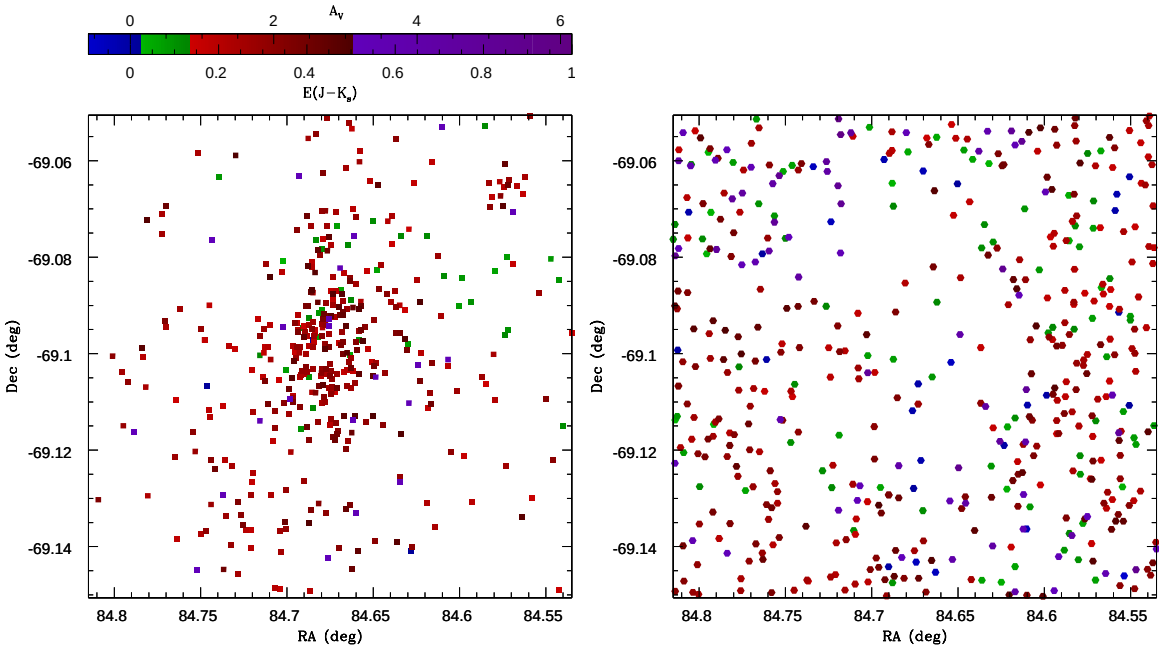

Figure 4.21: Reddening map of R136 region using CMD selection from Fig. 4.20 (left, squares) and RC stars (right, circles). The reddening scale is consistent with Figure 4.5.

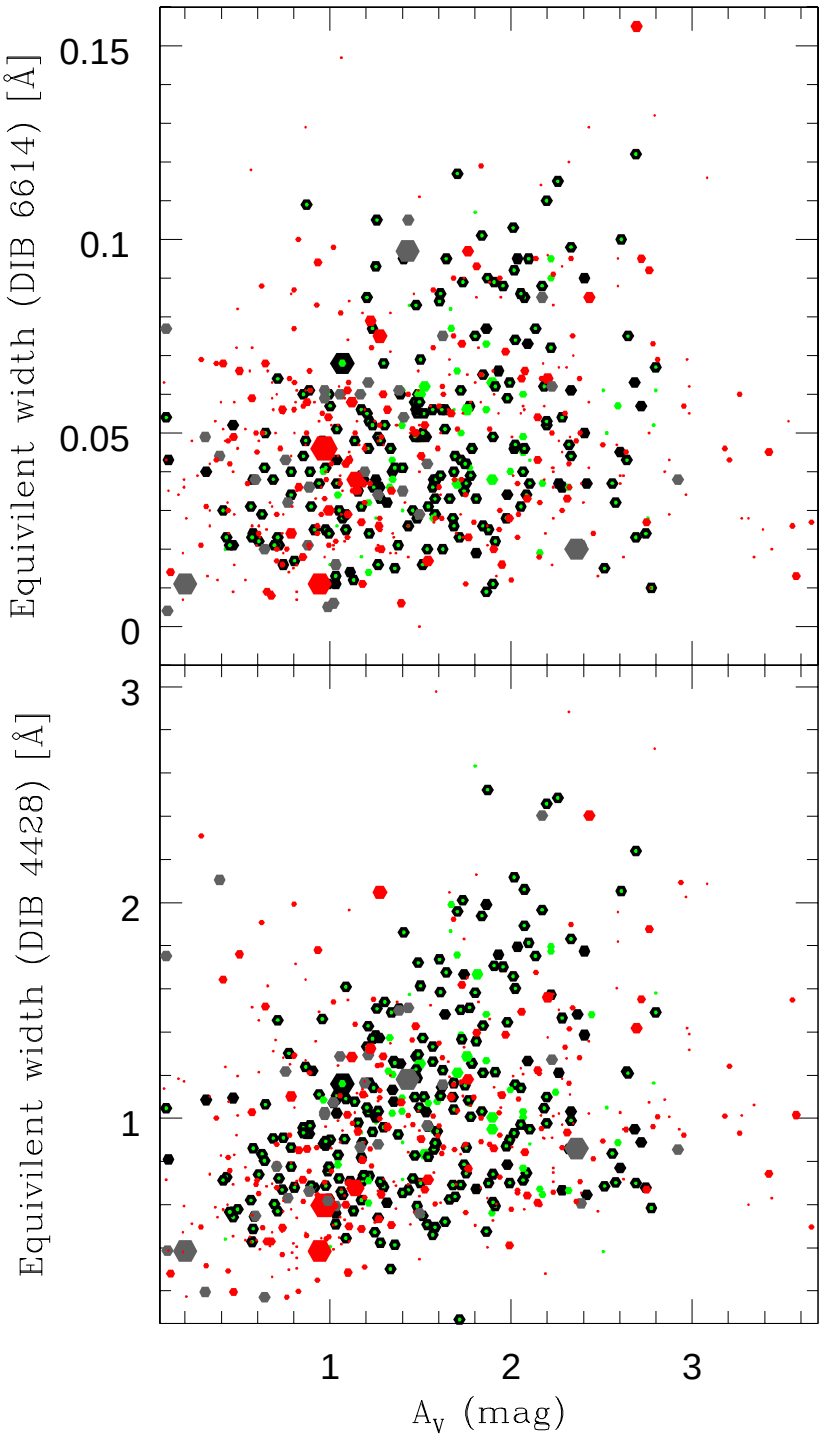

Figure 4.22: O- and B-type star DIB 6614Å (top), DIB 4428Å (bottom) equivalent widths (Å) vs. average extinction (A_V, mag) of nearby young stars and nearby RC stars. Average extinction of young stars within 1″ and 5″ are shown in black and green. Average extinction of RC stars within 5″ and 15″ are shown in grey and red. Greater number of stars in selection is depicted by larger points. Green and red points use smaller scale than black points and grey points.

Comparing Figure 4.22 to Figure vL I notice both plots have a lot of scatter and also the A_V range probed by the young stars is slightly smaller. The RC stars on the other hand are even more scattered. Looking at the data extremes and best fit of Figure vL and young stars, there is great similarity in the data range and the best fit up to $A_V = 2$ mag but after that my data becomes a bit narrower and steeper in comparison. This may be due to drop-off from a lack of sources. However, this steeper gradient suggests the young stars lie further behind the dust than the O- and B-type stars. The RC stars cover a wider extinction range and similar emission range. This suggests their population is more mixed with regards to position in dust. However what occurs at the high and low ends of extinction is interesting. At high extinction I see the DIBs are weak and there are few RC stars. These RC stars may be seen behind dense structure while the OB stars are seen though less dense structure. At low extinction I see more RC stars where a few regions have strong DIB absorption which suggests that these RC stars are in front or in between the bulk of the dust.

This subsection shows that it is possible to supplement the RC sample with other stellar populations within some regions. However, different populations probe the ISM differently and have different spatial positions in relation to the ISM.

5 Structure of the Large Magellanic Cloud

The Magellanic Clouds we see today are a result of star formation, stellar evolution and internal dynamics within them, their interactions between each other and the Milky Way. By studying their structure we can understand their past and study the evolution of galaxies. For instance, in both the LMC and SMC, warps are seen in the peripheral fields as a result of tidal interactions. In the LMC there is also the matter of the position and orientation of the central LMC bar region. This chapter focuses on the LMC and Chapter 6 examines the SMC. For both, I use the RC stars to present reddening maps, line-of-sight depth maps, least-squares fitted plane solutions and residual maps created from these solutions. These are then analysed and placed in context of the existing literature.

With the reddening map produced, dereddening is possible (which is not only an important preparation step for fitting a plane but also capable of producing interesting results in its own regard). These reddening maps and dereddening are applied to other parts of the Magellanic system.

The observation status of the VMC survey is sufficient to probe the structure of the LMC and SMC. The VMC data used here are the VSAv20170109 release and comprise 49 usable tiles from the LMC (out of a total area of 68 tiles). A tile is defined as usable when it has at least one epoch which has been observed in the Y, J and $K_{\rm s}$ bands and a source is defined as usable when it has the three aforementioned photometric bands present. Figure 5.1 shows a map of the LMC using the RC stars. The green density contours outline the LMC bar and the yellow density contours show the inner LMC region.

5.1 Reddening map and dereddening

The method of selecting RC stars from Section 3.1 was repeated for all usable tiles in the LMC. This was done for the $K_{\rm s}$ vs. $Y - K_{\rm s}$ CMDs due to lower extinction ranges

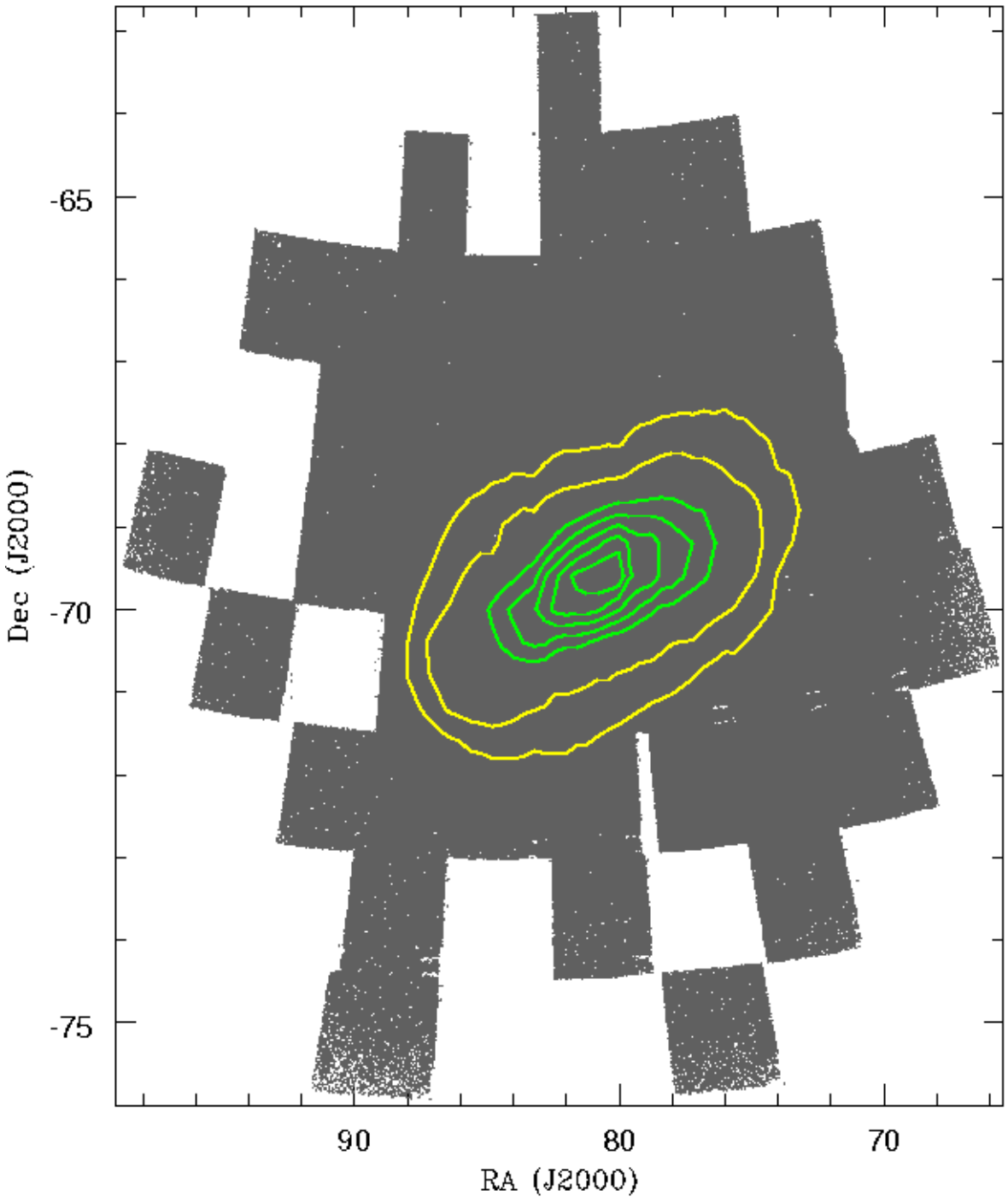

Figure 5.1: Map of the LMC from RC stars. Overplotted are density contours for 20%, 30% (yellow) and 50%–100% (green) with steps of 10%.

and because of problems with the J band caused by variable seeing as described in Section 2.4.2.2. The Y band calibration problems (present in earlier VMC datasets) had also been resolved at this time.

Table 5.1 contains information on the VMC tiles used including their central RA and Dec, total number of sources in tile, total number of sources used in RC star selection, contour peaks (for magnitude and colour), mean, standard deviation and median for colour.

Table 5.1: List of LMC tiles used and properties.

Tile	RA	Dec	Sources		Contour peak	Mean	SD	Median
	°	°	Total	RC	K_s	$Y - K_s$		
2_4	76.18	−75.08	249884	10728	16.95	0.88	0.898	0.054	0.892
2_7	88.94	−75.15	238264	9101	16.85	0.90	0.911	0.079	0.904
3_3	73.00	−73.47	331472	16062	16.95	0.91	0.911	0.053	0.907
3_5	80.68	−73.72	366330	16005	16.95	0.90	0.921	0.062	0.915
3_7	88.47	−73.70	244322	13124	16.85	0.91	0.918	0.056	0.912
4_2	70.38	−71.82	386197	20299	16.95	0.93	0.931	0.067	0.926
4_3	73.83	−72.03	489801	23615	16.95	0.92	0.928	0.066	0.920
4_4	77.35	−72.18	388106	25849	16.95	0.89	0.907	0.063	0.901
4_5	80.92	−72.27	592720	43961	16.95	0.89	0.907	0.066	0.902
4_6	84.50	−72.29	536627	39405	16.90	0.92	0.917	0.059	0.913
4_7	88.08	−72.25	428366	21152	16.90	0.91	0.910	0.058	0.905
4_8	91.64	−72.14	308811	12955	16.85	0.90	0.905	0.056	0.898
5_1	68.18	−70.14	250034	9762	16.95	0.91	0.923	0.054	0.916
5_2	71.33	−70.40	518282	26359	16.95	0.94	0.934	0.060	0.930
5_3	74.55	−70.59	656730	52369	16.95	0.92	0.923	0.073	0.918
5_4	77.82	−70.73	774182	87763	16.95	0.91	0.921	0.068	0.914
5_5	81.13	−70.81	780610	122027	16.90	0.93	0.945	0.091	0.935
5_6	84.45	−70.83	708732	137616	16.90	0.94	0.978	0.117	0.963
5_7	87.77	−70.79	732211	77502	16.90	0.91	0.946	0.112	0.927
5_9	94.33	−70.54	219882	12319	16.85	0.89	0.893	0.064	0.887
6_1	69.21	−68.73	317892	15796	16.95	0.90	0.897	0.062	0.891
6_2	72.16	−68.97	695857	42747	16.95	0.95	0.972	0.088	0.958
6_3	75.18	−69.15	778595	107902	16.95	0.95	0.936	0.071	0.931
6_4	78.23	−69.28	842559	197753	16.95	0.98	1.011	0.105	0.999
6_5	81.32	−69.35	884275	236207	16.95	0.95	0.981	0.128	0.966

Continued on next page

Table 5.1: List of LMC tiles used and properties.

Tile	RA	Dec	Sources		Contour peak	Mean	SD	Median
	°	°	Total	RC	K_s	$Y - K_s$		
6_6	84.42	−69.37	704422	127614	16.90	1.00	1.087	0.184	1.050
6_7	87.51	−69.34	629937	53277	16.85	0.97	1.021	0.134	0.993
6_8	90.59	−69.25	403643	16595	16.80	0.88	0.894	0.061	0.888
6_10	96.63	−68.90	159590	8838	16.8	0.87	0.880	0.058	0.874
7_2	72.90	−67.53	563241	33379	16.90	0.90	0.927	0.089	0.911
7_3	75.73	−67.70	633370	62387	16.90	0.91	0.949	0.098	0.931
7_4	78.60	−67.83	624773	70233	19.90	0.93	0.963	0.099	0.946
7_5	81.49	−67.90	567419	59241	16.85	0.94	1.024	0.136	0.991
7_6	84.40	−67.91	511041	46672	16.85	0.93	0.959	0.120	0.935
7_7	87.30	−67.88	532570	28105	16.80	0.88	0.938	0.116	0.909
7_8	90.19	−67.79	235996	17068	16.80	0.88	0.884	0.062	0.877
8_2	73.55	−66.10	405168	20953	16.90	0.87	0.913	0.107	0.891
8_3	76.22	−66.26	570278	29510	16.85	0.90	0.897	0.073	0.892
8_4	78.93	−66.37	486362	29853	16.85	0.89	0.916	0.093	0.900
8_5	81.66	−66.44	561568	30978	16.85	0.91	0.943	0.121	0.912
8_6	84.39	−66.45	461999	25326	16.80	0.90	0.934	0.112	0.910
8_7	87.13	−66.42	213846	19526	16.80	0.87	0.870	0.070	0.864
8_8	89.85	−66.34	408537	15696	16.80	0.88	0.862	0.059	0.859
8_9	92.54	−66.21	123636	13959	16.80	0.86	0.866	0.071	0.858
9_3	76.67	−64.81	356421	12779	16.90	0.84	0.851	0.073	0.842
9_4	79.23	−64.92	279019	16910	16.85	0.86	0.866	0.070	0.860
9_5	81.81	−64.98	215896	17827	16.85	0.88	0.876	0.067	0.869
9_7	86.98	−64.96	449803	15304	16.80	0.86	0.873	0.061	0.866
10_5	81.95	−63.52	327612	10361	16.85	0.86	0.864	0.064	0.856

There is an 0.15 mag range seen in the values of the K_s contour peaks and this follows a North to South pattern (where regions in the North are brighter than those in the South). The colours themselves, however, follow a different pattern becoming redder with increasing numbers of sources and proximity to the centre of the LMC.

Figure 5.2 shows the reddening map of the entire LMC in the $E(Y - K_s)$ scale; A_V values are provided and are converted using the same method used in Appendix

A.1.3. The green sources comprise the range covering 50% of the sources centred on the median where blue is lower than this, red higher and purple extremely high. Of note is that due to the rendering of the graphics there is visually a bias towards the highest reddening because these are drawn last. There is unfortunately a coverage gap between tiles 4_4 and 4_5 (around RA= 79.°14, Dec= $-71.°5$ to $-73°$) relating to tiling issues mentioned in Chapter 2.4.1.2.

The varying effects of detector 16 are clearly visible in many of the tiles as streaks of higher extinction and reduced coverage. While the highest extinction is mainly seen around 30 Doradus (tile 6_6; RA= 84.°4, Dec= $-69.°4$) the 6_5 and 5_6 tiles adjacent to it (around RA= $81° \,\&\, 86°$, Dec= $-69 \,\&\, -71°$, respectively) are also of interest.

5.2 Regional census

From what Table 5.1 has shown and the literature, one of the features present within the LMC should be a clear distance modulus gradient from North to South. A preliminary method to explore this structure is to use regional census by examining the RC sample only and assuming that the median is representative of the average RC star within regions binned of a certain size. Stellar density is important to account for because there are great variances in the LMC. The easiest consideration to make for this is to use density to determine the sizes of sub-regions. This was achieved by defining a cropped CMD of $K_s = 16$–18 mag (a range that more than sufficiently covers the RC range) and requiring each sub-region to contain 800–3800 sources where each sub-region is sized from $1° \times 1°$ down to $0.°15 \times 0.°15$ (in $0.°05$ increments). The range and bin sizes make it possible for sub-regions to overlap and lie on top of each other so the selection of sub-regions is truncated, removing any whose centre overlaps with another sub-region. Before truncation, there are 6893 sub-regions and after truncation, 2298 sub-regions. 1100 of these are defined as the 'inner' based on proximity to the LMC centre with the remaining 1198 classed as 'outer'. The inner sub-regions are no larger than $0.°25 \times 0.°25$ and lie within the 20% contour Eastward of RA= 77° and the 30% contour Westward

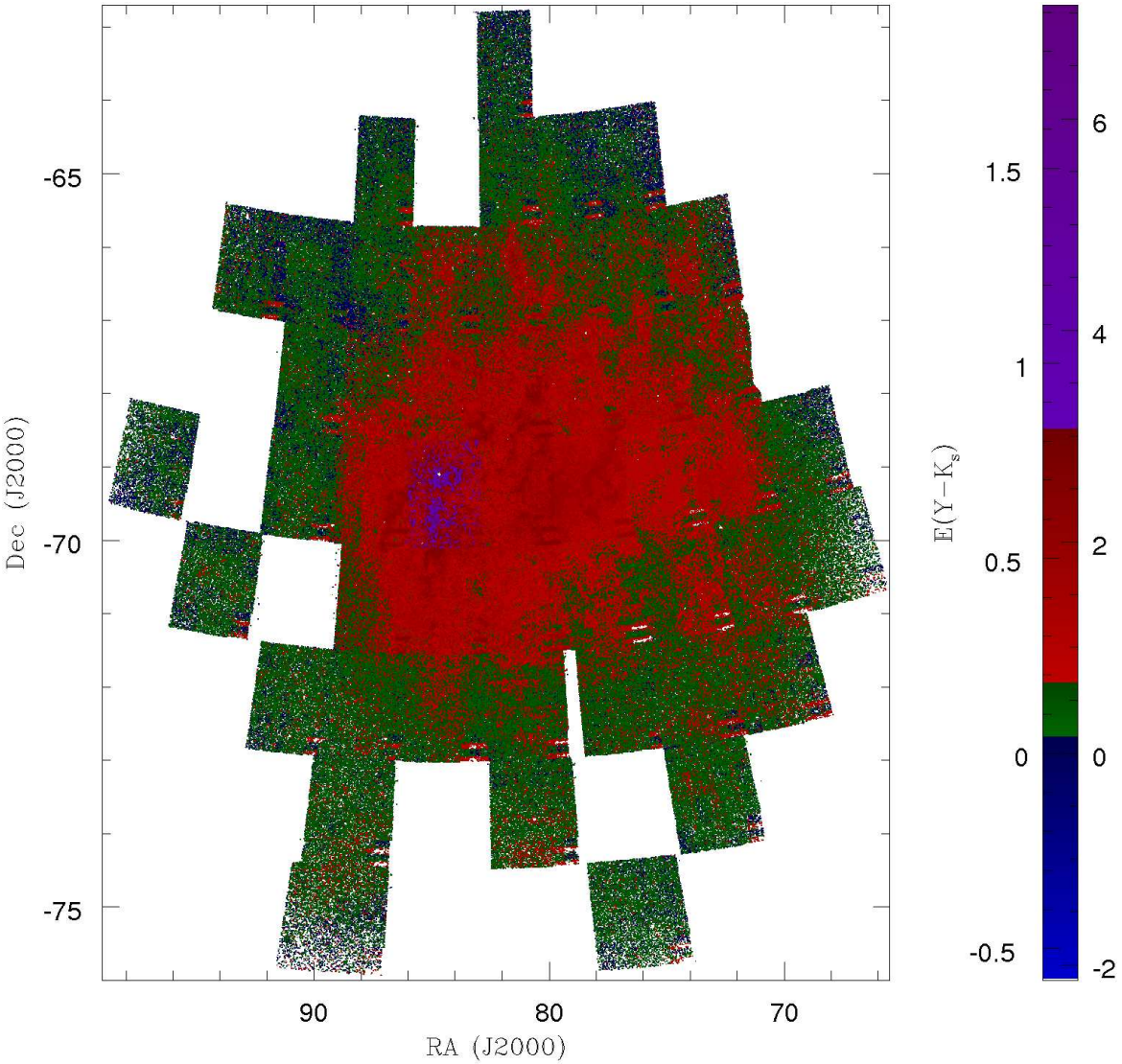

Figure 5.2: Reddening map of the LMC in $E(Y - K_s)$ (shown in legend, right axis shows A_V values) from RC stars. The green sources comprise the range covering 50% of the sources centred on the median where blue is lower than this, red higher and purple extremely high.

of RA= 77°. The outlines of these sub-regions after truncation are shown in Figure 5.3. For each sub-region the median $Y - K_s$ colour (before dereddening), median K_s

magnitude (both before and after dereddening) and contour peaks (after dereddening) are calculated. These are shown in Figure 5.4.

I see clearly in Figure 5.4 that the magnitudes dim towards the South–West and the 30 Doradus region before removal of extinction. The latter can be attributed to the effects of extinction (especially when coupled with the redder colours found there). The high extinction region of 30 Doradus was studied in more detail within Chapter 4. After removing extinction (using the procedure carried out in Section 3.2.3) this effect remains; in the case of the South–West corner this is unsurprising as it clearly is further away from us than the North–East corner. However, 30 Doradus still appears to lie further away to a small extent – which is unexpected. Using $K_{\rm s}$ mag contour level peaks instead of the median still illustrates the trend towards the South–West but narrows the magnitude range involved.

The median $Y - K_{\rm s}$ mag colour reveals an important region around tiles 6_5 and 5_5 (around RA= 81° & 83°, Dec= -69 & -71°, respectively). This is part of the LMC bar but appears to be bluer than the adjacent parts of the bar (mainly comprising the rest of tile 6_5). This discontinuity is contrary to the continuous distribution seen in the reddening maps but is in agreement with the ISM features. For example this is characterised by weak mid-IR emission (Figure 3 of Meixner et al. 2006) for the aforementioned region. This suggests a small subset of sources in this region are highly affected by reddening. A reason for this could be if they were located in the main body of the LMC behind a gas or dust feature where the majority of the sources would be part of the LMC bar in front of this and not be affected.

5.2.1 30 Doradus

With reference to Figure 5.4 the 30 Doradus region (RA= $84.^\circ4$, Dec= $-69.^\circ4$) bucks the trend of the South–West of the LMC being further away than the North–East by being dimmer (and further away) than that South–West region and this persists to a small extent even after dereddening (as seen in the top–right panel of Figure 5.4).

I investigated whether the larger reddening range in 30 Doradus (from its selec-

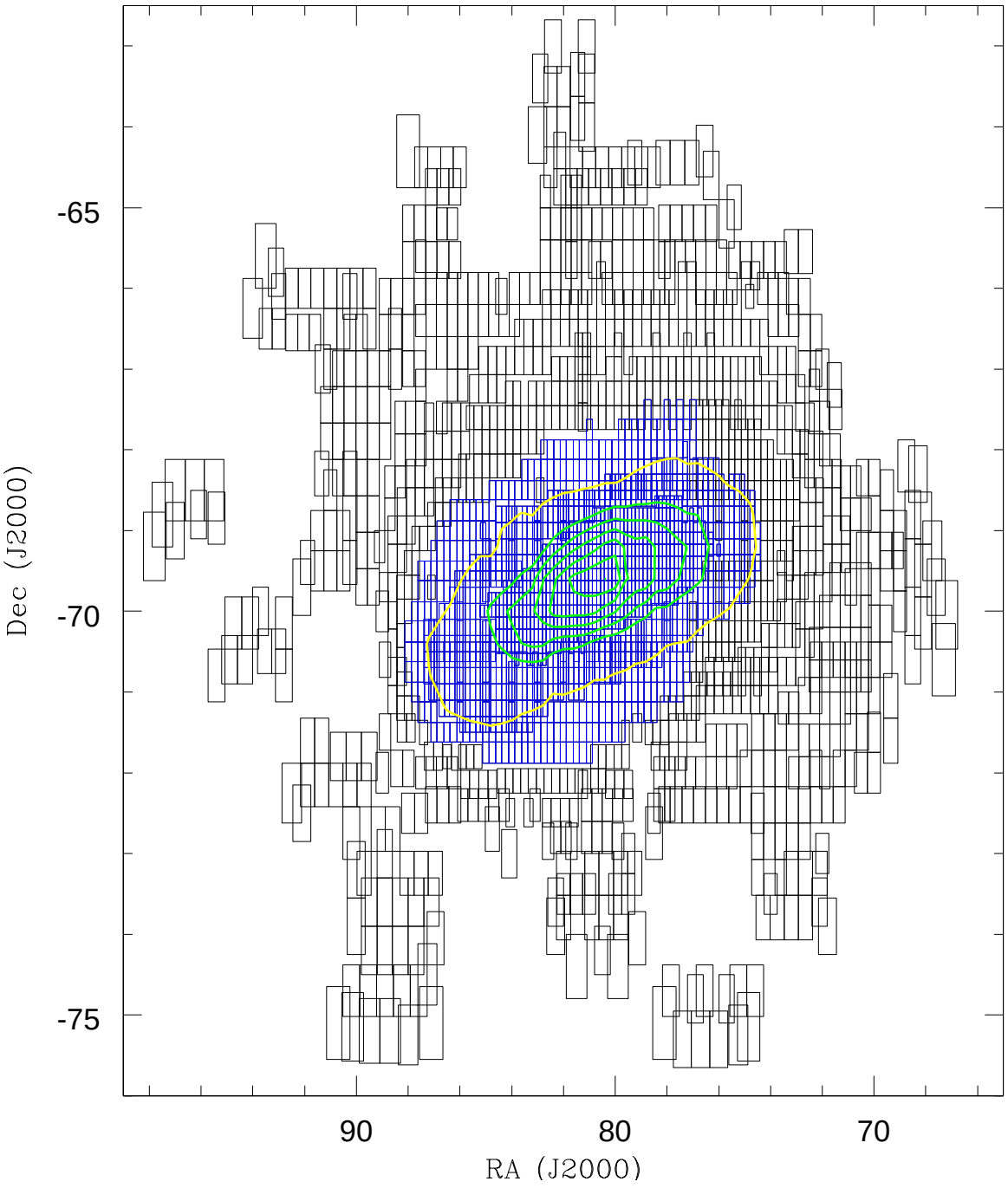

Figure 5.3: LMC map based on the regional census method, using the VMCv20170109 VSA release showing the census sub-regions after truncation. While there is overlap, the centre of each sub-region does not overlap another sub-region. Blue sub-regions are defined as inner LMC and are no larger than $0.^{\circ}25 \times 0.^{\circ}25$. Overplotted are density contours for 30% (yellow) and $50\% - 100\%$, steps of 10% (green).

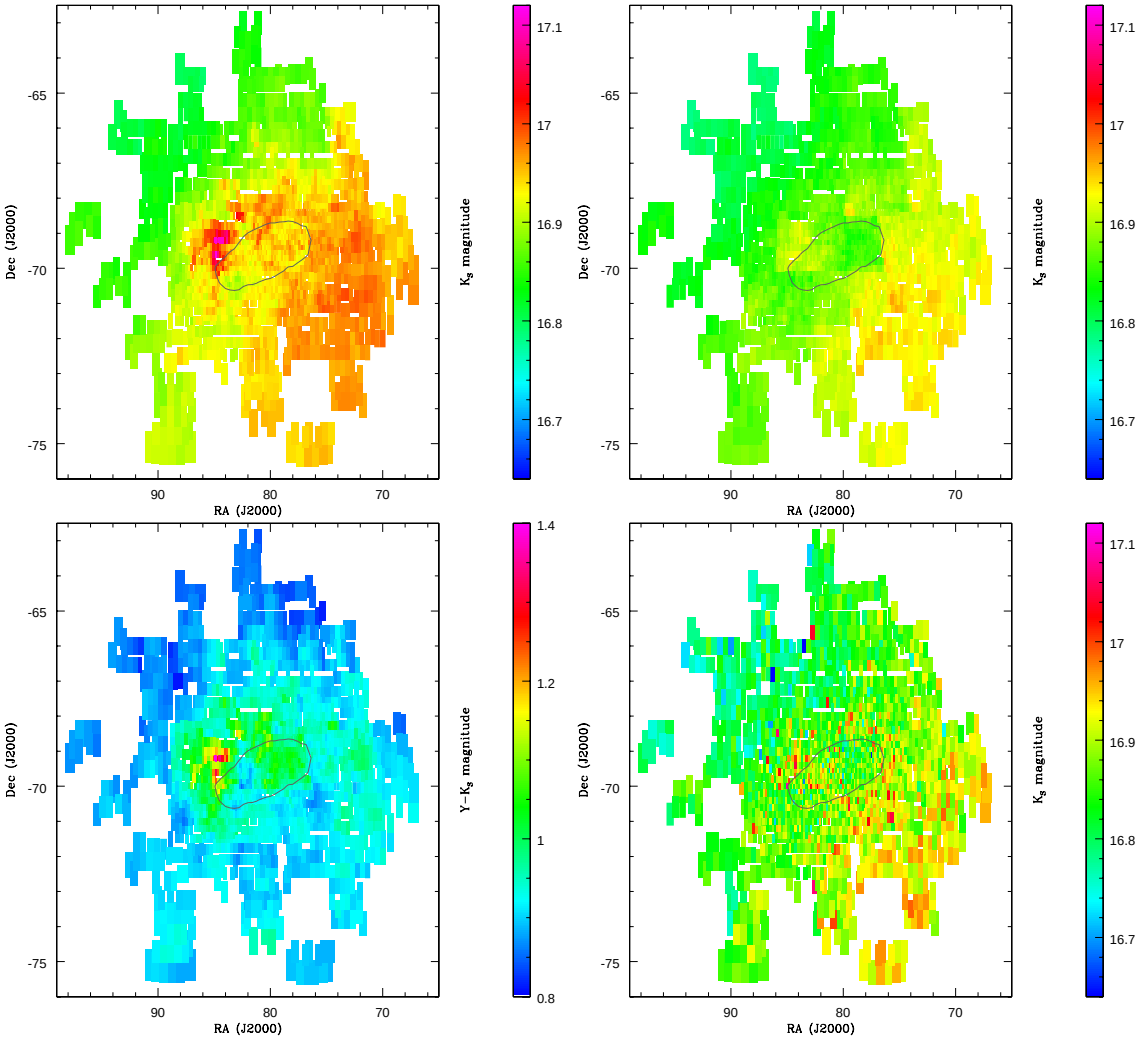

Figure 5.4: LMC maps of RC stars based on the regional census method, using the VMCv20170109 VSA release showing the median K_s magnitude before dereddening (top–left), after dereddening (top–right), median $Y - K_s$ mag colour (bottom–left) and K_s mag contour peaks after dereddening (bottom–right). The LMC bar region is overplotted in grey.

tion) was the cause. I did this by excluding stars above a certain colour ($Y - K_s > 1.2$ mag) from the sample because this is more consistent with the rest of the LMC. I found that the result was unchanged by carrying this out.

Alternatively, the cause could lie in the distribution of stars within the LMC bar in the adjacent tile to the West. If the LMC bar lies in front of the disc that means the stars within the bar are closer to us than their disc counterparts. This in turn affects the median magnitude in those regions. Evidence for this can be seen around RA= 78°, Dec= −69° which is brighter than its adjacent regions. However, the LMC bar is an incomplete explanation because it does not explain the adjacent South, East or North tiles.

Another possibility is a data related issue. 30 Doradus is a fairly crowded tile with lower completeness associated with it. Dimmer lower extinction sources might be more complete than their brighter higher extinction counterpart which overestimates average magnitude. Alternatively, the higher source density in this inner tile affects how photometry is processed. As the sky background is brighter, apertures containing this are also brighter which would cause an over correction in sky background subtraction. This effect should technically also be present in the higher stellar density tiles adjacent to the West (tiles 6_5 and 6_4; centred at RA= 79.°8, Dec= −69.°3) where the dominant LMC bar masks the symptoms. I shall return to this issue in the concluding Chapter 8.

5.3 LMC line-of-sight depth

In converting the magnitudes into distances (a step used for converting co-ordinates into the Cartesian system) I can consider the line-of-sight depth along the LMC, splitting the LMC into binned regions sized 0.°5 in RA and 0.°25 in Dec. For each binned region the full distance extent and the distance range of the two central quartiles are measured because the former is subject to emphasising outliers. Contour maps of these results are shown in Figures 5.5 & 5.6 for all sources and middle two quartiles (middle 50%),

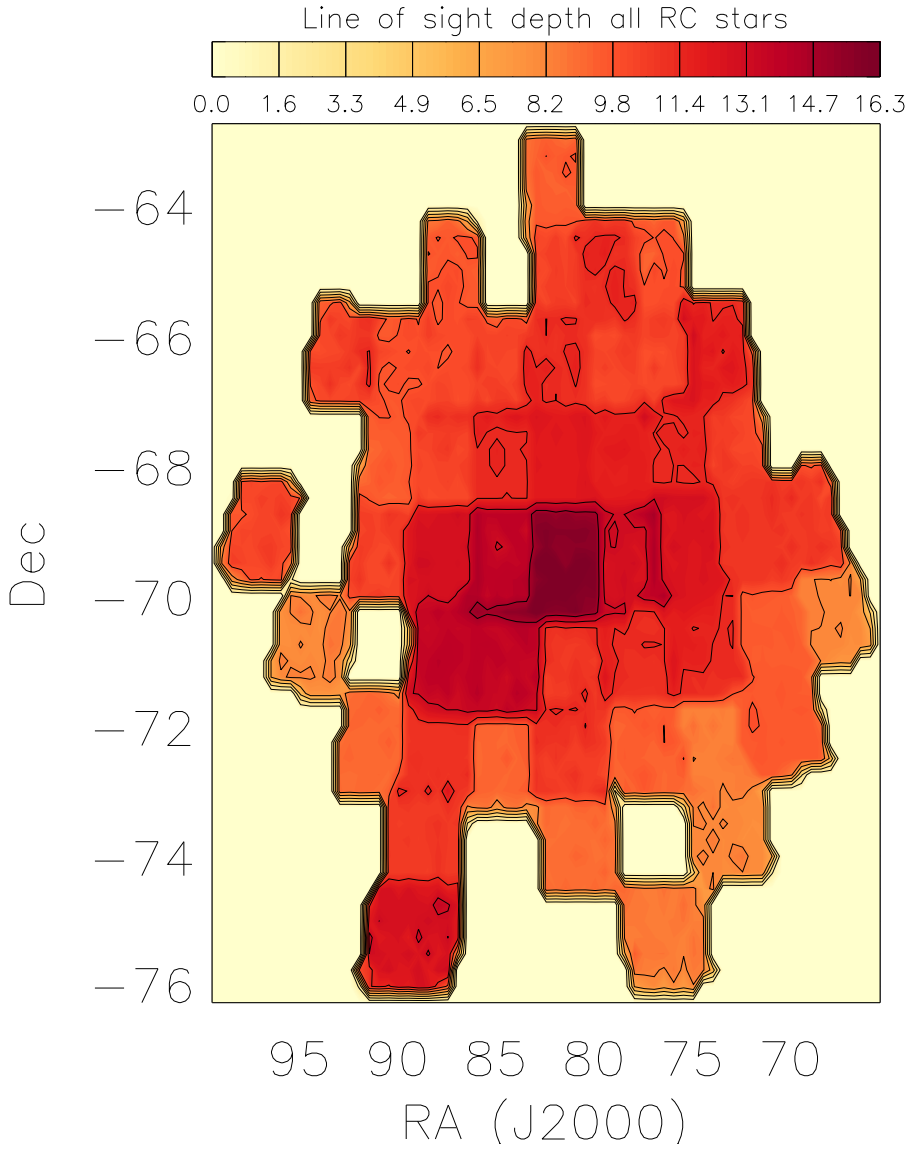

Figure 5.5: Contour map of LMC line-of-sight depths (in kpc) for all RC star candidates divided into 10 contour levels. The bin size is 0°.5 in RA and 0°.25 in Dec.

respectively.

One feature that stands out is how the contour levels tend to jump when transitioning from one tile to another, especially present in the 'all-sources' sample. This

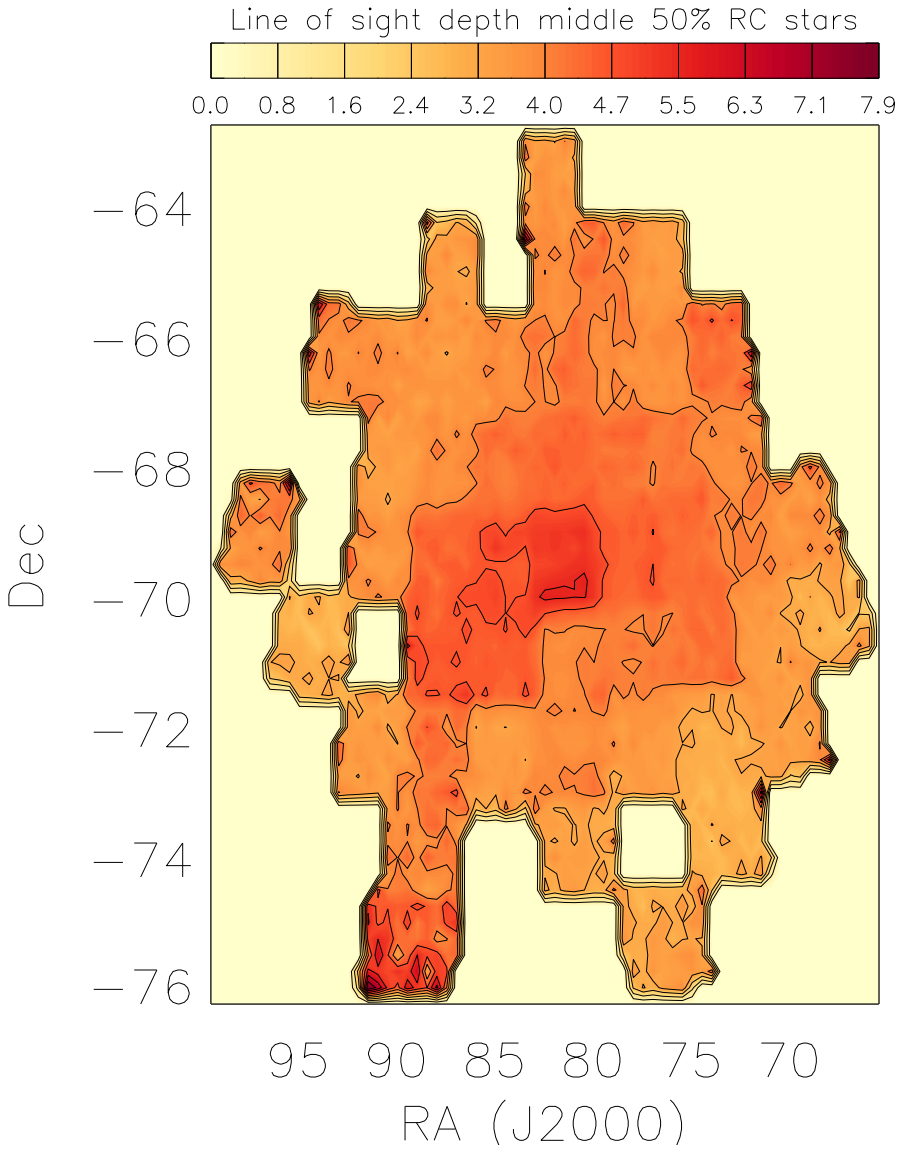

Figure 5.6: LMC line-of-sight depths (in kpc) for middle 50% of RC star candidates divided into 10 contour levels. The bin size is 0°.5 in RA and 0°.25 in Dec.

is simply a by-product of the RC stars being selected on a tile by tile basis guided by percentage-based contours. The magnitude ranges within tiles differ due to population variances and statistical effects from RGB contamination. In that sense it is an artificial structure.

In Figures 5.5 & 5.6, I see enhanced thickness in and around the LMC bar region. This could be a spheroidal component. From this two-dimensional plot there is no information on the position of the LMC bar but the larger line-of-sight depths suggest populations lying in front and behind. This is a point that will be returned to later on once a plane has been fitted.

In the most Southern–Eastern tile (2_7; RA= 88.°9, Dec= −75.°15) there is a line-of-sight depth gradient (increasing in the South–East direction) which includes the greatest depths seen across the LMC. This is unlikely to be a real morphological distortion as the density of sources in this tile is very low, which also causes a more uniform, non-RC contamination to have a more pronounced effect; hence why it shows up as an apparent distance spread in the 50% range.

5.4 Plane fitting

In this section I will fit a plane to the RC magnitude distribution, in order to facilitate examination of structure (including LMC bar, tidal warps and dynamical features).

The preparations for performing a least-squares plane fit were described in more detail in Chapter 3.4 but here I provide a summary. The spherical (RA, Dec, K_s mag) data are transformed into a Cartesian system of x, y, z. Two centres of the LMC were chosen for for this, viz. the H I centre and the optical centre. These vary by $\sim 0.°5$ in RA and Dec so may produce differing results. They have have the following coordinates:

RA: (79.°4,79.°9), Dec: (−69.°03,−69.°45) for H I and optical, respectively.

The fitting of the plane is carried out using the region census sub-regions. This

Table 5.2: Plane fitting results for the LMC.

Sub-regions	Optical centre		H I centre	
	Inclination	Position Angle	Inclination	Position Angle
	°	°	°	°
All	24.0 ± 1.0	141.4 ± 1.3	24.0 ± 0.9	142.5 ± 1.1
Inner	15.7 ± 2.7	146.9 ± 1.9	16.9 ± 1.1	147.8 ± 0.8
Outer	24.6 ± 0.6	143.9 ± 1.1	24.2 ± 0.5	144.1 ± 2.6

allows all regions to be properly considered without any requirements for weighting individual sources.

Table 5.2 contains summaries of the plane fitting results. In total there were 2298 sub-regions from the census method. The inner and outer LMC regions contain a near equal amount of data points (1100 for the inner, 1198 for the outer); Figure 5.3 showed where these sub-regions lie.

The plane fitting results, when including all sub-regions and only containing outer sub-regions, correlate with each other. This suggests the outer regions dominate the plane fitting (consequently, this makes the choice of centre less critical) and also the differences with the inner sample will be pointing out some sub-structure. These are things that should become more apparent when the residuals are mapped. The inner LMC result also exhibits a difference between the H I and Optical centres. However, this is the biggest difference between the H I and Optical centres and as a result, subsequent sections will focus on the Optical centre with the H I results included within Appendix A.2. I prefer using the Optical centre because it is based on observations of stellar light which is what I am studying.

The errors included in Table 5.2 describe the fact that the disc model does not describe all the data points perfectly, which in turn tells us the LMC is not a smooth, flat disc.

Table 5.3: LMC residual slice ranges (kpc) for optical centre solution.

Inner LMC selection plane (kpc)				
Quartile	1	2	3	4
Min	-8.773	-2.271	-0.016	1.996
Max	-2.271	-0.016	1.996	7.865
Range	6.501	2.256	2.012	5.869

Outer LMC selection plane (kpc)				
Quartile	1	2	3	4
Min	-9.393	-2.562	-0.305	1.690
Max	-2.562	-0.305	1.690	7.570
Range	6.831	2.258	1.995	5.880

Whole LMC selection plane (kpc)				
Quartile	1	2	3	4
Min	-9.227	-2.432	-0.175	1.820
Max	-2.432	-0.175	1.820	7.701
Range	6.794	2.257	1.995	5.881

5.5 Residuals

The aim of this section is to identify where populations lie in front or behind the plane. This is achieved by using the plane solution to find the fitted value of z for a star and comparing this to the actual value of z. Where the residual is negative, a point lies behind the plane and where it is positive, it lies in front. Figure 5.7 shows histograms of this (bin size 0.2 kpc) for the optical centre solution.

The histograms in the inner and outer selections are slightly offset from one another with the whole selection lying in-between these. This is true for both the optical and the H I centre. What is evident from Figure 5.7 is that the histograms are not perfect normal distributions. This means there are sources which lie outside of the expected variance. Next I will look at density maps splitting the data into quartiles. The statistics of these quartiles for the optical centre are shown in Table 5.3.

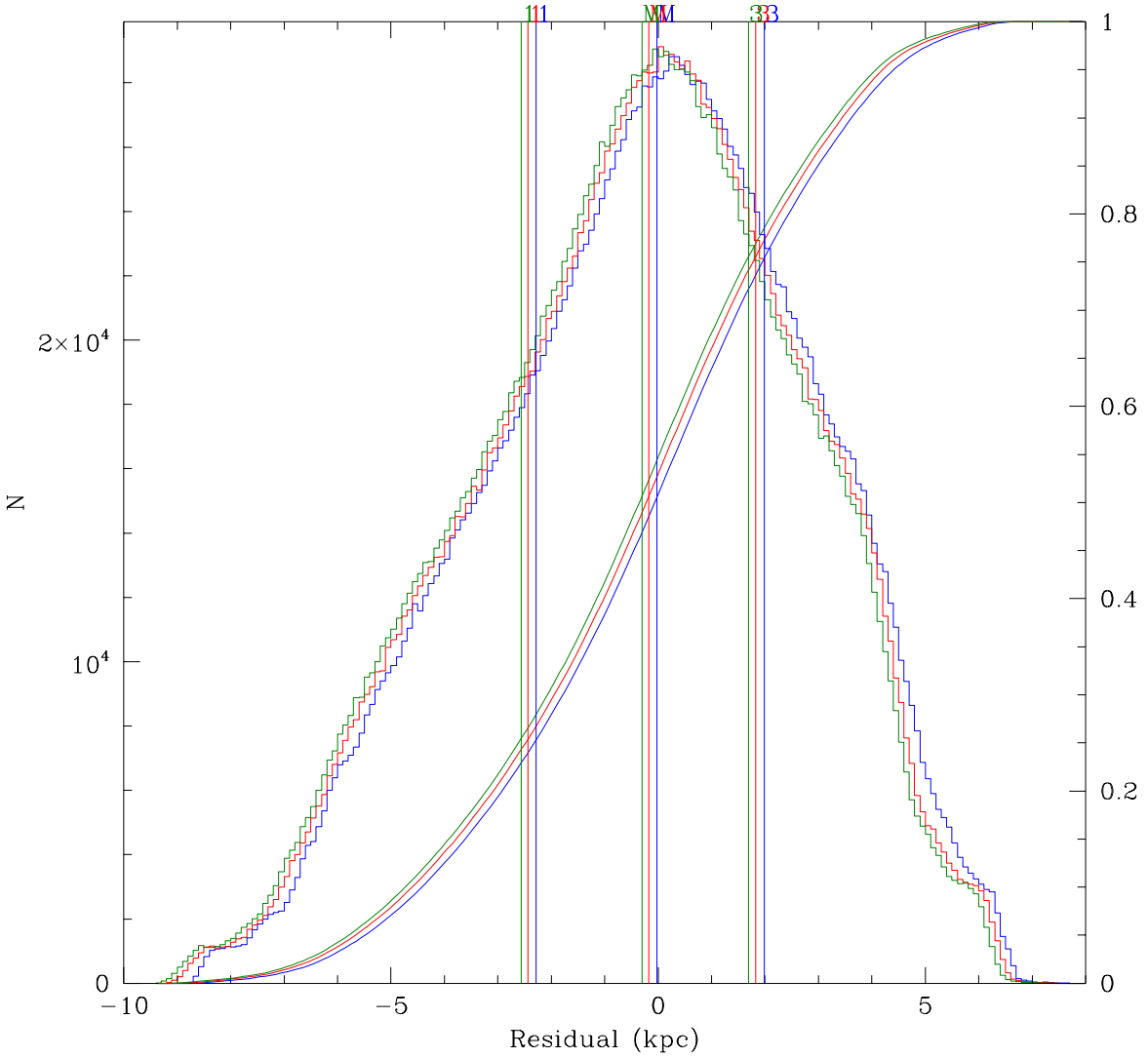

Figure 5.7: Histogram of residual from plane (bin size 0.1 kpc) for outer (green), whole (red) and inner (blue) LMC selections for the optical centre solution. 1st and 4th quartiles cover a wide range of distances (although for the former, much of this range is due to very few sources). Location of the boundaries of the 1st, 2nd and 3rd quartile are labelled as 1, M and 3, respectively using the same colours as the selections. Cumulative distributions are also illustrated (values on the right hand side of the y-axis).

5.5.1 Quartile maps

I look at the residual plane by splitting the data into four slices. The bottom row of Table 5.3 gives the ranges that are covered within each slice. By using the quartiles this ensures each slice has the same total number of sources. A sky map of each slice is created using the census method sub-regions. This is not presented as a numerical density map because it then becomes dominated by the inner LMC regions. Instead a percentage of total sources present in each slice for each sub-region is presented, offering insight into specific regions behind/in front of the plane.

Here I have chosen to only show these maps for the inner and outer solution for the optical centre. These are found in Figures 5.8 & 5.9 and the slices are ordered from behind to in front of the plane. The figures for the other maps can be found in Appendix A.2 because the whole selection is near identical to the outer selection and the H I centre solution is near identical to the optical centre solution (c.f. Figures 5.7 & A.7).

The common features of these maps are 30 Doradus (RA= 84.°4, Dec= −69.°4), the South–East corner of tile 7_4 (RA= 79°, Dec= −68.°3) and the Eastern parts of tiles 6_3 (RA= 76°, Dec= −69.°5) and 5_3 (RA= 75°, Dec= −71°) which are mainly found behind the plane. On the whole, in front of the plane is the Eastern half of the LMC bar (particularly tile 6_4; RA= 78.°2, Dec= −69.°3) and tile 5_6 (RA= 84.°5, Dec= −70.°8). Regarding the 30 Doradus tile, where the bar region lies, there are fewer sources behind the plane compared to the rest of the tile. The adjacent tile 6_5 (RA= 81.°3, Dec= −69.°3) has populations in front of the plane to the East and behind the plane to the West. This suggests the bar crosses the disc but is tilted with respect to it.

The differences between the plane solution are mostly contained in the South–West and North–East corners of the LMC. The inner sub-regions solution has a greater proportion of the North–East in the fourth (nearest) quartile while the outer solution shifts the South–West away from the second quartile and into the third. This suggests the disc is warped.

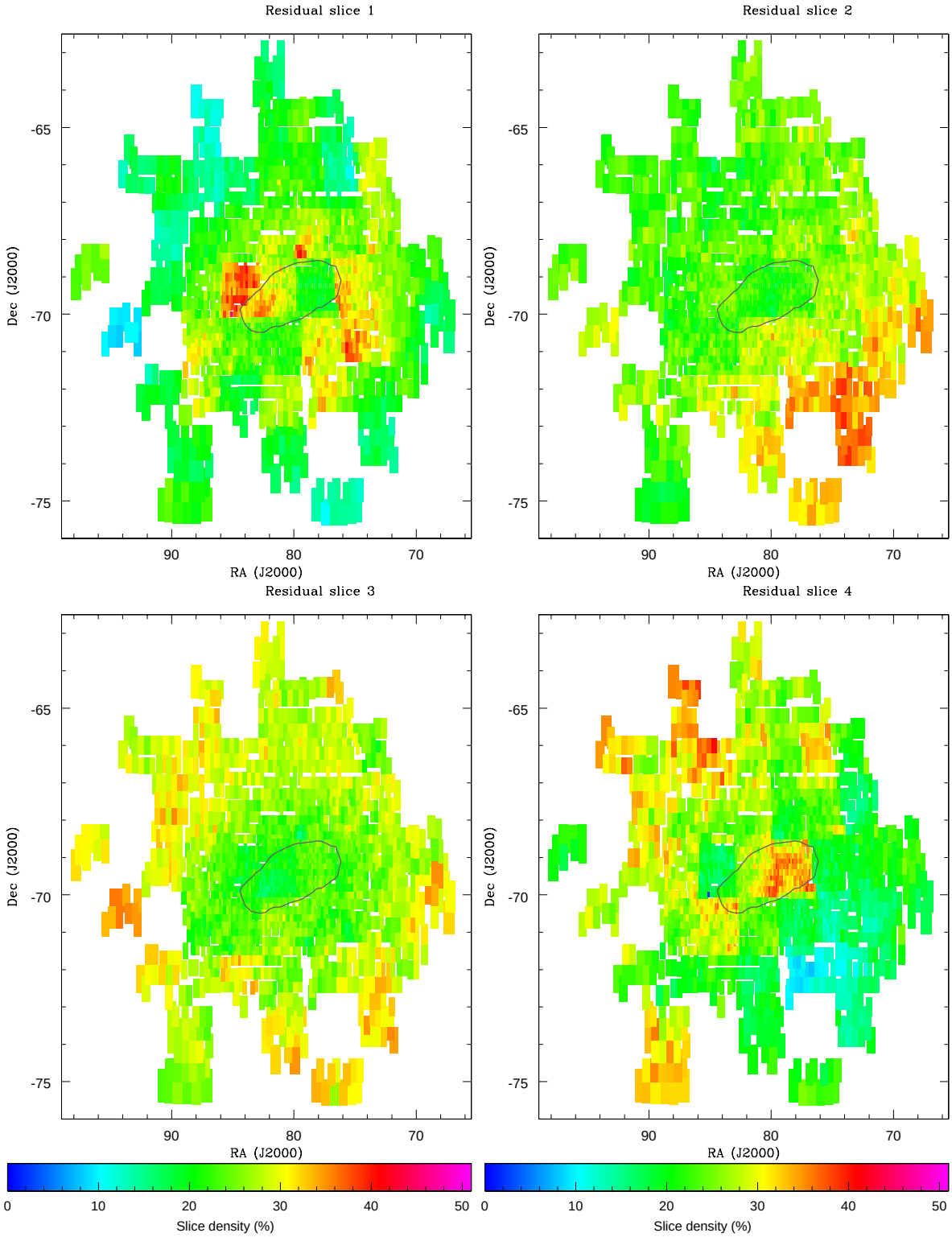

Figure 5.8: Distance residuals using the plane solution derived for the optical centre from the inner sub-regions and overlaid on regions from the census method. Each slice contains 25% of the total sample of RC stars. The slice density states what percentage of a given sub-region's sources are contained within that slice. The LMC bar region is overplotted in grey.

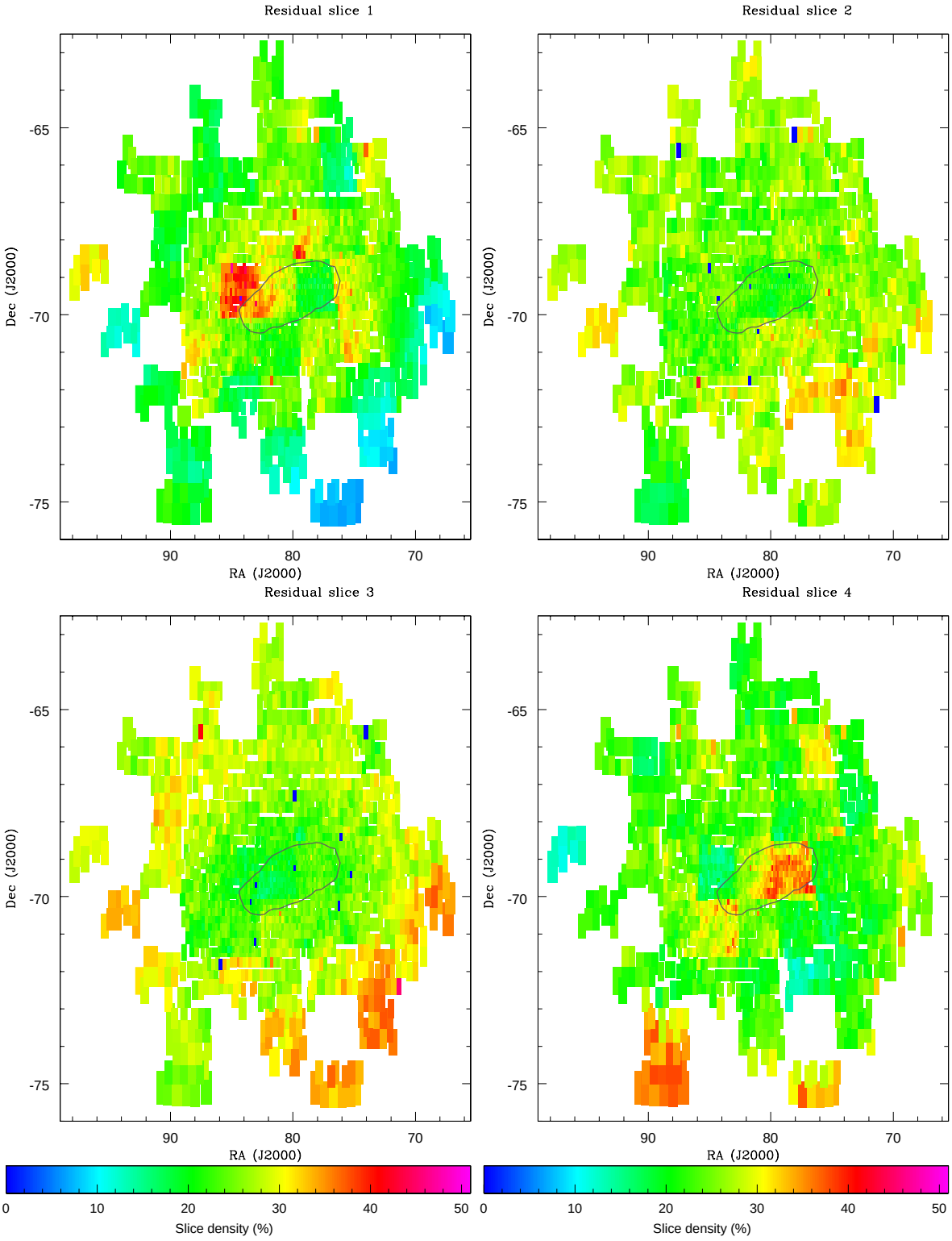

Figure 5.9: Distance residuals using the plane solution derived for the optical centre from the outer sub-regions and overlaid on regions from the census method. Each slice contains 25% of the total sample of RC stars. The slice density states what percentage of a given sub-region's sources are contained within that slice. The LMC bar region is overplotted in grey.

The South–Easternmost tile 2_7 (RA= 88.°9, Dec= −75.°15) once again displays interesting results, particularly in the whole LMC selection where there are double the number of sources in the fourth quartile than in the other three quartiles. However, the low stellar density of this region makes it more susceptible to contamination from the underlying structure of the RGB and the foreground.

5.5.2 Median residual maps

The median residual value contained within each census sub-region, when using the optical centre, is displayed in Figure 5.10. Once again the outer and all sub-regions results are very similar. The consistent findings between the three plane solutions are that 30 Doradus (RA= 82°, Dec= −69°) is always behind the plane (but by a smaller distance for the inner solution) and a region to the West (RA= 79°, Dec= −69°) associated with the LMC bar is in front of the plane. The North–East regions stand out in their inconsistency between the inner and outer solution. The inner solution finds the North–East in front of the plane whereas the outer solution finds this region to be slightly behind the plane. This is a clear indication of a warped disc, with the North–East part of the disc bent towards us, and the South–West part of the disc bent away from us.

5.6 Discussion

Using the VMC survey data I have created a reddening map which has been used in order to determine the angle of the disc component of the LMC, which in turn revealed the general structure of the LMC. In this section I will compare my work to others focusing on four areas; the reddening map, the disc component, the disc distortions and the LMC bar.

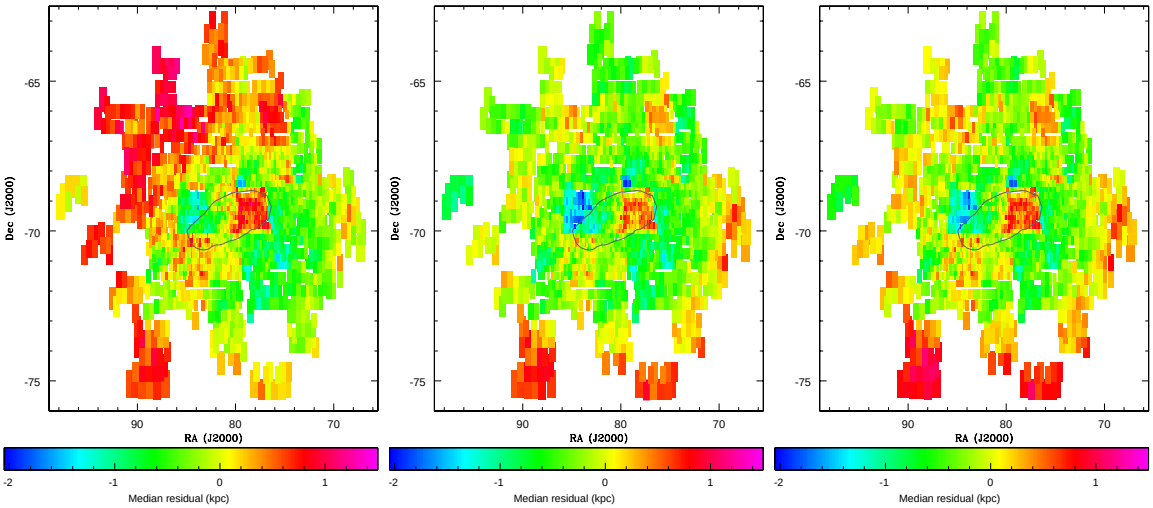

Figure 5.10: Map of median residual values for each census sub-region using the optical LMC centre and the plane solution derived for inner (left), outer (middle) and all (right) sub-regions. The LMC bar region is overplotted in grey.

5.6.1 Reddening

Returning to Figure 5.2, higher extinction is seen within and around the LMC bar. The bar is unlikely to be the cause as it is not seen as an ISM feature, only a stellar one. However, there is good agreement with what is seen in H I maps (Kim et al., 1998) and the MIR SAGE maps (Meixner et al., 2006) although they appear a bit more patchy than what I see in Figure 5.2; for example there is less ISM in the Eastern side of tile 6_5 (RA= 81.°3, Dec= −69.°3) while my extinction is fairly continuous. However, this feature does appear when looking at the average $Y - K_s$ colour (Figure 5.4, Bottom–Left). This is perhaps surprising as the Western part of the bar is seen in front of the disc; either also a sufficient fraction of the dust lies in front of the disc, or the extinction is sufficient that the contribution of the reddened stars in the disc still render the average colour redder. The ridge seen along tile 8_5 (RA= 81.°7, Dec= −66.°44) may also seem surprising. This does appear to be located around the LMC 5 supergiant shell (Dawson et al., 2013, their figure 6) and is also seen in the H I

maps and the MIR SAGE maps.

ISM maps are not the only comparison that can be made. Zaritsky et al. (2004) calculated the effective temperature (T_E) and line-of-sight extinction (A_V) using their optical photometry and the models of Lejeune et al. (1997). They produced two extinction maps for the central 64 $\deg^2$ of the LMC found within figure 8 of Zaritsky et al. (2004); one for older cooler stars and another for hotter younger stars. Overall they found extinction to be about 0.1 mag higher in the younger populations. The histograms of extinction values (shown in figure 9 of Zaritsky et al. (2004)) differ between younger and older populations and imply a geometry of stars being distributed in front and behind a dust plane and the younger population is found within this plane. In terms of extinction map, like my work they found high extinction around 30 Doradus and the regions to the East and North–East of the centre of the LMC. This is true for both maps but is seen to a greater extent with the younger population. I would have expected my results to be more similar to the older stars but the higher contrast between regions matches the younger stars more.

Haschke et al. (2011) determined the reddening in the optical for RR Lyrae and RC stars using OGLE-III data, where the LMC is split into sub-fields of differing spatial size based on stellar density. Their map (Haschke et al., 2011, figure 3) shows high reddening in 30 Doradus, the leading edge and the region North–East of the centre, but not the LMC bar. However, when looking at their differential reddening map instead (Haschke et al., 2011, figure 8), which contains only the central 32% sources, they found high values not only in regions such as 30 Doradus but also the densely populated region of the LMC bar. Comparing this differential reddening map to the median colour I show in Figure 5.4 (the census method being comprised of sub-fields makes a more apt comparison) shows striking similarity, especially in the higher reddening regions.

It is thus clear that stellar populations of different ages may be affected by different amounts of interstellar reddening depending on the way the stellar structure of the galaxy has changed in time. Conversely, differences in distribution of reddening between populations of different age may reveal such dynamical evolution.

5.6.2 Disc component

Comparing my results in Table 5.2 to those presented in Table 1.3, the position angles seen are similar and there was not much variance between my outer, inner and whole LMC selections. This suggests that a similar plane is being traced.

For the inclination however, the outer and whole LMC are on the shallower end of literature inclination values (but these are consistent with previous NIR RC studies such as Koerwer 2009 & Subramanian & Subramaniam 2013). The closest result to mine is the recent SMASH survey paper by Choi et al. (2018). Utilising RC stars they found $i = 25.^{\circ}86$, PA$= 149.^{\circ}23$. Their initial selection boxes are similar to mine although they applied some additional refinement by hand. They also used least-squares fitting (using scipy.optimize.leastsq). This shows studies using the RC stars are consistent. The question is why do other tracers find different results. This suggests that the structure is based on the epoch at which the tracer population formed, and any subsequent dynamical evolution. This is not surprising given the interaction history of the Magellanic Clouds.

On the other hand, the inner LMC dataset is shallower than anything reported previously but follows a pattern of being less inclined and having a greater PA (c.f. Subramanian & Subramaniam 2013, 2010). These contrasts suggest different structures are being traced. Evidence of this is present in the line-of-sight depths (Figure 5.6) where the depths increase in the inner LMC, inflating towards the centre of the LMC.

One cause of the lower inclination of the inner disc as seen in RC stars might be due to their age. RC stars may be old enough to have spread themselves more uniformly throughout the galaxy. Their larger scale height would make it harder to discern the presence of a disc component in the inner regions.

5.6.3 Disc distortion

In fitting the plane and looking at the residual maps, there are a number of regions that consistently deviated from this plane suggesting warps (especially as most of these

regions are found in the outer parts of the LMC). In general, the work of Haschke et al. (2012a) found that for nearer distances there were more sources in the East and Bar regions than in Western regions but that the opposite is true further away. Subramanian & Subramaniam (2010) found the North–East (and much of the East) to be warped as well.

An interesting region is the South–West region. Olsen & Salyk (2002) also found a variance in this region. However, in their case this region is in front of the plane. The work of Subramanian & Subramaniam (2010) supports this.

The distortions from a flat disc are more prevalent in the outer regions because this is where stars are found that are more loosely gravitationally bound to the LMC. They are thus more susceptible to the effects of tidal stretching, towards and away from the perturber – in this case presumably the Milky Way. Warps could also have a gas-dynamical origin if ram pressure between ISM within the disc of the LMC and the hot Galactic halo gas bends it – this would require the disc to tumble, otherwise the disc should be warped in the same, trailing direction on opposite sides, as in a wake. The RC stars are unlikely to follow such gas-dynamical structure anyway (given their age), and so the signature of a point-symmetric warped disc is evidence of tidal effects.

5.6.4 LMC bar

In the LMC bar, I saw a large line-of-sight depth and presence of sources in front of the plane, especially in the Northern end, which would suggest that the structure does extend out of the disc. Haschke et al. (2012a) also found that the bar protrudes out of the disc in their RR Lyrae sample but not for their Cepheid sample. The LMC bar is still present in the Cepheid sample and in fact the region appears to extend further (in RA and Dec). They concluded that the characteristics of the bar changes based on stellar tracer. The bar is partially in front of the LMC disc and is visible in both younger and older stellar populations. As I am specifically studying intermediate-aged RC stars I would expect my observations to have some resemblance to the older RR Lyrae population. Haschke et al. (2012a) also found their RR Lyrae star distribution

matched the intermediate-aged AGB star distribution of others.

An interesting point with many studies that find the LMC bar to be part of the disc is that they are using regional methods and base their analysis on mean magnitudes (e.g., Subramaniam & Subramanian (2009), who also use RC stars albeit in the optical). If there is both a bar and disc population, then the averages of these will dampen both out, especially if the disc population is much further behind. Looking at the residual slices (Figure 5.9) for the bar region, the Western half appears fairly uniform in the first three slices with a slight increase in the fourth slice (> 1.7 kpc in front of the plane). The South–Eastern half on the other hand is fairly uniform in the middle slides with an increase in the first slice.

However, such a big difference should be reflected in the CMDs. For a comparison, I looked at two regions: the 6_4 tile (RA$= 78\overset{\circ}{.}2$, Dec$= -69\overset{\circ}{.}3$) in the bar and the 6_8 tile (RA$= 90\overset{\circ}{.}6$, Dec$= -69\overset{\circ}{.}3$) outside of the bar. Using the CMD and overlaying contours I saw that the magnitude range for the 50% contour was 0.3 mag in 6_4 and 0.25 mag in 6_8. When extending to the 30% contour this is 0.5 mag for both tiles 6_4 and 6_8. To check that tile 6_8 was typical I looked at tile 4_8 (RA$= 91\overset{\circ}{.}6$, Dec$= -72\overset{\circ}{.}3$) finding magnitude ranges of 0.25 and 0.4 mag for 50% and 30% contour levels. This shows there is a slight difference in the bar region to spread the RC selection range but not enough for any noticeable double peaks. But looking at the contours is not conclusive as there is higher extinction in this region. It is possible that the bar – but not the disc – lies in front of the bulk of this extinction; the stars reflected in the contour level are relatively reddening free.

While a split is not obvious in the CMD, there is an indication for a thickening of the distribution, possibly due to a displacement of the (part of the) bar with respect to the disc. To pursue this further, I will examine the K_s luminosity functions for the LMC bar tile 6_4 and its surrounding four tiles 5_4, 6_3, 6_5 (also an LMC bar tile) and 7_4. The normalised histograms of these luminosity functions before and after dereddening are shown in Figure 5.11. The LMC bar tiles have an extended distribution for the brighter sources (as expected from their presence in front of the plane); tile 6_5 also extends to dimmer magnitudes as well (as expected from sources

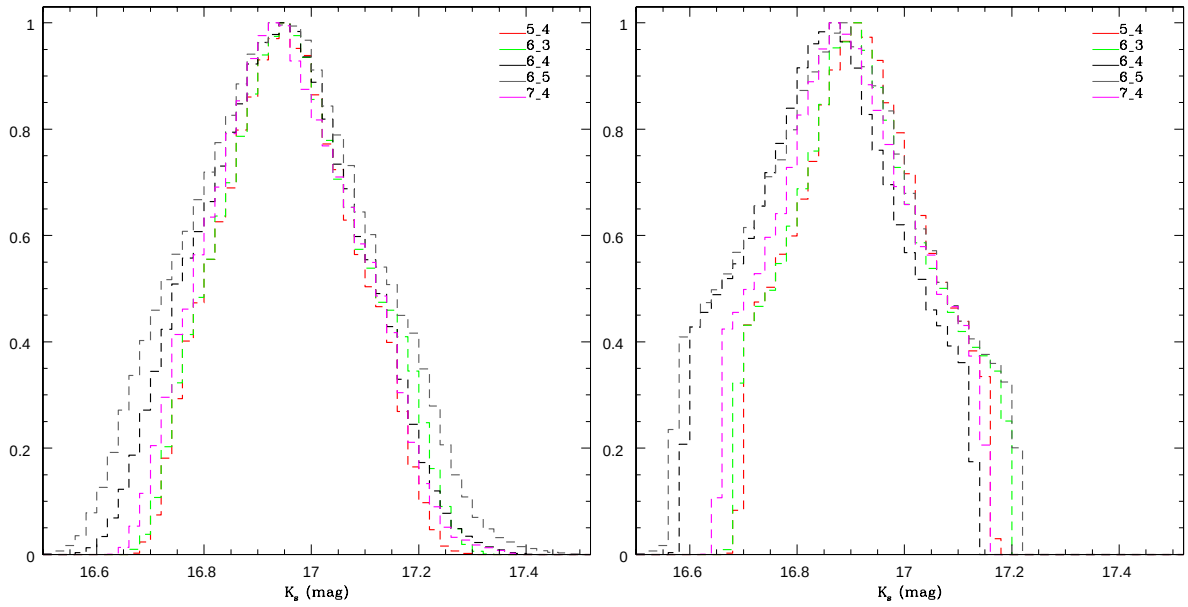

Figure 5.11: Normalised histograms of RC star $K_{\rm s}$ magnitude (bin size 0.02 mag) for five LMC tiles (described in legend) before dereddening (left panel) and after (right panel).

in front and behind the plane) whereas tile 6_4 can be described as offset (to brighter magnitudes) compared to tiles 5_4, 6_3 and 7_4. This is reflected in the line-of-sight depth, which is similar for tiles 5_4, 6_3, 7_4 as well as the bar tile 6_4, but broader for the more Western bar tile 6_5.

I thus find evidence that the bar is not a disc feature. This has implications for its origin. It cannot have resulted from a secular, morpho-dynamical evolution as the stellar populations age but must be dynamically isolated from the disc. Either the gaseous disc got perturbed after the bar had already formed, implying a relatively young disc, or the bar might be the result from a direct impact – e.g., induced by a collision between the SMC and LMC or even be an infallen smaller dwarf galaxy.

6 Structure of the Small Magellanic Cloud

In this chapter, I describe the results obtained from using the RC stars to map the structure of the SMC. While I attempt to fit a plane for any disc-like component, it will become clear that the lower-mass SMC is much more distorted than its more massive sibling, the LMC. I will present these distortions in various ways, and then place the results in the context of other recent work, presenting ideas on how these structures link to the dynamical history of the Magellanic–MW system.

The VMC survey covers every single one of the 27 SMC tiles with at least one epoch in every photometric band. However, one of these tiles could not be used in full (SMC 5_2; RA= 6.°7, Dec= −71.°9) because it contains 47 Tucanae (a globular cluster within the Milky Way; Cioni et al. 2016) which causes significant Galactic foreground contamination which transits the RC region (among other parts of the CMD). While there was an over-density present where the RC is expected and the RC is the dominant source, it was clear that this is not exclusively made up of SMC sources. The effect of this population is largely eliminated in outer parts of the tile, hence why those parts could be used (the excluded part of the tile is where RA< 7.°8 and Dec< −71.°4).

The PSF photometry was used for the SMC instead of aperture photometry in the analysis because of the zero point faults (discussed in Section 2.4.2.2) affecting tiles 4_6 (RA= 26.°14, Dec= −72.°7) and 6_4 (RA= 15.°9, Dec= −70.°9). The results based on aperture photometry will be discussed in the Appendix A.3.1.

Table 6.1 gives basic properties on the tiles including total sources in tile, contour peak levels (bin size 0.05 and 0.01 mag for K_s and $Y - K_\mathrm{s}$ respectively). Compared to the LMC, we see that the colours of the RC star population are bluer due to the lower metallicity environment of the SMC. The further distance of the SMC is also seen in the magnitude peaks being around 0.6 mag dimmer than those in the LMC. However, two central tiles (4_3 and 4_4; RA= 13.°8, Dec= −73.°1) buck this trend with colours similar to those seen in the LMC. This could be due to ISM features.

Table 6.1: List of SMC tiles used and properties when using PSF photometry. Given in the columns are the tiles, their centres, the number of sources with magnitude readings in all three photometry bands, the number of sources in the selected RC region then statistics on these RC regions of contour peak levels (bin size 0.05 and 0.01 mag for K_s and $Y-K_s$ respectively) and additionally for $Y-K_s$ mean, standard deviation and median values.

Tile	RA	Dec	Sources		Contour peak	Mean	SD	Median
	°	°	Total	RC	K_s	$Y-K_s$		
2_2	05.43	−75.20	84627	5486	17.45	0.82	0.822	0.065	0.810
2_3	11.15	−75.30	110576	10548	17.45	0.78	0.816	0.060	0.807
2_4	16.89	−75.27	137434	10941	17.50	0.80	0.906	0.179	0.830
2_5	22.55	−75.09	72423	5749	17.40	0.80	0.839	0.076	0.823
3_1	00.67	−73.89	76079	2068	17.40	0.75	0.792	0.075	0.780
3_2	05.90	−74.12	190401	18013	17.40	0.77	0.793	0.059	0.782
3_3	11.23	−74.21	1631078	56702	17.40	0.82	0.836	0.059	0.830
3_4	16.59	−74.18	288092	29794	17.40	0.83	0.840	0.058	0.834
3_5	21.88	−74.01	128290	7314	17.40	0.83	0.845	0.072	0.839
3_6	27.03	−73.72	97367	3542	17.40	0.78	0.818	0.074	0.803
4_1	01.39	−72.82	75399	1895	17.50	0.76	0.779	0.083	0.758
4_2	06.31	−73.03	245652	21829	17.45	0.78	0.809	0.070	0.794
4_3	11.31	−73.12	845029	125704	17.40	0.86	0.884	0.075	0.878
4_4	16.33	−73.09	693135	82330	17.40	0.86	0.872	0.075	0.868
4_5	21.30	−72.93	201070	11533	17.40	0.84	0.848	0.066	0.840
4_6	26.14	−72.66	70533	4310	17.00	0.81	0.828	0.069	0.815
5_2	06.67	−71.94	42860	3449	17.50	0.78	0.807	0.070	0.775
5_3	11.38	−72.03	2174210	45536	17.40	0.82	0.840	0.064	0.829
5_4	16.11	−72.00	536306	59231	17.35	0.84	0.858	0.069	0.849
5_5	20.79	−71.85	185805	14004	17.25	0.82	0.841	0.067	0.828
5_6	25.37	−71.60	93924	4151	17.00	0.77	0.799	0.068	0.782
6_2	07.00	−70.86	91744	3822	17.50	0.77	0.811	0.073	0.775
6_3	11.45	−70.94	123840	8814	17.50	0.79	0.830	0.061	0.817
6_4	15.92	−70.91	155280	12598	17.30	0.79	0.811	0.066	0.798
6_5	20.34	−70.77	118002	7433	17.00	0.77	0.796	0.066	0.781
7_3	11.52	−69.84	67270	3428	17.55	0.75	0.783	0.067	0.767
7_4	15.75	−69.82	77063	3632	17.50	0.78	0.798	0.066	0.783

Figure 6.1 shows a density map of the SMC for the $K_{\rm s}$ = 16–18 mag range for the aperture photometry (in this plot the zero point issues are not yet evident and the density is consistent with the PSF photometry). The gap between 5_3 and 5_4 (RA= 13.5 Dec= $-72°$) is caused by an unresolvable tile centring software issue (see Chapter 2.4.1.2). The large halo seen at RA= 5°, Dec= $-72°$ is foreground contamination from 47 Tucanae.

Compared to the LMC, the SMC has very low stellar density outside of its bar and the Galactic contamination is greater as well. In total 561, 843 RC star candidates were found. The inner and outer SMC regions are defined by a density contour map of the SMC for the RC stars where the outer SMC lies outside of the 20% contour level and this contains 161, 100 sources.

6.1 Reddening map

Figure 6.2 shows the reddening map of the entire SMC in the $E(Y - K_{\rm s})$ scale (with a conversion to A_V also provided).

The streaks of missing data and occasionally high extinction in a North–South direction are due to problems with detector 16. These show up in a different direction to the LMC due to the CCD rotation being different for SMC targets. The high extinction version of this feature is especially prevalent in tiles 3_2 (centred at RA= 6°, Dec= $-74°$) and 5_4 (centred at RA= 16°, Dec= $-72°$).

High extinction is mainly seen along the dense SMC bar. However, tile 5_3 (RA $\simeq$ 12°, Dec $\simeq$ $-72°$) appears to break this continuity despite being part of the bar. The strongest features however are seen almost exclusively within the 4_3 tile (RA= 11.3, Dec= -73.1). Evidently, the dust is concentrated in the bar region peaking where star formation is most intense. In general for the whole SMC, lower extinction is seen in the wing to the East of the bar.

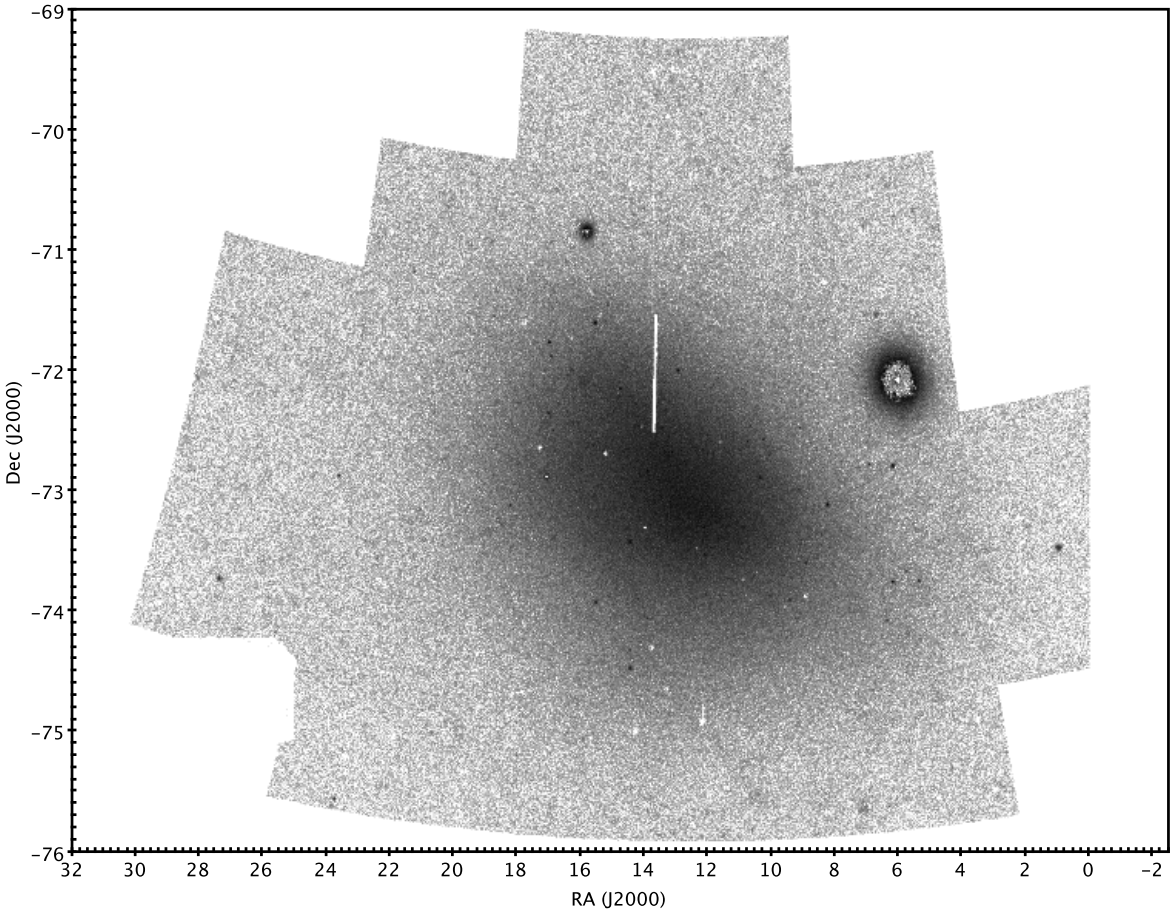

Figure 6.1: A source map of the SMC including all appropriate VMC tiles from VSA release VMCv20170109 where darker regions are higher density. The ring structure seen at RA= 5° Dec= −72° in tile 5_2 is caused by 47 Tucanae. The gap between 5_3 and 5_4 (seen at RA= 13.°5) is caused by an unresolvable tile centring software issue (see Chapter 2.4.1.2). This map contains all sources with K_s = 15–18 mag, Figure 6.2 contains only the RC stars.

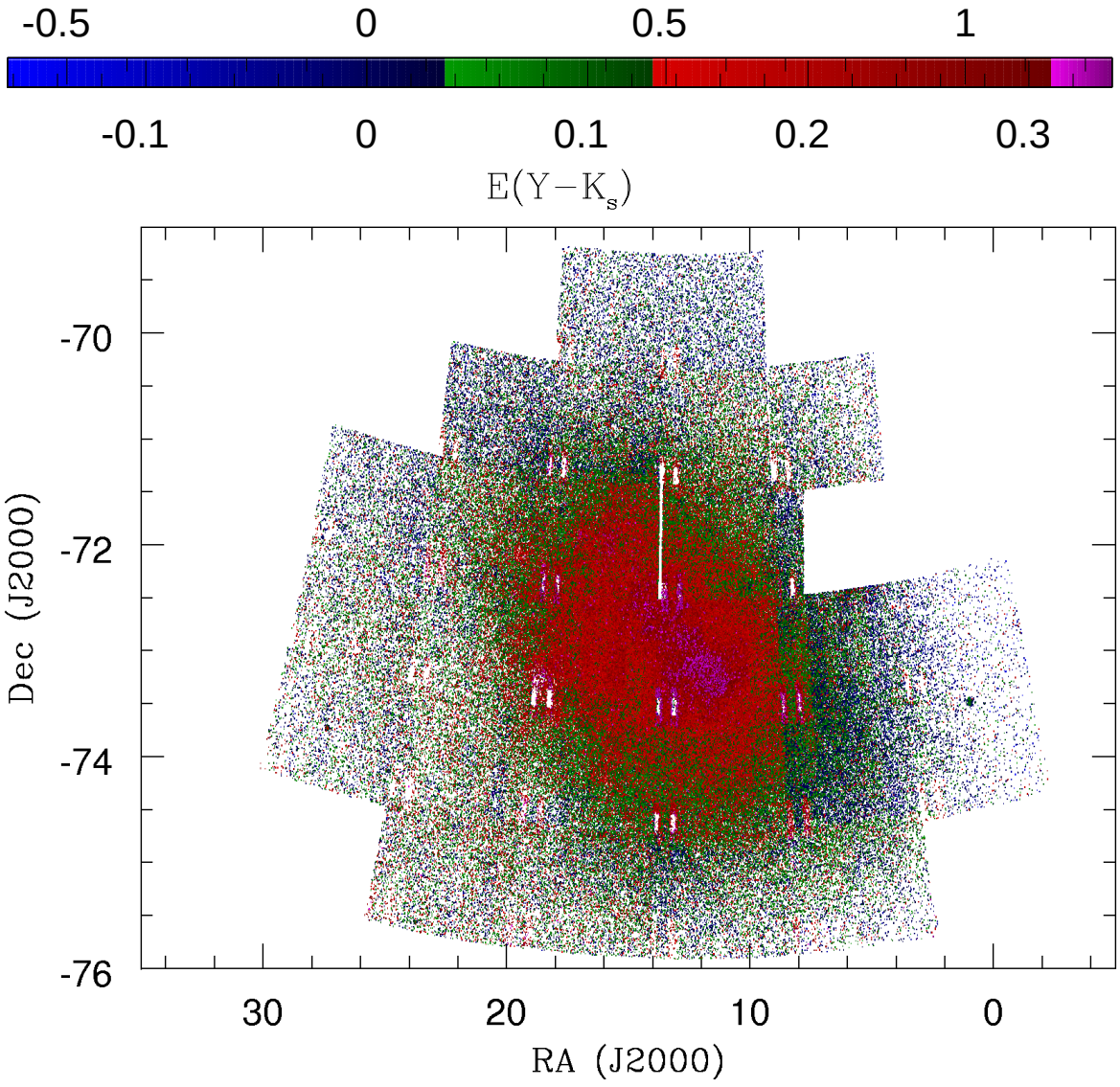

Figure 6.2: Reddening map of the SMC in $E(Y - K_s)$ (top side of legend shows this converted into A_V magnitude) from RC stars using the PSF photometry. The green sources are the range covering 50% of the sources centred on the median where blue is lower than this, red higher and pink shades extremely high.

6.2 Regional census

Unlike the LMC, using the regional census within the SMC has some issues caused by the very low source density of the outer SMC. It means that the census has less coverage than it does in the LMC. Each cell in this regional census contains between 500 and 2000 sources and has a size between $1\,\mathrm{deg}^2$ and $0.15\,\mathrm{deg}^2$ in increments of $-0.05\,\mathrm{deg}^2$. This produces a total of 976 sub-regions. These are plotted in Figure 6.3.

What is apparent is the median colour follows the general pattern of the reddening map where the inner SMC is redder than the outer. However the representation in this figure places more emphasis on high extinction regions, notably the area around RA$= 18^\circ$ Dec$= -73^\circ$. This is associated with star forming region NGC 602.

From the magnitudes it can be seen that the Eastern wing lies closer to us than the SMC bar, and the Western periphery of the SMC is the furthest away. But this is not a simple East–West gradient.

6.3 SMC line-of-sight depth

There is great motivation for looking at the line-of-sight depth in the SMC because it has been shown to have a thicker North–East side (e.g., Kapakos & Hatzidimitriou 2012).

By assuming that a RC star with $K_\mathrm{s} = 17.304$ mag corresponds to a distance of 61 kpc (average of distance values given by NED and Simbad) I can use the dispersion of distances in a binned region as a proxy for a thickness – i.e. a line-of-sight depth.

For binned regions of $0.^\circ5$ in RA and $0.^\circ25$ in Dec, I look at two things: the overall thickness range covered by all the RC stars and the thickness range of the two central quartiles (as it was seen that the first and fourth quartile cover a very large range). Contour maps of these are shown in Figures 6.4 and 6.5.

The depth values themselves are typical of what one finds in the literature with central depths of $\sim$ 6–14 kpc (Crowl et al., 2001; Subramanian & Subramaniam, 2012)

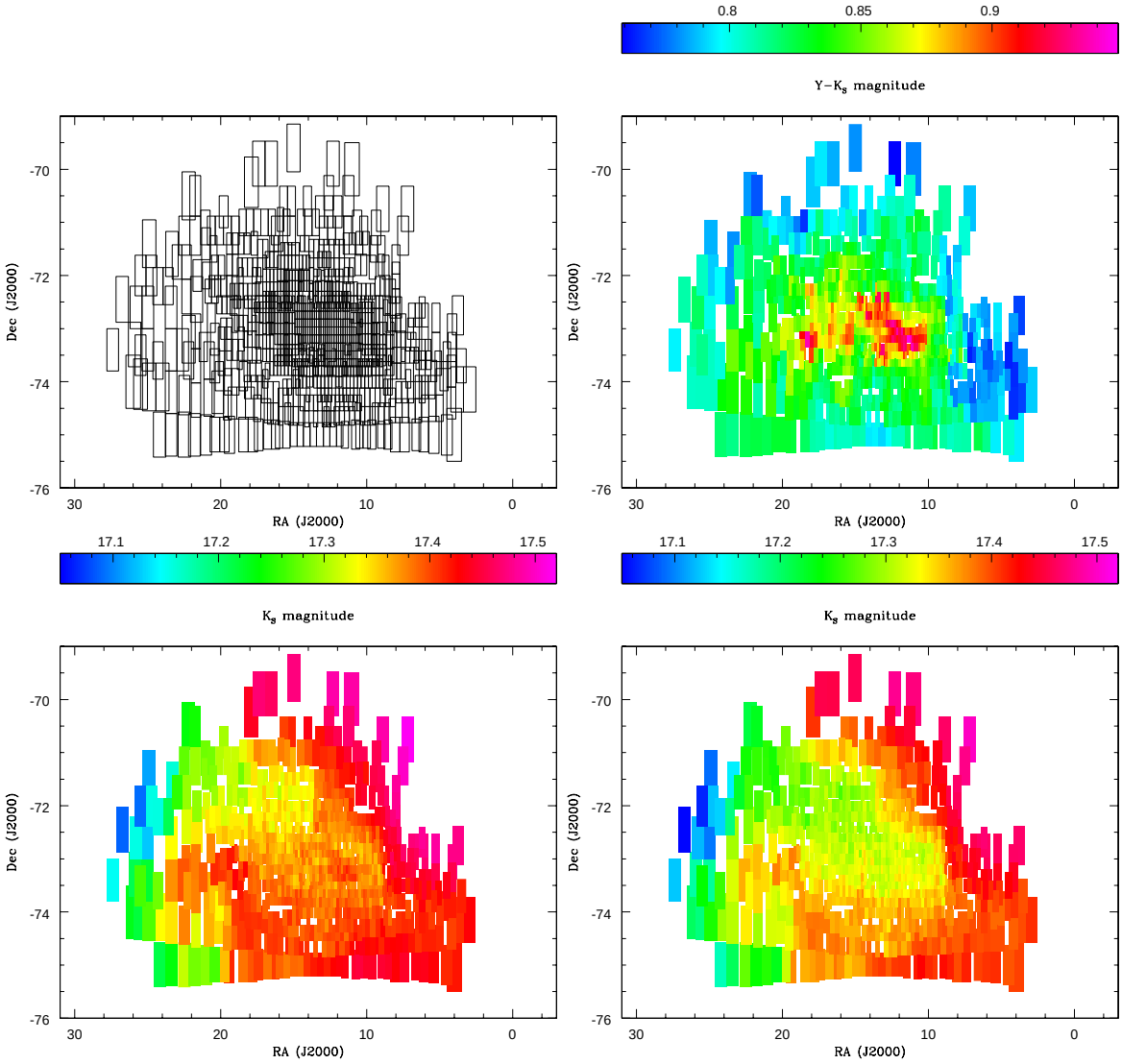

Figure 6.3: SMC maps based on the regional census method, using the PSF photometry. Shown are the outline of the sub-regions (top–left) median $Y - K_s$ colour (top–right), median K_s magnitudes before (bottom–left) and after (bottom–right) dereddening.

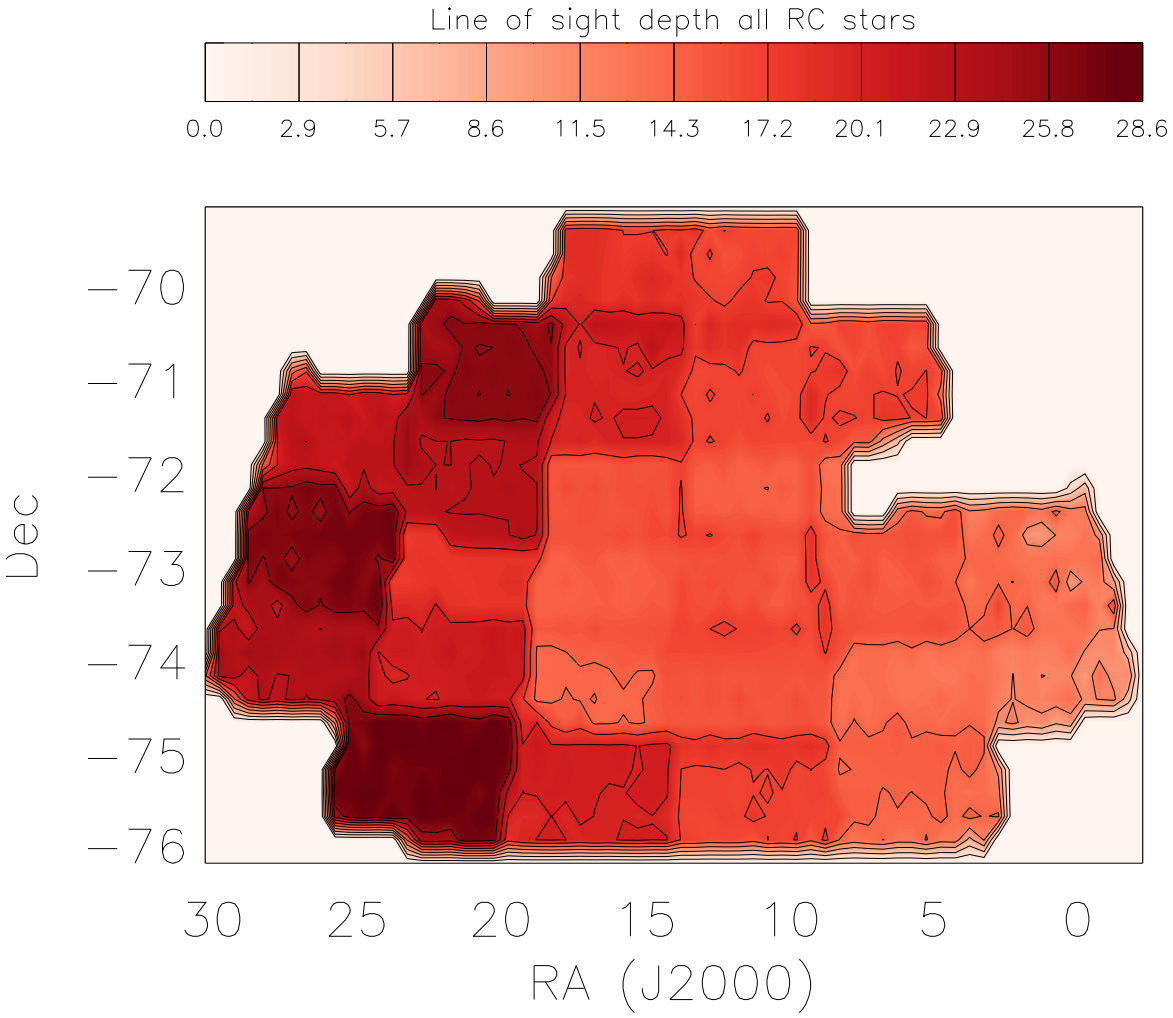

Figure 6.4: Line-of-sight depth of the SMC (in kpc) for all sources divided into 10 contour levels. The bin size is 0°.5 in RA and 0°.25 in Dec.

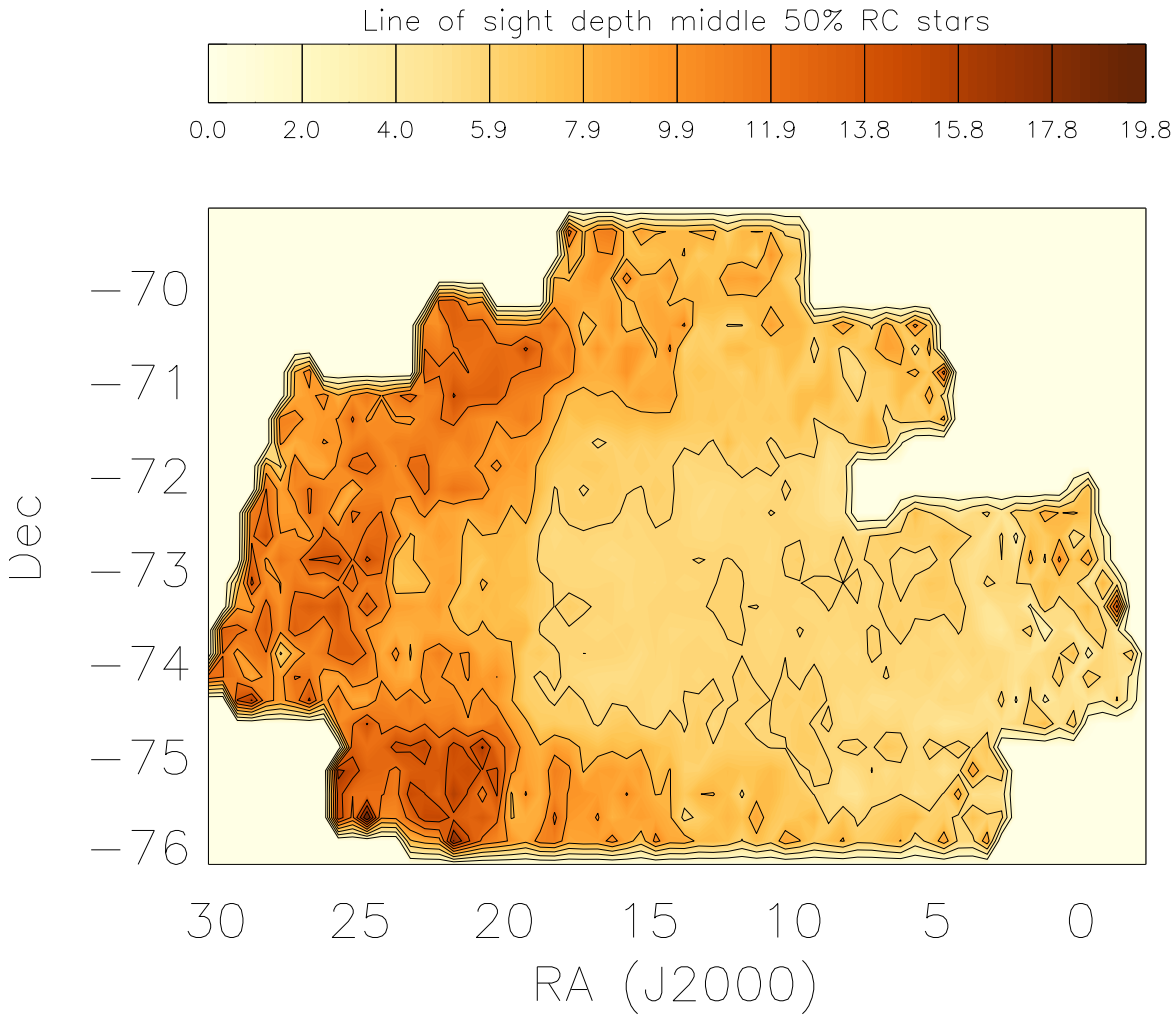

Figure 6.5: Line-of-sight depth of the SMC (in kpc) for middle quartiles of sources divided into 10 contour levels. The bin size is 0.°5 in RA and 0.°25 in Dec.

and Eastern depths of up to $\sim$ 23 kpc towards the Bridge (Nidever et al., 2013) (additionally Bica et al. 2015 found shorter distances to clusters within the Bridge).

As found in the LMC when looking at all sources one can see the effect of RC star selection and dereddening being conducted on a tile by tile basis with the contour levels typically changing between tile edges. Unlike the LMC there is still significant line-of-sight depth exhibited in the central quartile sample. The major contributors to this depth are mostly the Eastern SMC wing regions in the North–East and South—East but this is not a continuous band.

Another consideration is the distance moduli distribution within the SMC. This is carried out via histograms of the $K_{\rm s}$ magnitude for each tile and shown in Figure 6.6. It can be seen that for the Eastern periphery (mainly tiles X_5, X_6 where X is integer) the distribution of sources is not only along a larger magnitude range than it is in the central and Western regions but is double peaked (the peaks are fairly even in tiles 2_5 and 3_6). The fainter peak corresponds to the bulk of the SMC. However, the brighter peak dominates over the fainter peak in tiles 6_5, 5_6 and 4_6, which is in the direction of the LMC. The magnitude difference is around 0.4–0.5 (the magnitude difference between the LMC and SMC is around 0.6 mag). More information on this double RC feature can be found in Subramanian et al. (2017).

6.4 Plane fitting

In this section I will fit a plane to the RC magnitude distribution, in order to examine whether such disc-like component is present in the SMC, and to facilitate examination of structure by comparing the RC magnitude distribution relative to such plane of symmetry. This least-squares plane fitting is described in detail in Chapter 3.4.

A single centre was used for the SMC which is an average of the 2 optical ones; RA= $13\overset{\circ}{.}17$, Dec= $-72\overset{\circ}{.}81$ found on NED and Simbad. In total there are $561,843$ RC stars in the SMC with $161,100$ of these in the outer parts.

Plane fitting was carried out using all sources, outer sources and the census

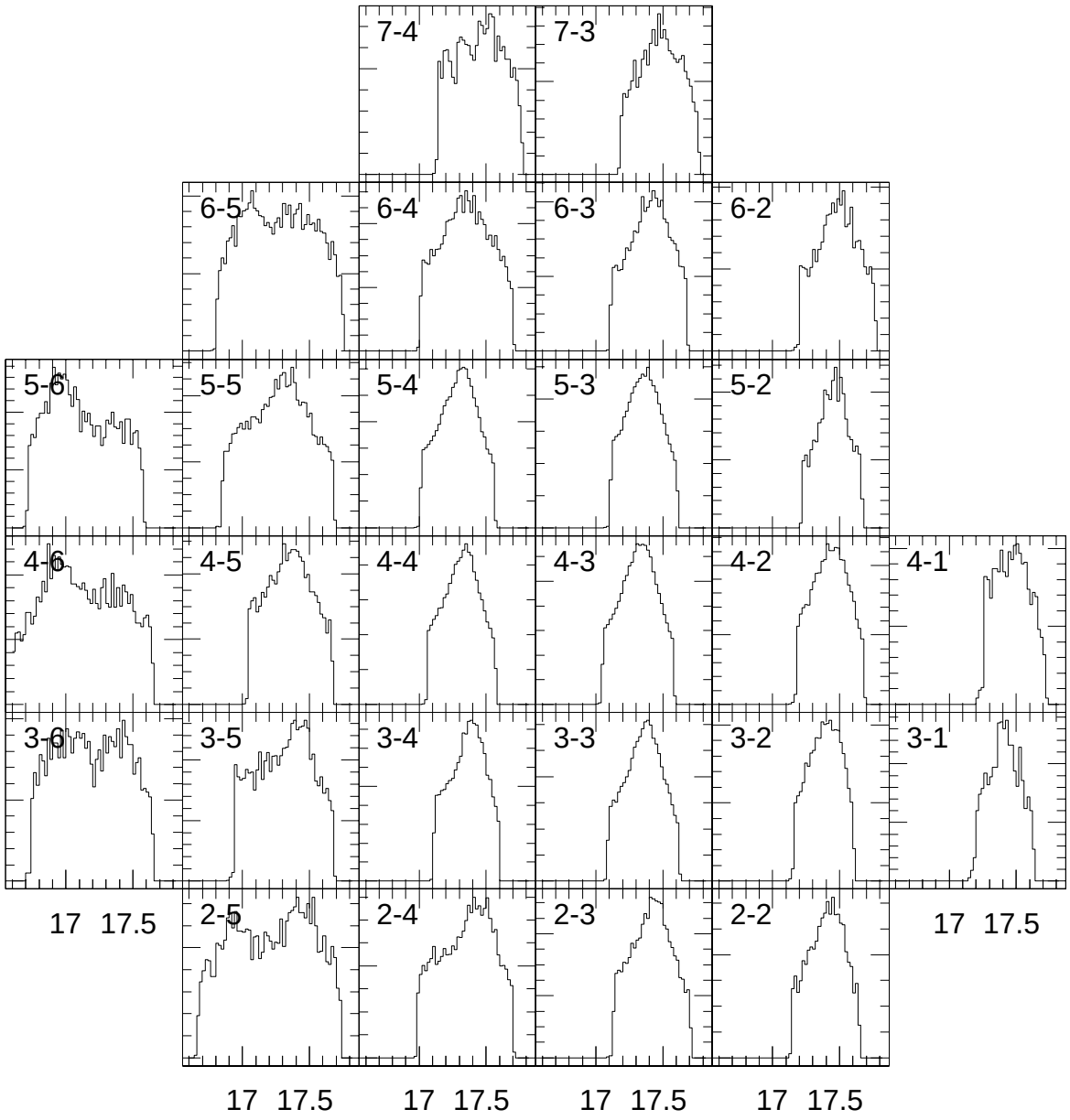

Figure 6.6: Histograms of dereddened RC star $K_{\rm s}$ magnitude (bin size 0.02 mag, range $K_{\rm s}$ = 16.5–18 mag) for each SMC tile labelled in the top–left of each panel. Of particular interest is the double RC seen in the Eastern fields.

Table 6.2: Plane fitting results for the SMC.

	Inclination $^\circ$	Position Angle $^\circ$
Outer	48.5 ± 0.1	186.3 ± 0.5
All	43.3 ± 0.1	179.2 ± 0.1
Census	35.4 ± 1.8	169.8 ± 3.1

method. The 'all sources' contained 561, 843 sources, the outer SMC contained 161, 100 sources and the census method contained 976 sub-regions. The results are summarised in Table 6.2.

The census method acts as an inner SMC selection due to mainly containing sub-regions that are within the main body of the SMC (referred to as the 'inner'). It is expected to have shallower inclination because that was seen in the LMC, and also because the line-of-sight depths were greatest, and had the most extreme values outside of the main SMC.

There is a lot of variance in the literature values for position angle and inclination and not many of these studies utilised plane fitting. The position angle from the 'outer' result returned a value of $-173.^\circ7$ but this is accepted as $186.^\circ3$, an equivalent value to match the rotation of the other results. The cause of the rotation for the 'outer' being reversed is most likely due to the centre of the Cartesian system being a void for that fit.

6.5 Residuals

Figure 6.7 shows the histograms of the residuals for the three selections using a bin size of 0.2 kpc, where negative values lie behind the plane and positive ones lie in front of the plane.

One can see that the residual range of the two central quartiles is around 6 kpc

which is a good description of the line-of-sight depth for the central and Western SMC inside Figure 6.5. The central region, in particular, contains a majority of the stars so this is not surprising. Examining the Eastern SMC, line-of-sight depths are double this value, which was explained by their extended and split RC population as seen in Figure 6.6.

Breaking up the residual into four quartiles of sources from behind to in front of the plane is conducted in Figure 6.8 for the whole SMC plane solution (the other two plane solutions were very similar so appear in the Appendix A.3.2). The bin size of these maps is $0\overset{\circ}{.}5$ in RA and $0\overset{\circ}{.}25$ in Dec. Displayed in these contour maps is the fraction of all sources for a given bin contained in that quartile in order that these maps give an indication to where structure is (a density map simply highlights that the main body of the SMC has a high density).

All my plane solutions produce very similar results. The main body of the SMC is found mostly in the latter three quartiles whereas the extent of this feature is small in the first (furthest) quartile. This would suggest the main body of the SMC is a single component and not too extended in depth. The North SMC (RA= 10°–20°, Dec $> -71°$) is a more concentrated example of a single component appearing mainly in the first quartile but non-existent in the fourth quartile.

The Eastern SMC is mostly found in the first and last quartiles though, suggesting some asymmetry and distortion. Interestingly, in the first quartile there is less seen in the North–East but more in the South–East and this trend is reversed in the fourth quartile. With reference to Figure 6.6, most North–East tiles (e.g. tile 5_6; RA= $25\overset{\circ}{.}4$ Dec= $-71\overset{\circ}{.}6$) have their largest peak of sources in the brighter magnitudes which are closer, and thus in front of the plane. This trend is reversed the South–East tiles (e.g. tile 3_5; RA= $21\overset{\circ}{.}9$ Dec= $-74\overset{\circ}{.}0$). The Eastern tiles in general also had greater line-of-sight depths (see Figure 6.5) which is reflected here in their presence in the first and fourth quartiles.

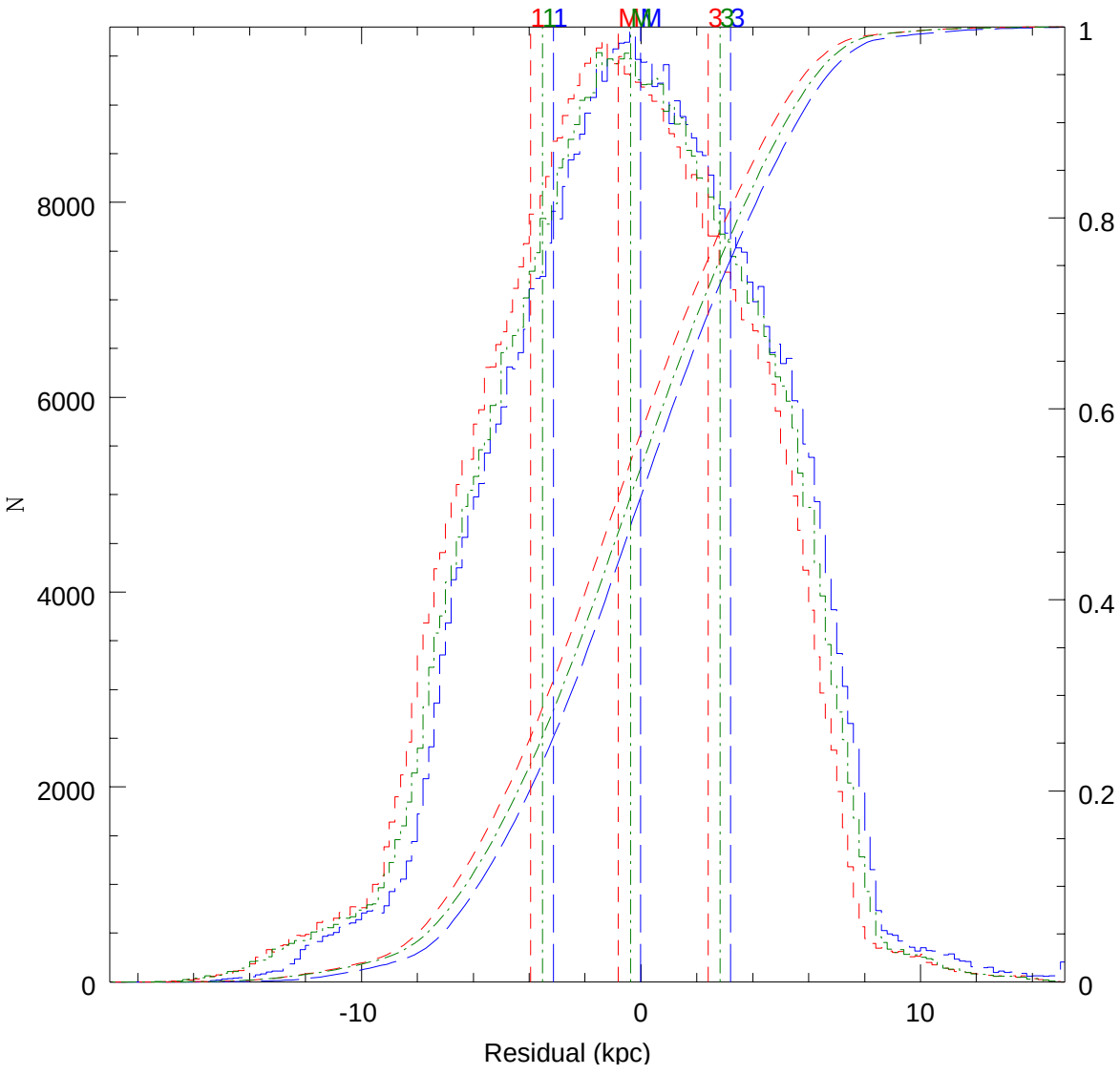

Figure 6.7: Histogram of residual from plane (bin size 0.2 kpc) for outer (blue), whole (green) and census (red) SMC selections. 1st and 4th quartiles cover a wide range of distances. Location of the boundaries of the 1st, 2nd and 3rd quartile are labelled as 1, M and 3, respectively using the same colours as the selections. Cumulative distributions are also illustrated (values on the right hand side of the y-axis).

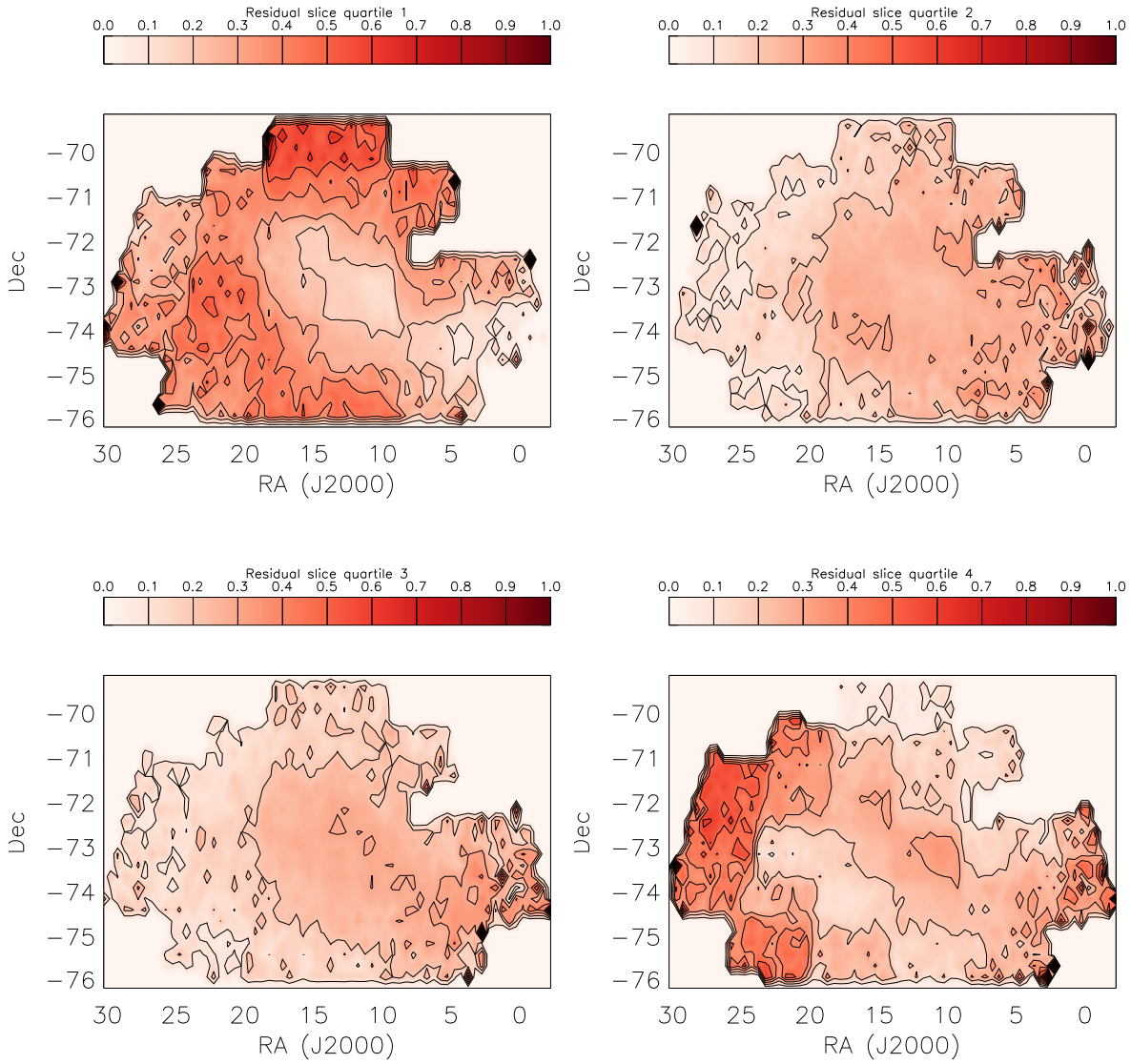

Figure 6.8: Residual slices using plane fitted the from whole SMC selection. Slices are ordered from behind the plane to in front of the plane. Each slice contains 25% of the total RC stars. The bin size is 0.°5 in RA and 0.°25 in Dec.

6.6 Discussion

There are three main topics to discuss from the results: the reddening, the disc components and the disc distortions.

6.6.1 Reddening (and dust)

In the Hα map of Kennicutt et al. (1995) the Western side of the bar has similar emission levels to the South–Eastern side. Comparing with the H I map of Stanimirović et al. (1999), MIR and FIR maps of Bolatto et al. (2007); Leroy et al. (2007) the Western side of the bar has weaker emission than the East. The contrasts between the Hα and other studies suggest there are changes in the dust-to-gas ratio between the Western and Eastern parts of the SMC bar. Dust emission is dependent on dust temperature and therefore the interstellar radiation field, whereas measured extinction is not. Thus, extinction is a less discriminating probe of dust.

In my extinction map I see weaker extinction in the North–Western side of the bar than I do in the South–East, corroborating what is seen in the H I, MIR and FIR. The strongest extinction features I see are best traced by the 8μm MIR data of Bolatto et al. (2007). The 160μm data of Gordon et al. (2009) covers the Wing and bar and, unlike the previously mentioned maps, exhibit strands of emission connecting the bar and Western Wing, whereas my map shows a more even distribution of moderate extinction between the two and strands do not appear to be visible. This discrepancy can be explained by recalling the drawback of using extinction, which is that it is only measured in front of stars, whereas the dust emission is seen wherever it is. Perhaps these strands of emission are predominantly behind the stars resulting in less extinction measured than dust emission observed.

In the Wing there is an interesting high average colour feature at around RA= 18.°5, Dec= $-73.°3$. I also clearly see this in the census map but it was not obvious from the reddening map (likely due to being near to detector 16). This is NGC 456

(an H II region) and its associates N83/N84 (a molecular cloud complex; Bolatto et al. 2003).

6.6.2 Disc components

The inclination and position angles in the literature (see Table 1.4) greatly vary depending on the tracer used as well as the method (where very few adopt to try fitting a plane in the SMC). This makes a direct comparison difficult. Younger Cepheid populations tend to have very steep inclination (this could also be a symmetrical tidal distortion) while older populations tend to have very shallow, almost non-existent inclination (the older population is more likely to be more spheroidal rather than being represented by a disc-like structure) and thus one would expect intermediate-aged populations to be somewhere between those, which is what I find.

However, Subramanian & Subramaniam (2012) found a very small inclination ($i = 0.^{\circ}5$) when using the RC star population – in contrast to my results. Their methodology however was to use axes ratios and to limit the sample to a small depth range, which may have inadvertently had an effect. Compared to the literature the position angles I find are most similar to Subramanian & Subramaniam (2015) although the literature paints doubts on the SMC being best fitted by a flat disc due to its distortions.

Rubele et al. (2015) found a mean $i = 39^{\circ}$ using distance fitting rather than being based on an individual tracer. This is shallower than what I find but does suggest a more dominant older population.

6.6.3 Distortions and other structures

Dias et al. (2016) described the SMC as being three bodies; Eastern Wing, central bar, Western halo. This is opposed to the traditional view of only the Wing and the bar. My work to some extent also finds a fourth body in the North but this has been found before and described as an extension to the Wing (e.g. Gardiner & Hawkins (1991)).

However, the reason these bodies are interesting is because of how different they are. The outer regions have been transformed by interactions leading to tidal stripping and spatially spread populations.

In fact using some tracers one can see these different geometric distributions simultaneously. In the case of the work by Ripepi et al. (2017) the young and old Cepheids (old Cepheids are around 300 Myr old so much younger than RC stars) both show off centre structures in the direction of the LMC. Subramanian et al. (2017) studied part of the SMC using VMC data (13 tiles compared to the 27 I use) also using RC stars, and to which my work contributed. They found a double RC feature manifesting itself as a distance bimodality in the Eastern SMC which their work focuses on. Due to using the same data it is unsurprising that I also find this in the regions they studied (see Figure 6.6). My work is able to confirm the distance bimodality is also seen within nearby tiles not studied in Subramanian et al. (2017); tiles 2_5 (RA= 22.°5, Dec= $-75.°1$), 4_6 and 3_6 (RA= 27°, Dec= $-72°$ to $-74°$). In addition Northern tile 7_4 (RA= 15.°8, Dec= $-69.°9$) also exhibits some bimodality but spanning a less extended magnitude range.

Muraveva et al. (2018) used VMC data to look at 2660 fundamental mode RR Lyrae (i.e. older than RC) stars in the SMC. The distribution of these is found to be ellipsoidal. Line-of-sight depths were in the range of 1.5–10 kpc with an average of 4.4 ± 1.0 kpc and these are around a factor of two smaller than the values I derived (for the central quartiles I see a range of 0.52–19.7 kpc with an average of 7.83 kpc). While they did not see a distance bimodality, they still found the Eastern tiles to be off centre and nearer towards the LMC.

Relating this to my work, I do see a distance bimodality in the Eastern tiles and the closer component is found around $K_{\rm s} \simeq 17.0$ mag making it much nearer to the LMC ($K_{\rm s} \simeq 16.9$ mag) than the SMC ($K_{\rm s} \simeq 17.4$ mag) which again confirms the findings of Subramanian et al. (2017) (who found this foreground population to be ~ 11 kpc in front of the main SMC body). Like the works previously mentioned this adds to the body of evidence for LMC–SMC interactions; the nearer component is a direct consequence while the further component was formed afterwards and has an age

constraint via its absence in the RR Lyrae data. The ages of the RC lie between those of the Cepheid and RR Lyrae stars so the similarity with the former can be taken as evidence of an interaction having occurred within the last couple of Gyrs.

However, these features are not seen in the whole Wing. Referring to regions in the West of the Wing; NGC 602 (RA= 18° Dec= −73°) and N83/N84, in the census maps I created, these are slightly spread apart in distance with NGC 602 further away. Both have a more significant SMC distance component than an LMC one. These may form part of a sub-structure. Hammer et al. (2015) show that interactions between the LMC and SMC may have resulted in multiple tidal and ram-pressure-stripped structures.

The line-of-sight depth also reflects on distance bimodality in the Eastern tiles. For example Nidever et al. (2013) found that the Eastern side of the SMC has a bimodal distribution with a near component at 55 kpc and a far component at 67 kpc. In the same Eastern regions I see a large line-of-sight depth and the sources are mainly in front of the plane (i.e. a near component). "he residual maps I created suggest the near component is dominant here. Subramanian & Subramaniam (2012) overall found typical line-of-sight depths (averages of 4.57 ± 1.03 kpc) which increased to 6–8 kpc in the North–East, and a region 0.5 kpc South–West of the optical centre (RA= 9°, Dec= $-73.^{\circ}3$) which contained higher depths than surrounding regions. I do see both features but the latter is easier to see in the full line-of-sight depth map (Figure 6.4; although given how this region runs around a tile edge for the VMC data, I am potentially looking at a feature arising from a tile by tile selection of data). It is worth noting that the line-of-sight depths of the RC stars as found by Subramanian & Subramaniam (2012) and those of the RR Lyrae as found by Muraveva et al. (2018) are comparable, potentially implying these populations occupy similar volumes.

It is not just the East that has distortions; In the West these are the previously described halo and the Counter-Bridge (Ripepi et al., 2017) feature. The Counter-Bridge is significant because it is predicted by the models of Diaz & Bekki (2012) as a remnant of the last close LMC–SMC encounter. However, due to the distances involved (70–80 kpc) its detection has so far only been reported by Ripepi et al. (2017).

The Western distortions I see are mainly on very small scales (about $0.5\,\mathrm{deg}^2$) and in front of the plane as opposed to behind and more likely the consequence of low source density.

The larger scale distortions in the East are not things that are there by chance. That is the direction of the LMC which implies the interactions between the SMC and LMC are responsible.

6.6.4 Population effects

While the photometric properties of the bulk of the RC stars are not very much affected by the effects of age or metallicity, especially in the NIR, it would be prudent to consider whether any of the apparent structures could in actual fact reflect such population variations. The North SMC (RA= 10°–20°, Dec> −71°) appears to have a very different distribution of sources being predominantly behind the plane (see Figure 6.8). The SFH work of Rubele et al. (2018) includes maps of star formation rate, mass and metallicity over age intervals. When looking at their metallicity map (their Figure 12) it can be seen that for the $\log(t/\mathrm{yr})= 9.3$ map the metallicity is about 0.3 dex less that that of the main body of the SMC (making the stars dimmer). However, it is unlikely that younger stars dominate in this region because the other maps show a much greater degree of star formation in the older populations (which have a more uniform metallicity). This makes a metallicity based explanation for this observation unlikely.

Another feature to be tested is the double RC. A metallicity gradient gradient (increasing the brightness) towards the South–East can be seen in the $\log(t/\mathrm{yr})= 9.5$ map but the map is cut off before reaching the South–East double RC region that was dominated by sources in front. This could offer a partial but inconsistent explanation because it is only the case for the South–East. In the North–East neither a more dominant population of age nor differences in metallicity can explain the observations (the metallicity is consistent across age as is star formation) so this would appear to be a distance effect. This also applies to the Western SMC.

7 Magellanic Bridge structure and stellar population

The Magellanic Bridge is the region lying between the Large and Small Magellanic Clouds. This gaseous region connects the two and is thought to be comprised of contents tidally stripped from the Magellanic Clouds during interactions. I set out to discover evidence for Red Clump (RC) stellar populations as their distribution can tell us more about the interactions that took place. Near infrared (NIR) photometry is used to probe the Bridge regions. The age of the RC is sufficient to cover both older stellar populations stripped in the formation of the Bridge and stars that have formed within the Bridge (but the RC is mainly treated as a representation of the former). From density maps the Red Clump is identified although it is clear there is a lot of foreground contamination. TRILEGAL foreground simulations are used to better understand this contamination and mitigate its effects. I present a density and significance map of the Bridge population of RC stars and compare this with recent studies, including my findings about the LMC and SMC from Chapters 5 and 6.

Of the 13 Bridge tiles VMC is observing (see Figure 2.6) this chapter uses data from 11 of these tiles, tiles 1_2 and 3_8 are the two tiles not included due to incomplete observations.

7.1 Colour–Magnitude Diagram and Red Clump identification

The colour–magnitude diagram (CMD) is an important tool for evaluating the sources contained in the data for this region. Figure 7.1 shows the CMD for tile 2_3 of the Bridge region (centred at RA= 33.°7, Dec= −74.°0). Overplotted are contours where the contour lines are drawn with the cell (bin sizes; $Y - K_{\rm s} = 0.1$ mag, $K_{\rm s} = 0.5$ mag) containing the most stars as the peak level and the colour contours are where

the number of sources range from 10%–30% of the peak with step of 5% in yellow, 50%–100% with step of 10% in green, and the 1% level in red. It can be seen that the field is largely dominated by a mix of foreground stars (peaking at around $Y - K_{\rm s} = 1.2$ mag) and background galaxies (at around $Y - K_{\rm s} \simeq 2$ mag).

There is a contour level increase seen in the expected CMD location for an RC star between 50 and 60 kpc away, covering the distances of the LMC and SMC, respectively. I therefore define the following CMD region as containing RC stars:

$$0.65 \leq (Y - K_{\rm s}) \leq 1.05\,{\rm mag} \tag{7.1}$$

$$16.7 \leq K_{\rm s} \leq 18.0\,{\rm mag} \tag{7.2}$$

However, the low density of the Magellanic Bridge means this does not exclusively contain RC stars and this CMD region will be referred to as the RC & foreground stars region. The next step is to determine the foreground content of this region so this can be rectified.

7.2 Galactic foreground estimation and removal

As Figure 7.1 showed, foreground estimation and removal is very important for this region due to the sheer amount of foreground. The best approach here is taking advantage of existing Galactic foreground simulations. TRILEGAL (Girardi et al., 2005) and Besançon (Robin et al., 2003, 2004) are two such models. I have chosen to use TRILEGAL here because its output is calibrated to the VISTA passbands (in fact, its stellar spectral library can potentially simulate the photometry for any broad-band system) making it easy to use and its design allows for easy updating of input libraries (evolutionary tracks, atmospheres) and functions of Galactic components (geometry, initial mass function, star formation rate, age–metallicity relation). The current version 1.6 has been calibrated against 2MASS and SDSS data (Girardi et al., 2012).

A simple description of the TRILEGAL simulation follows. A series of routines efficiently construct samples of stars by interpolating within grids of evolutionary mod-

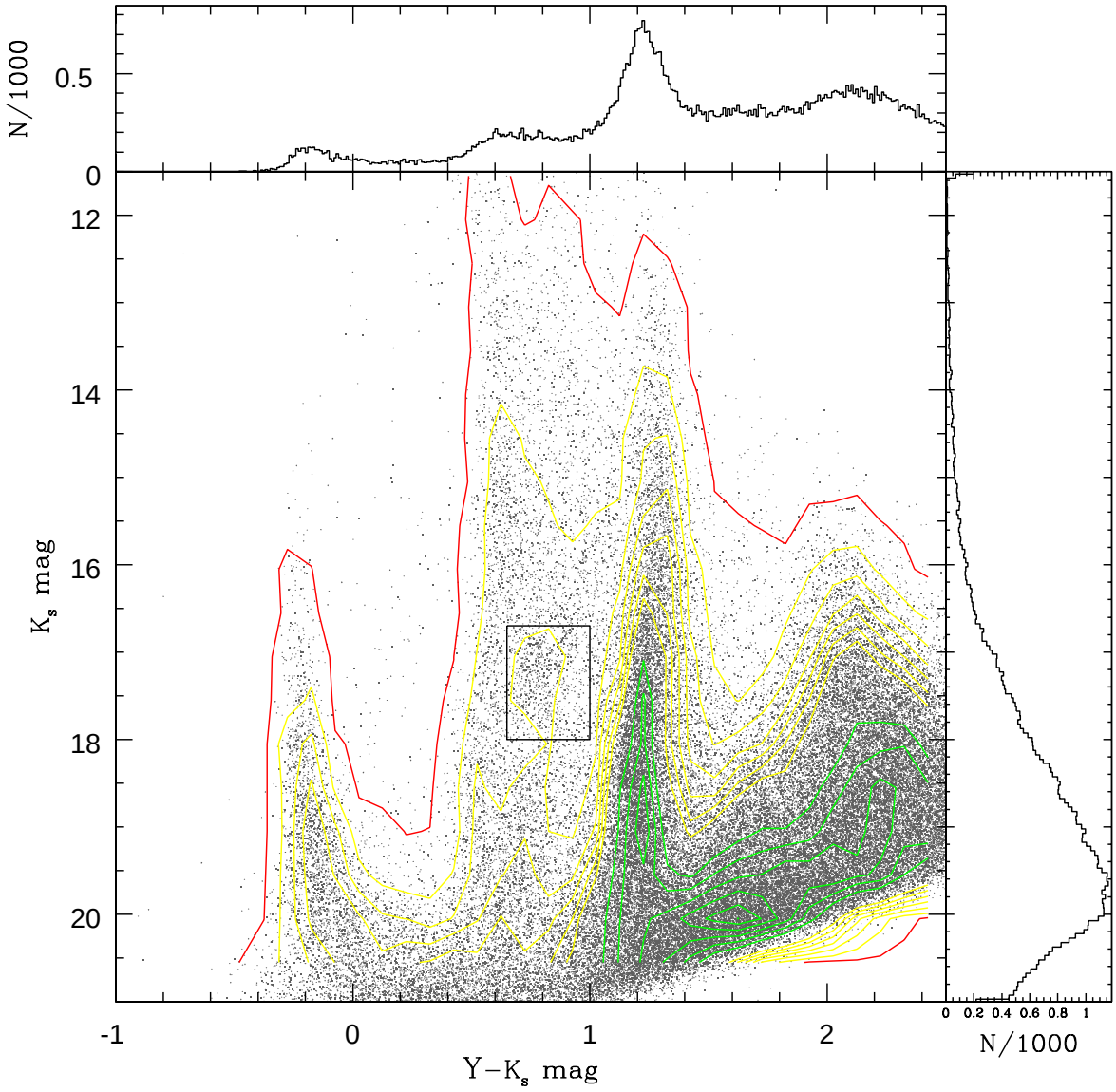

Figure 7.1: K_s vs. $Y - K_\mathrm{s}$ CMD of the tile 2_3 (Magellanic Bridge) accompanied by yellow contours representing density (levels 10%–30%, step 5%), green contours representing density (levels 50% – 100%, step 10%), red contour representing density (level 1%) and histograms of $Y - K_\mathrm{s}$ (bin size 0.1 mag) and K_s (bin size 0.5 mag). It can be seen that this field is largely made up of foreground stars ($Y - K_\mathrm{s} = 1.2$ mag) and background galaxies ($Y - K_\mathrm{s} \simeq 2$ mag). In black the RC & foreground stars region is outlined.

els from the Padova group. The grid is populated on the basis of the assumed star formation history and age–metallicity relation in the disc (and bulge) of the Milky Way. Photometric values are attributed to each star by consulting tables of bolometric corrections, after placing stars at various distances according to the exponential radial and vertical Galactic profiles for those populations (Girardi & Marigo, 2007).

For the input parameters (entered into the online tool at `http://stev.oapd.inaf.it/cgi-bin/trilegal`) a square $2^\circ \times 2^\circ$ region centred on each Bridge tile is used. Other settings were unchanged from their defaults. Due to the mechanisms behind TRILEGAL this was repeated 10 times for each tile and combined. The purpose of this was to remove statistical noise.

A TRILEGAL simulation is shown in Figure 7.2 using the same scale as Figure 7.1. The main difference is since TRILEGAL deals with Galactic foreground, the background galaxies are not visible. This is not a problem as the latter are not an important source of contamination within the RC stars & foreground region. It can be seen that the RC stars & foreground region is not heavily contaminated but has enough foreground contamination to require foreground subtraction to be conducted.

7.2.1 Foreground removal

I explored two approaches to using TRILEGAL for foreground removal. The first was to use the TRILEGAL CMD as a guide to identify numerically consistent *observed* CMD regions within the CMDs for the Bridge tiles. These were then subtracted to remove the foreground from the RC & foreground stars region, revealing the remaining RC population. The methodology of this approach is questionable due to unknowns about how contaminated the CMD boxes used as foreground were (as they overlap with the red giant branch) and how much their completeness varies.

The second approach (and the one used in this chapter) is using the TRILEGAL data for CMD subtraction. This involves binning both the target VMC tile CMD and the TRILEGAL CMD. As small uncertainties in the TRILEGAL simulation can lead to relatively large discrepancies when subtracting from the observed data, the

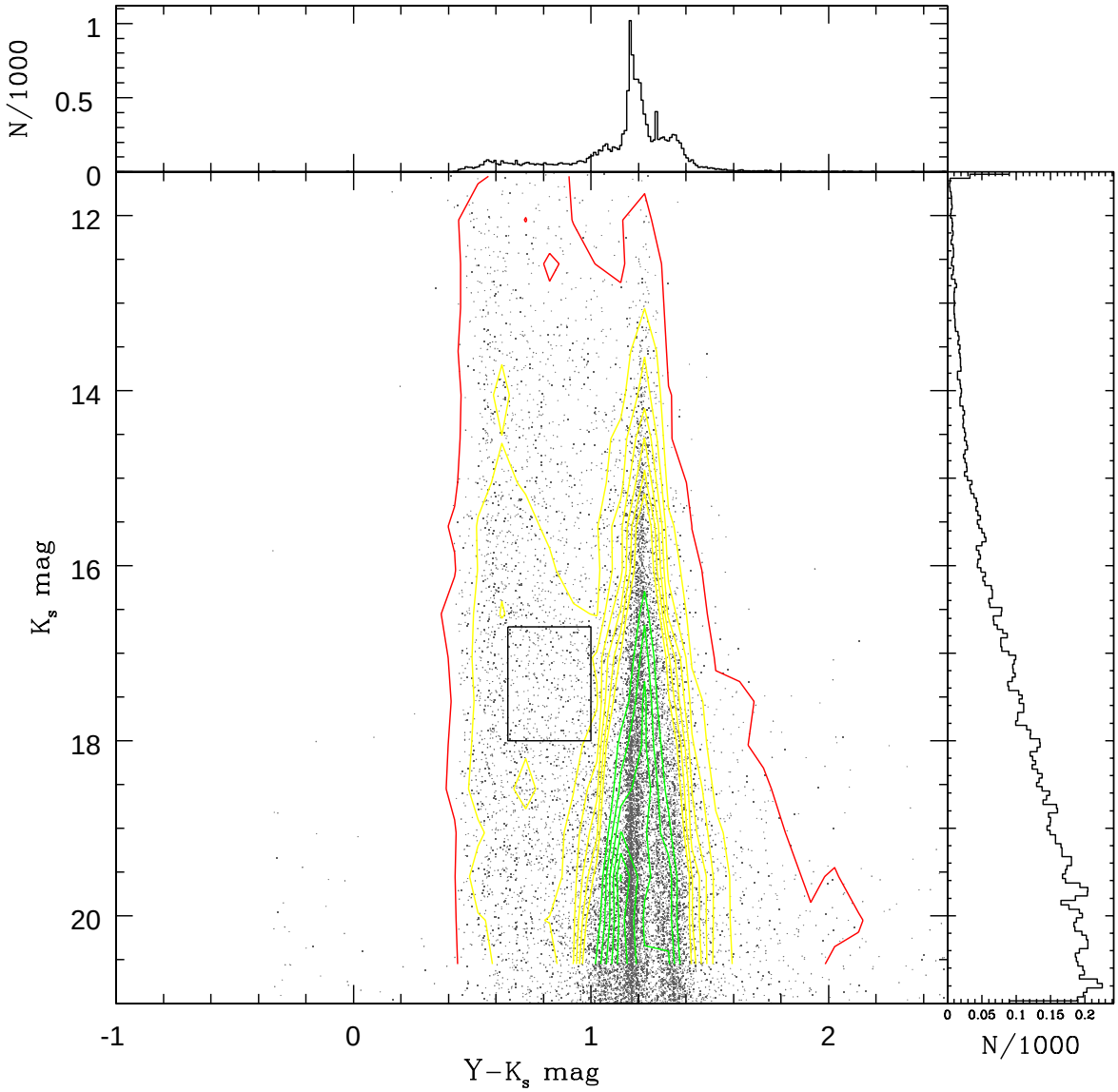

Figure 7.2: K_s vs. $Y - K_s$ CMD of a TRILEGAL simulation of foreground in the direction of tile 2_3 in the Magellanic Bridge. The contour levels and outlining box are the same as Figure 7.1.

TRILEGAL CMD needs to be normalised with respect to the target VMC tile CMD.

For each tile the CMD was binned into 0.05 mag × 0.1 mag regions in $Y - K_s$ and K_s, respectively. This was carried out for the VMC tile and the corresponding TRILEGAL CMD.

To prevent over subtracted foreground the TRILEGAL CMD values are first normalised with respect to those of the binned VMC tile CMD using the value in the CMD location of the TRILEGAL peak. This peak was in the region of $Y - K_s = 1.175 \pm 0.025$ mag and a magnitude range of $K_s = 19.25 - 19.85$ mag.

After this normalisation the binned TRILEGAL CMD is subtracted from the binned VMC tile CMD and the fraction of sources remaining post-subtraction is calculated. This fraction is then used as a confidence map for the original CMD so that sources in parts of poorer recovery of the CMD can be excluded completely from the analysis. This method preserves the RA and Dec information that I use (which the binned CMD lacks).

For the two methods the preliminary results were very similar. The second approach is preferred because it not only lacks the drawbacks described for the first method but the confidence map is a more useful product as it allows for different source filtering to be experimented with. I will now look at the results from this second method.

The histogram data of the binned CMDs can give us insight into the Red Clump population of the Bridge as Figure 7.3 shows (the magnitude range covers more than the RC). The tiles adjacent to the SMC and LMC have the greatest populations which are least affected by the foreground removal. The tiles within the Bridge do contain some peaks (usually around $K_s = 16.8$–17.2 mag) but these are far noisier and barely stand out from the RGB continuum. When omitting pixels where less than 50% of sources survived foreground removal (shown in the bottom panel of Figure 7.3) there is still some noise but the peaks become more clearly defined.

To extend this to the CMD itself Figure 7.4 shows the fraction of sources that survived foreground removal omitting those regions where less than 50% of sources survived foreground removal. The tiles which are most adjacent to the LMC and SMC

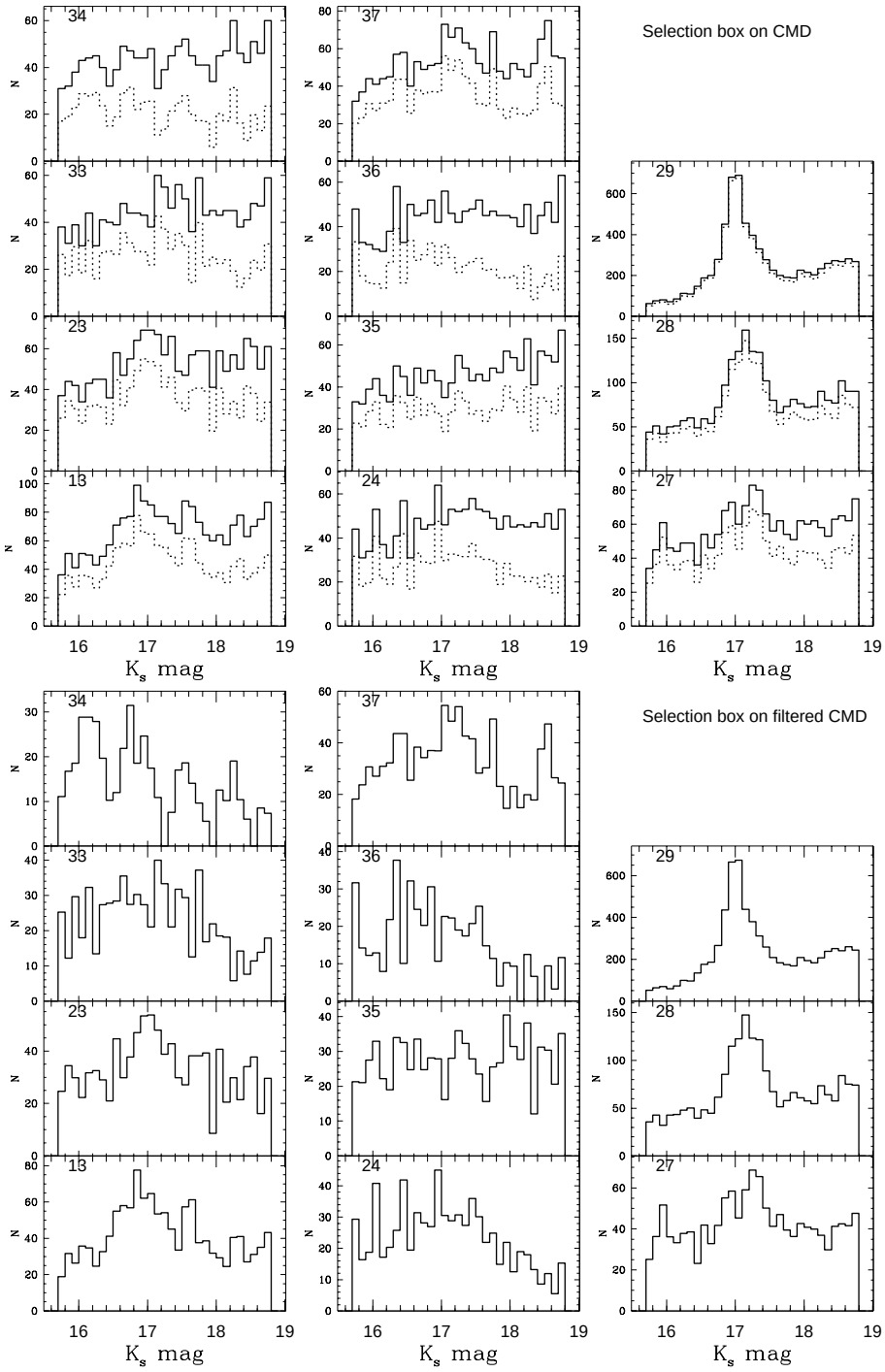

Figure 7.3: $K_{\rm s}$ histogram (bin size 0.05 mag) including the RC selection in Magellanic Bridge (the VMC tile is given in top corner of panel). The top panel shows effects before (solid) and after (dashed) foreground removal whereas the bottom panel omits pixels where less than 50% of sources survived foreground removal.

again have the strongest populations characterised by high amounts of sources after removal with the highest amounts of survival being in those regions associated with the RC stars. However, from this glance there does not appear to be much if any magnitude difference between the LMC and SMC sides. This suggests there is no magnitude gradient between the two. This may be caused by the Bridge connecting a part of the SMC that is nearer to us (due to distortions) with a part of the LMC that is further away from us (due to the disc orientation).

7.3 Results

Figure 7.5 shows a map of the Magellanic Bridge RC sources across the sky. These are placed into three filtered sub samples only containing sources where a certain percentage of sources have survived foreground removal (referred to as confidence). These percentages are stated in the caption of Figure 7.5. The bottom panel of Figure 7.5 shows this as a histogram along RA using bin sizes of 3°. The values are expressed per degree of Declination range which more effectively reflects the source density.

Clearly there are more sources towards the Clouds than there are in between, reducing to its minimum at about RA= 48° (this is essentially nothing when looking at the highest confidence). The pattern seen throughout is a dominant LMC side which is greatly reduced at about RA= 60°. The exact trend West of this depends on the source selection used. In the 'all sources' selection it is fairly constant after this point whereas the confidence selections further decrease, continuing until RA= 40°, followed by a small increase towards the SMC. The amplitude of these variations changes with respect to confidence. The contrasts are most prominent in the highest confidence sample. I would expect the greatest value on the SMC side nearest the SMC but instead I see it in the bin to the East. This is likely caused by data being truncated by the absence of the 1_2 tile. This is investigated further by plotting source density rather than totals.

In Figure 7.6, I produce four sets of maps with bin sizes of 1.°5 in RA and 0.°4

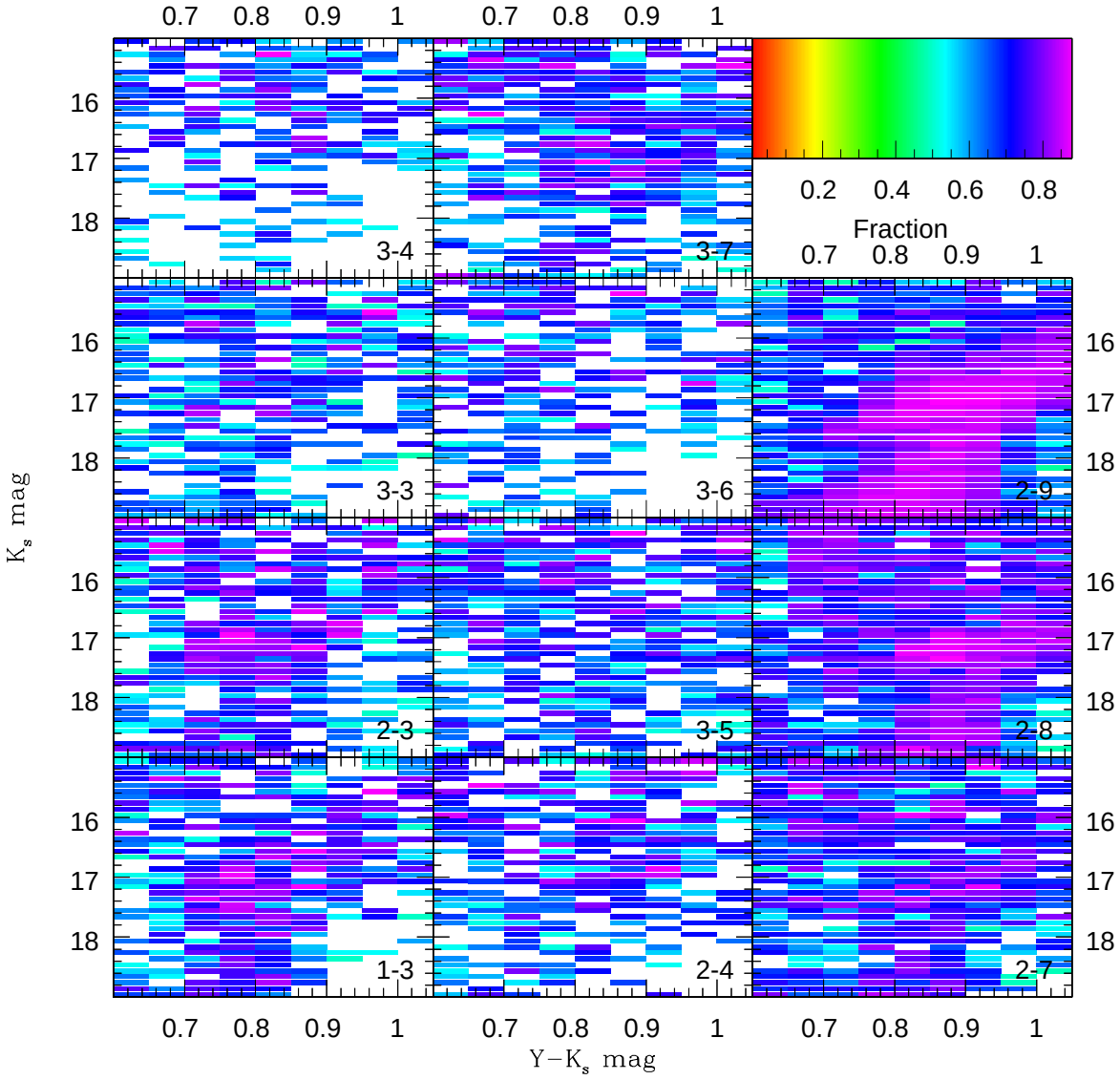

Figure 7.4: Binned CMD of K_s vs. $Y - K_\mathrm{s}$ histogram (bin sizes of 0.05 and 0.01 mag, respectively) in the Magellanic Bridge (VMC tile given in bottom corner of panel) only showing regions where more than 50% of sources survived foreground removal. The top right panel serves as a legend.

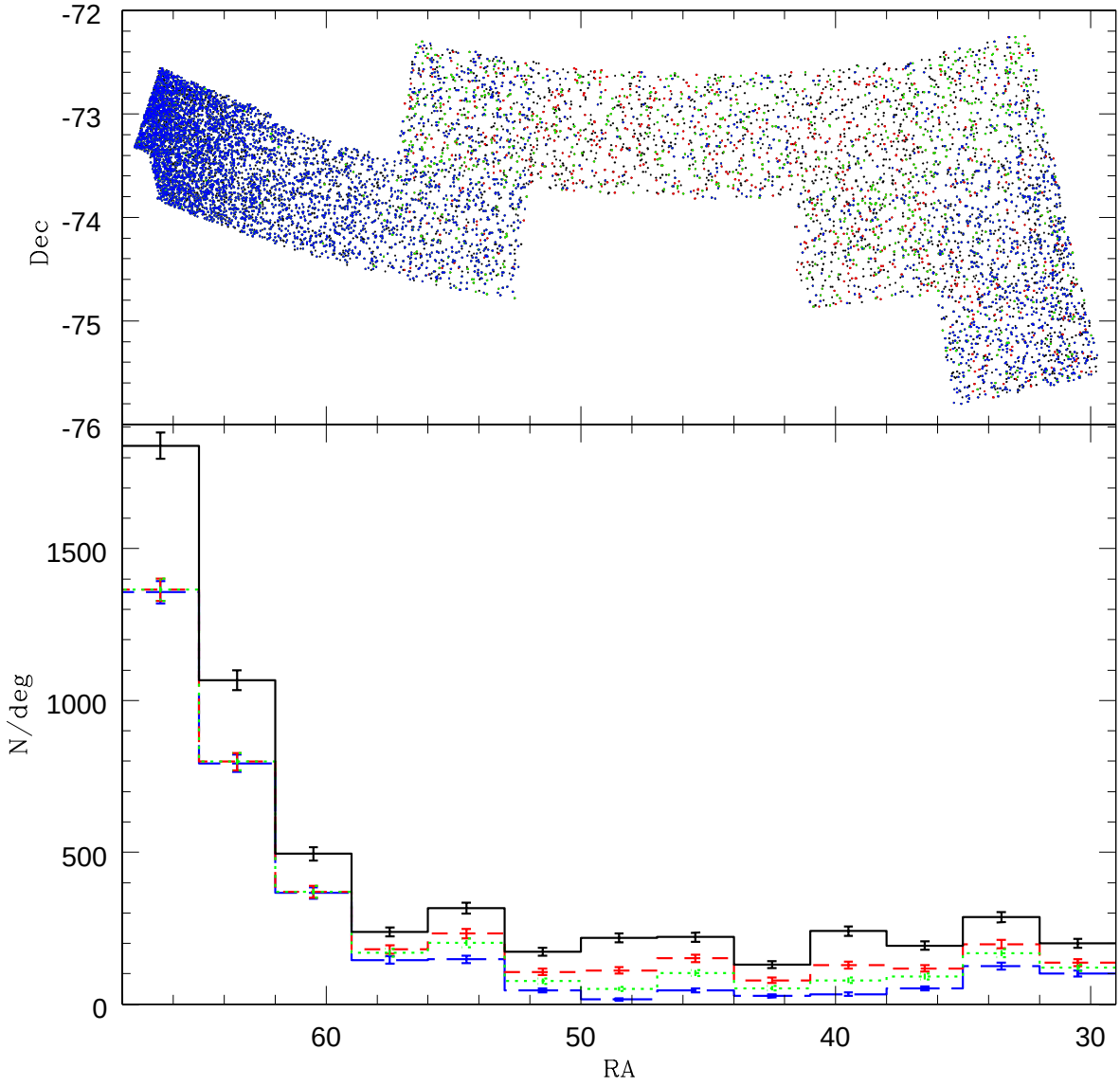

Figure 7.5: Top panel: sky distribution of all sources within the RC selection box (black), sources with a probability to have survived foreground removal of $> 50\%$ (red), $> 66\%$ (green), $> 75\%$ (blue). Bottom panel: Histogram of source distribution over RA per degree of declination using same colours as top panel. The bin sizes are 3° in RA.

in Dec. These maps show the number of sources per square degree (to account for variances in declination and sky projection) for the RC & foreground stars region and the three confidence levels. It can be seen that only including the regions with more than 75% confidence causes the map to contain very few sources between 36° <RA< 50°.

The most significant regions are found Eastward of RA= 57° and Westward of RA= 36°. The region in-between has a low stellar density which forms a continuous link under lower confidence but under the highest confidence is not statistically significant. While I do see increases towards the LMC and SMC this is much larger on the LMC side. The cause lies in Bridge tile 2_9 (RA= 64°, Dec= −73.5°) overlapping slightly with LMC tile 3_2 (see Figures 2.4 & 2.6) whereas the Bridge tile 1_3 does not overlap with any any SMC tiles. Both of these observations do appear to show evidence for extended tails from their respective galaxies though.

7.4 Discussion

At the time when the VMC survey regions were being proposed, the distribution of the stellar population of the Bridge was poorly known. The VMC survey looked at a limited region of the Bridge. This was based off the source densities of the 2MASS, DENIS and SuperCOSMOS databases (Cioni et al., 2011) where the VMC tiles would overlap some of this area while following a continuous pattern.

7.4.1 Comparison with previous optical surveys

Harris (2007) found evidence of a younger stellar population extending from the SMC towards the LMC. Their Eastward extent of population is truncated at RA= 45°. While it is true I also see a truncation around there, I also see a rise shortly after which could be a population effect (as they suggest the younger population can not form due to the H I gas density falling below the threshold required for star formation).

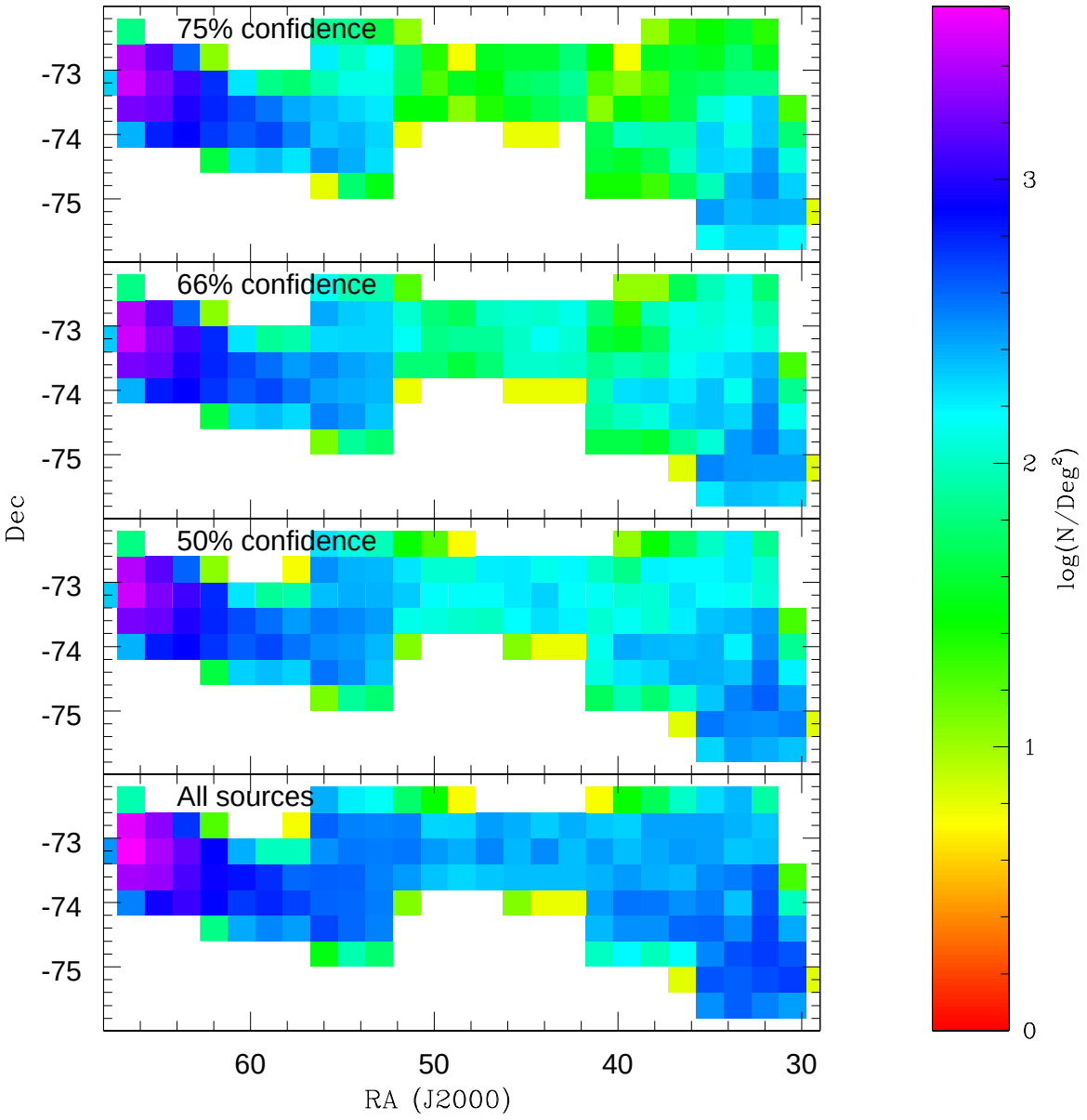

Figure 7.6: Maps of the Magellanic Bridge. Each region is $1.^{\circ}5 \times 0.^{\circ}4$. Numbers of RC star candidates are per square degree and scaled logarithmically. From bottom to top; all sources, with $> 50\%$, $> 66\%$, $> 75\%$ confidence.

Harris (2007) was unable to find evidence of an older population. Noël et al. (2015) & Mackey et al. (2017) also found younger populations correlated with H I density.

In the work of Noël et al. (2013) for the intermediate-aged stars, they found these were not present in fields at a similar distance from the SMC in a direction pointing away from the LMC. My work finds something slightly different. In Figure 7.3 peaks are more commonly seen at around $K_s = 17.0$ mag than they are at $K_s = 17.4$ mag. These provide potential evidence that these intermediate-age stars could have been tidally stripped from the SMC towards the LMC. The distribution of stars is looked at in Noël et al. (2015) finding that intermediate aged populations were mainly found in the Bridge but these are more spread out than the younger populations and have the properties of SMC stars. From my work it would appear the RC stars follow the H I gas connecting the LMC and SMC but the gas density itself only has minor effects on the star counts with distances from the main bodies being a larger contributing factor.

However, there have also been more recent works which have found older populations than these (and indication of tidal stripping) which I explore in the following subsections.

7.4.2 Comparison with a previous infrared survey

Bagheri et al. (2013) looked at the older populations via 2MASS data finding a number of sources with estimated ages between 0.4–5 Gyr. These sources need follow up for confirmation of Bridge membership.

While my data covers a narrower range of declination, I superimposed my foreground subtracted numerical map onto figure 9 from Bagheri et al. (2013) and the result is shown in Figure 7.7. Focusing on the blue plusses (representing previously unpublished sources) there is good general correlation with more sources in the East side toward the LMC and fewest sources around RA= 45°. In general the selection looks slightly offset when compared with the RC stars. This may be due to it being a different population (while their ages are in the range possible for RC stars the CMD region they used is not).

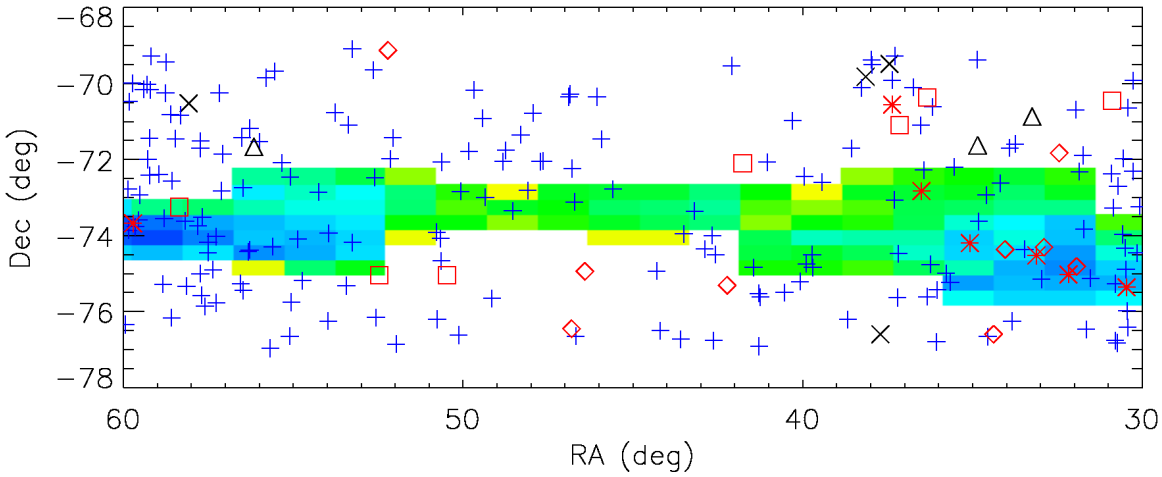

Figure 7.7: The 75% confidence map of Figure 7.6 superimposed onto figure 9 from Bagheri et al. (2013). The symbols represent: previously unpublished sources found by Bagheri et al. (2013) (blue plusses), Magellanic Cloud halo sources (red diamonds), known SMC sources (red stars), known Bridge objects (red squares), other known sources (triangles) and background galaxies (crosses).

One thing this comparison does suggest is that the VMC survey is justified in not covering the region around RA= 40°–45°, Dec=−74° (between tiles 2_4 and 2_7) because these would not yield a great change to the current results.

7.4.3 Comparison with the OGLE-IV survey

Skowron et al. (2014) examined the Bridge using OGLE IV data covering 270 square degrees. Their approach to foreground removal was to use tiles away from the Bridge to act as a sample foreground tile. They normalised and binned the CMD of these Bridge tiles and the foreground tiles and subtracted the CMDs from each other. This enabled them to observe multiple populations, not just the RC. They compared using this method of foreground tile subtraction to the TRILEGAL and Besançon simulations and found that the χ^2 for these were twice as large when compared to their data subtractions. Note that in my approach I normalised the TRILEGAL simulation to

the likely-to-be foreground part of the observed CMD, greatly reducing the χ^2.

For the 754 sub-fields of the Bridge, they provide the population density found per square degree in their Table 2, of which a full digital version is available from the OGLE website. Their subfields are $0.335\,\mathrm{deg}^2$ making them a subset of the $1.4\,\mathrm{deg}^2$ OGLE-IV fields. Selecting regions that lie around the VMC coverage region, I plot a triangulated map of the data in Figure 7.8 containing a truncated exponential. The triangulated maps use 200 of their sub-fields.

A complete comparison is not possible due to their coverage of a vastly wider area (over 15° of declination in comparison to the near 3° of VMC, although they state that the range from Dec= $-70°$ to $-75°$ is the conservative Bridge region). This means I can not make comparisons for the Southern region, which is of interest as it also showed a RC star population unlike the Northern where they found it traced the radial profile of the galaxies (my data are covering the central region).

The source counts are different between the data sets with my data having lower numbers. This suggests I may have been too aggressive with my foreground subtraction or that they did not sufficiently remove foreground. Numbers aside, there are some common features between the data sets with source counts increasing towards the LMC and SMC and greatly decreasing in-between, especially within the RA= 42°–52° region. The Skowron et al. (2014) data treats a lot of that as background due to low source counts. In terms of how the source counts scale Eastward of RA= 35° the LMC end (RA= 64°) has over three times as many sources than the SMC end for both sets of data.

Figure 7.9 shows the histogram created from the 200 sub-regions as a comparison to Figure 7.5. A similar pattern of dip occurs, with the LMC side having greater stellar density than the SMC side. The lowest value of the dip is fairly consistent between the Skowron et al. (2014), my findings and those of Harris (2007). The bottom of this dip represents the mid-point between the centres of the LMC and SMC. An interesting difference between Figures 7.5 and 7.9 is that there remains a greater continuity compared to my work which suggests the LMC to be extended out to RA= 40°. Another cause of this difference may be due to the region not covered by VMC (which

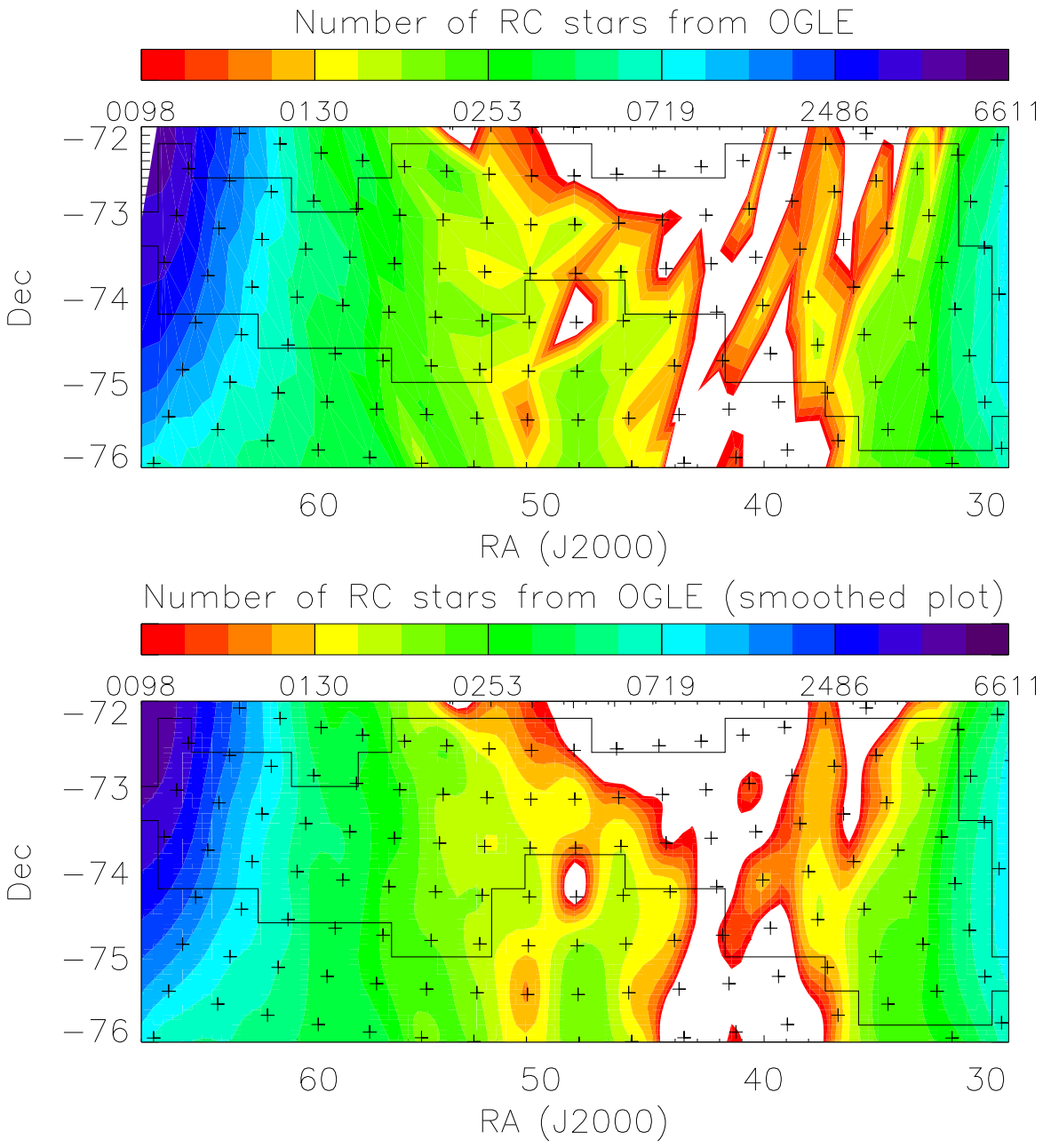

Figure 7.8: Skowron et al. (2014) mapped data for RC stars from 200 sub-regions showing number of stars per square degree, original data (top) and smoothed data (bottom). Sub region centres are marked with crosses. Black outline is the binned region of Figure 7.6. Regions where source counts are below 86 stars per square degree are not plotted as Skowron et al. (2014) treat these as background. Scale for contours is $86 + e^{((x/3)+2.45)}$ where $x = 0 - 19$.

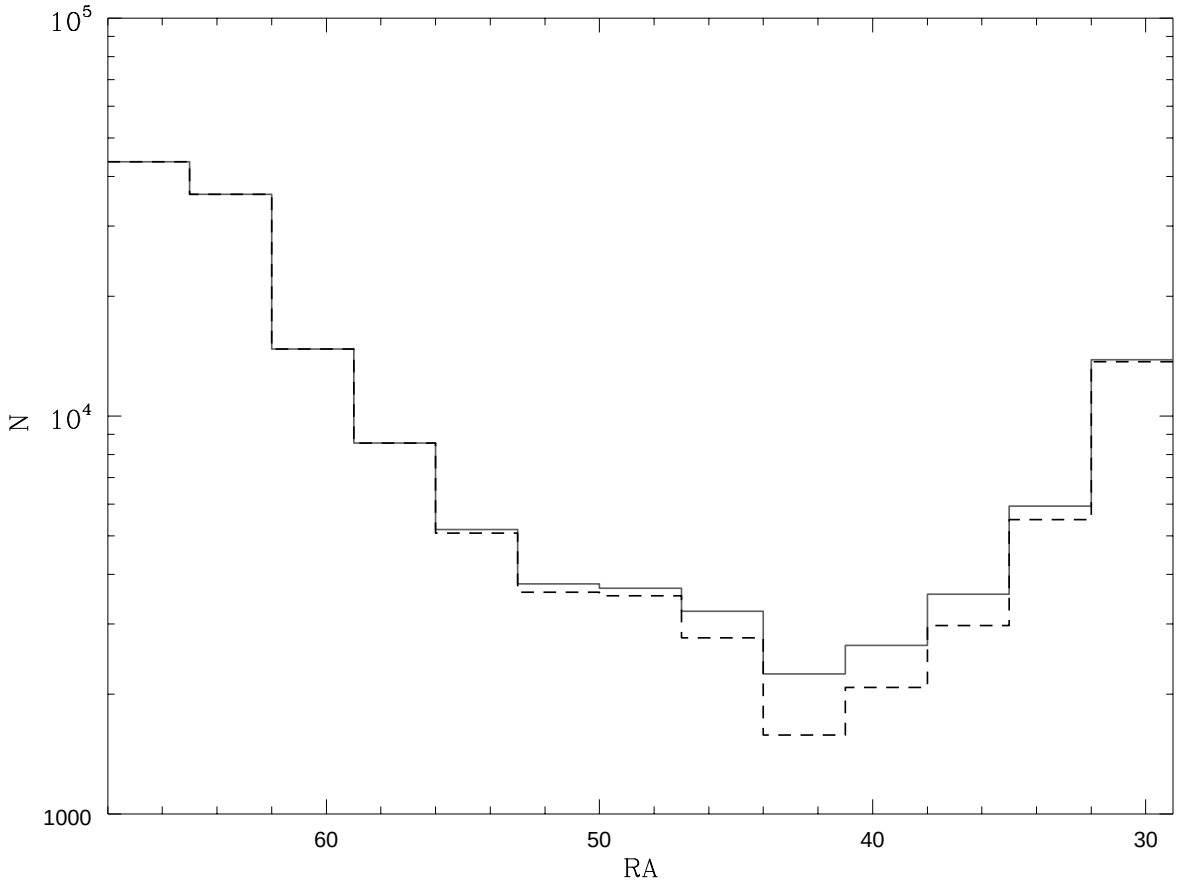

Figure 7.9: Histogram for RC stars (bin size 3°) based on Skowron et al. (2014) data. y axis is logarithmic sum of stars per square degree in the bin region. Dashed black lines exclude sub regions containing less than 86 RC stars (solid grey lines include these).

Figure 7.8 shows is just as significant as the fields North of it, although these are fairly insignificant regions in general).

7.4.4 Relation between Bridge and Clouds structure

Like Skowron et al. (2014), Belokurov et al. (2016) also investigated the region 5° South from the H I. However, they found evidence that the Bridge is a composite of LMC and SMC material based on two different RR Lyrae structures separated by distance. The

nearer of these structures, found at the LMC distance, is easier to detect (the other structure does have a smooth distance gradient going from the SMC to the LMC). Looking at Figures 7.3 & 7.4 it is possible the lack of K_s difference between the RC (as seen in CMDs and histograms) in the SMC and LMC end is evidence of a similar structure affecting the RC stars within the H I. I previously stated that the regions of the Bridge which VMC data observes connect to a part of the SMC that is nearer to us (due to distortions) and a part of the LMC that is further away from us (due to the disc orientation). There is evidence for this in the previous Chapters of my thesis. The South–West region of the LMC that connects to the Bridge is further away in distance than the main body (as implied by the dimmer magnitudes seen in Figure 5.4). This distance is due to the tilted plane and the region concerned fit well with the plane fitting. On the SMC side, while we are missing Bridge tile 1_2 (which connects with SMC tiles 2_7 and 3_8) I do see that the RC stars in South–East SMC had double peaks in front of and behind the plane. An extension of the feature in front of the plane would explain why I see the RC in Bridge tiles 1_3 and 2_3 at distances more typical of the LMC side of the Bridge.

8 Conclusions and Future work

In this thesis the well-defined luminosity and colour of the Red Clump (RC) stars allowed me to make maps of the interstellar reddening and distance modulus across the Magellanic System. Utilising the NIR $YJK_{\rm s}$ photometry of the VMC survey to select RC stars, using a method which combines selection boxes, Hess diagrams and reddening vectors, I was able to apply these techniques in a number of ways.

This chapter will be split into three sections; conclusions to the individual Chapters 4–7, an overall conclusion arising from this and the future work.

8.1 Research findings in 30 Doradus, the LMC, SMC and Magellanic Bridge

8.1.1 Dust around the 30 Doradus star forming complex

In Chapter 4, I used VMC observations to select RC stars in the 30 Doradus region in the LMC. Isochrones were combined with SFH to determine the intrinsic colour for a RC star for calculation of extinction. I converted this extinction into A_V values and produced a map of this made available in several formats. I was able to use the RC stars to probe extinction up to $A_V = 6$ mag.

I compared with the optical reddening map (also based on RC stars) of Haschke et al. (2011) (which were converted to A_V). I found the most disagreements at the extreme ends of the data as infrared is less affected by low extinction and optical being too heavily affected by high extinction. In general though I found that Haschke et al. for a given value of extinction had 75% of the A_V my work found.

I compared with H I column densities from Kim et al. (1998) by converting the A_V into total H column density. I encountered limitations in the H I ISM (at very high densities hydrogen becomes molecular) but was able to use this to determine the atomic–molecular transition starts at column densities of $N_H \simeq 4 \times 10^{21}$ cm^{-2} and is

largely complete at $N_H \simeq 6 \times 10^{21}$ cm^{-2}. Also, I was able to map out molecular cloud regions based on the total column density and excluding regions of atomic hydrogen.

I compared with the Spitzer SAGE dust emission from Meixner et al. (2006), finding overall agreement with some differences in the detail, due presumably to temperature variations of the emitting grains. In particular, an Eastern region is prominent in extinction maps and the H I (as high extinction and dense regions, respectively) but is not a feature in the MIR emission maps. This may highlight some small scale structure. In general I found the 70μm emission a better tracer than the 24μm emission. This may be due to RC stars not heating dust to the extent warm stars would and/or RC stars not being found in the proximity of warm stars (which would warm the dust).

Finally, I took another look at reddening in the R136 region using an abundance of young stars present in the region. I see the young stars have similar reddening to the RC stars and use them to examine the relationship between A_V and DIB equivalent width using data from the FLAMES Tarantula survey (van Loon et al., 2013) finding similar results to what they found when using O-and B-type stars. This shows it is possible to use other populations to supplement the reddening map.

8.1.2 Structure of the Large Magellanic Cloud

Using the VMC observations, in Chapter 5 I selected RC stars across a wide LMC region (49 of the 68 tiles that the survey is expected to cover), calculating extinction for each of these, which was used to de-redden them. The dereddened stars then had their relative distances calculated for looking at line of sight depth and then were placed into a Cartesian co-ordinate system in order to fit a plane based on minimization of the squared residuals. The data points in the plane were based on average values contained in sub-regions. The fitted planes had position angle and inclination values and the plane solutions were used to examine residuals.

The extinction map showed high extinction along the main body of the LMC. In contrast to the H I and MIR SAGE maps this was more continuous although the ridge located around the LMC 5 supergiant shell is seen in my map as well as the H I and

MIR SAGE maps.

A distance modulus gradient of around 0.2 mag is seen going from the North–East to the South–West of the LMC. I found line-of-sight depths of around 6 kpc within the LMC bar, 4.5 kpc in the main body of the LMC which decreased to around 3.2 kpc in the outer regions.

I found inclinations from the plane solution of $i \simeq 24°$ for the outer LMC which do agree with previous NIR RC studies. The inclination from the inner LMC plane solution is shallower than previous studies suggesting LMC bar influence and that the LMC bar is not part of the disc. This was further backed by its presence in front of the plane and the slightly extended magnitude range of bar regions. There were disc distortions seen in the North–East and South–West edges of the LMC.

8.1.3 Stellar structure of the Small Magellanic Cloud

In Chapter 6, I used the VSA PSF photometry covering the entire SMC to learn about the structure of the SMC as seen from the RC stars using several proxies. The first of these was a reddening map which showed agreement with dust emission (especially the MIR at 8μm) although an important H II region (NGC 456) was initially harder to spot.

Using the reddening map, a de-reddened line-of-sight depth map was created. The large depths seen in the East lead to re-examining magnitude distributions of the RC stars across the SMC. From this, a double RC component was seen whose nearer component is around LMC distance. While this feature has been reported in Subramanian et al. (2017), to which I had contributed, here I have shown how this feature varies across a larger area of the sky.

The residuals from plane fitting once again emphasised these Eastern regions revealing structure that is not described by a plane in the peripheries of the SMC. The inclinations from the plane fitting solutions ($i = 35.^{\circ}4 \pm 1.^{\circ}$ for the inner-dominated census selection) lie between the very shallow inclinations reported for older RR Lyrae populations ($i \simeq 2°$) and younger Cepheid populations ($i \simeq 60°$).

The structures within the SMC mainly arise from its past close interaction with the LMC which is evident in that the East – which is nearest to the LMC has the greatest distortions.

8.1.4 Magellanic Bridge structure and stellar population

In Chapter 7 I used the VMC survey to find evidence for an intermediate-aged population within the Magellanic Bridge along the central Bridge region covered ($-75° <$Dec$< -72°$). I selected a region containing RC stars and quantified the Galactic foreground using TRILEGAL. I produced maps with a cell size of $1.^{\circ}5 \times 0.^{\circ}4$ where each cell is foreground subtracted, and significance maps of these. Perhaps due to the low overall source counts I find the most significant population lies in the East, nearest to the LMC. Looking at magnitude distributions and the CMD after foreground removal there did not appear to be a distance modulus gradient between the LMC and SMC ends of the Bridge. Along the Bridge, the LMC tail seemed to dominate but seamlessly turn over to the SMC after a dip around RA $= 48°$. This is consistent with where H I levels drop off.

Comparing these findings to the literature, the younger populations (e.g. Harris 2007) correlate with H I levels and do not recover after dropping off Eastward from RA$= 40°$ unlike the intermediate-aged populations I examined. There is consistency with the older population found by Bagheri et al. (2013) although my results appear a little offset. When comparing with another RC study done by Skowron et al. (2014) using OGLE data the source counts appear very different. It is unclear whether I over-estimate foreground contamination or they under-estimate it. However, the trend with position along the Bridge agrees very well between my and their studies.

As I said before, I do not find a distance gradient along the Bridge – the RC population appears to be at the LMC distance even seen in direction close to that of the SMC. This is corroborated by the findings of Noël et al. (2015). Belokurov et al. (2016) identified an additional population (besides the one at LMC distance) which does appear to show a gradient in distance from the LMC to the SMC.

Unfortunately, the decisions for the locations of the VMC tiles along the Bridge were made before the Skowron et al. (2014) and Belokurov et al. (2016) results and, in hindsight, are not optimal for tracing all of the Bridge stellar population(s).

8.2 Overall conclusions

The selection of the RC stars combining CMDs, Hess diagrams and reddening vectors was by and large successful in obtaining a large stellar population across a wide extinction range. Relying on CMD density did have its problems, occasionally seen in low population regions around the edges of the Magellanic Clouds producing unusual results, and particularly in the Bridge region where a somewhat different approach had to be taken.

While observations in the NIR do not have to worry about dust and extinction as much as optical studies the RC is a powerful tool to use to map this out so that others using less fortunate data have an idea of what to expect. In mapping out the extinction this has allowed me to be less affected by interstellar dust and in fact, correct for the remaining effect while simultaneously being able to use the reddening as a tracer of the interstellar dust and the densest part of the ISM. For example in Chapter 4 it was demonstrated to be capable of mapping out molecular clouds around 30 Doradus.

The intermediate age of the RC stars means their population is well positioned to reveal the intrinsic structure of the Magellanic Clouds (LMC disc, for instance) as well as the distortions resulting from the interactions. I did see this in both the LMC and SMC. In the LMC these were in the form of tidal warps (also seen in Subramanian & Subramaniam 2010, for example). The SMC was more interesting where a double RC is seen in the East. These features, in addition to the LMC bar still need to be fully explained.

Finally, to return to the introduction I had three specific questions which I had hoped these data and methods would help to answer. I return to these questions:

Position and orientation of the LMC bar. My results show that at least part of

the LMC bar is found in front of the LMC and the orientation differs from the LMC. The orientation change is exhibited in how the plane fit of the LMC changes when exclusively containing this region.

Tidal warps and tails, in the LMC disc and extending from the SMC. In the LMC there was some evidence for warped structure shown in the form of some regions being offset from the plane itself. In particular the North–East and South–West corners.

The SMC tail is found along the Bridge and the distinct double RC feature in the Eastern SMC is a tidal warp. Both of these are features at distances closer to that of the LMC than the SMC (the other half of the double RC is at SMC distance).

Dynamical features that have hitherto evaded detection. A lot of the dynamical structures I saw did have explanations in the literature. The South–Western part of the LMC did not but I was unsure of its reliability due to low source density. However, the existing studies were usually on smaller scales and so with my data I could find these features on a large scale. An example is the intermediate-aged population along the H I in the Magellanic Bridge. Recent research, however shows this region is not the most abundant for stellar populations.

8.3 Future work

Ideally one would want the age and metallicity for every single RC star in the Magellanic System. However, considering that accurate metallicities for RC stars are obtained spectroscopically more limited census samples would have to be used instead. One spectroscopic approach is to use the calcium triplet (CaT). The strength of these lines has been correlated with the [Fe/H] metallicity, where Carrera et al. (2013) determined a calibration that is valid for a wide range of metallicity; $-4 \leq$[Fe/H]≤ 0.5. Instruments such as the Robert Stobie Spectrograph (RSS) on the Southern African Large Telescope (SALT) and FORS2 on the VLT are capable of measuring this and the application of this approach is tried and tested before with the RC (e.g. Mauro et al. 2014) and for the LMC (e.g. Cole et al. 2005). Age determinations on the other hand also make

use of this wavelength range employing spectral synthesis methods using Fe I and Mg I lines in conjunction with CaT (Kordopatis et al., 2011).

Another thing I wanted to explore with regards to the structure is seeing how the line-of-sight depth and true, plane-corrected depth differ. The true depth can be obtained by plane correcting the Cartesian coordinates using the plane solution.

While I showed reddening maps for the LMC and SMC I did not make detailed comparisons to existing ones in the literature. As Chapter 4 showed interesting findings when comparing optical RC and NIR RC extinction maps the 30 Doradus tile it would be interesting to see if these trends apply to the LMC as a whole or if there are regions where the optical and NIR data produce more similar results. I would also like to compare ISM studies (such as mid- and far-IR and H I and CO) in more detail for the MCs.

One mystery when looking at LMC structure was the 30 Doradus tile appearing dimmer than the surrounding tiles (see Figure 5.4, top–right panel). While I discussed some possible causes I had nothing conclusive. I have recently found out that this is in fact due to a systematic overestimation of magnitude within this tile. This effect is fairly small but does reach $\Delta K_{\rm s} = 0.05$ mag which is approximately how much dimmer the 30 Doradus tile is than its surroundings. The causes of this systematic error are the brighter backgrounds caused by crowding and nebular gas emission and this affects the aperture photometry but not the PSF photometry. This insight arrived too late to apply a re-calibration. Also as a word of caution this needs to be investigated in other tiles – especially the LMC bar tiles which also contain high stellar density and hence crowding. This systematic offset does have implications for absolute distance modulus determinations based on aperture photometry. Once the VMC has completed all observations, PSF photometry will become available also for the LMC, thus (hopefully) solving the issue.

As I suggested in the concluding remarks of Chapter 7, the Magellanic Bridge region requires a much more extensive survey region to fully appreciate the intermediate-aged population. While this is an unrealistic prospect to observe using VISTA there may be a suitable wide-field NIR survey instrument in the future.

Finally, it must be remembered that a huge motivation for looking at the Magellanic Clouds is what they can tell us about interacting pairs of galaxies and their distance to us means they will continue to be observed extensively.

A Appendix

A.1 30 Doradus reddening map

In this section the appendix of the work contained in Chapter 4 and Tatton et al. (2013a) is covered.

A.1.1 Red Clump peak variances

I analyse how the RC varies across the tile by splitting the tile into a 4×3 array (12 regions; shown in Figure A.1). I locate the CMD area of highest density, corresponding to the most populated bin (using the same bin sizes as before: 0.01 mag in $J - K_{\rm s}$ and 0.05 mag in $K_{\rm s}$; this limits their accuracy) and compare this with the median for colour and magnitude for each region; the values are in Table A.1. Figure A.2 shows the histogram distribution of the RC stars in colour (top) and magnitude (bottom). For each region the normalised (with respect to the peak) average of regions 0-0 and 3-2 are over-plotted in dashed red as a low extinction comparison. From this, it is seen that the regions with higher median colours have their source distribution extended in the redder component rather than a complete offset (i.e. they are positively skewed). This suggests that for a given region not all of the stars are affected by reddening but there is a multi-layer structure with some stars lying in front of the cause of the extinction. When comparing the contour peaks, which mirror the histogram peaks, to the median values, the difference is generally larger when the extinction is higher. The clearest example of this effect is in region 1-1 where 30 Doradus lies with a difference of 0.067 mag. Regions found to the North–West and South (1-0, 0-1, 0-2, 1-2) have similar difference. All these regions have strong H I and Hα emissions which may be related to the cause of this effect.

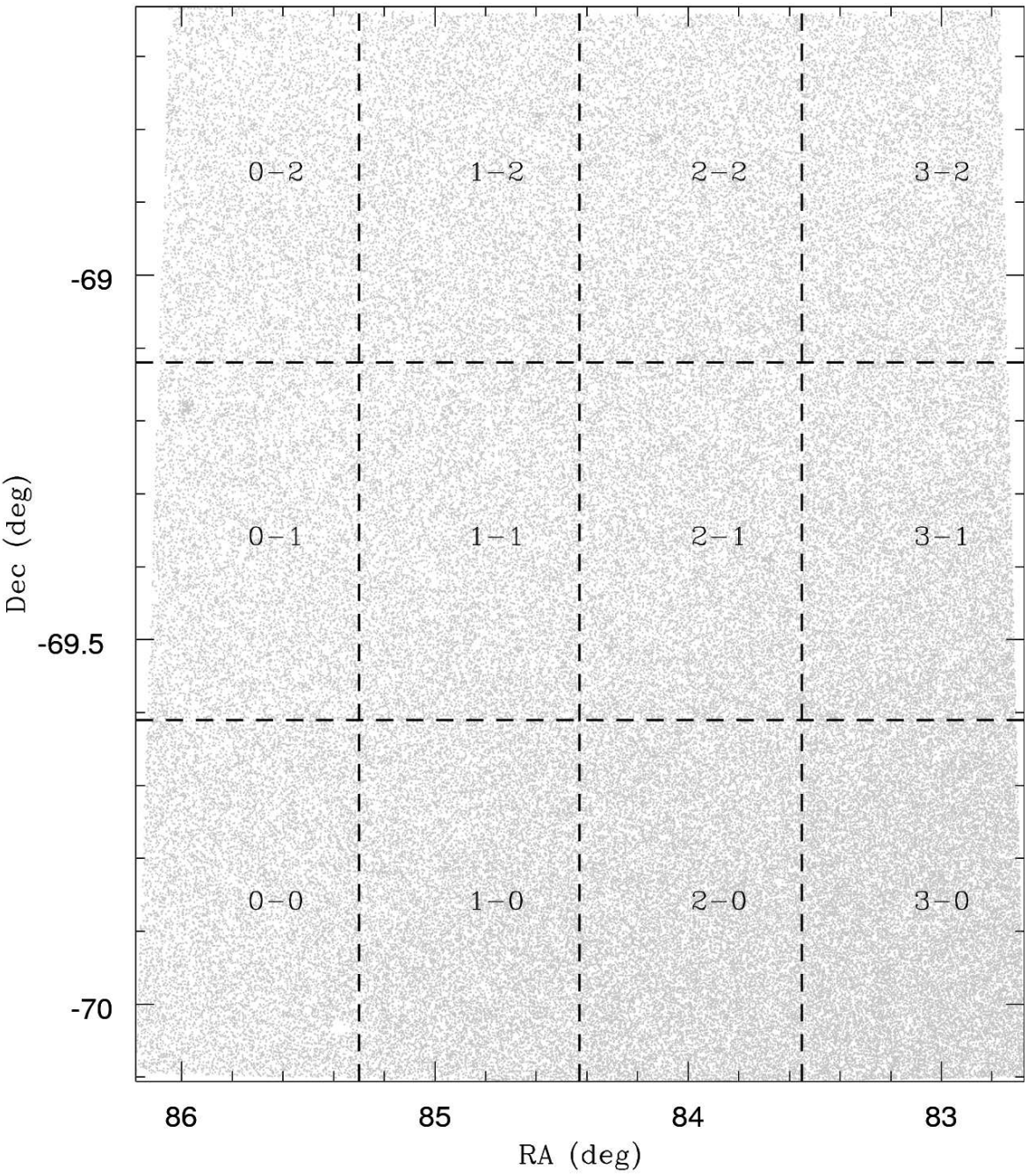

Figure A.1: Field 6_6 split into a 4×3 array for analysis of RC variance (shown in Figure A.2). Region names labelled.

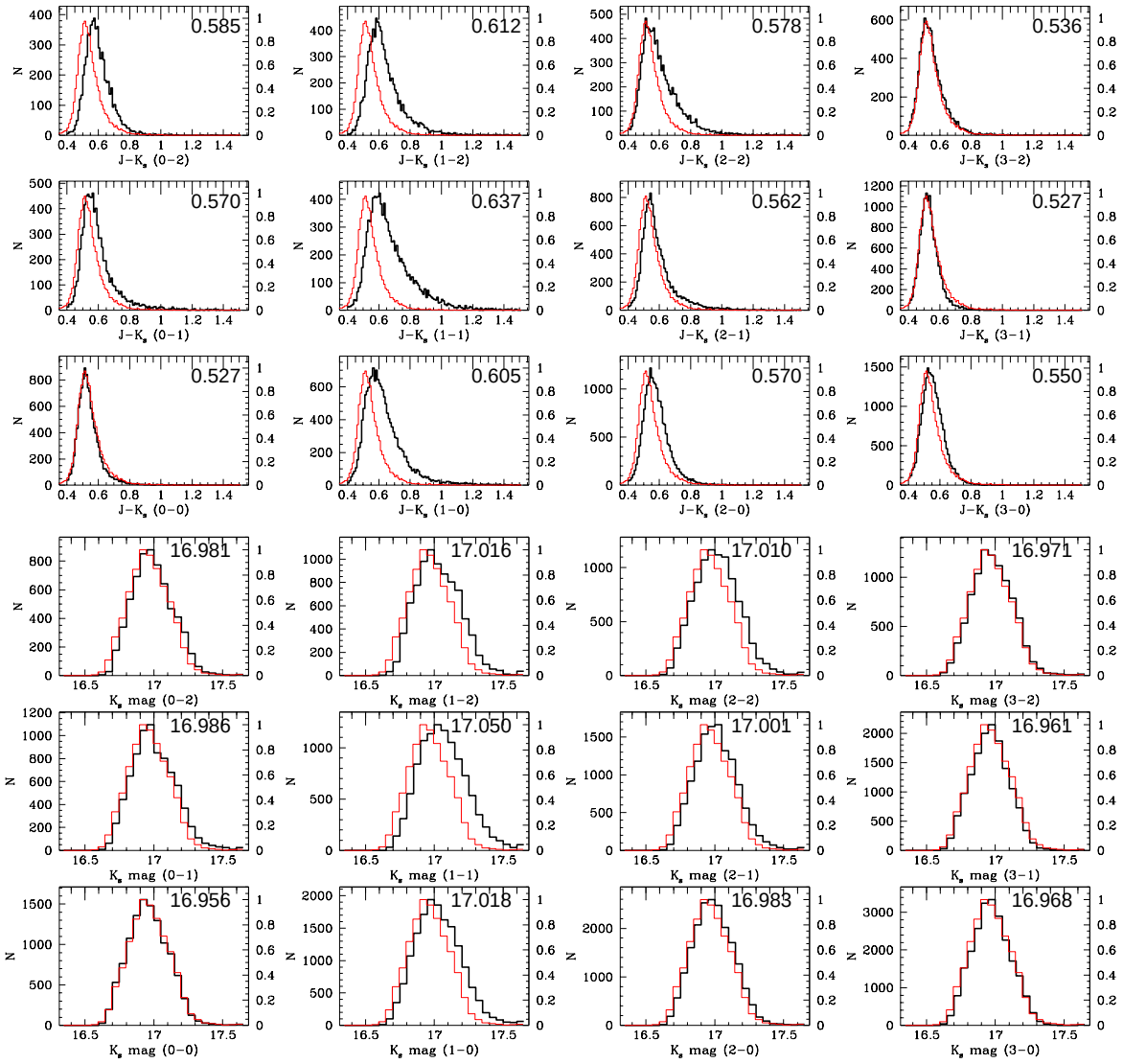

Figure A.2: Histograms of the $(J-K_{\rm s})$ colour (top 3 rows, bin size of 0.01 mag) and $K_{\rm s}$ magnitude (bottom 3 rows, bin size 0.05 mag) across the field (regions in parentheses defined in Table A.1). Value in top–right is the median. Overplotted in red is the normalised mean of regions 0-0 and 3-2.

Table A.1: RC peak position across field 6_6 from median in CMD region and contour map peak position.

Region	Centre (deg, J2000)		Median		Contour[a]	N_{RC}
	RA	Dec	$(J-K_s)$	K_s	$(J-K_s)$	#
0-0	85.74	−69.87	0.527	16.956	0.52	11396
0-1	85.74	−69.37	0.540	16.986	0.56	8168
0-2	85.74	−68.87	0.585	16.981	0.57	6389
1-0	84.87	−69.87	0.605	17.018	0.56	15894
1-1	84.87	−69.37	0.637	17.050	0.57	10619
1-2	84.87	−68.87	0.612	17.016	0.60	8613
2-0	83.99	−69.87	0.570	16.983	0.55	19677
2-1	83.99	−69.37	0.562	17.001	0.54	12763
2-2	83.99	−68.87	0.578	17.010	0.51	9658
3-0	83.11	−69.87	0.550	16.968	0.52	23180
3-1	83.11	−69.37	0.527	16.961	0.53	14534
3-2	83.11	−68.87	0.536	16.971	0.53	9432

Notes. [(a)] For contour method the peak in magnitude is always $K_s = 16.95$ mag.

A.1.2 Extinction laws

In section 3.2.2 I mentioned that there are alternative extinction laws that could have been used instead (or rather, would have to have been used had the $E(J-K_s)$ coefficients not already been calculated for our data in a model independent way). Here, I discuss these in more detail.

Table 6 of Schlegel et al. (1998) gives $A_J/A_V = 0.276$ and $A_K/A_V = 0.112$. Therefore, $E(J-K) = 0.164 \times A_V$. These Schlegel et al. values are for JHK for UKIRT's IRCAM3, while our observations are in VISTA YJK_s. Both the UKIRT and VISTA photometry are in a Vega magnitude system.

However, UKIRT's IRCAM3 and VISTA have different filter curves and system transmissions in detail, particularly in K/K_s. This causes the post-calibration magnitudes to vary slightly. In Figure A.3, the filter curves and synthetic spectra of a RC

Table A.2: Extinction ratio A_λ/A_V for VISTA passbands.

Passband	$\lambda_{\rm central}$ (μm)	$\lambda_{\rm eff}$ (μm)	a(x)	b(x)	A_λ/A_V
VISTA J	1.252[a]	1.254	0.3987	−0.3661	0.2806
VISTA $K_{\rm s}$	2.147[a]	2.149	0.1675	−0.1538	0.1179
UKIRT[b] J	1.250[c]	1.266	0.3926	−0.3605	0.2764
UKIRT[b] K	2.200[c]	2.215	0.1595	−0.1465	0.1123

Notes. References:
(a) `http://casu.ast.cam.ac.uk/surveys-projects/vista/technical/filter-set/vista-filter-set`
(b) UKIRT IRCAM3
(c) Schlegel et al. (1998)

star are shown (produced using model atmospheres from Castelli & Kurucz 2004). The J band widths are very similar, the main difference being at about 1.27 μm where the VISTA transmission dips while the UKIRT one rises. The $K_{\rm s}$ passband curve begins before the K passband, finishes before it and the overall width is nearly identical. The extinction coefficients do vary slightly with spectral type (van Loon et al., 2003). This variance is small in the NIR (0.004 mag from A0 to M10 star in the J band).

The $\lambda_{\rm eff}$ and central wavelength values are given in Table A.2. The ratios to A_V are derived from the $R_V = 3.1$ curve meaning the $A_{K_{\rm s}}/A_V$ value is derived using equations 1, 2a and 2b in Cardelli et al. (1989); the results are shown in the rightmost column of Table A.2.

Using the VISTA values the conversion becomes $E(J - K_{\rm s}) = 0.1627 \times A_V$, a difference of ~ 0.01 mag with band-by-band differences of ~ 0.05 mag when comparing the two systems. A drawback of this method is that it assumes the filter is well represented by the $\lambda_{\rm eff}$ point, rather than taking into account the full filter transmission curve. When comparing with the result from Section 3.2.2; $E(J-K_{\rm s}) = 0.16237 \times A_V$, I see this simplification has had a rather small effect on the conversion, finding 102% of the used value and a maximum A_V difference of ~ -0.013 mag.

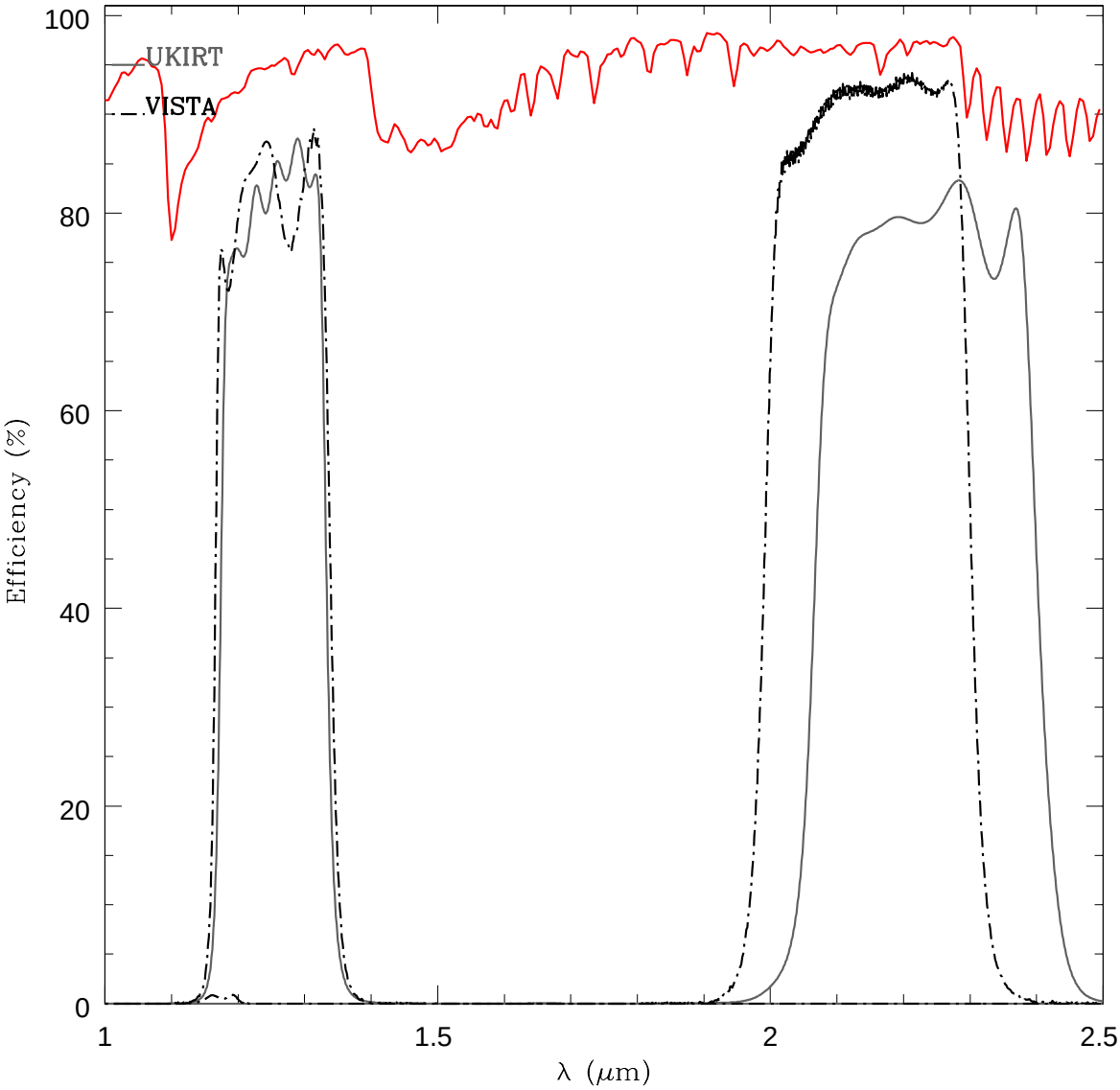

Figure A.3: Comparison of wavelength vs. efficiency for the transmission of UKIRT (IRCAM3) J and K filters (in grey) and VISTA J and K_s filters (in dashed black). Curves from JAC and ESO, respectively. Synthetic spectra of a typical RC star in red.

Some of the difference between UKIRT and VISTA values might be accounted for by how the $\lambda_{\rm eff}$ is calculated because the VISTA $\lambda_{\rm eff}$ values were calculated using equation 3 of Fukugita et al. (1996) (which was defined in Schneider et al. 1983) and accounting for the Quantum Efficiency curve while Schlegel et al. (1998) did not state how the UKIRT $\lambda_{\rm eff}$ was calculated (only that it represents the point on the extinction curve with the same extinction as the full passband).

A.1.3 Using the Y band

Figure A.4 shows a CMD of $K_{\rm s}$ mag vs. $(Y - K_{\rm s})$. It is very similar to the $K_{\rm s}$ vs. $(J - K_{\rm s})$ CMD seen in Figure 4.2 with the difference of an extended colour axis due to a larger wavelength difference between the two bands. Focusing on the region of the RC I overplot the isochrones used in Section 4.5. This is shown in Figure A.5. I see that the older isochrones lie bluer than the RC. This confirms, as expected, that the Y band is more affected by extinction towards the MCs than J or $K_{\rm s}$ are. When applying $A_V = 0.249$ mag (Schlegel et al., 1998) as foreground Galactic extinction the $(Y - K_{\rm s})$ and $(J - K_{\rm s})$ are in a consistent position in the context of the contour levels (around the 35% level). This shows that the Y band, being closer to optical is more affected by extinction which would be a boon for low extinction regions because the contrast between extinctions would be greater. However, for a high extinction region it offers no advantage and has the disadvantage of stars being fainter in Y than in $K_{\rm s}$. Colour–colour diagrams do not aid in selection of RC stars.

The RC selection box is defined like it is in Section 4.3. For $(Y - K_{\rm s})$ the reddening vector is shallower (with a gradient of 0.5) and the colour limits are $0.75 < (Y - K_{\rm s}) < 2$ mag. Combined with an intrinsic colour of $E(Y - K_{\rm s})_0 = 0.84$ mag and $E(Y - K_{\rm s}) = 0.2711 \times A_V$ the furthest I can probe is $A_V = 4.28$ mag. The histogram for the RC selection is shown in Figure A.6. Comparing with Figure 4.6 I see the peak is at a slightly higher A_V in the selection (due to greater foreground Galactic extinction probed). The percentage of stars relative to the peak at $A_V = 1$ mag and $A_V = 2$ mag is very similar in both histograms.

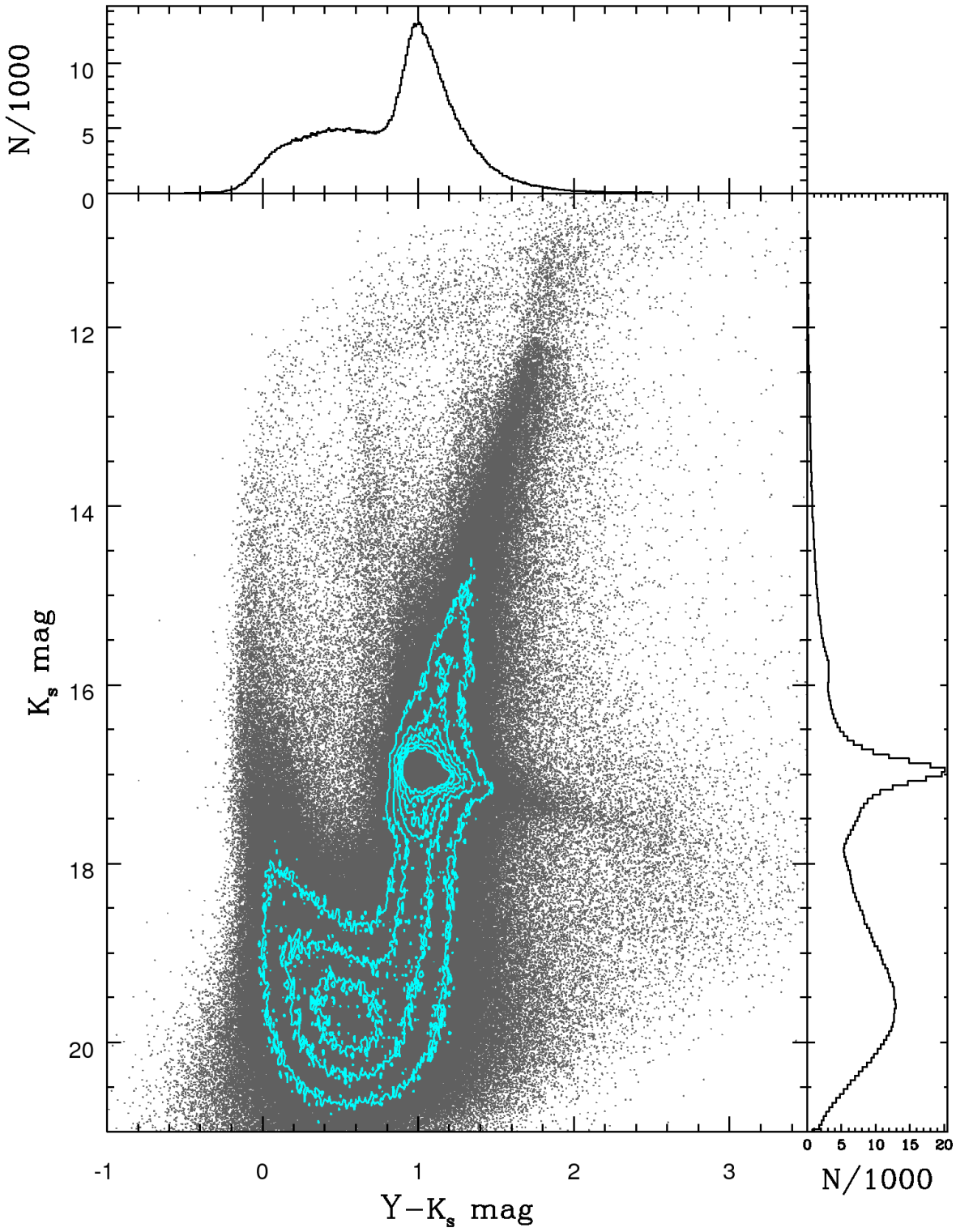

Figure A.4: K_s vs. $(Y - K_s)$ CMD of LMC field 6_6 accompanied by cyan contours representing density and histograms of $(Y - K_s)$ (bin size 0.01 mag) and K_s (bin size 0.05 mag). It can be seen that this field is largely made up of main sequence and RC stars.

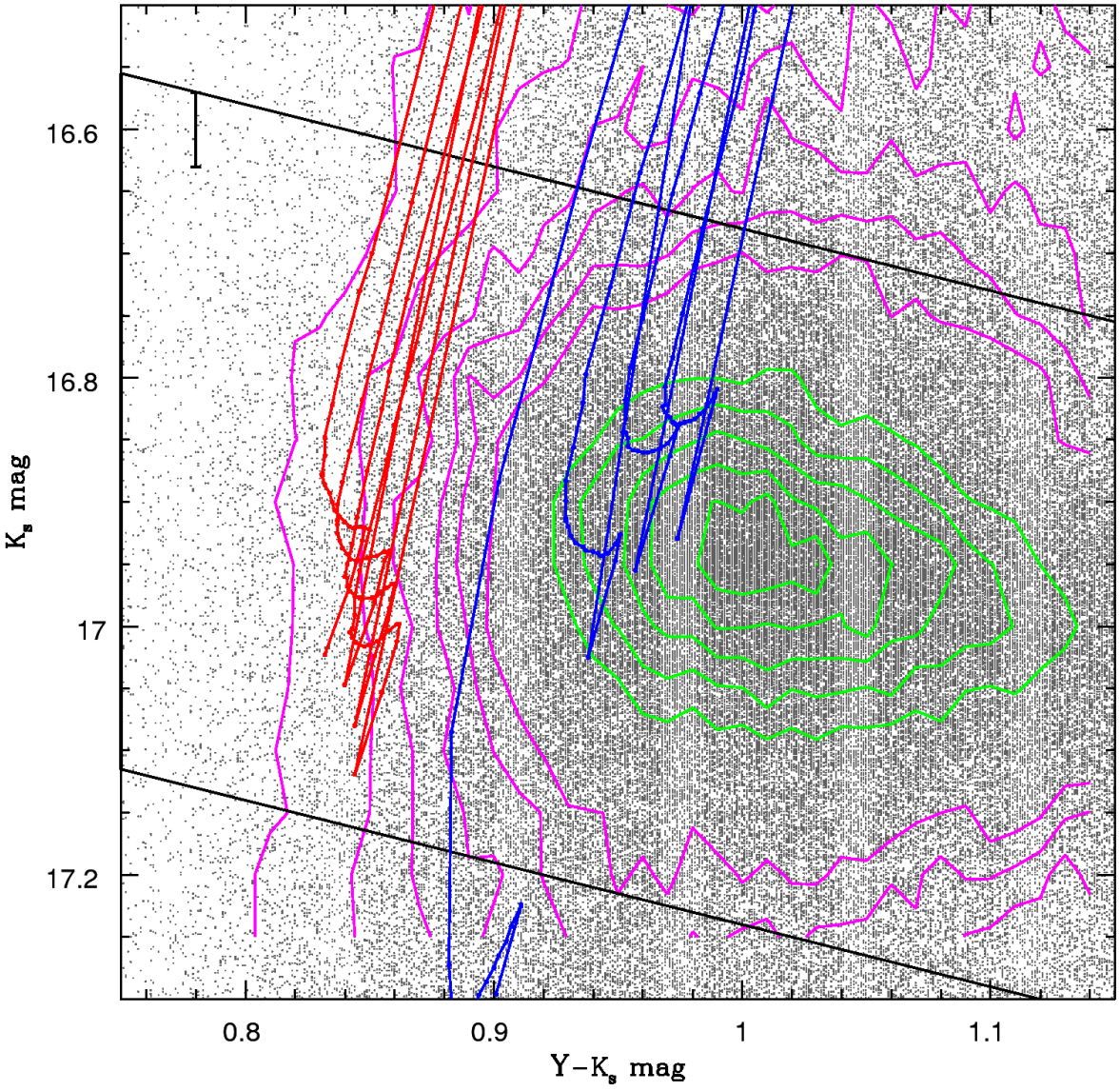

Figure A.5: $(Y - K_{\rm s})$ vs. $K_{\rm s}$ CMD with isochrone lines for the helium burning sequence for the same two metallicities and age ranges as in Section 4.5. Younger, more metal rich ($\log(t/{\rm yr}) = 9.0 - 9.4$, $Z = 0.0125$) are in blue and the older, more metal poor ($\log(t/{\rm yr}) = 9.4 - 9.7$, $Z = 0.0033$) are in red. Error bar represents error in LMC distance. Contours are plotted in magenta and green and have the same levels as in Figure 3.1. The older population can be seen to be at the 5% contour level.

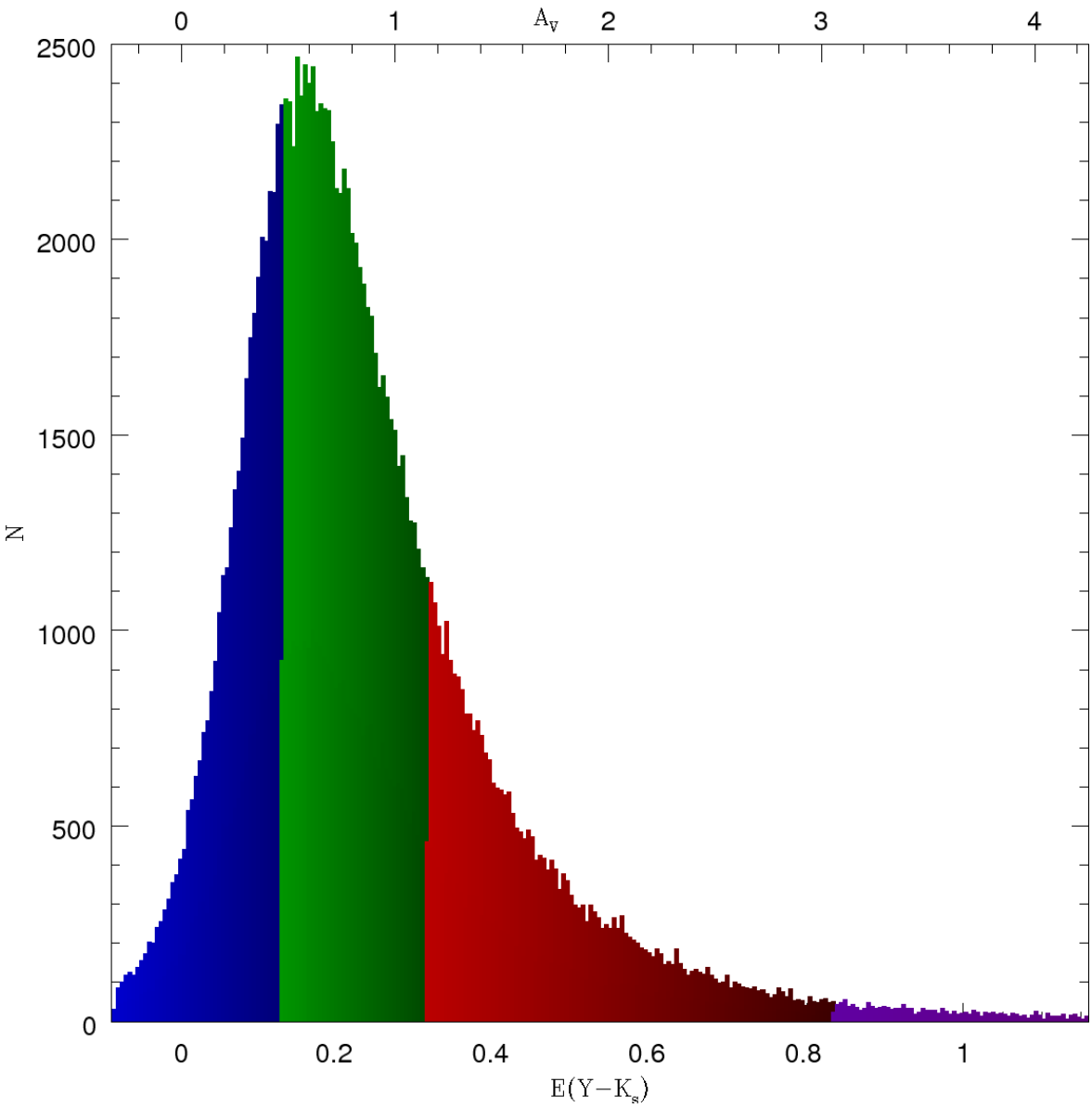

Figure A.6: Histogram of $E(Y - K_s)$ (bottom) and A_V (top) distribution with bin size of 0.005 mag. Green is the region covering 50% of the sources centred on the median where darker blue is lower than this and brighter red higher and purple extremely high.

Table A.3: LMC residual slice ranges (kpc) for H I centre solution.

Inner LMC selection plane (kpc)				
Quartile	1	2	3	4
Min	-8.831	-2.283	-0.022	1.991
Max	-2.283	-0.022	1.991	7.877
Range	6.548	2.261	2.013	5.886

Outer LMC selection plane (kpc)				
Quartile	1	2	3	4
Min	-9.391	-2.563	-0.302	1.698
Max	-2.563	-0.302	1.698	7.590
Range	6.828	2.262	1.999	5.892

Whole LMC selection plane (kpc)				
Quartile	1	2	3	4
Min	-9.243	-2.437	-0.176	1.823
Max	-2.437	-0.176	1.823	7.716
Range	6.806	2.261	1.999	5.892

A.2 LMC structure: residuals

Contained in this Appendix are the residual mainly from the H I centre solution. These were omitted from the main text due to them being too similar to those from the optical centre solution and thus having no merit to discuss them.

Figure A.7 shows a histogram of the residuals (bin size 0.2 kpc) for the H I centre solution. Table A.3 describes the statistics of the quartiles which are used to produce the residual quartile maps in Figures A.8–A.10 when using the inner, whole and outer plane solutions, respectively. The median residual value map for the H I centre solution is found in Figure A.11.

Finally, Figure A.12 shows the residual quartile maps for the optical centre solution when using the plane solution for all sub-regions.

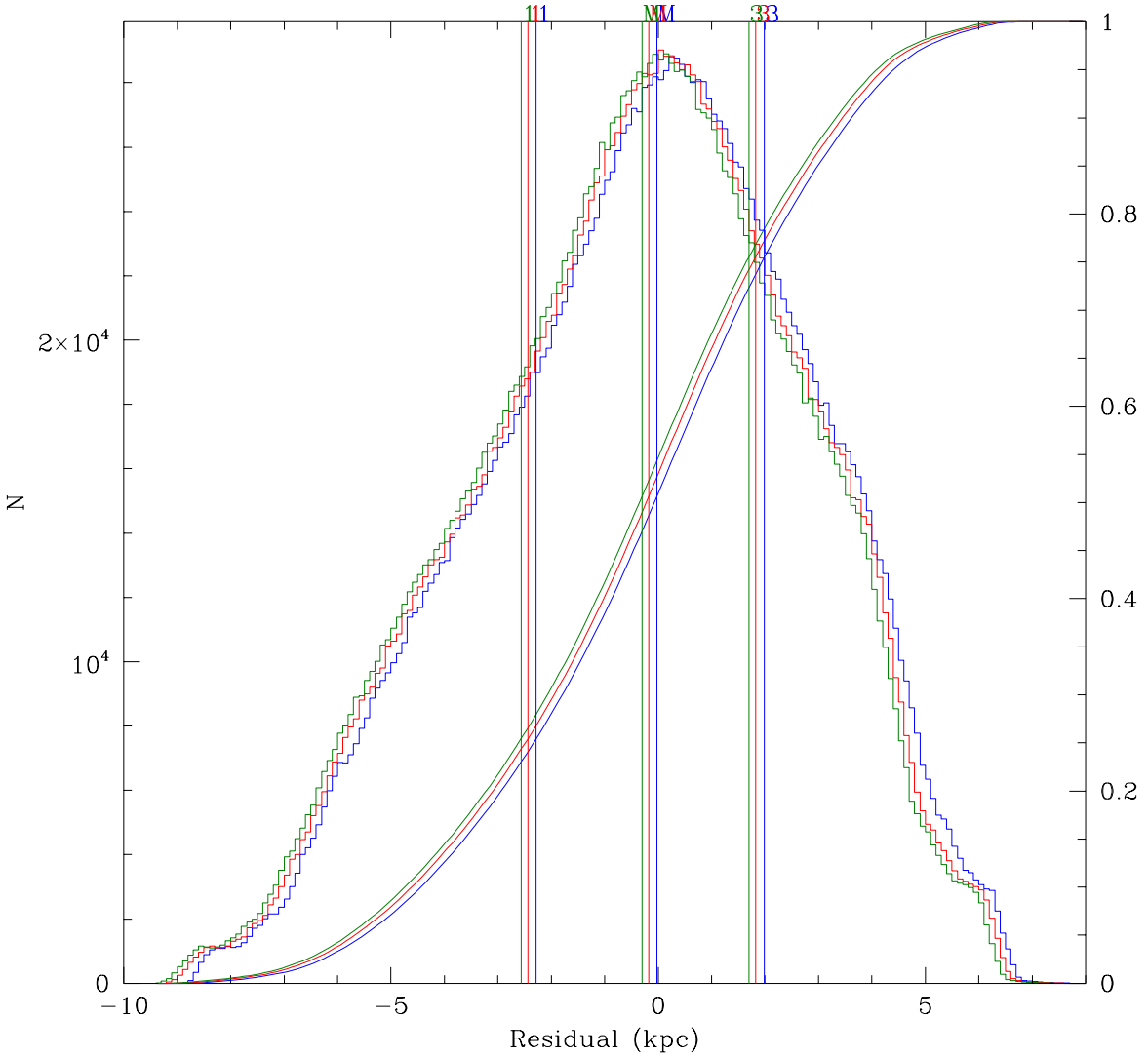

Figure A.7: Histogram of residual from plane (bin size 0.1 kpc) for outer (green), whole (red) and inner (blue) LMC selections with the H I centre solution. 1st and 4th quartiles cover a wide range of distances (although for the former, much of this range is due to very few sources). Location of the boundaries of the 1st, 2nd and 3rd quartile are labelled as 1, M and 3, respectively using the same colours as the selections. Cumulative distributions are also illustrated (values on the right hand side of the y-axis).

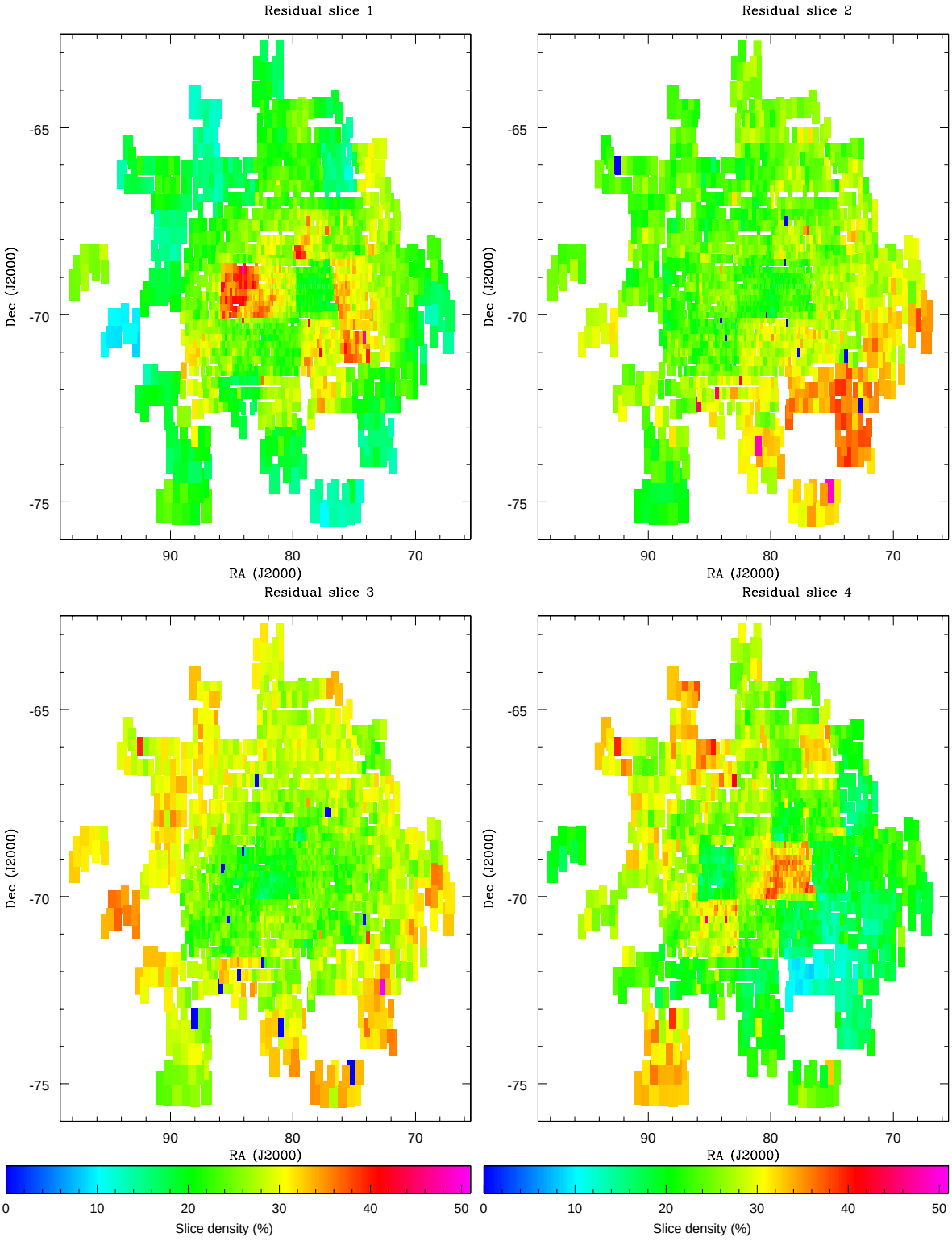

Figure A.8: For H I centre, using the plane solution derived from the inner sub-regions and overlaid on regions from census method. Each slice contains 25% of the total RC stars. The slice density states what percentage of a given sub-region's sources are contained within that slice.

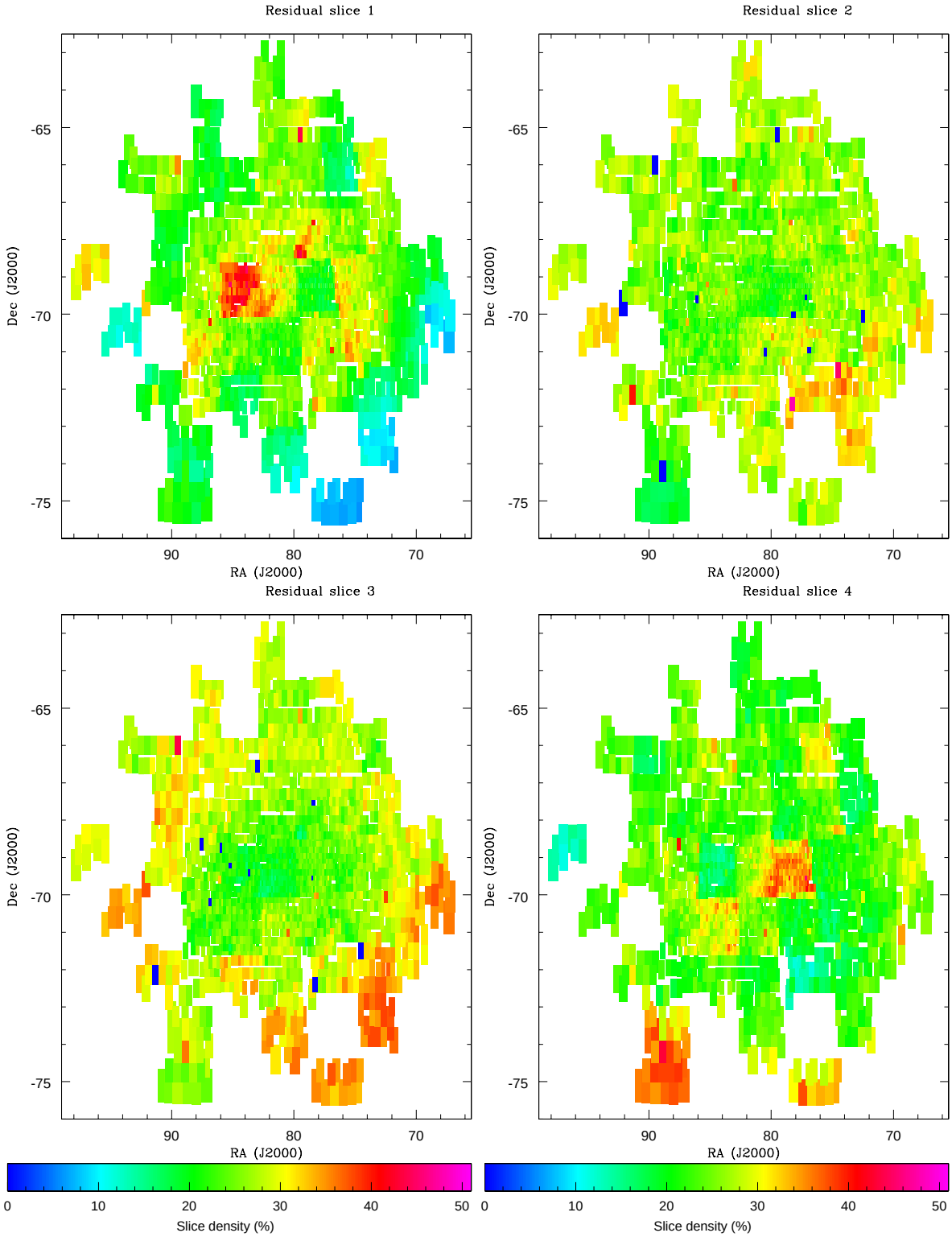

Figure A.9: For H I centre, the plane solution derived from the outer sub-regions and overlaid on regions from census method. Each slice contains 25% of the total RC stars. The slice density states what percentage of a given sub-region's sources are contained within that slice.

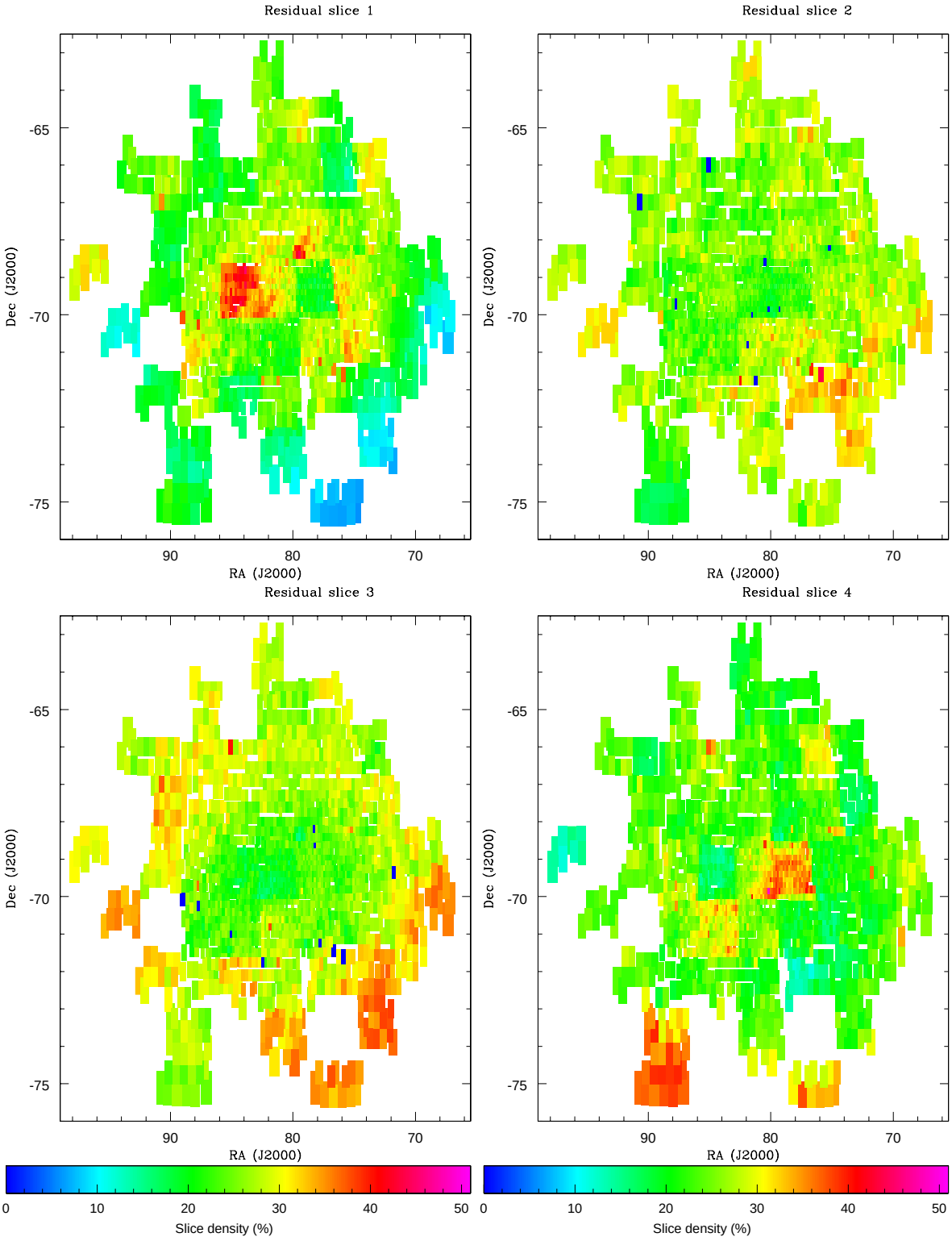

Figure A.10: For H I centre, the plane solution derived from the all sub-regions and overlaid on regions from census method. Each slice contains 25% of the total RC stars. The slice density states what percentage of a given sub-region's sources are contained within that slice.

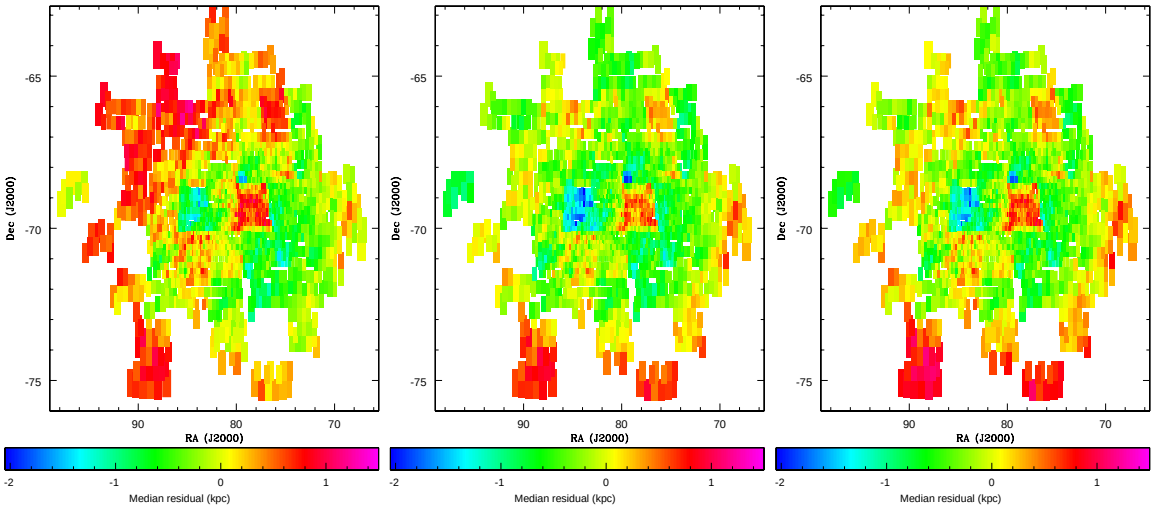

Figure A.11: Map of median residual values for each census sub-region using the H I LMC center and the plane solution derived for inner (top–left), outer (top–middle) and all (top–right) sub-regions. The values for these are shown in the legend (bottom).

A.3 SMC structure: aperture photometry and other PSF photometry residual maps

Covered in this Appendix are two topics related to the SMC structure Chapter 6. The first concerns some results from an initial analysis using aperture photometry and the second concerns some residual maps that were omitted due to their similarity to Figure 6.8.

A.3.1 Aperture photometry

This analysis was initially carried out using the VSA release. However this had zero points faults in a couple of tiles and eventually the PSF photometry was completed presenting an opportunity to use a superior data set.

Table A.4 describes the properties of the RC star selections for the aperture photometry. Tile 5_2 was excluded completely in this version of the analysis. Comparing

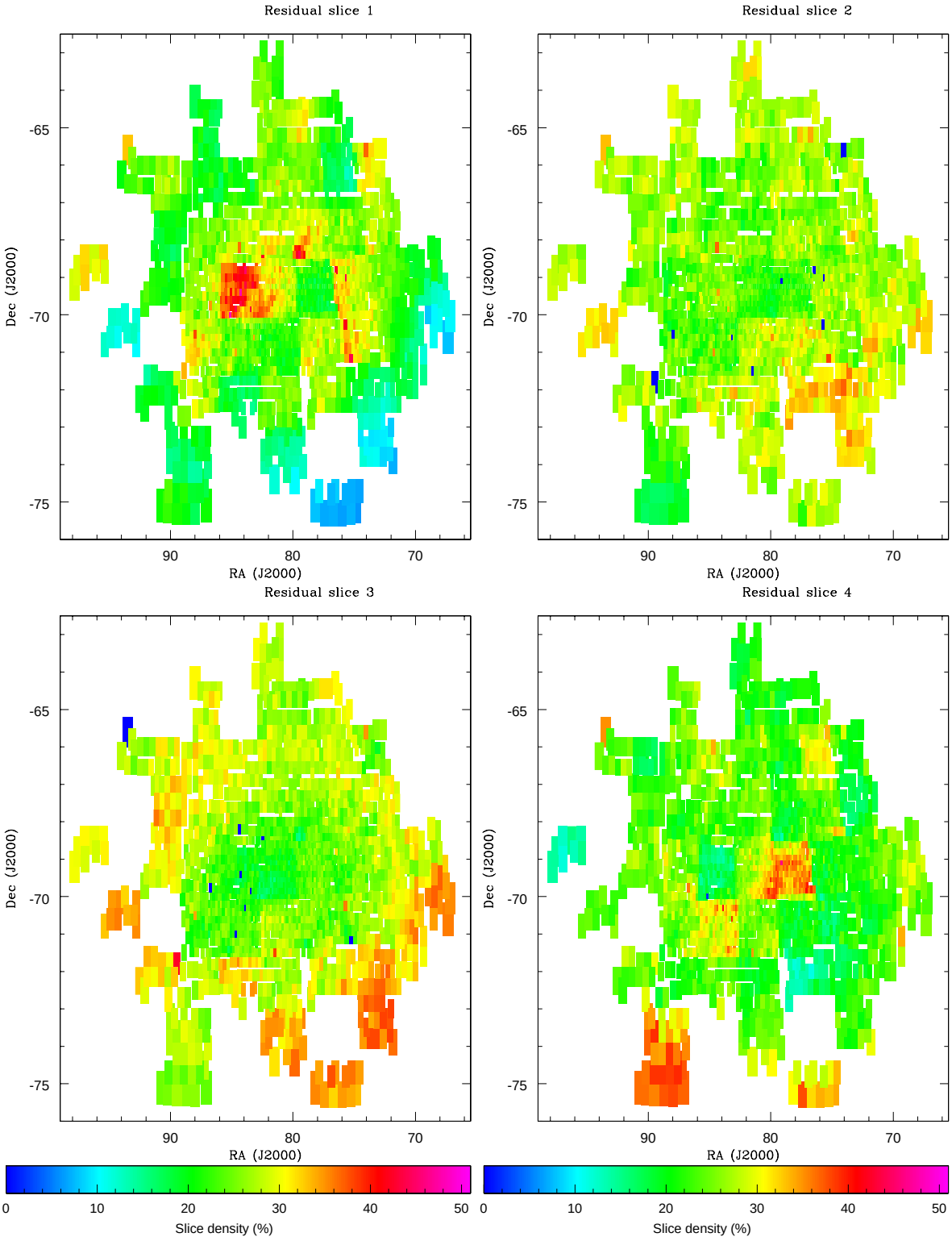

Figure A.12: For optical centre, using the plane solution derived from all sub-regions and overlaid on regions from census method. Each slice contains 25% of the total RC stars. The slice density states what percentage of a given sub-region's sources are contained within that slice.

the PSF photometry and aperture photometry shows that peaks are unchanged or change by a single bin but that means and medians can be slightly redder by 0.01–0.03 mag. For aperture photometry in total 512, 770 RC star sources were used in the SMC, of which 400, 338 were contained within the inner and dense regions comprising of the SMC bar region/main body.

Table A.4: List of SMC tiles used and properties when using aperture photometry

Tile	RA	Dec	Sources		Contour peak		Mean	SD	Median
	°	°	Total	RC	K_s	$Y-K_s$			
2_2	05.43	−75.20	121647	5027	17.50	0.79	0.820	0.068	0.806
2_3	11.15	−75.30	143311	10344	17.45	0.78	0.802	0.080	0.795
2_4	16.89	−75.27	162044	8537	17.45	0.80	0.817	0.075	0.806
2_5	22.55	−75.09	110771	5062	17.45	0.80	0.825	0.089	0.812
3_1	00.67	−73.89	112241	2344	17.45	0.76	0.793	0.080	0.780
3_2	05.90	−74.12	209778	20364	17.40	0.78	0.800	0.071	0.793
3_3	11.23	−74.21	367995	49331	17.40	0.80	0.818	0.066	0.814
3_4	16.59	−74.18	318215	27042	17.40	0.82	0.835	0.065	0.828
3_5	21.88	−74.01	151496	6563	17.50	0.81	0.827	0.078	0.822
3_6	27.03	−73.72	128777	3099	17.45	0.79	0.820	0.075	0.801
4_1	01.39	−72.82	105787	1726	17.50	0.77	0.787	0.079	0.775
4_2	06.31	−73.03	253111	20438	17.45	0.79	0.806	0.073	0.797
4_3	11.31	−73.12	703129	122277	17.40	0.85	0.870	0.092	0.861
4_4	16.33	−73.09	598479	76023	17.40	0.85	0.863	0.076	0.860
4_5	21.30	−72.93	240043	9298	17.40	0.82	0.830	0.069	0.823
4_6	26.14	−72.66	114055	1725	16.90	0.78			
5_3	11.38	−72.03	398487	39701	17.40	0.81	0.827	0.067	0.818
5_4	16.11	−72.00	546247	53978	17.35	0.86	0.862	0.074	0.855
5_5	20.79	−71.85	218710	12333	17.35	0.82	0.827	0.067	0.815
5_6	25.37	−71.60	128089	3849	16.95	0.77	0.784	0.074	0.778
6_2	07.00	−70.86	113736	3545	17.50	0.72	0.774	0.073	0.766
6_3	11.45	−70.94	152261	5373	17.45	0.78	0.787	0.078	0.780
6_4	15.92	−70.91	207309	11331	17.30	0.80	0.802	0.062	0.793
6_5	20.34	−70.77	150501	6684	17.40	0.77	0.797	0.067	0.785
7_3	11.52	−69.84	108655	3515	17.50	0.78	0.760	0.093	0.764
7_4	15.75	−69.82	117747	3261	17.35	0.76	0.789	0.063	0.776

Table A.5: Plane fitting results for the SMC.

	Inclination $^\circ$	Position Angle $^\circ$
Outer	49.3	189.8
All	42.7	173.3
Census	32.0	160.3

The extinction map is shown in Figure A.13. The grid pattern seen in tiles 6_3 and 4_6 are due to issues discussed in Section 2.4.2.2.

The plane solutions for the aperture photometry are shown in Table A.3.1.

A.3.2 PSF photometry – other residual maps

Figures A.14 & A.15 show the residual map slices using PSF photometry for the census and outer SMC plane solutions. These were not included in the main text to avoid repetition.

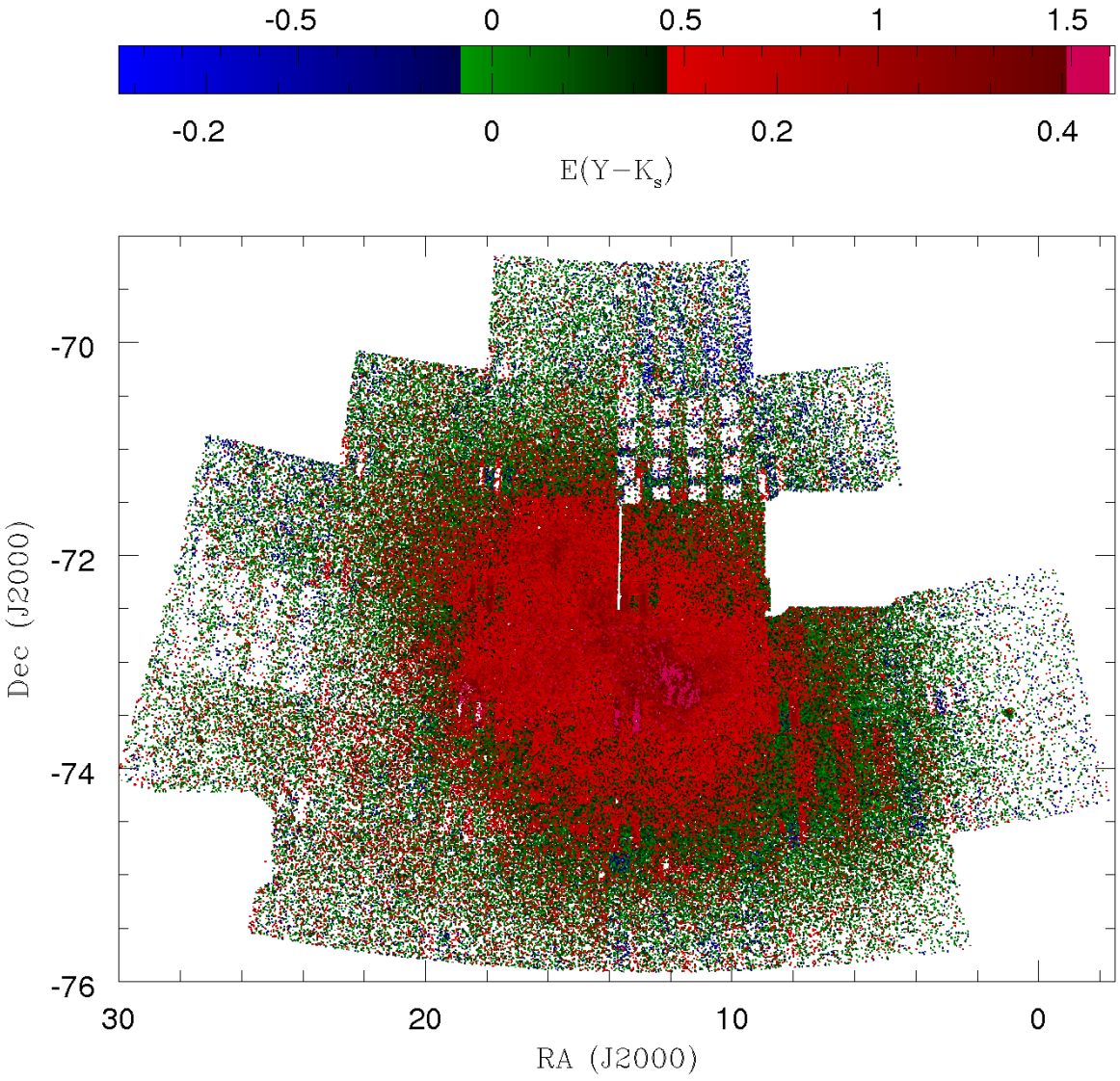

Figure A.13: Reddening map of the SMC in $E(Y - K_s)$ (top side of legend shows this converted into A_V magnitude) from RC stars using the VMCv20170109 VSA release. The green sources comprise the range covering 50% of the sources centred on the median where blue is lower than this, red higher and purple extremely high. The grid pattern seen in tiles 6_3 and 4_6 is due to issues discussed in Section 2.4.2.2.

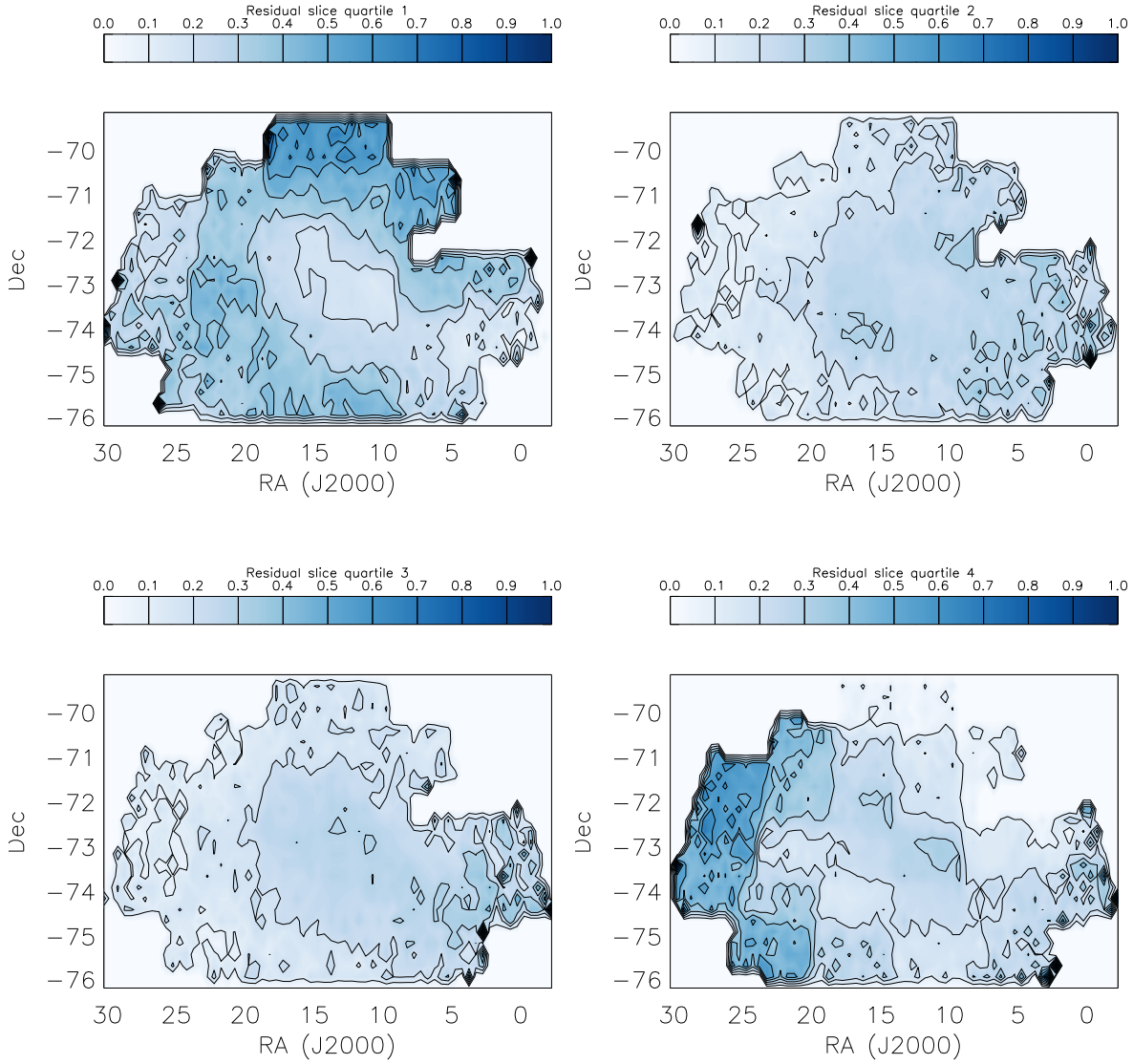

Figure A.14: Residual slices using plane from whole SMC solution from behind to in front of plane for the census selection. Each slice contains 25% of the total number of RC stars.

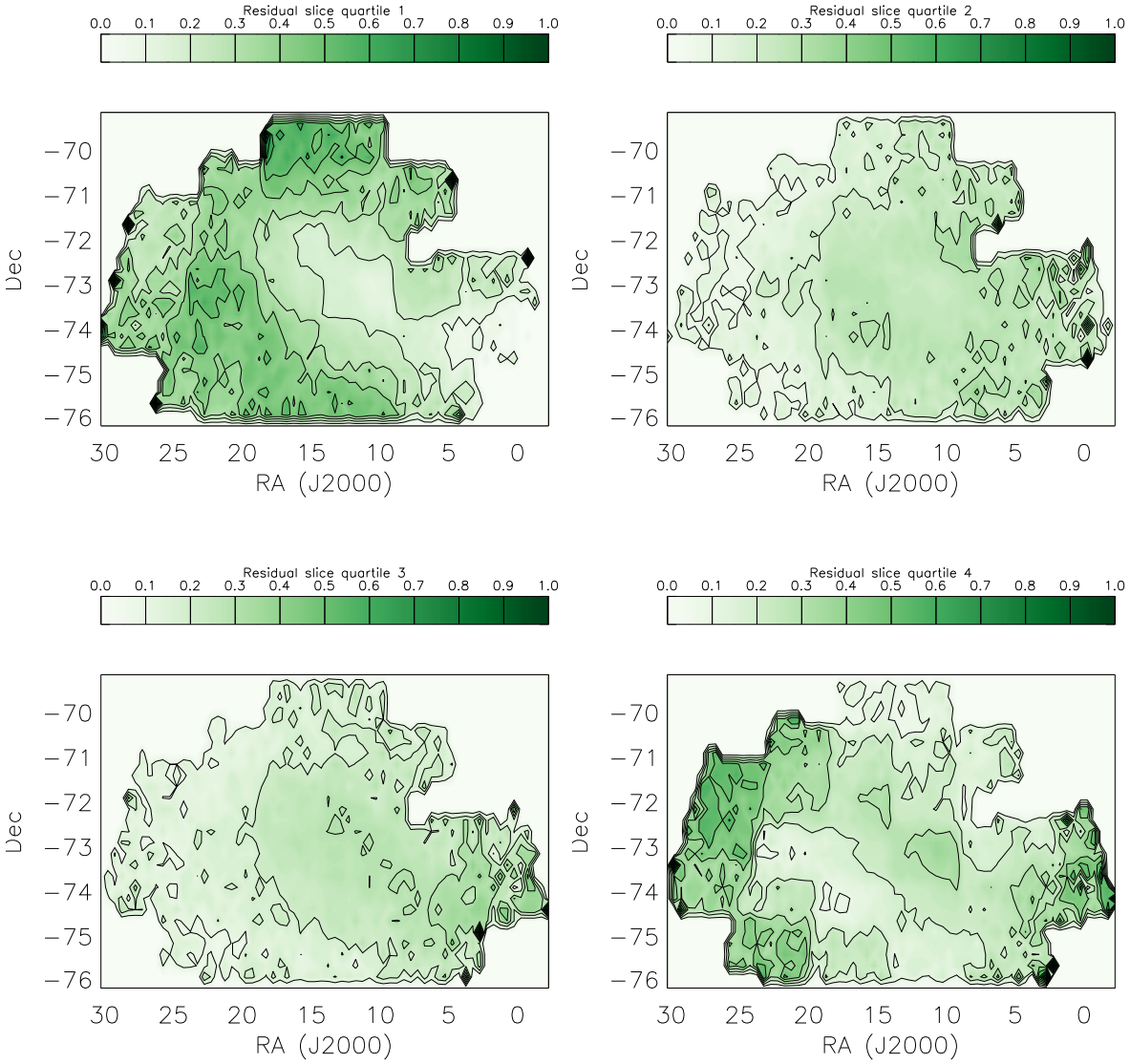

Figure A.15: Residual slices using plane from whole SMC solution from behind in to front of plane for the outer SMC selection. Each slice contains 25% of the total number of RC stars.

Bibliography

Alves, D. R. 2004, New A Rev., 48, 659

Bagheri, G., Cioni, M.-R. L., & Napiwotzki, R. 2013, A&A, 551, A78

Balbinot, E., Santiago, B. X., Girardi, L., Pieres, A., da Costa, L. N., Maia, M. A. G., Gruendl, R. A., Walker, A. R., Yanny, B., Drlica-Wagner, A., Benoit-Levy, A., Abbott, T. M. C., Allam, S. S., Annis, J., Bernstein, J. P., Bernstein, R. A., Bertin, E., Brooks, D., Buckley-Geer, E., Rosell, A. C., Cunha, C. E., DePoy, D. L., Desai, S., Diehl, H. T., Doel, P., Estrada, J., Evrard, A. E., Neto, A. F., Finley, D. A., Flaugher, B., Frieman, J. A., Gruen, D., Honscheid, K., James, D., Kuehn, K., Kuropatkin, N., Lahav, O., March, M., Marshall, J. L., Miller, C., Miquel, R., Ogando, R., Peoples, J., Plazas, A., Scarpine, V., Schubnell, M., Sevilla-Noarbe, I., Smith, R. C., Soares-Santos, M., Suchyta, E., Swanson, M. E. C., Tarle, G., Tucker, D. L., Wechsler, R., & Zuntz, J. 2015, MNRAS, 449, 1129

Barger, K. A., Haffner, L. M., & Bland-Hawthorn, J. 2013, ApJ, 771, 132

Barnes, J. E. & Hernquist, L. 1992, Nature, 360, 715

Battinelli, P. & Demers, S. 1998, AJ, 115, 1472

—. 2005, A&A, 434, 657

Bekki, K., Couch, W. J., Beasley, M. A., Forbes, D. A., Chiba, M., & Da Costa, G. S. 2004, ApJ, 610, L93

Bekki, K. & Stanimirović, S. 2009, MNRAS, 395, 342

Belokurov, V., Erkal, D., Deason, A. J., Koposov, S. E., De Angeli, F., Wyn Evans, D., Fraternali, F., & Mackey, D. 2016, MNRAS

Benedict, G. F., McArthur, B. E., Fredrick, L. W., Harrison, T. E., Lee, J., Slesnick, C. L., Rhee, J., Patterson, R. J., Nelan, E., Jefferys, W. H., van Altena, W., Shelus, P. J., Franz, O. G., Wasserman, L. H., Hemenway, P. D., Duncombe, R. L., Story, D., Whipple, A. L., & Bradley, A. J. 2002, AJ, 123, 473

Benson, A. J. & Bower, R. 2010, MNRAS, 405, 1573

Bernard, J.-P., Reach, W. T., Paradis, D., Meixner, M., Paladini, R., Kawamura, A., Onishi, T., Vijh, U., Gordon, K., Indebetouw, R., Hora, J. L., Whitney, B., Blum, R., Meade, M., Babler, B., Churchwell, E. B., Engelbracht, C. W., For, B.-Q., Misselt, K., Leitherer, C., Cohen, M., Boulanger, F., Frogel, J. A., Fukui, Y., Gallagher, J., Gorjian, V., Harris, J., Kelly, D., Latter, W. B., Madden, S., Markwick-Kemper, C., Mizuno, A., Mizuno, N., Mould, J., Nota, A., Oey, M. S., Olsen, K., Panagia, N., Perez-Gonzalez, P., Shibai, H., Sato, S., Smith, L., Staveley-Smith, L., Tielens, A. G. G. M., Ueta, T., Van Dyk, S., Volk, K., Werner, M., & Zaritsky, D. 2008, AJ, 136, 919

Besla, G., Kallivayalil, N., Hernquist, L., Robertson, B., Cox, T. J., van der Marel, R. P., & Alcock, C. 2007, ApJ, 668, 949

Besla, G., Kallivayalil, N., Hernquist, L., van der Marel, R. P., Cox, T. J., & Kereš, D. 2010, ApJ, 721, L97

—. 2012, MNRAS, 421, 2109

Besla, G., Martínez-Delgado, D., van der Marel, R. P., Beletsky, Y., Seibert, M., Schlafly, E. F., Grebel, E. K., & Neyer, F. 2016, ApJ, 825, 20

Bica, E., Santiago, B., Bonatto, C., Garcia-Dias, R., Kerber, L., Dias, B., Barbuy, B., & Balbinot, E. 2015, MNRAS, 453, 3190

Binney, J. & Merrifield, M. 1998, Galactic Astronomy, Princeton paperbacks (Princeton University Press)

Blow, D. M. 1960, Acta Crystallographica, 13, 168

Bolatto, A. D., Leroy, A., Israel, F. P., & Jackson, J. M. 2003, ApJ, 595, 167

Bolatto, A. D., Leroy, A. K., Jameson, K., Ostriker, E., Gordon, K., Lawton, B., Stanimirović, S., Israel, F. P., Madden, S. C., Hony, S., Sandstrom, K. M., Bot, C., Rubio, M., Winkler, P. F., Roman-Duval, J., van Loon, J. T., Oliveira, J. M., & Indebetouw, R. 2011, ApJ, 741, 12

Bolatto, A. D., Simon, J. D., Stanimirović, S., van Loon, J. T., Shah, R. Y., Venn, K., Leroy, A. K., Sandstrom, K., Jackson, J. M., Israel, F. P., Li, A., Staveley-Smith, L., Bot, C., Boulanger, F., & Rubio, M. 2007, ApJ, 655, 212

Bressan, A., Marigo, P., Girardi, L., Salasnich, B., Dal Cero, C., Rubele, S., & Nanni, A. 2012, MNRAS, 427, 127

Burstein, D. & Heiles, C. 1978, ApJ, 225, 40

—. 1982, AJ, 87, 1165

Caldwell, J. A. R. & Coulson, I. M. 1986, MNRAS, 218, 223

Calzetti, D. 2001, PASP, 113, 1449

Cannon, R. D. 1970, MNRAS, 150, 111

Caputo, F., Marconi, M., Musella, I., & Pont, F. 2001, A&A, 372, 544

Cardelli, J. A., Clayton, G. C., & Mathis, J. S. 1989, ApJ, 345, 245

Carrera, R., Gallart, C., Aparicio, A., Costa, E., Méndez, R. A., & Noël, N. E. D. 2008a, AJ, 136, 1039

Carrera, R., Gallart, C., Hardy, E., Aparicio, A., & Zinn, R. 2008b, AJ, 135, 836

Carrera, R., Pancino, E., Gallart, C., & del Pino, A. 2013, MNRAS, 434, 1681

Castelli, F. & Kurucz, R. L. 2004, ArXiv Astrophysics e-prints

Chapman, S. C., Ibata, R., Lewis, G. F., Ferguson, A. M. N., Irwin, M., McConnachie, A., & Tanvir, N. 2006, ApJ, 653, 255

Choi, Y., Nidever, D. L., Olsen, K., Blum, R. D., Besla, G., Zaritsky, D., van der Marel, R. P., Bell, E. F., Gallart, C., Cioni, M.-R. L., Johnson, L. C., Vivas, A. K., Saha, A., de Boer, T. J. L., Noel, N. E. D., Monachesi, A., Massana, P., Conn, B. C., Martinez-Delgado, D., & Munoz, R. R. 2018, ArXiv e-prints

Cignoni, M., Cole, A. A., Tosi, M., Gallagher, J. S., Sabbi, E., Anderson, J., Grebel, E. K., & Nota, A. 2012, ApJ, 754, 130

Cioni, M., Clementini, G., Girardi, L., Guandalini, R., Gullieuszik, M., Miszalski, B., Moretti, M., Ripepi, V., Rubele, S., Bagheri, G., Bekki, K., Cross, N., de Blok, W. J. G., de Grijs, R., Emerson, J. P., Evans, C. J., Gibson, B., Gonzales-Solares, E., Groenewegen, M. A. T., Irwin, M., Ivanov, V. D., Lewis, J., Marconi, M., Marquette, J., Mastropietro, C., Moore, B., Napiwotzki, R., Naylor, T., Oliveira, J. M., Read, M., Sutorius, E., van Loon, J. T., Wilkinson, M. I., & Wood, P. R. 2011, A&A, 527, A116

Cioni, M.-R. L. 2009, A&A, 506, 1137

Cioni, M.-R. L., Bekki, K., Girardi, L., de Grijs, R., Irwin, M. J., Ivanov, V. D., Marconi, M., Oliveira, J. M., Piatti, A. E., Ripepi, V., & van Loon, J. T. 2016, A&A, 586, A77

Cioni, M.-R. L., van der Marel, R. P., Loup, C., & Habing, H. J. 2000, A&A, 359, 601

Clayton, G. C. & Cardelli, J. A. 1988, AJ, 96, 695

Cohen, R. S., Dame, T. M., Garay, G., Montani, J., Rubio, M., & Thaddeus, P. 1988, ApJ, 331, L95

Cole, A. A., Tolstoy, E., Gallagher, III, J. S., & Smecker-Hane, T. A. 2005, AJ, 129, 1465

Cole, S., Aragon-Salamanca, A., Frenk, C. S., Navarro, J. F., & Zepf, S. E. 1994, MNRAS, 271, 781

Cook, D. O., Dale, D. A., Johnson, B. D., Van Zee, L., Lee, J. C., Kennicutt, R. C., Calzetti, D., Staudaher, S. M., & Engelbracht, C. W. 2014, MNRAS, 445, 881

Corbelli, E. & Salucci, P. 2000, MNRAS, 311, 441

Crandall, S. & Ratra, B. 2015, ApJ, 815, 87

Cross, N. J. G., Collins, R. S., Mann, R. G., Read, M. A., Sutorius, E. T. W., Blake, R. P., Holliman, M., Hambly, N. C., Emerson, J. P., Lawrence, A., & Noddle, K. T. 2012, A&A, 548, A119

Crowl, H. H., Sarajedini, A., Piatti, A. E., Geisler, D., Bica, E., Clariá, J. J., & Santos, Jr., J. F. C. 2001, AJ, 122, 220

Dalton, G. B., Caldwell, M., Ward, A. K., Whalley, M. S., Woodhouse, G., Edeson, R. L., Clark, P., Beard, S. M., Gallie, A. M., Todd, S. P., Strachan, J. M. D., Bezawada, N. N., Sutherland, W. J., & Emerson, J. P. 2006, in Society of Photo-Optical Instrumentation Engineers (SPIE) Conference Series, Vol. 6269, Society of Photo-Optical Instrumentation Engineers (SPIE) Conference Series

Dawson, J. R., McClure-Griffiths, N. M., Wong, T., Dickey, J. M., Hughes, A., Fukui, Y., & Kawamura, A. 2013, ApJ, 763, 56

de Boer, K. S., Braun, J. M., Vallenari, A., & Mebold, U. 1998, A&A, 329, L49

de Grijs, R. & Bono, G. 2015, AJ, 149, 179

de Grijs, R., Wicker, J. E., & Bono, G. 2014, AJ, 147, 122

de Vaucouleurs, G. & Freeman, K. C. 1972, Vistas in Astronomy, 14, 163

Deb, S. 2017, ArXiv e-prints

Deb, S. & Singh, H. P. 2014, MNRAS, 438, 2440

Deb, S., Singh, H. P., Kumar, S., & Kanbur, S. M. 2015, MNRAS, 449, 2768

Demers, S. & Battinelli, P. 1998, AJ, 115, 154

—. 1999, AJ, 118, 1700

Di Criscienzo, M., Greco, C., Ripepi, V., Clementini, G., Dall'Ora, M., Marconi, M., Musella, I., Federici, L., & Di Fabrizio, L. 2011, AJ, 141, 81

Dias, B., Kerber, L., Barbuy, B., Bica, E., & Ortolani, S. 2016, A&A, 591, A11

Diaz, J. D. & Bekki, K. 2012, ApJ, 750, 36

Dobashi, K., Bernard, J., Hughes, A., Paradis, D., Reach, W. T., & Kawamura, A. 2008, A&A, 484, 205

Dobashi, K., Bernard, J.-P., Kawamura, A., Egusa, F., Hughes, A., Paradis, D., Bot, C., & Reach, W. T. 2009, AJ, 137, 5099

Dobbie, P. D., Cole, A. A., Subramaniam, A., & Keller, S. 2014a, MNRAS, 442, 1663

—. 2014b, MNRAS, 442, 1680

D'Onghia, E. & Fox, A. J. 2016, ARA&A, 54, 363

Draine, B. T. 2003, ARA&A, 41, 241

Dubinski, J. 1999, in Astronomical Society of the Pacific Conference Series, Vol. 182, Galaxy Dynamics - A Rutgers Symposium, ed. D. R. Merritt, M. Valluri, & J. A. Sellwood

Efremov, Y. N. 1995, AJ, 110, 2757

Elmegreen, B. G. 2013, in IAU Symposium, Vol. 292, IAU Symposium, ed. T. Wong & J. Ott, 35

Emerson, J., McPherson, A., & Sutherland, W. 2006, The Messenger, 126, 41

Evans, C. J., Taylor, W. D., Hénault-Brunet, V., Sana, H., de Koter, A., Simón-Díaz, S., Carraro, G., Bagnoli, T., Bastian, N., Bestenlehner, J. M., Bonanos, A. Z., Bressert, E., Brott, I., Campbell, M. A., Cantiello, M., Clark, J. S., Costa, E., Crowther, P. A., de Mink, S. E., Doran, E., Dufton, P. L., Dunstall, P. R., Friedrich, K., Garcia, M., Gieles, M., Gräfener, G., Herrero, A., Howarth, I. D., Izzard, R. G., Langer, N., Lennon, D. J., Maíz Apellániz, J., Markova, N., Najarro, F., Puls, J., Ramirez, O. H., Sabín-Sanjulián, C., Smartt, S. J., Stroud, V. E., van Loon, J. T., Vink, J. S., & Walborn, N. R. 2011, A&A, 530, A108

Faulkner, D. J. & Cannon, R. D. 1973, ApJ, 180, 435

Feast, M. W., Abedigamba, O. P., & Whitelock, P. A. 2010, MNRAS, 408, L76

Feitzinger, J. V., Schmidt-Kaler, T., & Isserstedt, J. 1977, A&A, 57, 265

Fischera, J., Dopita, M. A., & Sutherland, R. S. 2003, ApJ, 599, L21

Freedman, W. L., Madore, B. F., Gibson, B. K., Ferrarese, L., Kelson, D. D., Sakai, S., Mould, J. R., Kennicutt, Jr., R. C., Ford, H. C., Graham, J. A., Huchra, J. P., Hughes, S. M. G., Illingworth, G. D., Macri, L. M., & Stetson, P. B. 2001, ApJ, 553, 47

Fukugita, M., Ichikawa, T., Gunn, J. E., Doi, M., Shimasaku, K., & Schneider, D. P. 1996, AJ, 111, 1748

Fukui, Y., Kawamura, A., Minamidani, T., Mizuno, Y., Kanai, Y., Mizuno, N., Onishi, T., Yonekura, Y., Mizuno, A., Ogawa, H., & Rubio, M. 2008, ApJS, 178, 56

Gardiner, L. T. & Hawkins, M. R. S. 1991, MNRAS, 251, 174

Gardiner, L. T. & Noguchi, M. 1996, MNRAS, 278, 191

Gaustad, J. E., McCullough, P. R., Rosing, W., & Van Buren, D. 2001, PASP, 113, 1326

Gieren, W., Górski, M., Pietrzyński, G., Konorski, P., Suchomska, K., Graczyk, D., Pilecki, B., Bresolin, F., Kudritzki, R.-P., Storm, J., Karczmarek, P., Gallenne, A., Calderón, P., & Geisler, D. 2013, ApJ, 773, 69

Girardi, L. 1999, MNRAS, 308, 818

Girardi, L., Barbieri, M., Groenewegen, M. A. T., Marigo, P., Bressan, A., Rocha-Pinto, H. J., Santiago, B. X., Camargo, J. I. B., & da Costa, L. N. 2012, Astrophysics and Space Science Proceedings, 26, 165

Girardi, L., Dalcanton, J., Williams, B., de Jong, R., Gallart, C., Monelli, M., Groenewegen, M. A. T., Holtzman, J. A., Olsen, K. A. G., Seth, A. C., Weisz, D. R., & ANGST/ANGRRR Collaboration. 2008, PASP, 120, 583

Girardi, L., Groenewegen, M. A. T., Hatziminaoglou, E., & da Costa, L. 2005, A&A, 436, 895

Girardi, L. & Marigo, P. 2007, in Astronomical Society of the Pacific Conference Series, Vol. 378, Why Galaxies Care About AGB Stars: Their Importance as Actors and Probes, ed. F. Kerschbaum, C. Charbonnel, & R. F. Wing, 20

Girardi, L. & Salaris, M. 2001, MNRAS, 323, 109

Girardi, L., Williams, B. F., Gilbert, K. M., Rosenfield, P., Dalcanton, J. J., Marigo, P., Boyer, M. L., Dolphin, A., Weisz, D. R., Melbourne, J., Olsen, K. A. G., Seth, A. C., & Skillman, E. 2010, ApJ, 724, 1030

Glatt, K., Grebel, E. K., Sabbi, E., Gallagher, III, J. S., Nota, A., Sirianni, M., Clementini, G., Tosi, M., Harbeck, D., Koch, A., Kayser, A., & Da Costa, G. 2008, AJ, 136, 1703

Gonidakis, I., Livanou, E., Kontizas, E., Klein, U., Kontizas, M., Belcheva, M., Tsalmantza, P., & Karampelas, A. 2009, A&A, 496, 375

González-Fernández, C., Hodgkin, S. T., Irwin, M. J., González-Solares, E., Koposov, S. E., Lewis, J. R., Emerson, J. P., Hewett, P. C., Yoldaş, A. K., & Riello, M. 2018, MNRAS, 474, 5459

Gordon, K. D., Bot, C., Muller, E., Misselt, K. A., Bolatto, A., Bernard, J.-P., Reach, W., Engelbracht, C. W., Babler, B., Bracker, S., Block, M., Clayton, G. C., Hora, J., Indebetouw, R., Israel, F. P., Li, A., Madden, S., Meade, M., Meixner, M., Sewilo, M., Shiao, B., Smith, L. J., van Loon, J. T., & Whitney, B. A. 2009, ApJ, 690, L76

Gordon, K. D., Clayton, G. C., Misselt, K. A., Landolt, A. U., & Wolff, M. J. 2003, ApJ, 594, 279

Gordon, K. D., Meixner, M., Meade, M. R., Whitney, B., Engelbracht, C., Bot, C., Boyer, M. L., Lawton, B., Sewiło, M., Babler, B., Bernard, J.-P., Bracker, S., Block, M., Blum, R., Bolatto, A., Bonanos, A., Harris, J., Hora, J. L., Indebetouw, R., Misselt, K., Reach, W., Shiao, B., Tielens, X., Carlson, L., Churchwell, E., Clayton, G. C., Chen, C.-H. R., Cohen, M., Fukui, Y., Gorjian, V., Hony, S., Israel, F. P., Kawamura, A., Kemper, F., Leroy, A., Li, A., Madden, S., Marble, A. R., McDonald, I., Mizuno, A., Mizuno, N., Muller, E., Oliveira, J. M., Olsen, K., Onishi, T., Paladini, R., Paradis, D., Points, S., Robitaille, T., Rubin, D., Sandstrom, K., Sato, S., Shibai, H., Simon, J. D., Smith, L. J., Srinivasan, S., Vijh, U., Van Dyk, S., van Loon, J. T., & Zaritsky, D. 2011, AJ, 142, 102

Górski, M., Pietrzyński, G., Gieren, W., Catelan, M., Pilecki, B., Karczmarek, P., Suchomska, K., Graczyk, D., Konorski, P., Zgirski, B., & Wielgórski, P. 2016, AJ, 151, 167

Gouliermis, D. A., Schmeja, S., Dolphin, A. E., Gennaro, M., Tognelli, E., & Prada Moroni, P. G. 2012a, ApJ, 748, 64

Gouliermis, D. A., Schmeja, S., Ossenkopf, V., Klessen, R. S., & Dolphin, A. E. 2012b, ArXiv e-prints

Gratton, R. G., Bragaglia, A., Clementini, G., Carretta, E., Di Fabrizio, L., Maio, M., & Taribello, E. 2004, A&A, 421, 937

Grcevich, J. & Putman, M. E. 2009, ApJ, 696, 385

Grebel, E. K. 2004, Origin and Evolution of the Elements, 234

Green, R. 1985, Spherical Astronomy (Cambridge University Press)

Grocholski, A. J. & Sarajedini, A. 2002, AJ, 123, 1603

Grocholski, A. J., Sarajedini, A., Olsen, K. A. G., Tiede, G. P., & Mancone, C. L. 2007, AJ, 134, 680

Groenewegen, M. A. T. 2000, A&A, 363, 901

—. 2008, A&A, 488, 935

Guhathakurta, P. & Reitzel, D. B. 1998, in Astronomical Society of the Pacific Conference Series, Vol. 136, Galactic Halos, ed. D. Zaritsky, 22

Gullieuszik, M., Groenewegen, M. A. T., Cioni, M.-R. L., de Grijs, R., van Loon, J. T., Girardi, L., Ivanov, V. D., Oliveira, J. M., Emerson, J. P., & Guandalini, R. 2012, A&A, 537, A105

Guo, Q., White, S., Boylan-Kolchin, M., De Lucia, G., Kauffmann, G., Lemson, G., Li, C., Springel, V., & Weinmann, S. 2011, MNRAS, 413, 101

Güver, T. & Özel, F. 2009, MNRAS, 400, 2050

Hambly, N. C., Collins, R. S., Cross, N. J. G., Mann, R. G., Read, M. A., Sutorius, E. T. W., Bond, I., Bryant, J., Emerson, J. P., Lawrence, A., Rimoldini, L., Stewart, J. M., Williams, P. M., Adamson, A., Hirst, P., Dye, S., & Warren, S. J. 2008, MNRAS, 384, 637

Hammer, F., Yang, Y. B., Flores, H., Puech, M., & Fouquet, S. 2015, ApJ, 813, 110

Harris, J. 2007, ApJ, 658, 345

Haschke, R., Grebel, E. K., & Duffau, S. 2011, AJ, 141, 158

—. 2012a, AJ, 144, 106

—. 2012b, AJ, 144, 107

Haschke, R., Grebel, E. K., Duffau, S., & Jin, S. 2012c, AJ, 143, 48

Hatzidimitriou, D., Cannon, R. D., & Hawkins, M. R. S. 1993, MNRAS, 261, 873

Hatzidimitriou, D. & Hawkins, M. R. S. 1989, MNRAS, 241, 667

Hindman, J. V., Kerr, F. J., & McGee, R. X. 1963a, Australian Journal of Physics, 16, 570

Hindman, J. V., McGee, R. X., Carter, A. W. L., Holmes, E. C. J., & Beard, M. 1963b, Australian Journal of Physics, 16, 552

Hodgkin, S. T., Irwin, M. J., Hewett, P. C., & Warren, S. J. 2009, MNRAS, 394, 675

Hyland, A. R., Straw, S., Jones, T. J., & Gatley, I. 1992, MNRAS, 257, 391

Indebetouw, R., Brogan, C., Chen, C.-H. R., Leroy, A., Johnson, K., Muller, E., Madden, S., Cormier, D., Galliano, F., Hughes, A., Hunter, T., Kawamura, A., Kepley, A., Lebouteiller, V., Meixner, M., Oliveira, J. M., Onishi, T., & Vasyunina, T. 2013, ApJ, 774, 73

Indebetouw, R., de Messières, G. E., Madden, S., Engelbracht, C., Smith, J. D., Meixner, M., Brandl, B., Smith, L. J., Boulanger, F., Galliano, F., Gordon, K., Hora, J. L., Sewilo, M., Tielens, A. G. G. M., Werner, M., & Wolfire, M. G. 2009, ApJ, 694, 84

Indu, G. & Subramaniam, A. 2011, A&A, 535, A115

Irwin, M. J., Demers, S., & Kunkel, W. E. 1990, AJ, 99, 191

Irwin, M. J., Kunkel, W. E., & Demers, S. 1985, Nature, 318, 160

Irwin, M. J., Lewis, J., Hodgkin, S., Bunclark, P., Evans, D., McMahon, R., Emerson, J. P., Stewart, M., & Beard, S. 2004, in Society of Photo-Optical Instrumentation Engineers (SPIE) Conference Series, Vol. 5493, Society of Photo-Optical Instrumentation Engineers (SPIE) Conference Series, ed. P. J. Quinn & A. Bridger, 411

Jameson, K. E., Bolatto, A. D., Wolfire, M., Warren, S. R., Herrera-Camus, R., Croxall, K., Pellegrini, E., Smith, J.-D., Rubio, M., Indebetouw, R., Israel, F. P., Meixner, M., Roman-Duval, J., van Loon, J. T., Muller, E., Verdugo, C., Zinnecker, H., & Okada, Y. 2018, ApJ, 853, 111

Joshi, Y. C. & Joshi, S. 2014, New A, 28, 27

Kallivayalil, N., van der Marel, R. P., & Alcock, C. 2006a, ApJ, 652, 1213

Kallivayalil, N., van der Marel, R. P., Alcock, C., Axelrod, T., Cook, K. H., Drake, A. J., & Geha, M. 2006b, ApJ, 638, 772

Kapakos, E. & Hatzidimitriou, D. 2012, MNRAS, 426, 2063

Kapakos, E., Hatzidimitriou, D., & Soszyński, I. 2011, MNRAS, 415, 1366

Kauffmann, G., White, S. D. M., & Guiderdoni, B. 1993, MNRAS, 264, 201

Kennicutt, Jr., R. C., Bresolin, F., Bomans, D. J., Bothun, G. D., & Thompson, I. B. 1995, AJ, 109, 594

Kerber, L. O., Girardi, L., Rubele, S., & Cioni, M.-R. 2009, A&A, 499, 697

Khochfar, S., Emsellem, E., Serra, P., Bois, M., Alatalo, K., Bacon, R., Blitz, L., Bournaud, F., Bureau, M., Cappellari, M., Davies, R. L., Davis, T. A., de Zeeuw, P. T., Duc, P.-A., Krajnović, D., Kuntschner, H., Lablanche, P.-Y., McDermid, R. M., Morganti, R., Naab, T., Oosterloo, T., Sarzi, M., Scott, N., Weijmans, A.-M., & Young, L. M. 2011, MNRAS, 417, 845

Kim, S., Rosolowsky, E., Lee, Y., Kim, Y., Jung, Y. C., Dopita, M. A., Elmegreen, B. G., Freeman, K. C., Sault, R. J., Kesteven, M., McConnell, D., & Chu, Y.-H. 2007, ApJS, 171, 419

Kim, S., Staveley-Smith, L., Dopita, M. A., Freeman, K. C., Sault, R. J., Kesteven, M. J., & McConnell, D. 1998, ApJ, 503, 674

Kim, S., Staveley-Smith, L., Dopita, M. A., Sault, R. J., Freeman, K. C., Lee, Y., & Chu, Y. 2003, ApJS, 148, 473

Koerwer, J. F. 2009, AJ, 138, 1

Kordopatis, G., Recio-Blanco, A., de Laverny, P., Bijaoui, A., Hill, V., Gilmore, G., Wyse, R. F. G., & Ordenovic, C. 2011, A&A, 535, A106

Kunkel, W. E., Demers, S., & Irwin, M. J. 2000, AJ, 119, 2789

Kunth, D. & Östlin, G. 2000, A&A Rev., 10, 1

Lah, P., Kiss, L. L., & Bedding, T. R. 2005, MNRAS, 359, L42

Laney, C. D. & Stobie, R. S. 1986, MNRAS, 222, 449

Larson, R. B. & Tinsley, B. M. 1978, ApJ, 219, 46

Lejeune, T., Cuisinier, F., & Buser, R. 1997, A&AS, 125, 229

Leroy, A., Bolatto, A., Stanimirović, S., Mizuno, N., Israel, F., & Bot, C. 2007, ApJ, 658, 1027

Li, A., Wang, S., Gao, J., & Jiang, B. W. 2015, ArXiv e-prints

Luks, T. & Rohlfs, K. 1992, A&A, 263, 41

Mackey, A. D., Koposov, S. E., Da Costa, G. S., Belokurov, V., Erkal, D., Fraternali, F., McClure-Griffiths, N. M., & Fraser, M. 2017, ArXiv e-prints

Mackey, A. D., Koposov, S. E., Erkal, D., Belokurov, V., Da Costa, G. S., & Gómez, F. A. 2016, MNRAS, 459, 239

Maíz Apellániz, J. 2013, in Highlights of Spanish Astrophysics VII, 583–589

Marigo, P., Girardi, L., Bressan, A., Groenewegen, M. A. T., Silva, L., & Granato, G. L. 2008, A&A, 482, 883

Marx-Zimmer, M., Herbstmeier, U., Dickey, J. M., Zimmer, F., Staveley-Smith, L., & Mebold, U. 2000, A&A, 354, 787

Mastropietro, C. 2009, in IAU Symposium, Vol. 256, IAU Symposium, ed. J. T. van Loon & J. M. Oliveira, 117

Mathewson, D. S., Ford, V. L., & Visvanathan, N. 1986, ApJ, 301, 664

—. 1988, ApJ, 333, 617

Mauro, F., Moni Bidin, C., Geisler, D., Saviane, I., Da Costa, G. S., Gormaz-Matamala, A. C., Vasquez, S., Chené, A.-N., Cohen, R., & Dias, B. 2014, A&A, 563, A76

McClure-Griffiths, N. M., Pisano, D. J., Calabretta, M. R., Ford, H. A., Lockman, F. J., Staveley-Smith, L., Kalberla, P. M. W., Bailin, J., Dedes, L., Janowiecki, S., Gibson, B. K., Murphy, T., Nakanishi, H., & Newton-McGee, K. 2009, ApJS, 181, 398

Meixner, M. 2008, PASA, 25, 149

Meixner, M., Gordon, K. D., Indebetouw, R., Hora, J. L., Whitney, B., Blum, R., Reach, W., Bernard, J.-P., Meade, M., Babler, B., Engelbracht, C. W., For, B.-Q., Misselt, K., Vijh, U., Leitherer, C., Cohen, M., Churchwell, E. B., Boulanger, F., Frogel, J. A., Fukui, Y., Gallagher, J., Gorjian, V., Harris, J., Kelly, D., Kawamura, A., Kim, S., Latter, W. B., Madden, S., Markwick-Kemper, C., Mizuno, A., Mizuno, N., Mould, J., Nota, A., Oey, M. S., Olsen, K., Onishi, T., Paladini, R., Panagia, N., Perez-Gonzalez, P., Shibai, H., Sato, S., Smith, L., Staveley-Smith, L., Tielens, A. G. G. M., Ueta, T., van Dyk, S., Volk, K., Werner, M., & Zaritsky, D. 2006, AJ, 132, 2268

Mizuno, N., Rubio, M., Mizuno, A., Yamaguchi, R., Onishi, T., & Fukui, Y. 2001, PASJ, 53, L45

Mo, H., van den Bosch, F. C., & White, S. 2010, Galaxy Formation and Evolution

Moretti, M. I., Clementini, G., Muraveva, T., Ripepi, V., Marquette, J. B., Cioni, M.-R. L., Marconi, M., Girardi, L., Rubele, S., Tisserand, P., de Grijs, R., Groenewegen, M. A. T., Guandalini, R., Ivanov, V. D., & van Loon, J. T. 2014, MNRAS, 437, 2702

Mottini, M., Romaniello, M., Primas, F., Bono, G., Groenewegen, M. A. T., & François, P. 2006, Mem. Soc. Astron. Italiana, 77, 156

Muraveva, T., Subramanian, S., Clementini, G., Cioni, M.-R. L., Palmer, M., van Loon, J. T., Moretti, M. I., de Grijs, R., Molinaro, R., Ripepi, V., Marconi, M., Emerson, J., & Ivanov, V. D. 2018, MNRAS, 473, 3131

Nidever, D. L. 2014, in Astronomical Society of the Pacific Conference Series, Vol. 480, Astronomical Society of the Pacific Conference Series, ed. M. S. Seigar & P. Treuthardt, 27

Nidever, D. L., Majewski, S. R., & Butler Burton, W. 2008, ApJ, 679, 432

Nidever, D. L., Monachesi, A., Bell, E. F., Majewski, S. R., Muñoz, R. R., & Beaton, R. L. 2013, ApJ, 779, 145

Nigra, L., Stanimirović, S., Gallagher, III, J. S., Wood, K., Nidever, D., & Majewski, S. 2012, ApJ, 760, 48

Nikolaev, S., Drake, A. J., Keller, S. C., Cook, K. H., Dalal, N., Griest, K., Welch, D. L., & Kanbur, S. M. 2004, ApJ, 601, 260

Nikolaev, S. & Weinberg, M. D. 2000, ApJ, 542, 804

Nishiyama, S., Haba, Y., Kato, D., Baba, D., Hatano, H., Tamura, M., Nakajima, Y., Ishihara, A., Nagata, T., Sugitani, K., Matsunaga, N., Fukushi, H., Kusakabe, N., & Sato, S. 2007, ApJ, 658, 358

Noël, N. E. D., Conn, B. C., Carrera, R., Read, J. I., Rix, H.-W., & Dolphin, A. 2013, ApJ, 768, 109

Noël, N. E. D., Conn, B. C., Read, J. I., Dolphin, A., & Rix, H.-W. 2015, ArXiv e-prints

O'Donnell, J. E. 1994, ApJ, 422, 158

Oliveira, J. M., van Loon, J. T., Chen, C.-H. R., Tielens, A. G. G. M., Sloan, G. C., Woods, P. M., Kemper, F., Indebetouw, R., Gordon, K. D., Boyer, M. L., Shiao, B., Madden, S., Speck, A. K., Meixner, M., & Marengo, M. 2009, ApJ, 707, 1269

Olsen, K. A. G. & Massey, P. 2007, ApJ, 656, L61

Olsen, K. A. G. & Salyk, C. 2002, AJ, 124, 2045

Olsen, K. A. G., Zaritsky, D., Blum, R. D., Boyer, M. L., & Gordon, K. D. 2011, ApJ, 737, 29

Paczynski, B. & Stanek, K. Z. 1998, ApJ, 494, L219

Pak, S., Jaffe, D. T., van Dishoeck, E. F., Johansson, L. E. B., & Booth, R. S. 1998, ApJ, 498, 735

Parisi, M. C., Grocholski, A. J., Geisler, D., Sarajedini, A., & Clariá, J. J. 2009, AJ, 138, 517

Peñarrubia, J., Gómez, F. A., Besla, G., Erkal, D., & Ma, Y.-Z. 2016, MNRAS, 456, L54

Pejcha, O. & Stanek, K. Z. 2009, ApJ, 704, 1730

Perryman, M. A. C. 1997, in ESA Special Publication, Vol. 402, Hipparcos - Venice '97, ed. R. M. Bonnet, E. Høg, P. L. Bernacca, L. Emiliani, A. Blaauw, C. Turon, J. Kovalevsky, L. Lindegren, H. Hassan, M. Bouffard, B. Strim, D. Heger, M. A. C. Perryman, & L. Woltjer, 1

Perryman, M. A. C., Lindegren, L., Kovalevsky, J., Turon, C., Hoeg, E., Grenon, M., Schrijver, H., Bernacca, P. L., Creze, M., Donati, F., Evans, D. W., Falin, J. L., Froeschle, M., Gomez, A., Grewing, M., van Leeuwen, F., van der Marel, H., Mignard, F., Murray, C. A., Penston, M. J., Petersen, C., Le Poole, R. S., & Walter, H. G. 1995, A&A, 304, 69

Persic, M. & Salucci, P. 1995, ApJS, 99, 501

Persson, S. E., Madore, B. F., Krzemiński, W., Freedman, W. L., Roth, M., & Murphy, D. C. 2004, AJ, 128, 2239

Piatti, A. E. & Geisler, D. 2013, AJ, 145, 17

Piersimoni, A. M., Bono, G., & Ripepi, V. 2002, AJ, 124, 1528

Press, W. H. & Schechter, P. 1974, ApJ, 187, 425

Rezaeikh, S., Javadi, A., Khosroshahi, H., & van Loon, J. T. 2014, MNRAS, 445, 2214

Ripepi, V., Cioni, M.-R. L., Moretti, M. I., Marconi, M., Bekki, K., Clementini, G., de Grijs, R., Emerson, J., Groenewegen, M. A. T., Ivanov, V. D., Molinaro, R., Muraveva, T., Oliveira, J. M., Piatti, A. E., Subramanian, S., & van Loon, J. T. 2017, MNRAS, 472, 808

Ripepi, V., Moretti, M. I., Marconi, M., Clementini, G., Cioni, M.-R. L., Marquette, J. B., Girardi, L., Rubele, S., Groenewegen, M. A. T., Grijs, R. d., Gibson, B. K., Oliveira, J. M., van Loon, J. T., & Emerson, J. P. 2012, MNRAS, 3283

Robin, A. C., Reylé, C., Derrière, S., & Picaud, S. 2003, A&A, 409, 523

—. 2004, A&A, 416, 157

Rubele, S., Girardi, L., Kerber, L., Cioni, M.-R. L., Piatti, A. E., Zaggia, S., Bekki, K., Bressan, A., Clementini, G., de Grijs, R., Emerson, J. P., Groenewegen, M. A. T., Ivanov, V. D., Marconi, M., Marigo, P., Moretti, M.-I., Ripepi, V., Subramanian, S., Tatton, B. L., & van Loon, J. T. 2015, MNRAS, 449, 639

Rubele, S., Girardi, L., Kozhurina-Platais, V., Goudfrooij, P., & Kerber, L. 2011, MNRAS, 414, 2204

Rubele, S., Girardi, L., Kozhurina-Platais, V., Kerber, L., Goudfrooij, P., Bressan, A., & Marigo, P. 2013, MNRAS, 430, 2774

Rubele, S., Kerber, L., Girardi, L., Cioni, M.-R., Marigo, P., Zaggia, S., Bekki, K., de Grijs, R., Emerson, J., Groenewegen, M. A. T., Gullieuszik, M., Ivanov, V., Miszalski, B., Oliveira, J. M., Tatton, B., & van Loon, J. T. 2012, A&A, 537, A106

Rubele, S., Pastorelli, G., Girardi, L., Cioni, M.-R. L., Zaggia, S., Marigo, P., Bekki, K., Bressan, A., Clementini, G., de Grijs, R., Emerson, J., Groenewegen, M. A. T., Ivanov, V. D., Muraveva, T., Nanni, A., Oliveira, J. M., Ripepi, V., Sun, N.-C., & van Loon, J. T. 2018, MNRAS, 478, 5017

Sabbi, E., Anderson, J., Lennon, D. J., van der Marel, R. P., Aloisi, A., Boyer, M. L., Cignoni, M., de Marchi, G., de Mink, S. E., Evans, C. J., Gallagher, III, J. S., Gordon, K., Gouliermis, D. A., Grebel, E. K., Koekemoer, A. M., Larsen, S. S., Panagia, N., Ryon, J. E., Smith, L. J., Tosi, M., & Zaritsky, D. 2013, AJ, 146, 53

Salaris, M. 2012, Ap&SS, 341, 65

Salaris, M. & Girardi, L. 2002, MNRAS, 337, 332

Sarajedini, A., Grocholski, A. J., Levine, J., & Lada, E. 2002, AJ, 124, 2625

Savage, B. D. & Mathis, J. S. 1979, ARA&A, 17, 73

Schaefer, B. E. 2008, AJ, 135, 112

Schaye, J. 2001, ApJ, 562, L95

Schlafly, E. F. & Finkbeiner, D. P. 2011, ApJ, 737, 103

Schlafly, E. F., Finkbeiner, D. P., Schlegel, D. J., Jurić, M., Ivezić, Ž., Gibson, R. R., Knapp, G. R., & Weaver, B. A. 2010, ApJ, 725, 1175

Schlegel, D. J., Finkbeiner, D. P., & Davis, M. 1998, ApJ, 500, 525

Schneider, D. P., Gunn, J. E., & Hoessel, J. G. 1983, ApJ, 264, 337

Schomaker, V., Waser, J., Marsh, R. E., & Bergman, G. 1959, Acta Crystallographica, 12, 600

Schommer, R. A., Suntzeff, N. B., Olszewski, E. W., & Harris, H. C. 1992, AJ, 103, 447

Scowcroft, V., Freedman, W. L., Madore, B. F., Monson, A., Persson, S. E., Rich, J., Seibert, M., & Rigby, J. R. 2016, ApJ, 816, 49

Skowron, D. M., Jacyszyn, A. M., Udalski, A., Szymański, M. K., Skowron, J., Poleski, R., Kozłowski, S., Kubiak, M., Pietrzyński, G., Soszyński, I., Mróz, P., Pietrukowicz, P., Ulaczyk, K., & Wyrzykowski, Ł. 2014, ApJ, 795, 108

Skrutskie, M. F., Cutri, R. M., Stiening, R., Weinberg, M. D., Schneider, S., Carpenter, J. M., Beichman, C., Capps, R., Chester, T., Elias, J., Huchra, J., Liebert, J., Lonsdale, C., Monet, D. G., Price, S., Seitzer, P., Jarrett, T., Kirkpatrick, J. D., Gizis, J. E., Howard, E., Evans, T., Fowler, J., Fullmer, L., Hurt, R., Light, R., Kopan, E. L., Marsh, K. A., McCallon, H. L., Tam, R., Van Dyk, S., & Wheelock, S. 2006, AJ, 131, 1163

Soszyński, I., Udalski, A., Szymański, M. K., Kubiak, M., Pietrzyński, G., Wyrzykowski, Ł., Szewczyk, O., Ulaczyk, K., & Poleski, R. 2009, Acta Astron., 59, 1

Stanek, K. Z. & Garnavich, P. M. 1998, ApJ, 503, L131

Stanimirović, S., Staveley-Smith, L., Dickey, J. M., Sault, R. J., & Snowden, S. L. 1999, MNRAS, 302, 417

Stanimirović, S., Staveley-Smith, L., & Jones, P. A. 2004, ApJ, 604, 176

Staveley-Smith, L., Kim, S., Calabretta, M. R., Haynes, R. F., & Kesteven, M. J. 2003, MNRAS, 339, 87

Stetson, P. B. 1987, PASP, 99, 191

Subramaniam, A. 2003, ApJ, 598, L19

—. 2004, ApJ, 604, L41

—. 2005, A&A, 430, 421

Subramaniam, A. & Subramanian, S. 2009, ApJ, 703, L37

Subramanian, S., Rubele, S., Sun, N.-C., Girardi, L., de Grijs, R., van Loon, J. T., Cioni, M.-R. L., Piatti, A. E., Bekki, K., Emerson, J., Ivanov, V. D., Kerber, L., Marconi, M., Ripepi, V., & Tatton, B. L. 2017, MNRAS, 467, 2980

Subramanian, S. & Subramaniam, A. 2009, A&A, 496, 399

—. 2010, A&A, 520, A24

—. 2012, ApJ, 744, 128

—. 2013, A&A, 552, A144

—. 2015, A&A, 573, A135

Tatton, B. L., van Loon, J. T., Cioni, M.-R., Clementini, G., Emerson, J. P., Girardi, L., de Grijs, R., Groenewegen, M. A. T., Gullieuszik, M., Ivanov, V. D., Moretti, M. I., Ripepi, V., & Rubele, S. 2013a, A&A, 554, A33

—. 2013b, VizieR Online Data Catalog, 355, 49033

Toomre, A. & Toomre, J. 1972, ApJ, 178, 623

Torres-Flores, S., Barbá, R., Maíz Apellániz, J., Rubio, M., Bosch, G., Hénault-Brunet, V., & Evans, C. J. 2013, A&A, 555, A60

Udalski, A. 2000, ApJ, 531, L25

—. 2003, ApJ, 590, 284

Udalski, A., Szymanski, M., Kaluzny, J., Kubiak, M., & Mateo, M. 1992, Acta Astron., 42, 253

Udalski, A., Szymanski, M., Kubiak, M., Pietrzynski, G., Wozniak, P., & Zebrun, K. 1998, Acta Astron., 48, 1

Udalski, A., Szymański, M. K., & Szymański, G. 2015, Acta Astron., 65, 1

van Albada, T. S., Bahcall, J. N., Begeman, K., & Sancisi, R. 1985, ApJ, 295, 305

van der Marel, R. P. 2001, AJ, 122, 1827

van der Marel, R. P. 2006, in The Local Group as an Astrophysical Laboratory, ed. M. Livio & T. M. Brown, Vol. 17, 47–71

van der Marel, R. P., Alves, D. R., Hardy, E., & Suntzeff, N. B. 2002, AJ, 124, 2639

van der Marel, R. P. & Cioni, M. 2001, AJ, 122, 1807

van der Marel, R. P. & Kallivayalil, N. 2014, ApJ, 781, 121

van der Marel, R. P., Kallivayalil, N., & Besla, G. 2009, in IAU Symposium, Vol. 256, The Magellanic System: Stars, Gas, and Galaxies, ed. J. T. Van Loon & J. M. Oliveira, 81–92

Van der Swaelmen, M., Hill, V., Primas, F., & Cole, A. A. 2013, A&A, 560, A44

van Loon, J. T., Bailey, M., Tatton, B. L., Maíz Apellániz, J., Crowther, P. A., de Koter, A., Evans, C. J., Hénault-Brunet, V., Howarth, I. D., Richter, P., Sana, H., Simón-Díaz, S., Taylor, W., & Walborn, N. R. 2013, A&A, 550, A108

van Loon, J. T., Gilmore, G. F., Omont, A., Blommaert, J. A. D. L., Glass, I. S., Messineo, M., Schuller, F., Schultheis, M., Yamamura, I., & Zhao, H. S. 2003, MNRAS, 338, 857

van Loon, J. T., Marshall, J. R., & Zijlstra, A. A. 2005, A&A, 442, 597

Wakker, B. P. 2001, ApJS, 136, 463

Walker, A. R. 2012, Ap&SS, 341, 43

Walter, F., Brinks, E., de Blok, W. J. G., Bigiel, F., Kennicutt, Jr., R. C., Thornley, M. D., & Leroy, A. 2008, AJ, 136, 2563

Weinberg, M. D. & Nikolaev, S. 2001, ApJ, 548, 712

Weisz, D. R., Dolphin, A. E., Skillman, E. D., Holtzman, J., Dalcanton, J. J., Cole, A. A., & Neary, K. 2013, MNRAS, 431, 364

Welch, D. L., McLaren, R. A., Madore, B. F., & McAlary, C. W. 1987, ApJ, 321, 162

White, S. D. M. & Frenk, C. S. 1991, ApJ, 379, 52

White, S. D. M. & Rees, M. J. 1978, MNRAS, 183, 341

Wong, T., Hughes, A., Ott, J., Muller, E., Pineda, J. L., Bernard, J.-P., Chu, Y.-H., Fukui, Y., Gruendl, R. A., Henkel, C., Kawamura, A., Klein, U., Looney, L. W., Maddison, S., Mizuno, Y., Paradis, D., Seale, J., & Welty, D. E. 2011, ApJS, 197, 16

Zaritsky, D. 2004, ApJ, 614, L37

Zaritsky, D., Harris, J., Thompson, I. B., & Grebel, E. K. 2004, AJ, 128, 1606

Zaritsky, D., Harris, J., Thompson, I. B., Grebel, E. K., & Massey, P. 2002, AJ, 123, 855

Zhao, H. & Evans, N. W. 2000, ApJ, 545, L35

Zwicky, F. 1933, Helvetica Physica Acta, 6, 110